Assessment of the ternary phase diagram on the stoichiometric and hypo-stoichiometric U-Nd-O system

Bernardo Herrero Bocco

université
PARIS-SACLAY

Assessment of the ternary phase diagram on the stoichiometric and hypo-stoichiometric U-Nd-O system

Thèse de doctorat de l'Université Paris-Saclay

École doctorale n° 573, Interfaces : approches interdisciplinaires, fondements, applications et innovation
Spécialité de doctorat: Physique
Unité de recherche: Université Paris-Saclay, CentraleSupélec, CNRS, Laboratoire SPMS, 91190, Gif-sur-Yvette, France.
Référent: : CentraleSupélec

Thèse présentée et soutenue à Cadarache, le 6 fevrier 2020, par

Bernardo HERRERO

Composition du jury:

Hans Seifert Professeur, KIT, Karslruhe	Président
Olivier Masson Professeur, IRCER, Université de Limoges	Rapporteur
Olivier Tougait Professeur, UCCS, Université de Lille	Rapporteur
Christine Guéneau Directeur de recherche, CEA, Saclay	Examinatrice
Nicolas Clavier Chargé de recherche, ICSM, Marcoule	Examinateur
Lionel Desgranges Ingénieur de recherche, CEA, Cadarache	Examinateur
Fabienne Audubert Directeur de recherche, CEA, Cadarache	Co-directrice
Gianguido Baldinozzi DR2, Centrale Supélec, Université de Paris-Saclay	Directeur

Thèse de doctorat

NNT: 2020UPASC008

Acknowledgements

This PhD would have not been possible without the support of a number of people who helped me moving forward across the different circumstances during these past three years. For you all, I dedicate a few words to express my gratitude.

First, I would like to begin with the president and rapporteurs of the jury: Pr. Seifert, Pr. Masson and Pr. Tougait to find the time to read my work and to contribute with precious insights during the thesis defense.

Secondly, to the also members of the jury: Christine Guéneau, Nicolas Clavier and Lionel Desgranges. Christine, thank you for your time, your patience and goodwill to help me throughout the most stressful moments of my PhD. You have been an example of professionalism and a compass that pointed North. Nicolas, the help you gave me was priceless. I would not have been able to do this work neither without the samples, nor the experiments that you facilitate. Thank you to find the time to work with me, to receive me each time I needed to go to the ICSM, or to exchange emails at every moment. And Lionel, thank you for the hours you dedicated on every discussion. It was because of your most imaginative ideas that I end up asking myself the most fundamental questions.

Next, I would like to thank my thesis director, Gianguido Baldinozzi. Thank you, Guido, for everything you told me. Thank you for always being there, for the endless amount of emails we exchanged, but most of all, for that human decency that defines you. The following person I would like to thank is Fabienne Audubert. A few words would not suffice to express my gratitude for everything you have done. You were there from the moment zero, and still there until the end. Thank you for your time, your patience and for always showing your human sensible side, you told me not only to be a better scientist but also to be a better person.

I will pass now on to all my colleagues of the CEA in Cadarache. Starting from the service, thank you Beatrice and Chrystelle for being open to dialogue regardless the problem, and for always letting us know, the students, that we are not on our own. Respecting the laboratory LAMIR, Isabelle, thank you for making my work easier each time a situation came up, you

were always supportive and showed goodwill over the few problems I encountered throughout the PhD. A special mention should be made for Fred and Patrice, who made of all the experiments we did the most grateful and fruitful moments. Thanks to the Jeremies (Jeremy and Jeremie) for the moments we shared both at work and outside of it. Thanks also to all the co-workers for showing the best mood every day, they are Hélène, Sidonie, Seb, Jean-Christophe, Yves, Franck, Kélian, Guillaume, Marion...

Special words are dedicated to Corine. Thank you, Corine, for being so kind and so willing to help others. The French administration was as challenging as any other topic I came across during my PhD. You were there to help me every time I needed and I consider myself lucky that we worked only two offices away.

To the colleagues of the LCPC laboratory, thank you Doris for being so kind and professional at all times, for the time we spent at the TMN or doing the GMN, working with you was always pleasant and easy. Also thank you, Andréa and Nico, for the metallo and XRD experiments, throughout the whole three years of the PhD. Thank you also, Renaud, for assist me every time with the refinements or the experiments, your help was always precious. For the experiments performed at CEA, Saclay. Thank you, Dominique, for the time you dedicated to me and the goodwill you showed at every moment during my time at Saclay. I would like also to thank Martiane, of the laboratory CP2M of the Université Aix-Marseille, your sympathy made always a pleasant moment while getting the thin films by FIB, or taking those images by SEM or TEM.

Thanks to my friends in Aix for the special moments we shared, the biers, laughs, birthdays, for making my PhD a moment I will remember forever. Thanks to all my friends in Argentina, particularly Fede, Andre, Nicope, Andrés, Nadu, Sole, Carlitos, Kito, Negro, Nico..., who helped me and showed me their support at all times, you were there even before I stepped foot in France. A special mention goes to Ernesto. Sato, thank you for lifechanging the opportunity you gave me by telling me of the open position and thank you for always being there, even it was not the best moment.

I will pass now to one of the most important people in my life, Claire Le Gall. Chick, you were the most influential person during my PhD. Beside the scientific discussions, proposals, posters, publications, presentations, calculations or even French lessons, we spent two unforgettable years. All the laughs, songs we heard and things we shared, motivated me and put a smile on me to face the difficulties on every single day. As I say to you

every day, which is as true as it was the first day, I am the luckiest man on the world for having you by my side.

Las últimas palabras de mis agradecimientos son para mi familia. Gracias a mis padres por el apoyo incondicional y por sus palabras del día a día para sobrellevar todos y cada uno de mis desafíos. Y por último, gracias a mis hermanos, Gorda, Fercho, Vale, Meli y Lourdes por darme ese aliento y esas ganas de volver a la Argentina que me hacen sentir en mi hogar en todo momento.

Contents

Introduction and objectives

"La terre nous en apprend plus long sur nous que tous les livres. Parce qu'elle nous résiste. L'homme se découvre quand il se mesure avec l'obstacle."

-Antoine De Saint-Exupéry

Economic and industrial context

A sustainable and balanced energetic matrix is essential for any society to develop a robust economy. Fossil fuel such as coal, crude oil or natural gas, represents today around the 80% of the world energy supply [1]. These types of energies have been wildly used to provide any ordinary citizen as well as the industrialized nations affordable energy to enable the use of state of the art technology, economic grow and higher quality of life. Even if the world's most accessible reserves of fossil fuel have been significantly depleted, new and more complex techniques to extract these types of fuel are in constant development, which means that the extraction of fossil fuels is increasingly more expensive and yields a lower energy return on energy invested. Furthermore, there is a global consensus on the impact of carbon emissions on the climate of our planet. This situation is further aggravated by continue population growth and accumulation of wealth at rates where the difference between the energy needed and the energy provided by the society is increasingly higher [2]. In this context, nuclear energy provides a middle-term valuable alternative capable of playing a key role on balancing the energy matrix. Indeed, one of the most important benefits of using nuclear energy is the low carbon emissions to the atmosphere. The difference on the greenhouse gas emissions between nuclear power plants with coal-fired power plants is very significant (20 g CO_2/kW.h vs 1000 g CO_2/kW.h) [3]. For this reason, nuclear energy along with the other sustainable types of energy such as photovoltaic, wind or hydroelectric plays a major role on powering the world's future.

Pressurized Water Reactors (PWR) and Boiling Water reactors (BWR) are nuclear reactors that have been developed for over six decades. These reactors are capable of working using an enriched amount of ^{235}U ($\sim$5%). In the case of PWR, this reactor is also designed to work with mixed oxides (MOX) fuel where the fissile cores are based of ^{235}U (contained in depleted uranium), but also of ^{239}Pu ($\sim$8%). More innovative types of reactors are still today being developed to produce energy by burning a large part of the waste produced in conventional PWR and BWR. These

reactors are named as Generation IV, and they are meant to run with concentrations of Pu sensibly higher than those of the MOX fuels (from 23 to 45% ^{239}Pu).

Independently the type of reactor, all nuclear reactors are designed under the same mechanism: the generation of energy after self-sustaining chain reactions that produce neutrons, fission products (FP) and energy. The FP are not randomly produced inside the nuclear reactor. On the contrary, the fission of a fissile core results in the formation of two atoms with different mass, one lighter and another heavier. The bimodal distribution of FP for ^{235}U is presented in Figure 1. Among the high yield FP it is possible to distinguish mainly Xe, Zr, Nd, Ce, La, Y, Eu and Pr [4].

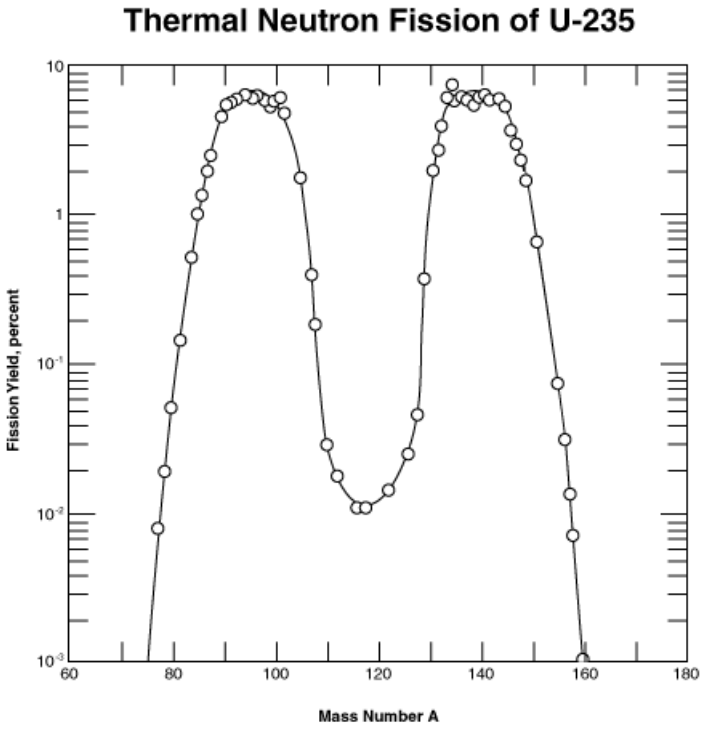

Figure 1: Distribution of FP after the fission reaction for ^{235}U.

During operational conditions, the fission reactions do not take place uniformly along the nuclear pellet. In UO_2-based PWRs there is a higher density of nuclear reactions (or local burn-up) at the external rim of the pellet, since the ^{235}U atoms located in this region are more likely to react with the neutron located on the putter side of the fuel pin. In the case of MOX fuels, the local burn-up is concentrated around the regions enriched with ^{239}Pu, which are distributed along the fuel pellet. These regions affected with higher local burn-up present sensible microstructural changes respecting initial the grain size and pore density, defining a particular structure commonly known as High Burn-up Structure (HBS). On the HBS region there is an important accumulation of FP [5–10]. Figure 2a displays the burn-up profile along with the retained Xe on the matrix of the fuel and Figure 2b shows the Nd

concentration profile respecting the radius of the pellet. In both cases the amount of FP at the external region is higher than the inner region.

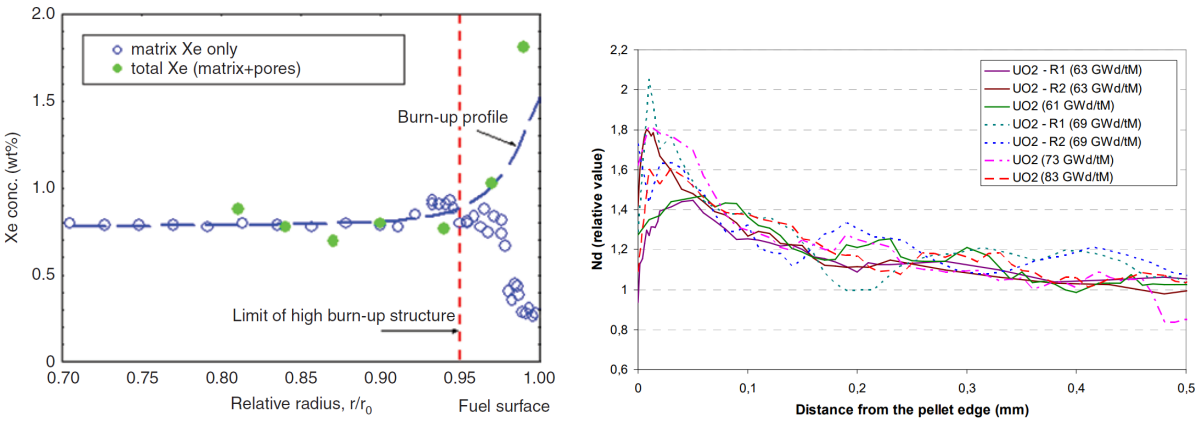

(a) (b)

Figure 2: (a) Burn-up profile and Xe retained fraction along the relative radius and (b) Nd concentration profile along the distance from the pellet edge of UO_2-based fuel. [7, 10] .

FP can be found under many forms in irradiated fuel, some can be found under the form of precipitates, others are found as gas FP, and others dissolved on the UO_2 matrix. However, it is the chemical concentration of soluble FP the one capable for changing sensibly the properties of irradiated fuel, such as the oxygen chemical potential (μ_{O_2}) or the thermal conductivity, among others. Therefore, in order to better understand the behavior and thermochemical properties of irradiated fuel, it is of great interest to study different UO_2-based systems doped with soluble FP. In this scenario, the study of the U-Nd-O system is of major importance, since Nd is the most abundant lanthanide of all, and represents an important fraction of the nuclear inventory [8]. Therefore, this work focuses on the assessment of the solubility of Nd in order to define the U-Nd-O system.

Scientific context and aim of the dissertation

Fuel development and qualification are traditionally spread over decades, and the process is costly. The basis for fuel development has long been empirical and experience based since the underlying physical mechanisms are not fully understood. This is especially true for fuel fabrication where the experienced-based approach is generally used to establish a basic recipe that provides a consistent and reproducible industrial product. Parametric studies lead to a limited understanding of the effects of process variables because of the system complexity (multi-scale problem). Among the advanced fuel candidates, lanthanide-doped urania, dispersion fuels and transmutation fuels reducing actinide inventories using PWR are particularly important systems. Spent fuels are also important systems that require accurate description to

predict their long-term behavior in interim and final storage conditions. While fuels were already irradiated in test reactors, the limited neutron exposure and limited available irradiation temperatures that are and will be available will be insufficient to fully understand their structural behavior and their microstructural stability during commercial operation, waste management, and accident conditions. The primary irradiation effects occurring in fuels during commercial operation are swelling, decrease in thermal conductivity, and changes in mechanical properties. Swelling at low temperature is generally related to defect accumulation. The number of surviving defects at a given temperature depends on the diffusion and recombination of point defects that reduces the lattice strain, which is related to the structural and microstructural characteristics of the fuel that determine the transport properties. The knowledge of the phase occurring in these systems is an important starting point for modelling and predicting how those mechanisms change the properties of the fuels. The thermal conductivity of all ceramics degrades with neutron irradiation and tends to saturate at a very low dose (less than 1 dpa). The cause of this degradation in thermal conductivity is phonon-scattering by irradiation-induced defects (primarily vacancies and small vacancy clusters). Although the unirradiated thermal conductivity is dependent on the sample material and processing route, the thermal conductivity following radiation is a function of the radiation parameters that drive the final microstructures. The knowledge of the possible phases occurring at-the-equilibrium and out-of-equilibrium in the substituted urania fluorite structure are again an important factor for understanding and predicting these effects. Similar considerations apply to the description of the effects of irradiation on the strength, elastic modulus, or fracture toughness of ceramics, especially at intermediate and high temperature.

The current industrial fabrication process for conventional oxide fuels is based on a dry powder route [11]. This is typically made by blending and milling two powders in several stages to obtain a material that can be compacted and that will give the required homogeneity and microstructure after sintering at high temperature. This process is very compatible with separation processes as they yield the separated products in oxide form, the most stable chemical form of the actinides under atmospheric conditions. Unfortunately, this process also involves high temperature reduction processes that can be incompatible with the volatility of some compounds (for instance americium) that can lead to process losses that need to be captured and recycled in other ways. Also, the cooling down to room temperature of these nuclear fuel pellets produced at high temperature can leave them in out-of-equilibrium conditions that display properties that cannot be extrapolated from at equilibrium systems. This can be addressed by reducing process temperatures, and possibly by novel fabrication processes, but this is certainly beyond the understanding provided by a conventional parametric study approach. Structural and thermodynamic data, combined with fundamental material properties, is used for mechanistic models in fuel performance codes, which can be employed for predicting behavior beyond existing experimental data. However, there is a substantial lack of knowledge on fundamental materials properties even for conventional unirradiated fuel materials, and essentially no information exists for most of the advanced actinide/lanthanide containing fuels.

This situation has persisted for three main reasons. First, the experimental basis for the properties of most simple compounds of the minor actinides is small, principally because the engineering needs did not exist in the past. Second, many of the required experiments are complicated: not only the materials can be radioactive, but inherent difficulties exist due to the fact that the properties of these systems can change sharply with composition. Third, reliable fundamental thermochemical and thermophysical information cannot yet be generated using computational techniques due to the lack of an adequate underlying theory for the electronic structures in actinides.

This dissertation tries to provide elements to describe the thermochemical and thermophysical properties of two different ternary systems: U-Nd-O and U-Ce-O, relevant for advanced fuels. Accurate modeling of these systems has been unsuccessful to date because of the complicated electronic structure associated with these materials where the behavior of 5f-electrons is the controlling parameter. Specific attention is devoted to microstructural evolution because of its effects on the thermomechanical response of fuel. Many of the mechanisms relevant to microstructure evolution in these systems seem to involve into complex structures where oxygen sublattice defects and cation substitutions can order, and some of those features can be of kinetic origin rather than at-the-equilibrium features. These structural and microstructural features influence the atomistic behavior of point defects and the way they cluster, the fission gas nucleation, migration, coalescence, bubble growth, and also phases and precipitate formation and their thermal evolution under irradiation. Pieces of this information are intended to enable the development of atomistic simulations for these systems where a strong interaction between structure and defect migration and accumulation is expected. For these reasons, a research effort is required to analyze the impact of synthesis approaches and processes for advanced nuclear fuel forms that include sol-gel techniques and soft chemistry processes that can change drastically the sintering protocols and the atomistic distributions of the system components. These methods hold promise for controlling the structural characteristics of the fuel as well as the distribution of substituted ions and stoichiometry of these innovative fuels. We believe that this reassessing of the structures and microstructures observed in U-Nd-O and U-Ce-O systems can provide key elements for advancing in the challenge to develop a fundamental understanding of these complex multicomponent and multiphase systems that irradiation is driving far from equilibrium.

Organization of the manuscript

This dissertation describes mainly the experimental characterization and thermodynamic modeling of the U-Nd-O system on stoichiometric and hypo-stoichiometric conditions. A critical review of published experimental data of the three composing binaries as well as the U-Nd-O ternary phase diagram, crystallographic structures, and thermodynamic properties are presented in Chapter 1. This chapter also includes the comparison with similar U-Ac,Ln-O systems (where Ac=Pu and Ln= Ce, La and Gd). This review highlights the experimental conditions needed to evaluate the cur-

rent miscibility gap predicted for the U-Nd-O system and the possible shortcomings of this description. Chapter 2 addresses these shortcomings by extended characterization of the Nd-doped samples by different techniques Scanning Electron Microscopy (SEM), Transmission Electron Microscopy (TEM), X-ray Diffraction (XRD) and X-ray Absorption Spectroscopy (XAS)). Thermal annealing is also performed under controlled reducing conditions. In Chapter 3 *in-situ* High Temperature-XRD (HT-XRD) and a high temperature thermal annealing experiments are carried out to probe the system maintained in substoichiometric conditions at lower oxygen to metal (O/M) ratios. This chapter also analyses experimentally the U-Ce-O system to establish a direct comparison of the phase diagrams between these two systems. Finally, in Chapter 4, the data collected in this work are used to revise and optimize the initial thermodynamic model of the U-Nd-O system using the CALPHAD method.

Chapter 1

Review of the literature data on the chemistry of UO_2-based solutions

"Science is the father of knowledge, but opinion breeds ignorance."

-Hippocrates

The first part of this work is dedicated to analyze experimentally the U-Nd-O system, making a particular focus on the presence of the miscibility gap, and the second place of this work intents to develop a thermodynamic model to describe as precisely as possible the ternary system U-Nd-O using the CALPHAD method. Therefore, to initiate this work it is crucial to make a critical review of the published data. For this purpose, this section presents an overview of the crystal structures, phase diagrams and thermodynamic properties of the three binaries of the U-Nd-O system. In addition, a global review of the different U-Ac,Ln-O systems (being Ac=Pu and Ln=Ce, La, Gd) is made about their phase diagrams and the experimental conditions used to describe them. This overview reflects the starting point for the optimization of the existent thermodynamic model of the U-Nd-O system.

1.1 The U-Nd-O ternary system

The first step on the assessment of an existing ternary system is to carefully evaluate existent data related to it. The necessary data to describe a ternary system and define its thermodynamic model can be classified basically into three groups. They are:

- Phase diagram: all phase diagrams must be considered. In a ternary system it is first necessary to define all three possible binaries and then the ternaries at different temperatures.
- Crystallographic structure: the description of the spatial symmetry and motif of all atoms, oxidation states, vacancies or interstitial defects.

- Experimental thermodynamic properties: they are necessary to define the end members or to fit the model, like the formation enthalpy, the standard Gibbs free energy, the heat capacity, the enthalpy increment or the oxygen chemical potential.

1.1.1 The U-O system

Phase diagrams

The U-O system has been studied over the years due to its importance in nuclear power plants. A critical assessment of the thermodynamic properties such as chemical potential, melting point, oxygen solubility or heat capacity of the stoichiometric and sub-stoichiometric UO_2 region, as well as the U_4O_9 and U_3O_8 phases allows to have a fair description of the U-O system. All this information was compiled by Guéneau *et al.* to model this system through the CALPHAD method in [12], leading to the binary diagram in Figure 1.1.

According to this diagram, the formation of U^{+3} below 1500 K is not possible. This means that for the stoichiometric UO_2 (when the molar fraction of O equals to 0.66), the equilibrium below this temperature for the hypo-stoichiometric region is only shared between stoichiometric UO_2 and metallic uranium.

Metallic uranium can exist under different polymorphs depending on the temperature [13]. From room temperature until 961 K, it exists as orthorhombic α-phase, from 961 K until 1048 K it exists as tetragonal β-phase, and from 1048 K until its melting point, 1407 ± 20 K, it exists as body-centered cubic γ-phase.

At higher temperatures, liquid uranium is at equilibrium with UO_{2-x} [14–16]. However, a miscibility gap has been identified for the liquid phase at 3090 K [17]. These results helped to describe the transition between the liquid phase rich in uranium and the fluorite phase with near stoichiometric oxygen content at 2709 K.

Unlike the hypo-stoichiometric region, the hyper-stoichiometric region of UO_{2+x} starts to appear at a much lower temperature, that is around 500 K. The formation of interstitials of oxygen on the anionic sublattice on stoichiometric UO_2 is more favored than the formation of vacancies. However, at room temperature UO_2 will be only in equilibrium with U_4O_9, since the fluorite phase of UO_2 cannot stabilize the presence of oxygen on an interstitial position [18, 19].

Between room temperature and 1400 K, U_4O_9 can exist under different polymorphs [20–24]. They are the α-U_4O_9 (space group R3c), which is stable from room temperature until 353 K. It transforms into $\beta - U_4O_9$ (space group $F\bar{4}3d$), stable until 873 K, followed by a transition to its final polymorphic state under the form of γ-U_4O_9, stable between 873 K and the maximum temperature of 1400 K [25, 26].

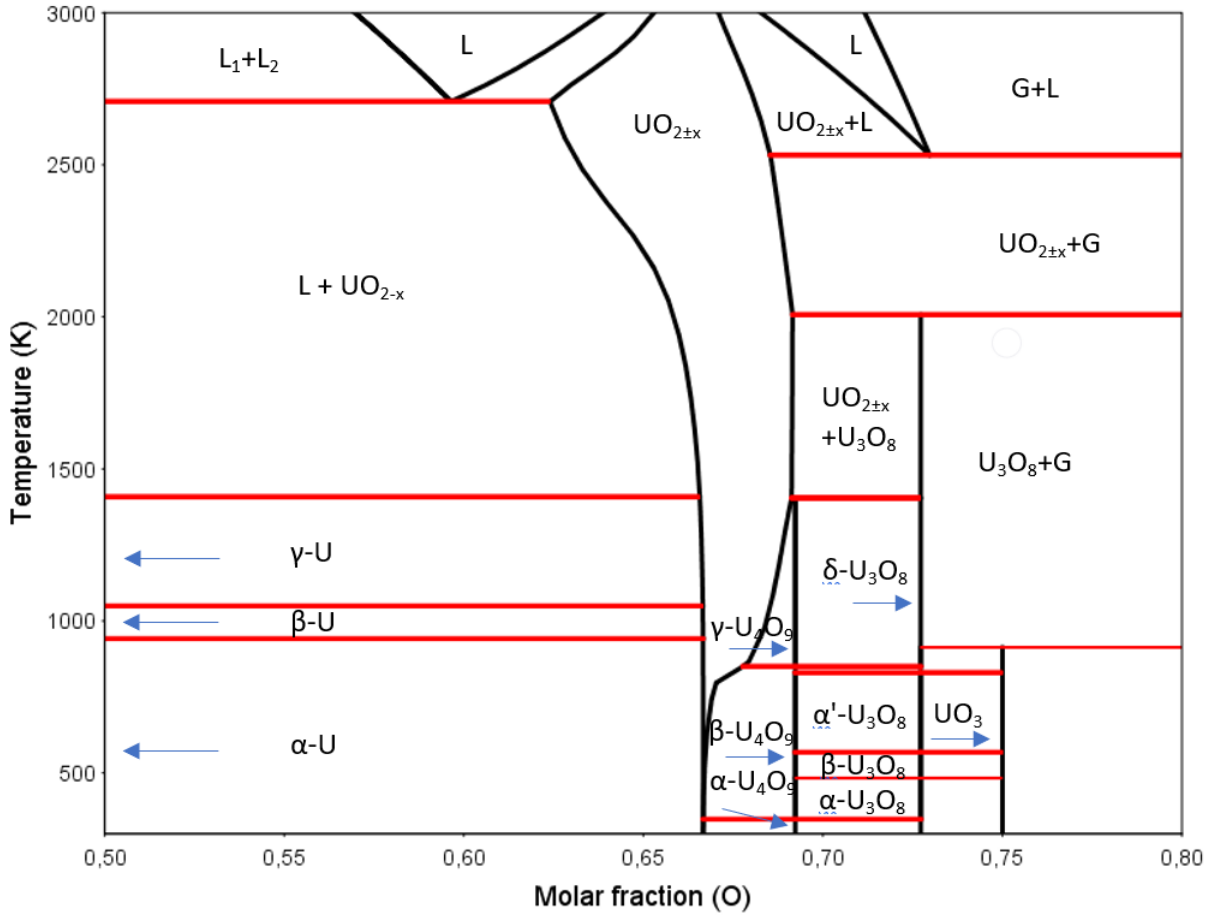

Figure 1.1: Representation of the U-O binary diagram according to the model developed by Guéneau *et al.* in [12]. Solids are presented according to their chemical formula and the liquid and gas phases are presented as L and G, respectively.

The region of existence of U_3O_8 is not completely defined. The domain of existence of the U_3O_{8-x} can change according to the authors, some of them have found a coexistence between $\gamma - U_4O_9$ and different intermediate phases such as γ-U_3O_8 [27] or γ-U_5O_{13} [28], others defined at lower temperatures a coexistence between the phases α-U_4O_9 or β-U_4O_9 with α-U_3O_7, β-U_3O_7 or γ-U_3O_7 and U_3O_7 with U_3O_8 too [29–34]. Finally, UO_3 can be present also under several polymorphs, they are α, β, γ, δ and $\epsilon - UO_3$, also several authors have identified an amorphous UO_3 phase [35–38].

Crystallographic structure

$UO_{2\pm x}$

$UO_{2\pm x}$ is spatially organized according to the fluorite-type structure. This structure was initially defined after calcium fluoride (CaF_2) and is the one that describes many UO_2-based systems doped with different lanthanides (La, Ce, Gd, Nd) or ac-

tinides (Am, Pu) [39–56]. The space group is $Fm\bar{3}m$ (number 225).

Stoichiometric UO_2 displays a perfect fluorite long-range structure, where uranium atoms have formally an oxidation state of +4. All uranium atoms are located at face-centered cubic (FCC) positions, with coordination number 8, and all oxygen atoms occupy the tetrahedral sites, with coordination number 4. Figure 1.2 shows the atomic disposition of the atoms of uranium and oxygen on the fluorite structure for stoichiometric UO_2.

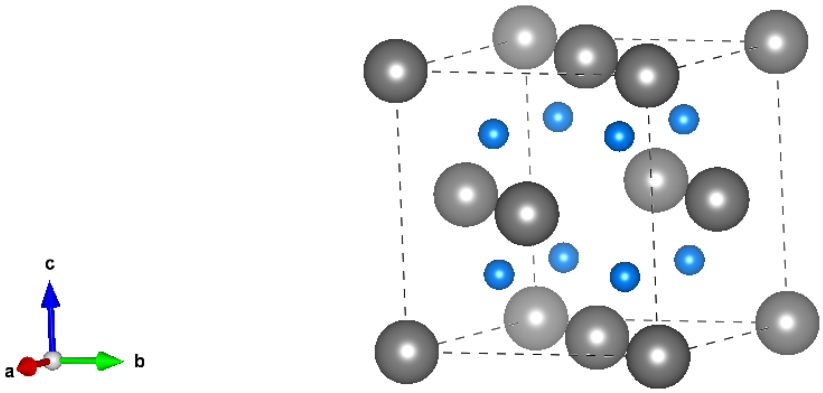

Figure 1.2: Fluorite structure of UO_2, the grey spheres represent the atoms of uranium and the blue spheres represent the atoms of oxygen.

The fluorite structure has a cubic unit cell with a lattice parameter (a) equal to 5.47127(8) Å (at 293 K and O/U ratio of 2.000(1)) [57]. The presence of defects change the original stoichiometry of UO_2 such as vacancies or interstitials on the anionic sublattice and have consequences upon the symmetry of the resulting structures.

UO_2 consists formally of U^{+4}. Nevertheless, at higher temperatures uranium can also exist as U^{+3}, that causes the local relaxation of the oxygen environment and increases its volume [58]. In contrast, the excess of oxygen will create interstitial and vacancy defects, and U^{+4} oxidizes to U^{+5} to maintain the local charge neutrality of the system [18, 59, 60].

Oxygen atom positions in a single crystal with composition of $UO_{2.13}$ were assessed by neutron diffraction by Willis *et al.* and Murray *et al.* in several papers [44, 61–63] . Oxygen is at three different specific sites for this hyper-stoichiometric sample. These three particular oxygen sites were referred as O, for the oxygen atoms located at the classic fluorite positions, O' and O" , for the interstitial oxygen atoms, displaced 1 Å along the directions $< 110 >$ and $< 111 >$, respectively. The displacement of

these oxygen atoms is associated with oxygen vacancies. This mechanism of atomic rearrangement leads to the idea that oxidation of UO_2 develops through the formation of defect groups, e.g. 2:2:2 clusters or Willis defects. An illustration of the anionic sublattice showing the 2:2:2 defect is presented in Figure 1.3.

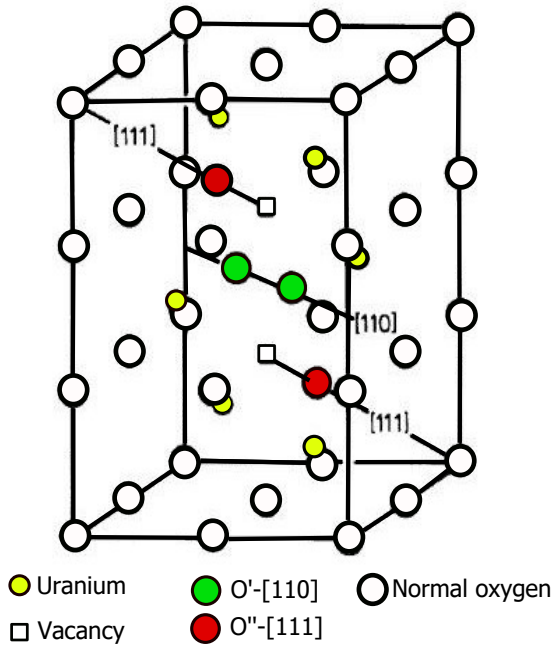

Figure 1.3: The 2:2:2 cluster defect proposed by Willis *et al.* [63].

At higher O to U ratios, the initial structure develops more complex fluorite-related phases where anion excess forms clusters with different rearrangements such as the cuboctahedron unit U_6O_{36} or U_6O_{37} [61, 63].

U_4O_9

Depending on the temperature, U_4O_9 can be present under different phases. From room temperature, until 350 K U_4O_9 is stable as α-U_4O_9. A first attempt to describe the transition of the structure α-U_4O_9 to the structure β-U_4O_9 was made using X-ray diffraction [20]. These results on attempting the characterization of the structure of the α-U_4O_9 were not conclusive, but they indicate that it might present a trigonal structure with the space group R3c, number 161. Even today, a number of studies through different techniques such as X-ray diffraction or neutron diffraction to characterize the atomic arrangement of the α-U_4O_9 phase are still in progress [19, 21, 24, 25].

Unlike the α-U_4O_9 phase, the β-U_4O_9 has been well described by a number of authors. Different studies agreed that the structure of β-U_4O_9 develops a long-range ordering superlattice in which a single unit cell contains 4x4x4 fluorite-related subcells [20, 21, 31, 61, 63], with the space group $I\bar{4}3d$, number 220. The arrangement of atoms

is related to the one on the fluorite structure. Its cationic sublattice remains FCC composed by uranium atoms, however, the anionic sublattice hosts a cuboctahedron cluster instead of a cube, like the one seen in Figure 1.2 for UO_2. This arrangement is composed by 12 oxygen atoms placed in all the 12 vertices of the cuboctahedron plus a 13^{th} placed in the center, see Figure 1.4. The 5 extra oxygen atoms of the β-U_4O_9 compared to stoichiometric UO_2 affect the O to U ratio (2.2345 instead of 2.25) [13, 21].

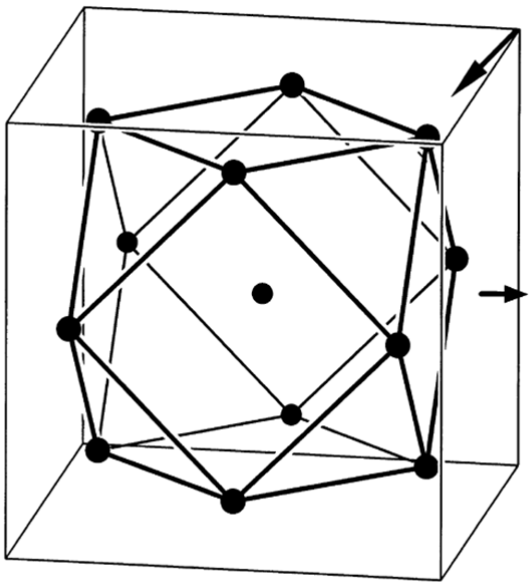

Figure 1.4: Oxygen motif of β-U_4O_9 proposed by Willis [61]. The outer cube stands is the uranium sublattice and the inner cuboctahedron presents the arrangement of the oxygen atoms with 12 vertices and an extra oxygen atom in its center. The arrows (out of scale) show the relaxation of the neighboring atoms of uranium (not shown) from their original fluorite positions [21, 22, 31] .

The third polymorphic phase of U_4O_9 is the γ-U_4O_9, which appears above 873 K [64]. The accurate description of the crystallographic structure of γ-U_4O_9 is still in progress [23], however, numerous authors suggest that the anionic sublattice can also be represented, similarly to β-U_4O_9, through the arrangement of cuboctahedral clusters [31, 64].

U_3O_7

U_3O_7 is not a thermodynamically stable compound and it is capable of transforming into a mixture of U_4O_9 and U_3O_8 [65]. Desgranges *et al.* showed that oxidation of U_3O_7 can start only 17 hours after its formation at temperatures as low as 483 K [25]. U_3O_7 has been identified in three polymorphic states, α, β and γ. All these 3

phases display a tetragonal distortion. The ordering of the clusters varies; this affects the unit cell parameters. For the α-U_3O_7, the c/a ratio is the shortest of all three phases, c/a=0.986-0.989 with the space group I/4m, number 87 [31], whereas for the β-U_3O_7 c/a=1.03-1.034 with a space group of $I\bar{4}2d$ [25, 31]. Finally, the c/a ratio for γ-U_3O_7 is 1.016. The group of γ-U_3O_7 is still unknown [30, 31].

U_3O_8

U_3O_8 can exist under two different crystallographic forms, α-U_3O_8 and β-U_3O_8. Normally α-U_3O_8 is found, which has space group C2mm, number 38, but under special circumstances of oxidizing atmospheres and temperatures (1623 K) β-U_3O_8 is obtained [66], with space group Cmcm, number 63. The transition to the hexagonal UO_3 structure when heated in air is at 523 K. However, this value is very sensitive to pressure; it was found that under primary vacuum conditions the temperature can increase up to 673 K [67].

The crystallographic structure of α-U_3O_8 and β-U_3O_8 are related to α and γ UO_3 phase, also orthorhombic. In α-U_3O_8 the missing oxygen atom is located on the third row of UO_3, whereas in β-U_3O_8 two oxygen atoms are replaced by one halfway. Figure 1.5 shows the relationships between α-U_3O_8, β-U_3O_8 and UO_3.

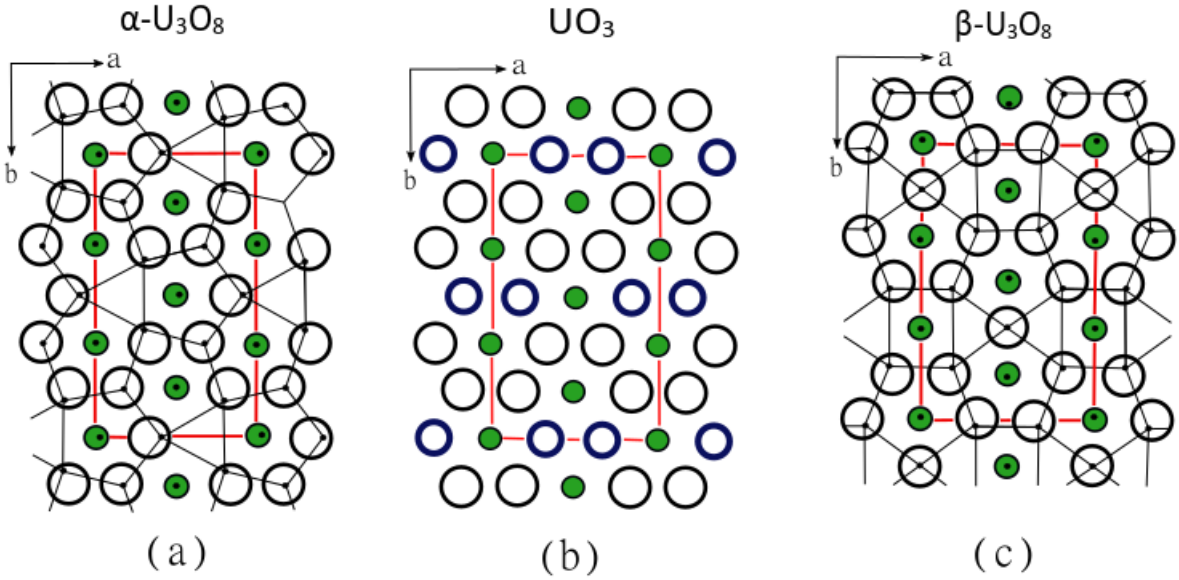

Figure 1.5: (a) the structure of α-U_3O_8, (b) UO_3 and (c) β-U_3O_8 at room temperature. The green circles represent the atoms of uranium, the white circles the atoms of oxygen, and the right-hand blue circles disappear to form α-U_3O_8 [66].

UO_3

UO_3 can be found under different polymorphic phases depending on the manufacturing process [30]. It can appear as amorphous UO_3, or it can be present as α, β, γ, δ or ϵ-UO_3. The structures that define all these phases are diverse, they can vary from hexagonal for the $\alpha - phase$, orthorhombic for the β and γ-phase, cubic for δ-phase or triclinic for the ϵ-phase [13, 30].

Thermodynamic properties

The thermodynamic properties of the different U-O compounds are presented in this section. Starting from the standard formation enthalpies, standard entropies and formation Gibbs free energies at room temperature, followed by the increment enthalpies, the heat capacity and oxygen chemical potential.

Standard formation enthalpies, entropies and Gibbs free energies

The measures of standard formation enthalpies, entropies and Gibbs energies were reported by Konings *et al.* and Grenthe *et al.* in [37, 68], see Table 1.1.

Compound	$\Delta_f H^\circ (kJmol^{-1})$	$S^\circ (JK^{-1}mol^{-1})$	$\Delta_f G^\circ$
UO_2	-1085.0 ± 1	77.03 ± 0.2	1031.833 ± 1.004
$\alpha - U_4O_9$	-1128 ± 1.7	83.53 ± 1.7	-1069.125 ± 1.702
$\alpha - U_3O_8$	-1191.6 ± 0.8	94.18 ± 0.17	-1123.157 ± 0.804
$\gamma - UO_3$	-1223.8 ± 1.2	96.11 ± 0.4	-1145.739 ± 1.207

Table 1.1: Formation enthalpies, entropies and Gibbs free energies for the different uranium oxides at room temperature [37, 68].

High temperature enthalpy increment and heat capacity

Experimental thermodynamic data of UO_2 were characterized by a number of authors. Measures of enthalpy increment and heat capacity can extend to temperatures as high as 8000 K. Figures 1.6 and 1.7 show the evolution of both the enthalpy increment [69–77] and heat capacity of UO_2 [74, 76, 78–84], respectively. It can be seen that there is a general agreement between authors. Rochi and Hyland [85] stated that the increase of the heat capacity from room temperature until 1000 K is governed by progressive excitation of the harmonic lattice vibrations, which can be approximately described by the Debye model. From 1000 K to 1500 K, the heat capacity continues to slowly increase as a result of the progressive increase in the anharmonicity of

the lattice vibrations. After that, from 1500 K to 2670 K the increasing is governed mainly by the formation of lattice and electronic defects. Hutchings *et al.* [86, 87] and Clausen *et al.* [88] analysed this anomalous behavior by performing neutron scattering measurements, they stated that thermally induced disorder can be caused by Frenkel pair formation on the oxygen sublattice at temperatures greater than 2000 K.

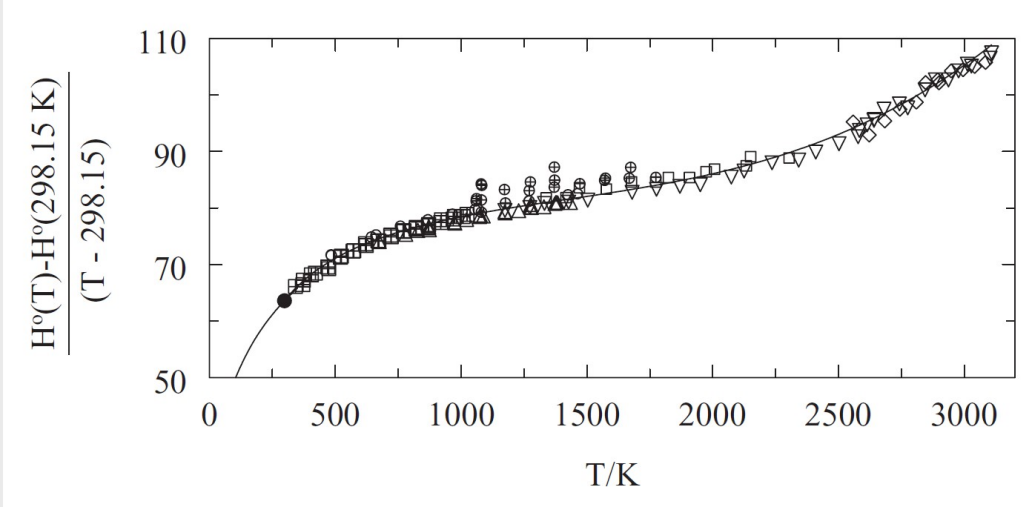

Figure 1.6: Reduced enthalpy increment of UO_2 [69–77].

Konings *et al.* re-fitted the experimental data to define the heat capacity as a function of temperature [68] including the results presented by Ronchi *et al.* in the pre-melting and liquid range [79] in a combined treatment of enthalpy increment and heat capacity, which gives,

$$\begin{aligned} C_p^{\circ}(JK^{-1}mol^{-1}) = 66.7437 + 43.1393x10^{-3}(T/K) - 35.64x10^{-6}(T/K)^2 \\ +11.655x10^{-9}(T/K)^3 \\ -1.16863x10^{6}(T/K)^{-2} \end{aligned} \quad (1.1)$$

Oxygen chemical potential

The oxygen chemical potential, μ_{O_2}, is a partial molar property, therefore, it can also be referred as $\overline{\Delta G}_{O_2}$. The oxygen chemical potential is a very important property of the system, since it links directly the partial pressure of oxygen with the stoichiometry of the system, O/M, at the thermodynamic equilibrium. It can be defined as,

$$\mu_{O_2} = \overline{\Delta G}_{O_2} = -\frac{\partial G}{\partial n_{O_2}}_{T,P} = RTln(\frac{P_{O_2}}{P_{O_2}^{ref}}) + \mu_{O_2}^{ref} \quad (1.2)$$

where R is the gas constant equal to 8.314 $Jmol^{-1}K^{-1}$, T is the temperature in Kelvin, and P_{O_2} is the oxygen partial pressure, $P_{O_2}^{ref}$ and $\mu_{O_2}^{ref}$ are the partial pressure and the oxygen chemical potential of the reference state, respectively.

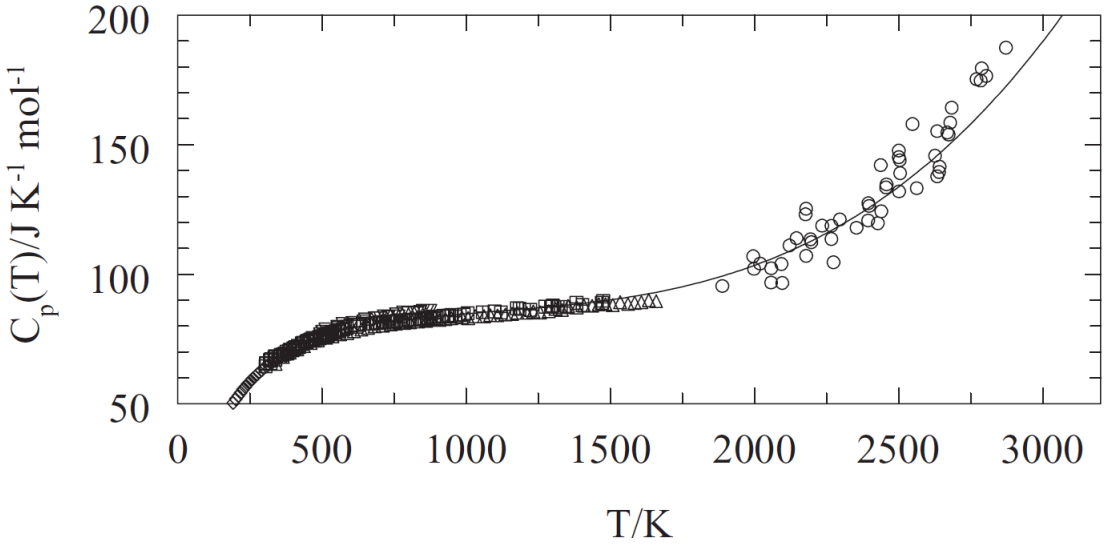

Figure 1.7: Evolution of the heat capacity of UO_2 as a function of temperature.

The evolution of the oxygen chemical potential presents typically a very rapid increment around O/M=2. In Figure 1.8 it is possible to see that there are no experimental values of the chemical potential for O/M<2 at temperatures lower than 1500 K, where U metal formation occurs. UO_{2-x} starts to appear at temperatures higher than 1500 K.

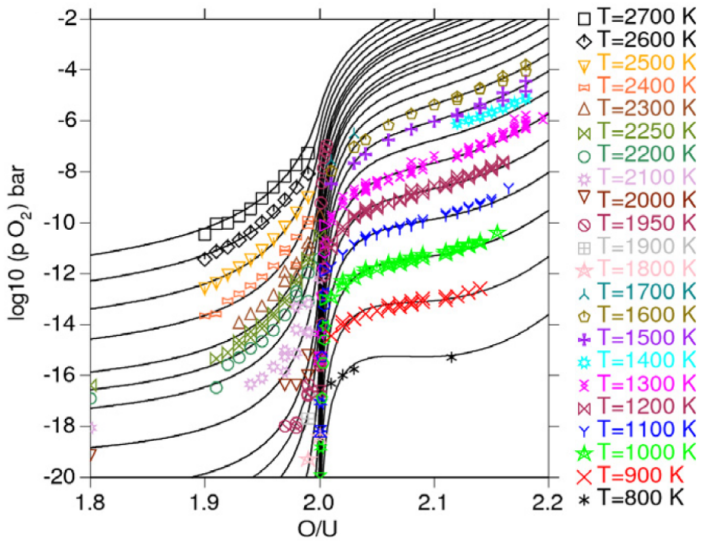

Figure 1.8: Modeling of the oxygen chemical potential for $UO_{2\pm x}$ with Thermo-Calc in comparison with experimental data by Guéneau *et al.* [12, 26, 89]

1.1.2 The Nd-O system

Phase diagram

Experimental data concerning the phase diagram of the Nd-O system were measured by Sano *et al.* [90] at temperatures between 1000 K and 1800 K. The measures of oxygen solubility in solid and liquid neodymium were made by diffusion couple method and solid state electrotransport. Dottavio *et al.* reported a thermodynamic model where the binary diagram Nd-O was fairly described with a very good agreement with the results presented by Sano *et al.*, see Figure 1.9 [91].

In contrast with this model, Lee *et al.* also modeled the Nd-O binary but without taking into account the experimental values presented by Sano *et al.* (Fig 1.10) [51]. The binary diagram Nd-O published by Lee *et al.* neglects the low solubility of oxygen on the α-Nd and β-Nd phases and it establishes directly the equilibrium between these two phases and A-Nd_2O_3. At higher temperatures, they propose also an equilibrium between the β-Nd phase and the liquid phase, in contrast with the observations made by Sano *et al.* [90].

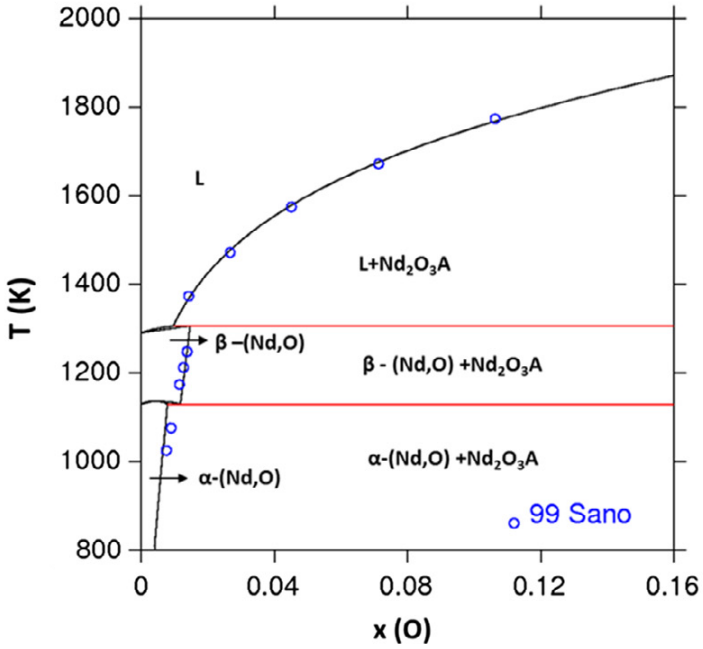

Figure 1.9: Calculated binary phase diagram of Nd-O for $0 < x < 0.16$, reported by Dottavio *et al.* [91]. The experimental points published in [90] are marked in blue.

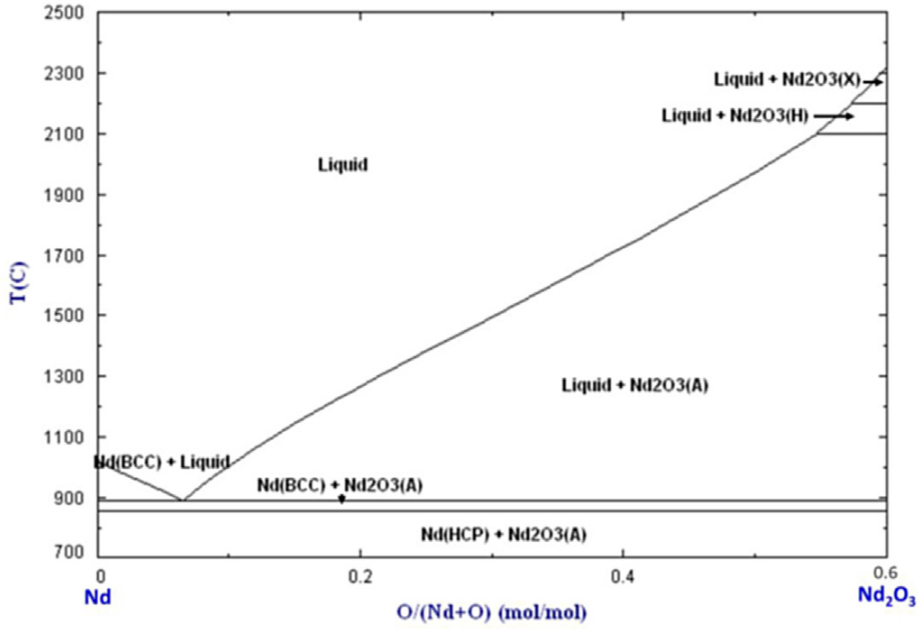

Figure 1.10: Calculated binary phase diagram of Nd-O, reported by Lee *et al.* [51].

Crystallographic structure

Nd_2O_3 has a special behavior among the lanthanide-based sesquioxides. At room temperature, Nd_2O_3 is found typically under the trigonal A-type structure (space group $P\bar{3}m1$, number 164). However, it can also appear under a metastable cubic C-type structure which is the bixbyite structure (space group $Ia\bar{3}$, number 206) [92]. This difference is accepted since the transition of lanthanides from the A-type to the C-type structure occurs around (or at) Nd_2O_3 [93]. In general terms, published thermodynamic data referred to A-Nd_2O_3 as the stable polymorphic form at room temperature. Figure 1.11 shows the crystallographic structure of A-Nd_2O_3.

At higher temperatures, A-Nd_2O_3 exhibits the same behavior as the lanthanide-based sesquioxides with higher ionic radius, which are praseodymium, cerium and lanthanum, see Figure 1.12. The first phase transition is the transition A→H at 2373 K [94, 95]. The H-Nd_2O_3 has an hexagonal structure, with a space group $P6_3/mmc$, number 194. Finally, the latest transition before reaching the melting point happens at 2473 K , which is the H→X [95]. X-Nd_2O_3 has a cubic structure and a space group $Im\bar{3}m$, number 229.

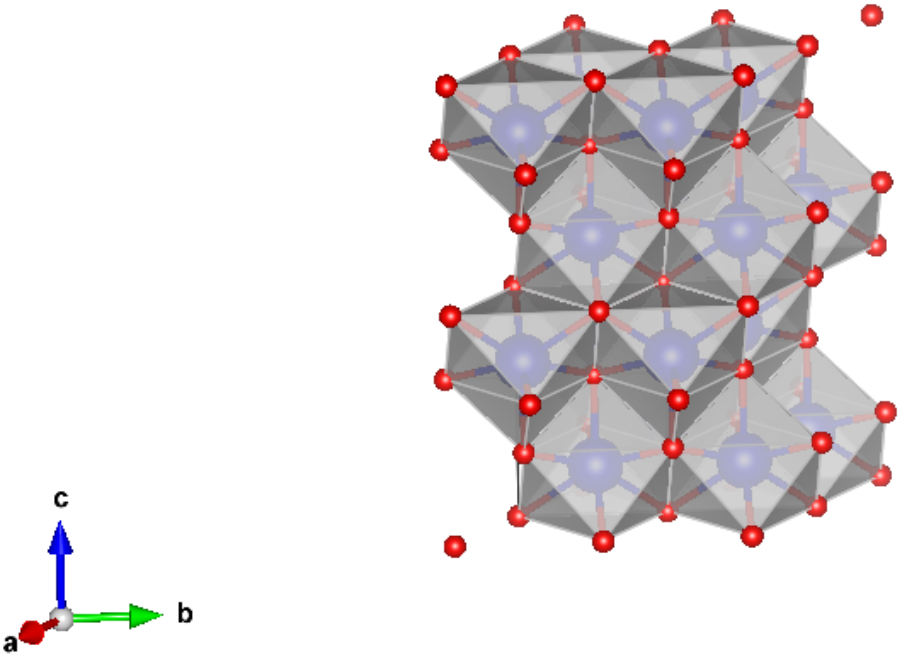

Figure 1.11: Polyhedral representation of A-Nd_2O_3. The blue spheres represent the atoms of neodymium and the smaller red spheres represent the atoms of oxygen. The sticks red and blue are the bonds between the atoms of neodymium and oxygen.

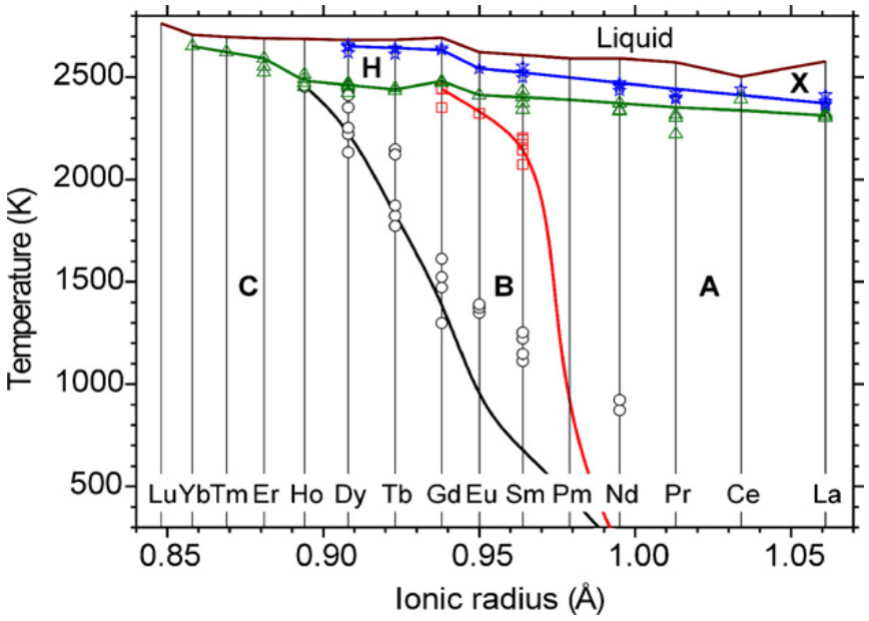

Figure 1.12: Evolution of the temperature-dependent polymorphic transition of lanthanide sesquioxides. The symbols represent the values reported in literature [96].

Thermodynamic properties

Standard formation enthalpies, entropies and Gibbs energies

The standard formation enthalpies, entropies, transition temperatures, transition enthalpies and transition entropies for the different Nd_2O_3 phases reported by Zinkevich et al. and Konings *et al.* [68, 96] are shown in table 1.2.

Compound	$T(K)$	S°	$\Delta_f H^\circ$	Transition	$\Delta_{trans} H^\circ$	$\Delta_{trans} S^\circ$
$A - Nd_2O_3$	298.15	157.89	-1809.9	-	-	-
$H - Nd_2O_3$	2373	-	-	$A \rightarrow H$	33189	13.986
$X - Nd_2O_3$	2473	-	-	$H \rightarrow X$	11300	4569
$Nd_2O_3(liq)$	2593	-	-	$X \rightarrow L$	99132	38.23

Table 1.2: Transition temperature, entropy, formation enthalpy, types of transition and transition enthalpy and entropy for the different neodymium oxides.

The reported values of the melting point after the X-Nd_2O_3 transition can vary depending on the authors [97–103]. The values of the melting point start from 2486 ±30 K [97] and can go until 2613±10 K [100], the selected melting point on this document is the one presented by Granier *et al.* of 2598 K [103].

Similar to the estimation of the melting point, the enthalpy of formation of A-Nd_2O_3 was calculated by many authors using different methods such as combustion calorimetry or solution calorimetry [68, 104–107]. There is a reasonable good agreement, this document selects the value presented by Dinsdale *et al.* of 1809 kJ.mol^{-1} [108].

High temperature enthalpy increment and heat capacity

The measurements of the enthalpy increments were made by Blomeke and Ziegler and Pankratz *et al.* from temperatures of 384 K until 1172 K and 400 K until 1795 K, see Figure 1.13 [109, 110]. The heat capacity of the A-Nd_2O_3 has been measured from very low temperatures by different authors [111, 112]. Measures can start from 5 K and go on until room temperature [112]. A very good agreement between these two authors allowed Konings *et al.* to recommend an equation of the heat capacity based on the polynomial fit of the studies [68], which can be extrapolated until the transition temperature (2373 K),

$$C_p^\circ(JK^{-1}mol^{-1}) = 117.1079 + 28.13655.10^{-3}(T/K) - 1.25845.10^6(T/K)^2 \quad (1.3)$$

The heat capacity for the H, X and liquid phases have been only estimated, since there is no reported experimental measurements, Konings *et al.* selected these values [68] as,

$$C_p^\circ(H,T) = C_p^\circ(X,T) = 145J.K^{-1}$$

$$C_p^\circ(H = liq,T) = 160J.K^{-1}$$

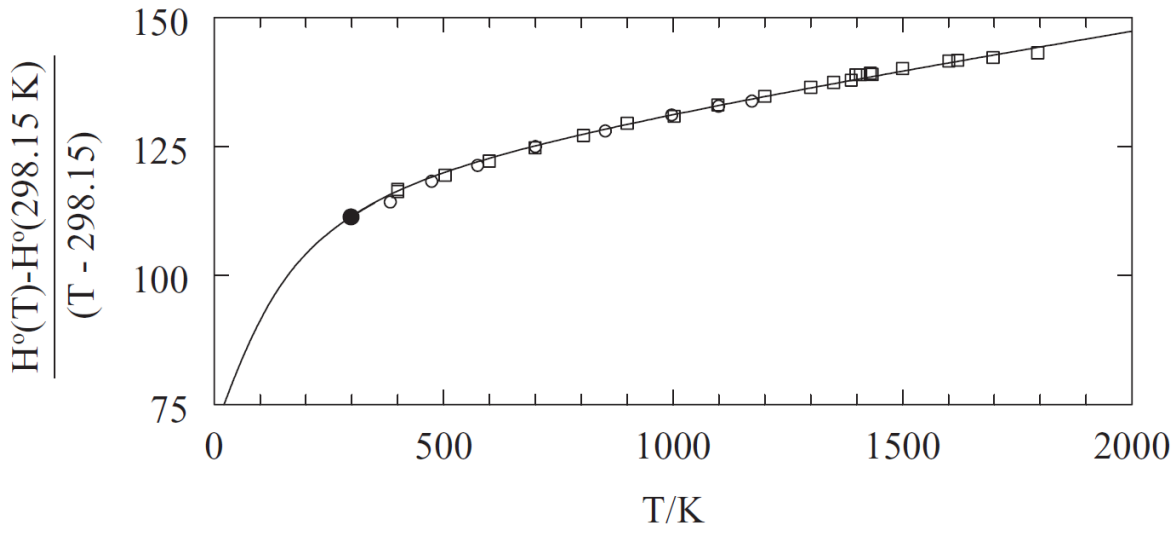

Figure 1.13: Enthalpy increment in Nd_2O_3 presented by Konings *et al.* [68].

1.1.3 The U-Nd system

Phase diagram

To our knowledge, not many characterizations were made on the U-Nd binary system. Haefling and Daane evaluated the solubility of different rare-earths in uranium with equal amounts of each compound [113]. Their results on the U-Nd phase diagram showed that both uranium and neodymium have almost negligible solubility with each other, and that the phases present on the system are basically the metallic elements on their stable form at a given temperature. The solubility of rare-earths in uranium for temperatures above 1273 K is shown in Figure 1.14,

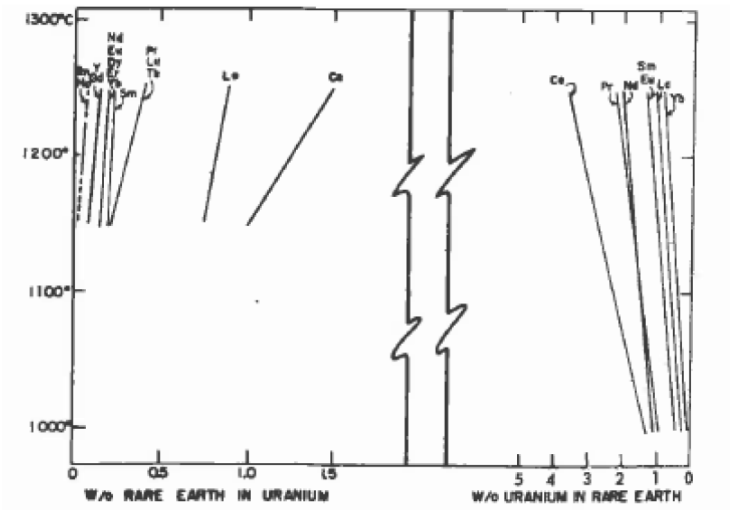

Figure 1.14: Solubility of rare-earths in uranium for temperatures of 1273 K -1523 K [113].

The U-Nd system was modeled by Dottavio *et al.* and Lee *et al.* using the CALPHAD method [51, 91], see Figures 1.15 and 1.16. Both models present important differences, the model made by Dottavio *et al.* takes into account the results published by Haefling *et al.*[113] whereas the model published by Lee *et al.* does not. Therefore, the model presented by Lee *et al.* has two phases completely insoluble with each other. On the contrary, Dottavio *et al.* defined a region where there is solubility between uranium and neodymium on the liquid phase, which increases with temperature up to concentrations of uranium near to 2% and 0.5% for Nd at 1500 K.

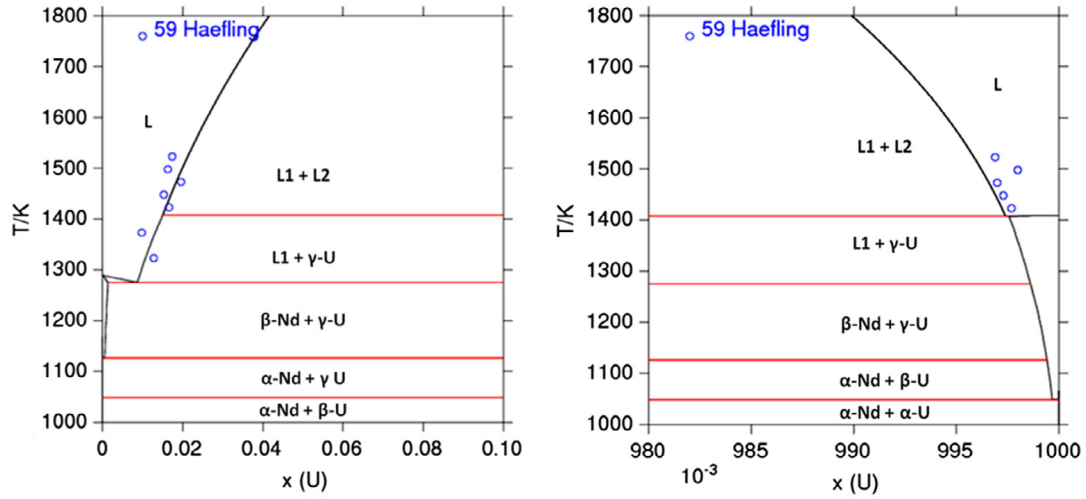

(a) (b)

Figure 1.15: (a) and (b) show on the extremes of the phase diagram to appreciate the low solubility of both metals [91].

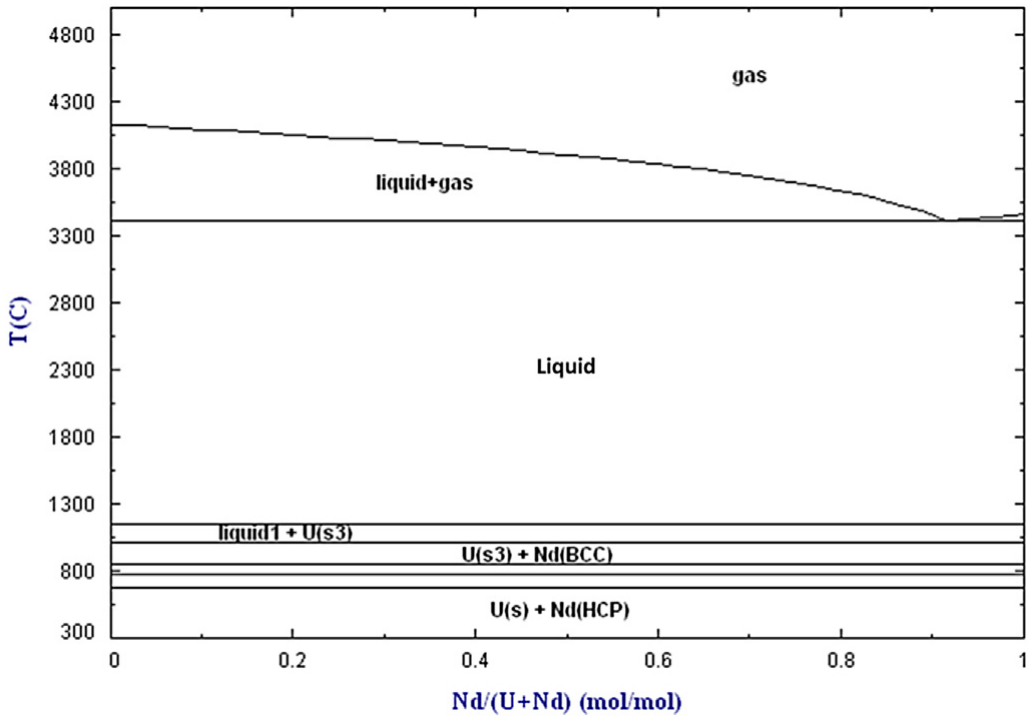

Figure 1.16: Calculated U-Nd binary diagram after the proposed thermodynamic model [51].

Crystallographic structure

The solubility of uranium in neodymium is very low at temperatures beneath 1273 K (less than 3%).Thus, it is not meaningful to refer to a crystallographic structure made from these two metals.

1.1.4 The U-Nd-O system

Phase diagram

Neodymium can substitute in UO_2 as a FCC mixed oxide. Concerning the solubility of Nd in U, there is not a general agreement between the different authors. Some of them propose the existence of a miscibility gap at room temperature on the hypo-stoichiometric region of the phase diagram [114], other proposed the existence of a miscibility gap on the hyper-stoichiometric region of the phase diagram [51] while other propose a full miscibility up to 50% of Nd [52]. This section is dedicated to analyze thoroughly the description of the phase diagram of these authors and expose the differences between them.

The U-Nd-O ternary system was first assessed by Lambertson in [115] by studying the pseudo-binary diagram UO_2 - Nd_2O_3. In this work, the system presents a single solution for temperatures above 2073 K for concentrations of Nd lower than 64%, see

Figure 1.17. After this value, there is a coexistence region between the single FCC solution and the trigonal A-Nd_2O_3 phase.

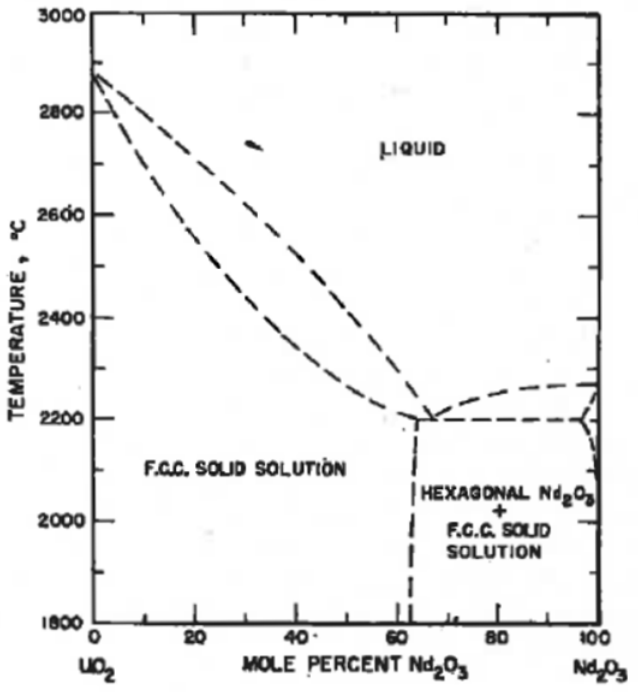

Figure 1.17: Description of the U-Nd-O system made by Lambertson through the pseudo-binary diagram T vs UO_2-Nd_2O_3 [115].

Another description of the phase diagram was made by Keller and Boroujerdi in the region UO_2-U_3O_8-Nd_2O_3 at 1623 K [116], Figure 1.18. On this isotherm it was seen a coexistence region between the single FCC solution and a rhombohedral phase for a concentration of Nd between 75% and 85%. In addition, for higher concentrations of Nd they stated a coexistence region between a rhombohedral phase and the A-Nd_2O_3 phase.

Wadier *et al.* schematized the U-Nd-O system at 1123 K (850°C) using an orthogonal representation of the pseudo-binary O/(U+Nd) vs Nd/(U+Nd) in [52], Figure 1.19. A general agreement concerning the solubility of Nd is found with the precedent representations. In this case, the rhombohedral phase is seen above 80% Nd and the trigonal phase starts to appear above 84% Nd.

The major disagreements for describing the U-Nd-O phase diagram exist at room temperature. Therefore, the assessment of this isotherm will not only involve the description of the phase diagram, but also the conditions under which each author defines it.

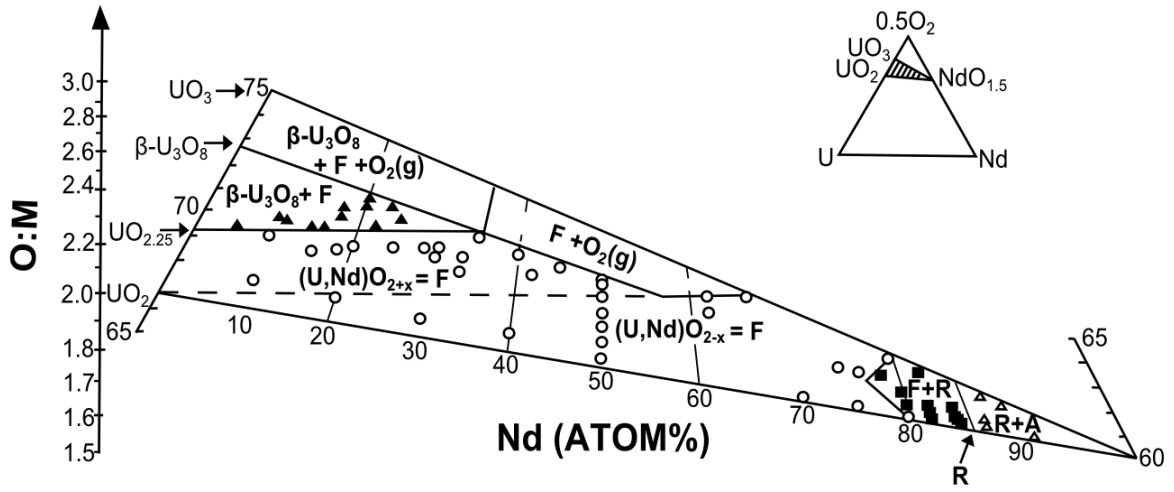

Figure 1.18: Extract of the phase diagram at 1623 K reported by Keller and Boroujerdi [116].

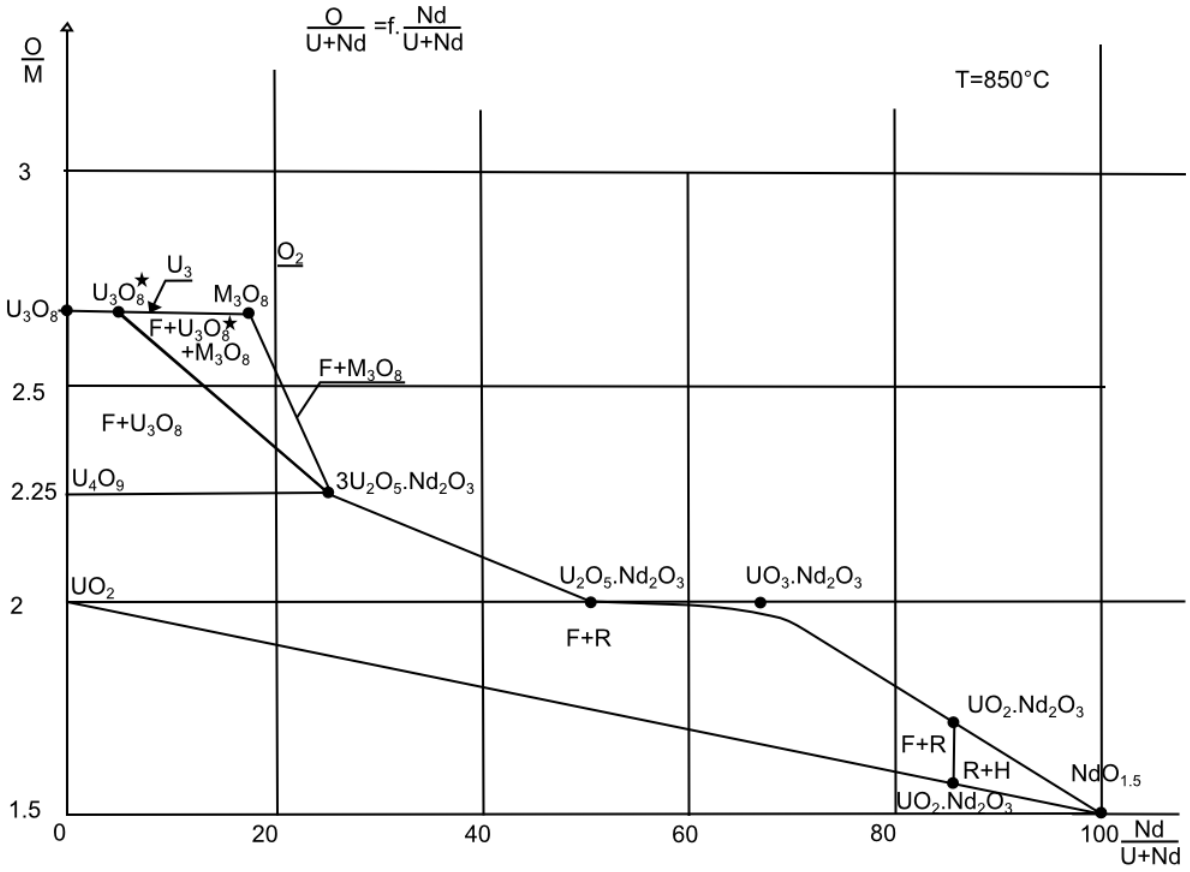

Figure 1.19: U-Nd-O phase diagram proposed by Wadier in [52] at 1123 K (850°C).

Desgranges *et al.* first assessed the stoichiometric and hypo-stoichiometric region of the U-Nd-O system at room temperature by describing the existence of a miscibility gap using samples manufactured by the co-grinding of the initial UO_2 and Nd_2O_3 oxides, sintered at 1623 K [114], see Figure 1.20. In this work, two FCC phases coexist with two different lattice parameters. This difference was explained by the oxygen to metal ratio (O/M) of each phase, where the phase rich in oxygen is described as $U_{1-y}Nd_yO_2$ and the phase poor in oxygen as $U_{1-y}Nd_yO_{2-x}$, similar to what is observed on the systems U-Pu-O or U-Ce-O [43, 54]. Figure 1.20a shows the difference of the lattice parameter for each phase and Figure 1.20b schematizes the proposed U-Nd-O phase diagram.

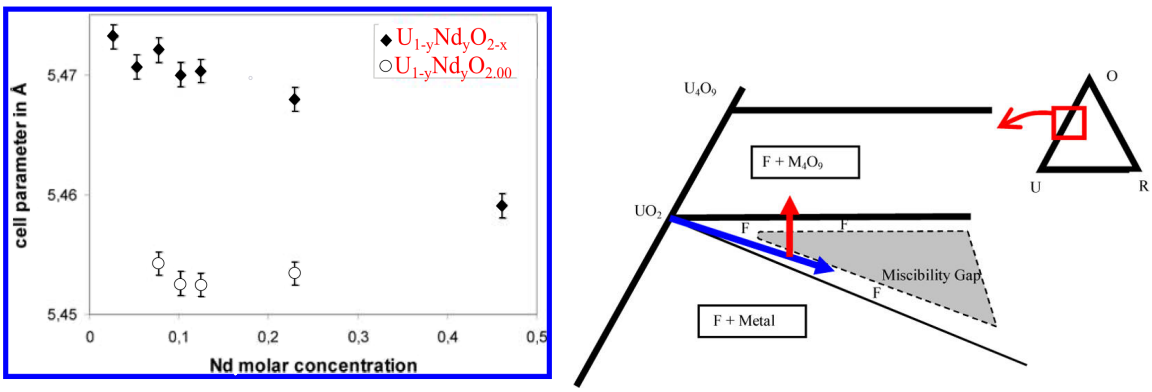

(a) (b)

Figure 1.20: (a) Lattice parameter of both the stoichiometric $U_{1-y}Nd_yO_2$ phase and the hypo-stoichiometric $U_{1-y}Nd_yO_{2-x}$ phase, and (b) extract of the phase diagram of the (U,Nd,O) system at room temperature reported by Desgranges *et al.* [114].

The description of the phase diagram proposed by Desgranges *et al.* was not the line with the observations made by Venkata *et al.* through a series of XRD patterns, showing a single solid solution for samples with different concentrations of Nd and different O/M ratio, Figure 1.21 [117]. This work used samples manufactured by the chemical precipitation of the metals using nitric and citric acid and the only biphasic system was seen for samples with a concentration of Nd greater than 85%, whose origin was explained by the limited solubility of Nd in U.

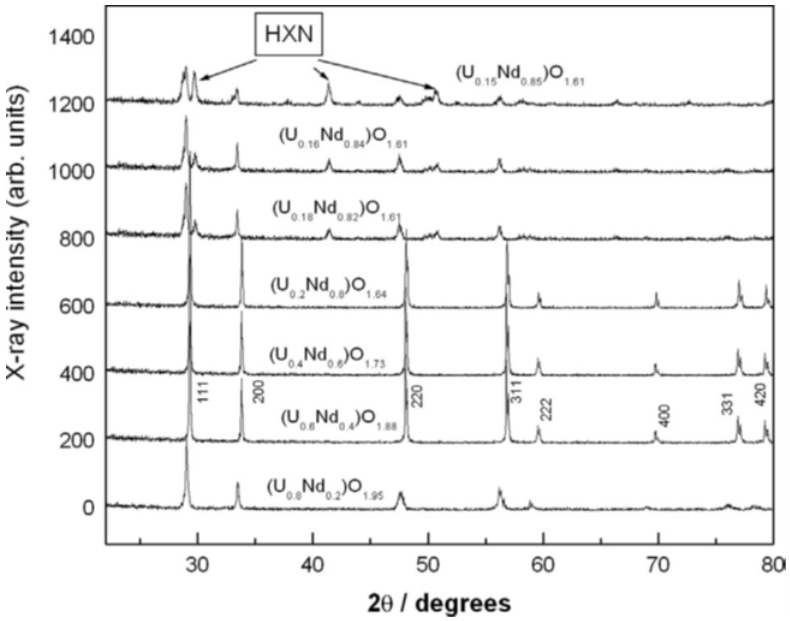

Figure 1.21: XRD patterns for samples with different Nd concentration and hypo-stoichiometric O/M ratios [117]. All samples display a single solution except the sample $U_{15}Nd_{85}O_{1.61}$, which shows a coexistence between the FCC structure and the Nd_2O_3 hexagonal phase.

Dottavio *et al.* were also able to spot the miscibility gap at room temperature by performing one HT-XRD measurement on a sample doped with 28% of Nd under reducing conditions (Figure 1.22), also made by the mechanical mixing process. This study consisted on probing the reversible nature of phase separation by defining a transition temperatures where the system reaches full miscibility and the biphasic system becomes monophasic, being this particular temperature equal to 745 K. Figure 1.23 presents the phase diagram deduced from the HT-XRD measurement.

Figures 1.22 (a) and (b) compare the evolution in temperature of two samples sintered at two different temperatures: 1973 K and 1673 K. The samples sintered at 1973 K display a reversible evolution whereas the samples sintered at 1673 K does not. This contradicted behavior was explained by the author as a consequence of a non-sufficiently high sintering temperature. It was explained that 1673 K as a sintering temperature could not allow to obtain homogeneous samples, unlike 1973 K where complete homogeneity was stated to be found. These results question the validity of the observations made by Desgranges *et al.* in [114], since the samples used in that work were sintered at 1673 K, which were proven to by heterogeneous on the work presented by Dottavio *et al.* in [118].

The thermodynamic description of the miscibility gap of the system U-Nd-O through the CALPHAD method using the software Thermo-Calc was made by Dottavio *et al.* in [91]. The model used on this work is compatible with the previous observation in temperature and further studies by XRD at room temperature. where

the miscibility gap is located on the hypo-stoichiometric region (Figure 1.24 (a)) and 745 K is the temperature at which the biphasic system becomes monophasic for a sample doped with 27%Nd (Figure 1.24 (b)).

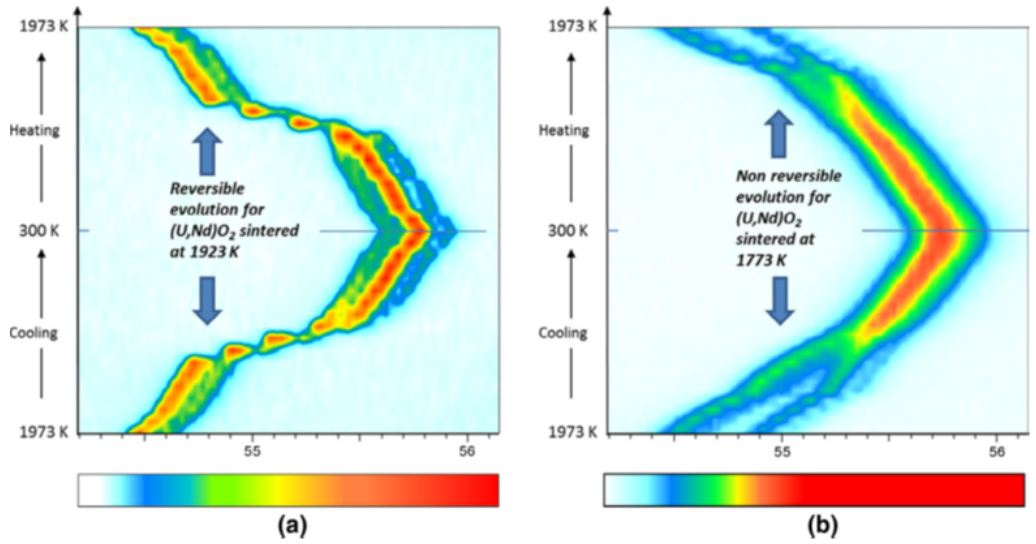

Figure 1.22: Isodensity maps of the HT-XRD measures reported by Dottavio *et al.* in [91] for samples doped with 28% Nd. The picture on the left shows the reversible behavior of samples sintered at 1973 K and the picture on the right shows the non-reversible evolution of samples sintered at 1673 K.

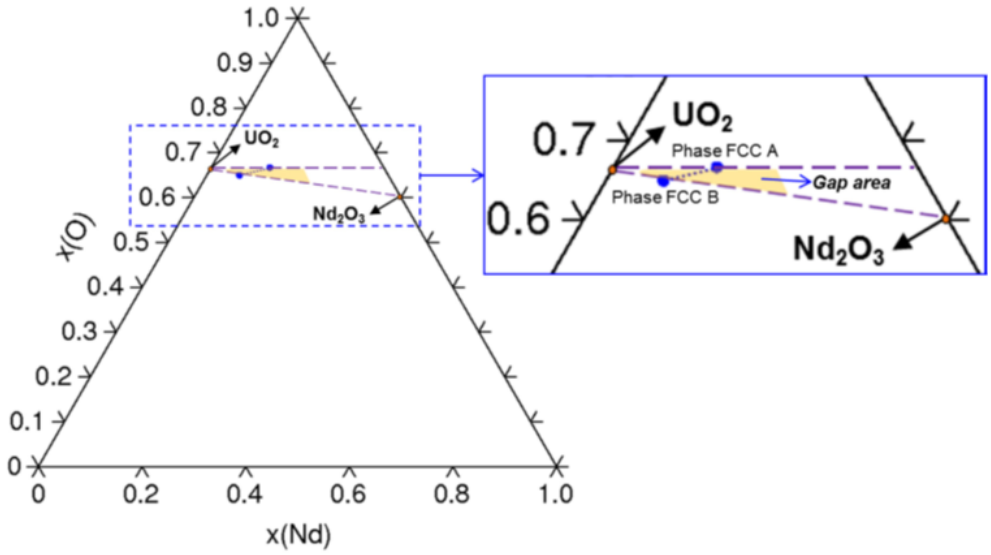

Figure 1.23: Deduced description of the U-Nd-O phase diagram reported in [118]. The yellow region stands for the miscibility gap and the blue line represents the tie line that the defines both FCC A and FCC B phase at the thermodynamic equilibrium.

At this point, an important remark concerning the Figures 1.23 and 1.24 (a)

should be made. Figure 1.23 schematizes the miscibility gap of the U-Nd-O system based on a single HT-XRD measure. On this image the tie line (defined as the lines on the phase diagram that join the two phases stable at the thermodynamic equilibrium) indicates a phase FCC A with higher concentration of oxygen and higher concentration of Nd than the phase FCC B. On the contrary, the Figure 1.24 (a) displays three tie lines that evolve on the opposite way, that is, the phase FCC 1 has higher concentration of oxygen but lower concentration of Nd than the phase FCC 2. These behaviors are incompatible, and require mass transport of the metals in the cation sublattice. Cationic mobility in UO_2-based systems was analyzed in multiple occasions. Depending on the system, rearrangement of the cationic sublattice can take weeks, since normally metallic diffusion coefficients are small in comparison with oxygen diffusion coefficients (typically several orders of magnitude) [41, 119–121] .

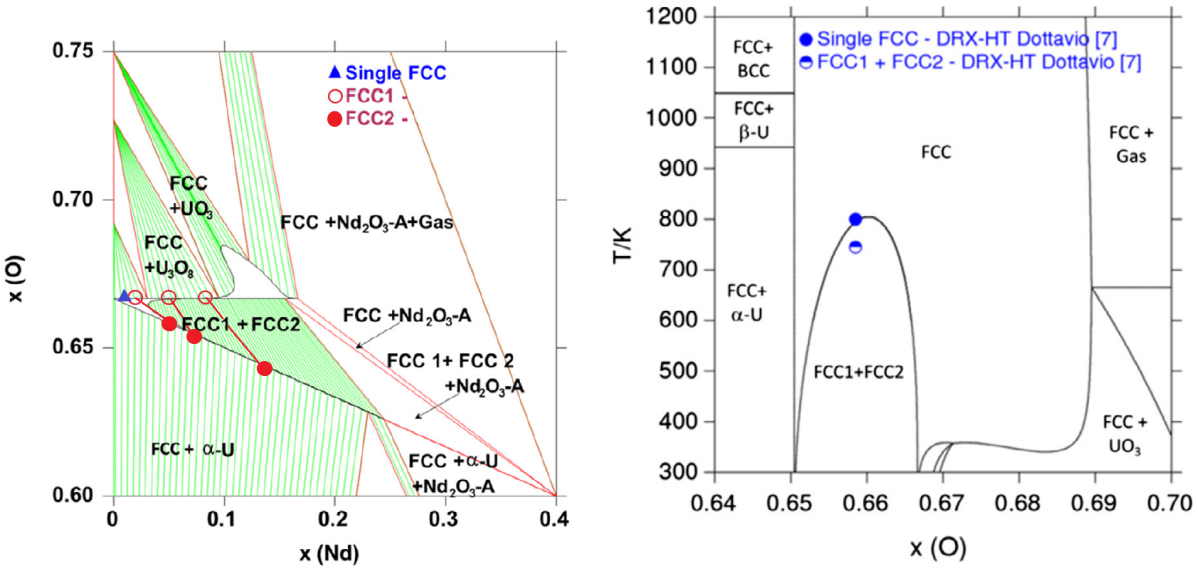

Figure 1.24: (a) Calculated U-Nd-O phase diagram from the model developed in [91] at room temperature showing the formation of two phases joined by the tie lines, and (b) pseudo-binary diagram in temperature. The blue dot stands the transition temperature from the biphasic to the monophasic system obtained after the HT-XRD acquisitions.

Another thermodynamic representation of the U-Nd-O system was made by Lee et al.in [51]. Also through the CALPHAD method, but using the software Factsage, the model uses A-Nd_2O_3 and rhombohedral phases at 1523 K and 1123 K seen in Figures 1.18 and 1.19 from [52, 116]. The miscibility gap is located on the hyper-stoichiometric region of the phase diagram, see the isotherm at 800 K in Figure 1.25. This prediction is not supported by empirical evidence yet.

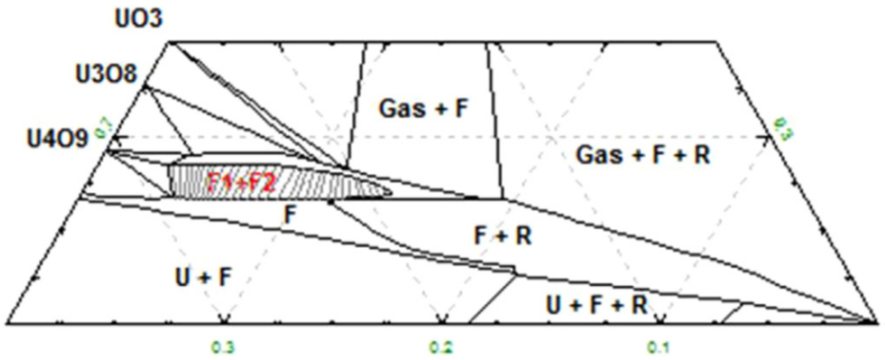

Figure 1.25: Calculated U-Nd-O ternary isotherm at 800 K from the model developed in [51].

Thermodynamic properties

Calorimetric measurements: enthalpy increment and heat capacity

Measurements of the enthalpy increment for samples in the temperature range 800 K - 1800 K were reported in [117] and were fitted into a four term polynomial function as follows,

$$H_T - H_{298}(Jmol^{-1}) = AT + B.10^{-3}T^2 + C.10^{-5}T^3 + D.10^{-4}T^4 \qquad (1.4)$$

The concentration in Nd for the samples analyzed in [117] were 20, 40, 60, 80% Nd and the coefficients of the polynomial function are presented in table 1.3.

Coefficients	$(U_{0.8}Nd_{0.2})O_{2\pm x}$	$(U_{0.6}Nd_{0.4})O_{2\pm x}$	$(U_{0.4}Nd_{0.6})O_{2\pm x}$	$(U_{0.2}Nd_{0.8})O_{2\pm x}$
A	77.81	69.01	68.16	68.5
B	1.859	3.714	2.846	1.616
C	13.4035	6.8215	8.6122	9.2436
D	-2.7859	-2.3193	-2.3463	-2.3665
Error $(J\ mol)^{-1}$	609	761	755	949

Table 1.3: Coefficients of the polynomial expression of the enthalpy increment measured on temperature rang of 800 K - 1800 K [116].

In addition, measurements of the heat capacity by differential scanning calorimetry (DSC) along with the fitted polynomial were reported also in [117]. Figure 1.26 presents the results of the measurement for the set of samples from the polynomial

functions based on the experimental results calculated on the temperature rang of 280 K - 1800 K (table 1.4) in comparison with a baseline calculated between 280 K-900 K. The values were extrapolated until 1800 K to visualize growing tendency of the heat capacity at temperatures above 1200 K (similar to the behavior of pure UO_2 showed in Figure 1.7), explained also by the progressive formation of Frenkel pair oxygen defects.

The correspondent expressions for the baseline heat capacity and the experimental heat capacity are,

$$C_p(Baseline) = A + BxT + CxT^{-2} \tag{1.5}$$

$$C_p(Experimental) = A + BxT + CxT^{-2} + DxT^2 \tag{1.6}$$

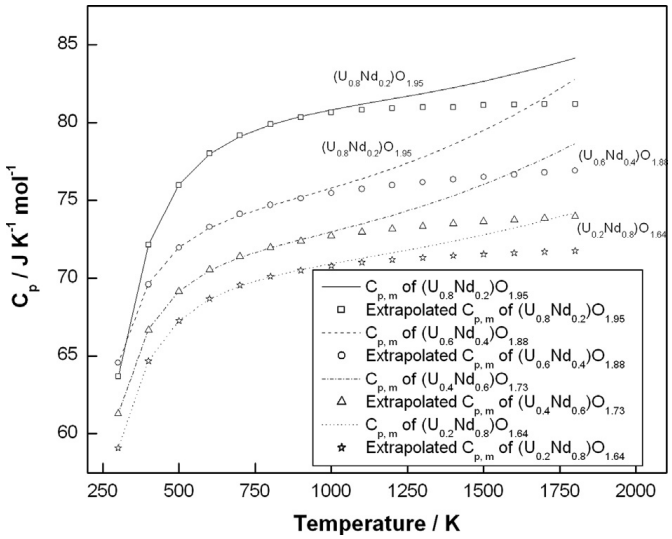

Figure 1.26: Heat capacity measures in [117] with the fitted polynomials.

Sample	Fit equation ($J.K^{-1}.mol^{-1}$)	S. Error ($J.K^{-1}.mol^{-1}$)
$(U_{0.8}Nd_{0.2})O_{2\pm x}$	85.49-5.89.$10^{-3}T$ - 1.828603.10^6T^{-2}-3.0328.10^6T^{-2}	0.35
$(U_{0.6}Nd_{0.4})O_{2\pm x}$	78.3-7.29.$10^{-3}T$ -1.134468.10^6T^{-2}+5.3802.10^6T^{-2}	0.69
$(U_{0.4}Nd_{0.6})O_{2\pm x}$	75.76-5.86.$10^{-3}T$ - 1.179640.10^6T^{-2}+4.2573.10^6T^{-2}	0.92
$(U_{0.2}Nd_{0.8})O_{2\pm x}$	73.10-3.24.$10^{-3}T$ - 1.193696.10^6T^{-2}+2.2558.10^6T^{-2}	0.52

Table 1.4: Coefficients of the polynomial expression of the heat capacity measured on temperature range of 298 K-1800 K [116].

Oxygen chemical potential

Not many characterizations of the oxygen chemical potential have been made for the U-Nd-O system. Tetenbaum measured the oxygen chemical potentials for samples doped with 10% and 20% Nd through a transpiration technique at the temperatures of 2155 K and 2485 K [122]. Wadier analyzed samples doped with 20%, 30% 40% and 50% Nd at 1123 K by measuring the O/M ratio with a thermobalance with different CO/CO_2 and Ar-O gas mixtures [52]. Une and Oguma also calculated the chemical potential for samples doped with 14% and 27% at temperatures of 1273 K, 1573 K and 1773 K measuring the O/M ratio by a spectrophotometric method [123]. Finally, Lee *et al.* extended this study for samples doped with 5.6%, 15.5%, 29.5% and 53% Nd at the temperatures of 1281 K, 1586 K, 1790 K and 1944 K [51]. Figure 1.27 shows the thermodynamic calculations of the oxygen chemical potential made by Lee *et al.* along with the experimental points measured by Lee *et al.* and Une and Oguma.

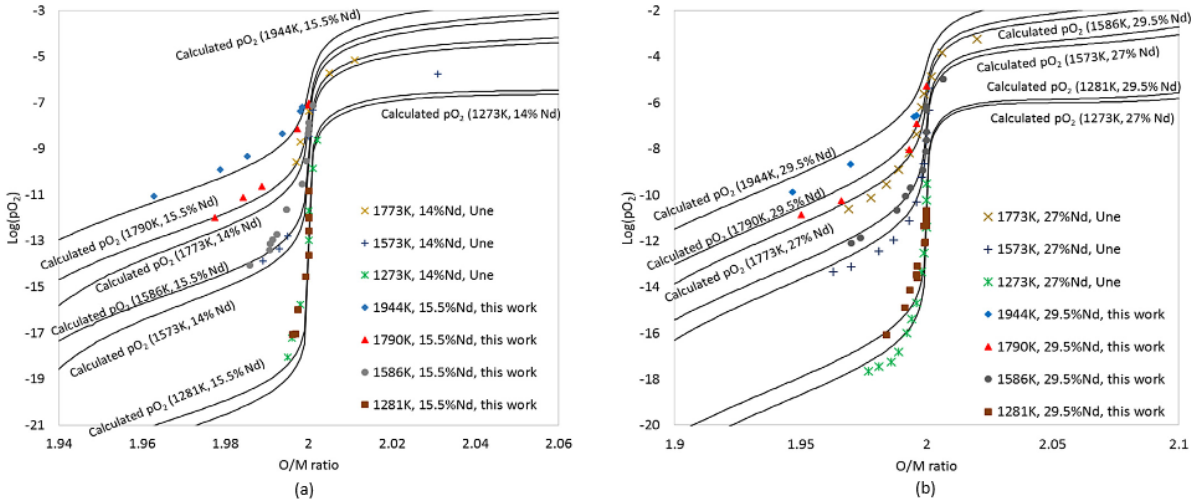

Figure 1.27: Oxygen chemical potential for the U-Nd-O system for samples doped with 14% and 15.5% Nd (a), and 27% and 29.5% Nd at various temperatures [51].

1.1.5 Conclusion

The analysis of the existent data respecting the U-Nd-O system showed that there is a disagreement on the definition of the phase diagram. Some authors detected the presence of a biphasic domain for concentrations of Nd greater than 9% and O/M ratio < 2, others detected the presence of the biphasic domain for O/M ratios > 2, and others reported the full miscibility of Nd in the FCC phase. To have a more comprehensive knowledge about what might cause this difference, it is essential to assess other similar Ac,Ln-based ternary systems. For that purpose, next section is dedicated to present a global overview of U-Ac,Ln-O phase diagrams.

This approach allows us to make a global comparison on the solubility of different dopants on the UO_2 matrix, and their influence on the formation of the different phases that compose the phase diagram.

1.2 Review of the literature data on the U-Ac,Ln-O ternary systems

The following sections propose to analyze different systems based on Pu, which is an actinide formed after the neutronic absorption of U^{238}, and other high yield fission products, they are, Ce, La and Gd.

For each assessed ternary, the analysis consists on presenting the set of samples used by each authors along with the used manufacturing process and the definition of the phase diagram reported by each author. This procedure allows us to detect the differences and similarities reported by each author concerning the definition of the phase diagram.

1.2.1 The U-Pu-O system

The phase diagram of this system was defined on both the hypo-stoichiometric and hyper-stoichiometric region. The following subsection is then dedicated to describe in detail the U-Pu-O phase diagram, particularly paying attention at the biphasic domain.

Ever since the 1960s, the ternary system U-Pu-O has been of great interest on the scientific community. Nuclear fuel based on U and Pu mixed oxides (MOX) are still today used on Light Water Reactor (LWR) and are meant to be used in the modern Generation IV Fast Breeder Reactor (FBR) [124]. Studies on the crystallographic chemistry of $(U,Pu)O_2$ indicated that the Pu atoms are placed at the same position as U in its original FCC structure, see Figure 1.28a. Indeed, if all atoms of U and Pu maintain their oxidation state as U^{+4} and Pu^{+4}, the fluorite structure remains as such varying only its size with the addition of Pu. This behaviour can be visualized on the Figure 1.28b where is presented the variation of the lattice parameter as a function of the Pu concentration for O/M=2. The systems follows the Vegard's Law [56].

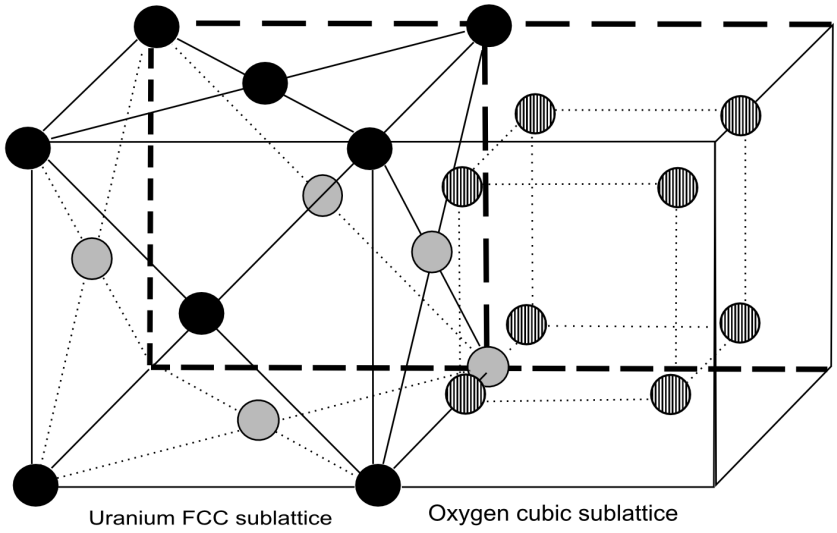

(a)

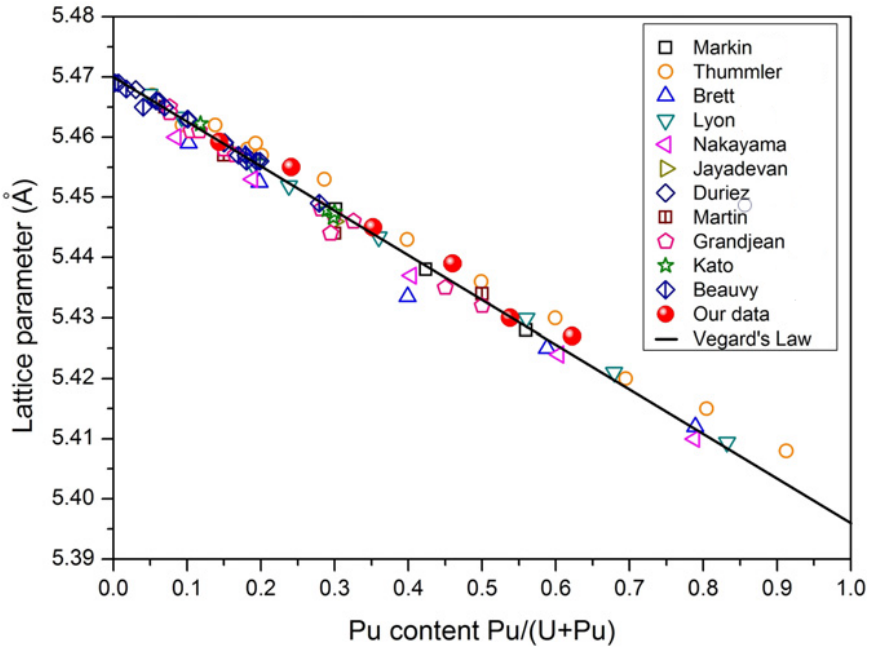

(b)

Figure 1.28: (a) black and grey circles represent the FCC structure formed by both U and Pu cations [125], and dashed circles represent the anionic sublattice in form of a cube on U-Pu-O mixed oxides. (b) evolution of the lattice parameter for different concentrations of Pu on the U-Pu-O system published by Truphémus *et al.* in [56]

Manufacturing processes used to assess the U-Pu-O phase diagram

To describe the U-Pu-O phase diagram, the authors used different manufacturing methods. Sari *et al.* studied the uranium-plutonium mixed oxide on samples doped with 5 to 97%Pu by co-precipitating ammonium diuranate and plutonium hydroxide from a nitrate solution [126]. The procedure consisted on calcining, compacting to pellets and sintering in a N_2+8%H_2 mixture at about 1923 K. Markin and Street also used samples made by co-precipitation of ammonium diuranate and plutonium hydroxide, these precipitated powder was filtered, washed and dried in air at 373 K for several hours and then heated in an H_2 flowing stream at 973 K for 2h [127]. The powder was pelleted, and sintered in vacuum at 1823 K for 4h. Kato *et al.* and Komeno *et al.* used samples manufactured through the mechanical blending method, the mixed powders were pressed and sintered at 1923 K for 3h in an atmosphere of Ar+5%H_2 with added moisture [55, 128]. Finally, Truphémus *et al.* and Vauchy *et al.* used samples made through the co-grinding process. Then, the powder was pressed and sintered at 2023 K under Ar+5%H_2+∼5 ppm HO_2 for 24h under Ar+5%H_2 [56, 129–131]. A summary table presenting the manufacturing methods used by the different authors is presented below, see table 1.5.

Author	Route	Concentration range (%Pu)
Sari *et al.*	Wet route	5-97
Markin and Street	Wet route	11-58
Kato *et al.*	Dry route	30
Komeno *et al.*	Dry route	30
Truphémus *et al.*	Dry route	15-65
Vauchy *et al.*	Dry route	28-45

Table 1.5: Manufacturing processes and concentration ranges of the different authors that described the U-Pu-O phase diagram [54–56, 126, 128–131] .

Description of the U-Pu-O phase diagram

Markin and Street, and Sari *et al.* were the first authors that described the hypo-stoichiometric region of the U-Pu-O phase diagram at room temperature [54, 126]. For values of O/M<2, they identified a region where the system does not behave as a monophasic system. The limits of this biphasic region are slightly different between these authors, Markin and Street proved that this region starts for concentrations

of Pu greater than 35% and Sari *et al.* stated that it starts above 17%Pu. Today, the phase diagram commonly proposed in open literature is the one proposed by Sari *et al.* and this biphasic domain is defined as a miscibility gap, see Figure 1.29.

For concentrations below 45%Pu, the miscibility gap defines two FCC phases, one phase rich on oxygen where all Pu is found as Pu^{+4} and another with lesser amounts of oxygen where Pu appears as Pu^{+3}. At the limit of the miscibility gap, the system has a transition region from FCC to BCC for the phase poor in oxygen, marked on the graphic as the zone with blue stripes [55, 126, 128, 132]. On this region, it is possible to find a triphasic system between two FCC phases, and the third BCC phase. At higher Pu amount, there is a biphasic system between the stoichiometric FCC phase and the hypo-stoichiometric BCC phase.

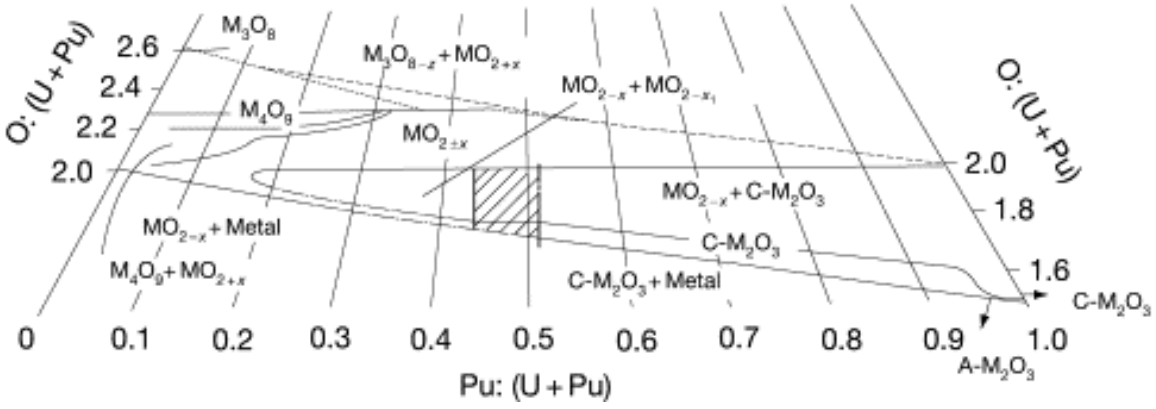

Figure 1.29: Isotherm of the ternary diagram of the U-Pu-O system schematized in [Gunéneau 2012]. The dashed central region represents the transition region where the hypo-stoichiometric FCC structure becomes a BCC structure.

A representation of the evolution of the lattice parameter for different concentration assessed by Sari *et al.* and Truphémus *et al.* is schematized in Figure 1.30 [56]. In both cases, there is a good agreement concerning the lower limit of the miscibility gap. Sari *et al.* stated a larger difference between the lattice parameters of the two FCC phases than Truphémus *et al.* for concentration of 25%Pu. From then on, there is a global general agreement on the calculation of the lattice parameter for both hypo-stoichiometric and stoichiometric phases.

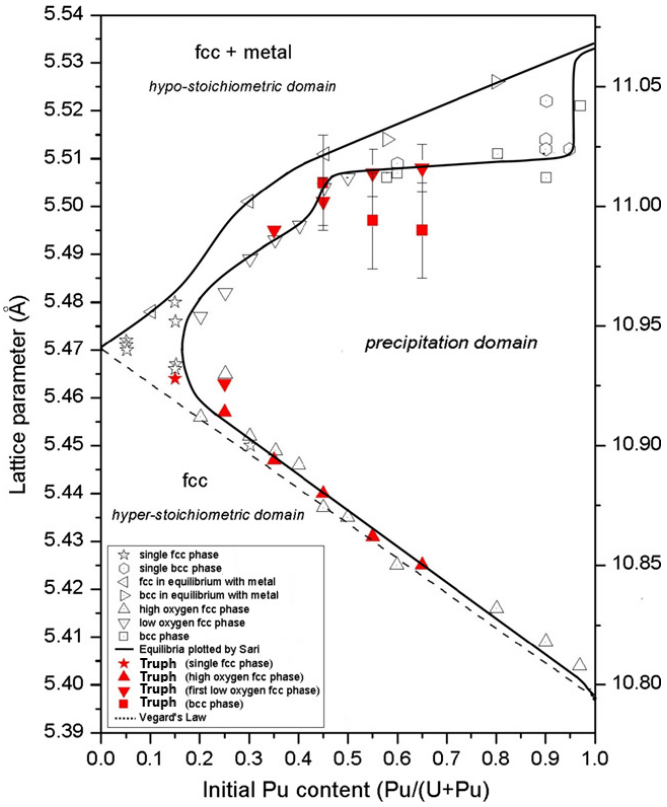

Figure 1.30: Lattice parameter of the U-Pu-O as a function of the Pu concentration. Grey symbols were acquired by Sari *et al.* and red symbols by Truphémus *et al.* [56, 126].

The miscibility gap on the U-Pu-O system is also capable of evolving with temperature. Multiple authors assessed the critical temperature of the system for concentrations between 22 and 95%Pu [54–56, 126, 128–131] . The biphasic domain can exist at temperatures greater than 900K for Pu concentrations over 95% [126]. Its evolution in temperature was modeled by Guéneau *et al.* through the CALPHAD method using the software Thermo-Calc [12], see Figure 1.31.

The description of the phase diagram established between the different authors is coherent regardless the synthesis process used to produce the samples. All authors indicate the presence of a miscibility gap at room temperature for O/M ratios <2 and concentrations of Pu greater than 20%. Comparing Figures 1.24a with 1.29, one can easily say that the systems are similar, considering the presence of a biphasic domain and the concentration at which this region appears. The most evident differences appear for higher concentrations of Nd (>50%), where the miscibility gap ends and begins the equilibrium with the A-Nd_2O_3 phase. Another important observation can be made considering the kinetics of phase separation. Both biphasic domains were observed within the time of acquisition of the XRD patterns, which means that phase separation is governed by the oxygen mobility since it occurs at relatively low temperatures (<745K).

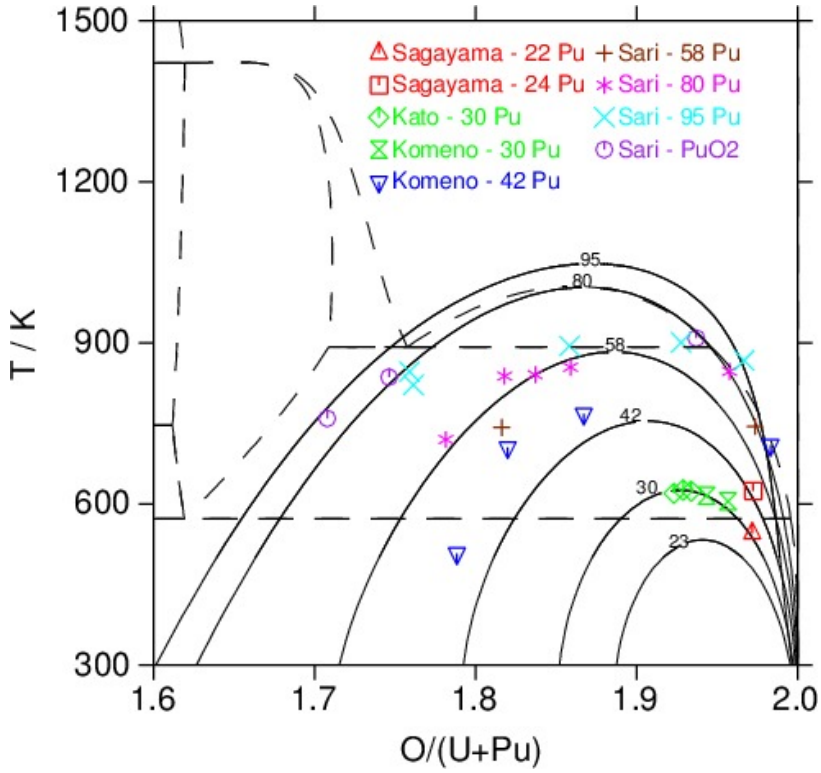

Figure 1.31: Calculated phase separation temperatures for the concentrations 23, 30, 42, 58, 90 and 95%Pu from [12] in comparison with experimental results at the different concentrations published in [55, 126, 128, 132] . The results reported in [56, 130] are also compatible with the development of the miscibility gap but they are not included in this figure.

1.2.2 The U-Ce-O system

Ce is a high yield fission product capable of dissolving extensively into the UO_2 matrix. Thus, in order to predict the chemistry of nuclear fuel, it is of major importance to understand its chemical behaviour. CeO_2, like UO_2 and PuO_2, has fluorite structure, it also has similar ionic radii to Pu, and it is capable of existing as Ce^{+3} and Ce^{+4} in solid solution [133–135]. These shared characteristics between Ce and Pu have been the motivation to use Ce as a surrogate for Pu due to the many obstacles associated to the handling of PuO_2. However, this is not in agreement with the thermophysical properties. A number of publications have shown that heat capacity, thermal diffusivity or thermal conductivity of CeO_2 exhibit important differences with PuO_2 [136–139].

Independently of these differences and similarities with the U-Pu-O system, the U-Ce-O system is considered to have a major role in nuclear fuel performance in high burn-up fuels. Therefore, a summary of the manufacturing processes used to describe the phase diagram is presented. The next section is dedicated to describe the U-Ce-O phase diagram at both room temperature and in temperature.

Manufacturing processes used to describe the U-Ce-O phase diagram

The U-Ce-O system was described using samples manufactured by different means. Markin *et al.* defined the phase diagram using samples prepared by evaporating the uranyl nitrates and cerium nitrates with a stream of argon at 973 K for 2h. Then, the remaining powder was pelleted and sintered in vacuum at 1873 K for 2 h, crushed, re-pelleted and sintered again at 1873 K for another 2h. Finally, the final stoichiometry was achieved by heating with a gas mixture 1/1 of CO/CO_2 at 1123 K[43]. Lorenzelli, on the other hand, defined the phase diagram employing samples manufactured by co-grinding and then sintered twice at 1973 K under an atmosphere of Ar+10%H_2 to guarantee a good homogeneity of the solid solution [42]. Finally, Simeone *et al.* studied a single sample doped with 44%Ce made by the co-precipitation of an oxalic precursor followed by a calcination stage and sintering at 1973 K for 4h under an atmosphere of Ar+5%H_2 and 0.12% of water vapor [140].

Author	Route	Concentration range (%Ce)
Markin *et al.*	Wet route	34-75
Lorenzelli	Dry route	20-70
Simeone *et al.*	Wet route	44

Table 1.6: Manufacturing processes and concentration ranges of different authors that described the U-Ce-O phase diagram [42, 43, 140].

Description of the U-Ce-O phase diagram

The first preliminary description of the U-Ce-O phase diagram at room temperature has been made in the earlies 1950 [141]. However, a detailed and more precise description of the U-Ce-O phase diagram both at room temperature and in temperature was made later on by Markin *et al.*, and Lorenzelli [42, 43]. Similarly to what was seen on the U-Pu-O system, the U-Ce-O presents a biphasic domain for concentrations above 30%Ce. These authors agreed on the definition of the lower limit of the miscibility gap and its development in temperature. Nonetheless, they present some differences on the lattice parameter and therefore on the O/M ratio of the phase poor in oxygen. Figure 1.32 displays the description of the U-Ce-O phase diagram reported by Markin and Street in [43]. A quick comparison with Figure 1.29 can highlight the similarities with the U-Pu-O phase diagram. In this case, the biphasic domain starts at concentrations of Ce over 30% also with two FCC phases. Unlike the U-Pu-O system, in this case there is no BCC phase, meaning that the miscibility gap consists of two FCC phases and covers the phase diagram from 30%Ce up to CeO_2-$CeO_{1.818}$. The O/M ratio for any point inside the miscibility gap is always <2, which involves one phase

constantly stoichiometric and another always hypo-stoichiometric. To define the U-Ce-O phase diagram the authors needed to take some careful precautions. Markin *et al.* stressed the importance of carrying on a dwell at 323 to 333 K for several days to induce phase separation on samples doped with concentrations of Ce over 34% [43]. Lorenzelli, on the other hand, needed to perform a very slow cooling of the samples in order to achieve separation, otherwise the system would remain monophasic [42].

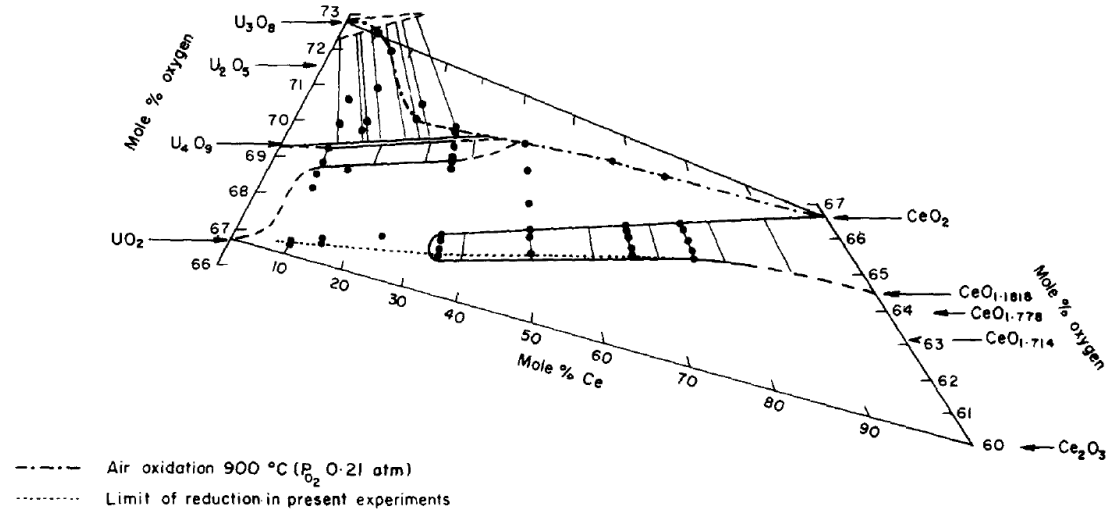

Figure 1.32: Phase diagram of the system U-Ce-O described by Markin *et al.* in [43] showing the full extension of the miscibility gap at room temperature.

Concerning the evolution with temperature, the critical temperature for a given Ce concentration is much lower than the one seen for the same Pu concentration, e.g. the T_C for 50%Ce is 473 K, whereas the T_C for 42%Pu is 648 K. Between the results published by Markin and Street and Lorenzelli there is a global agreement on the definition of the biphasic domain in temperature. On the contrary, Simeone *et al.* detected the phase separation for a sample doped with 44%Ce at a higher temperature, 573 K, where it was stated by neutron diffraction means that the hypo-stoichiometric phase was not an FCC phase, but instead it was the oxygen-deficient C-type bixbyite. Table 1.7 sums up the critical temperatures for each Ce concentration reported by all authors.

To sum up, the U-Ce-O system was reported to form also a miscibility gap at room temperature by numerous authors. This region starts around 30%Ce and it appears only for O/M ratios <2. The U-Ce-O phase diagram is very similar to the one of U-Pu-O, excepting for the formation of a BCC phase (present for >50%Pu). An important difference between these two systems is related to the kinetic of phase separation. It has been showed that the biphasic domain for the U-Nd-O and the U-Pu-O systems appeared almost instantaneously during the acquisitions of the XRD patterns. On the contrary, phase separation on the U-Ce-O system needs careful measures in terms of cooling and dwelling at low temperatures the induce the formation of the second phase, otherwise the system remains monophasic [42, 134].

Markin-street		Lorenzelli		Simeone *et al.*	
%Ce	T_C(K)	%Ce	T_C(K)	%Ce	T_C(K)
		20	-		
34	353	30	333		
		40	413	44	573
50	473	50	473		
66	573	70	533		
75	673				

Table 1.7: Critical temperatures estimated on different concentrations for each author [42, 43, 140].

1.2.3 The U-La-O system

La is a high yield FP. Along with U-Nd-O, the U-La-O system is one of the most extensively studied system compared to other U-Ln-O ternaries. Like Nd, La is capable of existing in solution exclusively as La^{+3}, which makes the phase diagram and its evolution in temperature suitable for direct comparison with the U-Nd-O system. Hence, the next section is dedicated to present the manufacturing processes and phase diagram of the system U-La-O. Differences and commonalities are highlighted in comparison with the already presented ternary systems.

Manufacturing processes used to describe the U-La-O phase diagram

The authors used different manufacturing methods to assess the U-La-O phase diagram. Diehl and Keller assessed the system by precipitating equimolar mixed hydroxides in ammonia, then preheated and finally sintered at 1823 K. Herrero *et al.*, Rojas *et al.* and Garcia-Chain *et al.* used samples prepared through a mixed ceramic/organic precursor proceeding. The mixture consisted in grounding uranyl propionate and the lanthanum sesquioxide at 1023 K, and then calcinating at 1623 K in air for 150h, and quenching on a metallic plate [41, 142, 143]. Finally, Venkata *et al* analyzed the solubility of La by the methods of combustion synthesis and solid-state route. The first one consists on dissolving U_3O_8 and La_2O_3 in nitric acid by heating at 353 K. Citric acid was added and mixed to get a clear solution. The remaining solution was dried in a plate at 573 K, and heated at 1073 K for 4h to remove the carbonaceous material. The resultant powder was compacted into pellets and sintered at 1873 K for 6h. The second method consisted on grounding U_3O_8 with La_2O_3 in a mortar,

then calcinating the sample in air for 8h at 873 K and finally sintering at 1873 K for 6h. A summary table is presented below comparing the different authors and the manufacturing methods they used to analyze the U-La-O system (Table 1.8).0

Author	Route	Concentration range (%La)
Diehl and Keller	Wet route	0-100
Garcia-Chain *et al.*	Dry route	70-80
Herrero *et al.*	Dry route	56-67
Rojas *et al.*	Dry route	56-67
Venkata *et al.*	Wet route/Dry route	10-90/60-80

Table 1.8: Manufacturing processes and concentration ranges of different authors that described the U-La-O phase diagram [41, 142–144].

Description of the U-La-O phase diagram

U-La-O phase diagram was described at different temperatures by multiple authors. At room temperature, Venkata *et al.* analyzed the solubility of La in UO_2 on samples manufactured by two different methods: the combustion synthesis and solid-state route in [39]. The combustion method displayed a full solubility of La until 80%, whereas the solid-state route only until 70%. For higher concentrations the hexagonal La_2O_3 was present in equilibrium with the FCC phase. This difference was explained by the fact that the kinetics of diffusion process to form a solid solution in combustion synthesis process was more favorable than the solid-state process. A more detailed description of the U-La-O phase diagram at 1523 K was made by Diehl and Keller in [144], see Figure 1.33. On this diagram it is possible to see that La is capable of forming multiple biphasic domains between the FCC phase, two rhombohedral phases named as RI and RII, and the A-La_2O_3 phase. The fluorite phase is present over a wide domain of La concentration, at around 72% it appears the RII phase, defined as $U_2La_6O_{15}$, at 82% the fluorite is in equilibrium with the phase RI, which is the delta (δ) phase ULa_6O_{12}, and finally, after 86%La the RI phase coexists with A-La_2O_3. In addition, at lower temperatures the system also presents a third rhombohedral phase RIII for concentrations over 52%La, described as $(U,La)_8O_{16}$. This latter phase was also described in detail by both XRD and neutron diffraction in [41] after performing a long annealing at 1373 K for 200h. This thermal treatment was made in such way to allow cationic ordering achieve the equilibrium phase, RIII, otherwise the U and La atoms would not have sufficient energy to move and the system would have remained a fluorite.

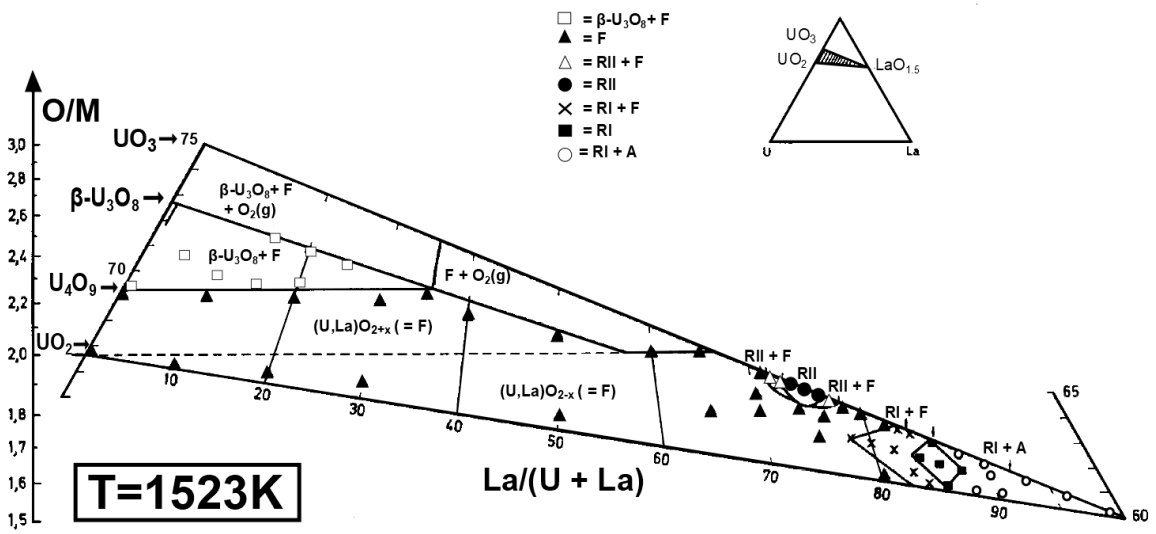

Figure 1.33: Extract of the U-La-O ternary diagram at 1523 K on the sections UO_2-U_3O_8-La_2O_3 reported in [144].

Diehl and Keller also reported the phase diagram for the pseudobinary system UO_{2+x}-La_2O_3 [144], showed in Figure 1.34. In this diagram it is visible that the RIII phase starts to appear at 52%, and it is no longer stable at 1523 K, this is the reason why this phase does not exist in Figure 1.33.

At 1523 K, it is possible to establish some clear similarities with the system U-Nd-O. In first place, both systems exhibit a large solubility of the dopant (La^{+3} or Nd^{+3}) into UO_2, since they are capable of forming the FCC phase up to concentrations of over 70%. Further, both systems also display the formation of at least one rhombohedral phase. In the case of Nd, it is only capable of forming the δ-phase, and in the case of La, it is capable of forming the δ-phase, and two other designated as RII and RIII. Unlike the systems U-Ce-O or U-Pu-O, both Nd and La can only be trivalent, this is why the formation of a rhombohedral phase is stable at high concentration of dopant, where the crystallographic arrangement is basically based on U^{+6} and Ln^{+3} cations. This is not the case on the systems U-Ce-O and U-Pu-O, as they can exist as Ce^{+4} and Pu^{+4}, which allows to form a cubic structure, even for concentrations of dopant above 90%.

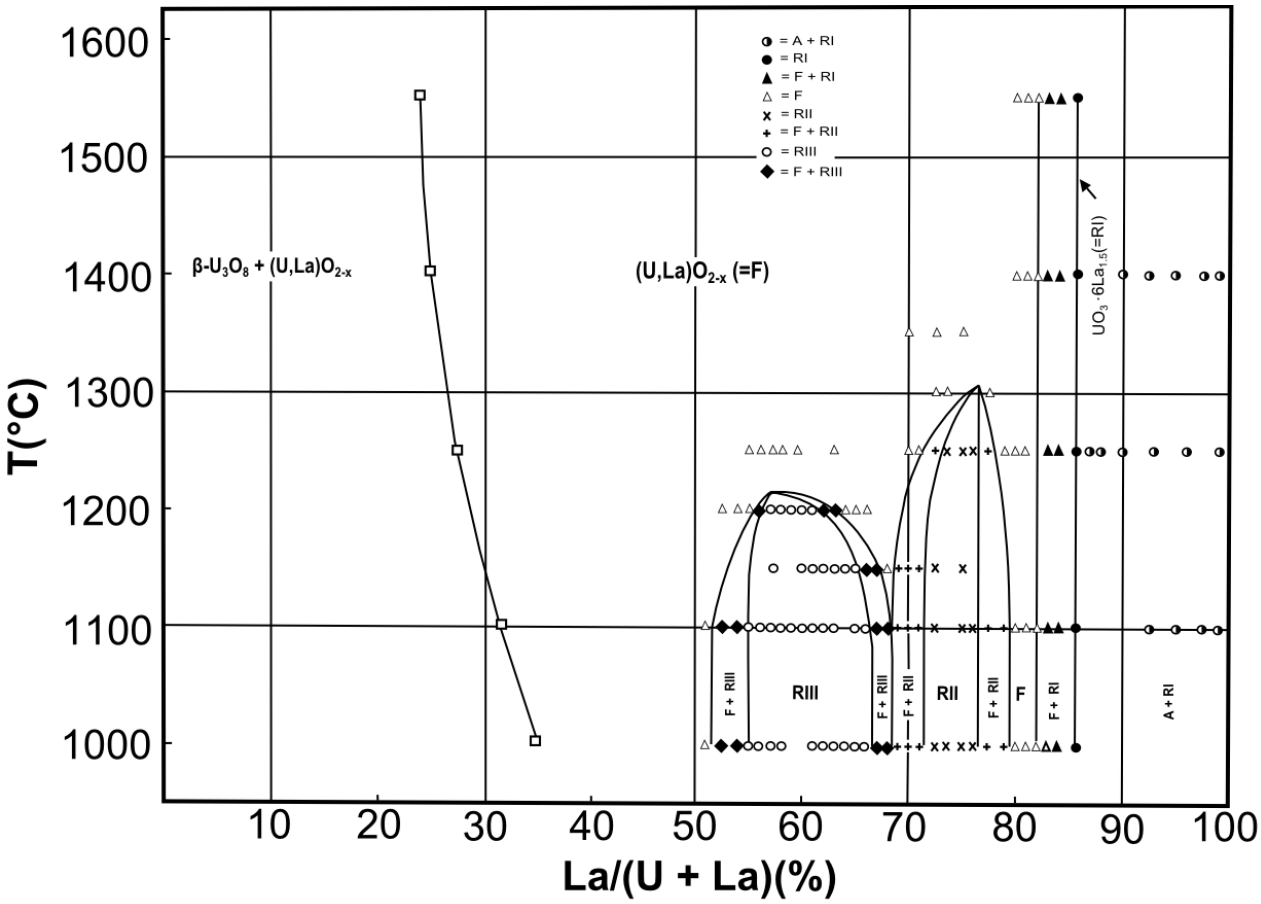

Figure 1.34: Phase diagram of the pseudobinary system UO_{2+x}-La_2O_3 reported by Diehl and Keller in [144].

1.2.4 The U-Gd-O system

Gd is another trivalent lanthanide that is formed as a product of the fission reaction, and while it is not a high yield fission product (like Nd or Ce), its study is of major importance since it behaves as a burnable poison and limits the initial excess of reactivity of the reactor core [145, 146].

The first UO_2-Gd_2O_3 poisoned fuel was introduced in 1967 in the Boiling Water Reactor (BWR) type Dresden 2 reactor, and it has been routinely used in this type of reactors since then [147]. The maximum usually incorporated Gd_2O_3 in BWR fuel is about 4%, whereas in PWR the amount required to regulate the reactivity is higher and can reach 10%.

Gd, like Nd and La, is an exclusively trivalent lanthanide, which makes also the U-Gd-O system suitable for direct comparison with U-Nd-O and U-La-O systems. Indeed, several authors described the U-Gd-O phase diagram taking as reference the Nd solubility on the U-Nd-O system [46, 49].

Manufacturing processes used to describe the U-Gd-O phase diagram

Lindemer and Sutton investigated the oxygen chemical potential in samples made with Gd/(U+Gd) ratios of 0.1 to 0.8 by using the thermal denitration process. This process consists on precipitating the metals on a solution of NH_4NO_3, then calcinating in air at 1075 K to produce the oxides, sintering the sample at 1275 K under an atmosphere of Ar+4%H_2, and finally at 2273 K in Ar for 2h. On the other hand, Une and Oguma measured the oxygen chemical potential on samples manufactured by mechanical grinding of the UO_2 and Gd_2O_3 powers. Each mixed powder was pressed at 350 MPa into pellets, and sintered at 1973 K in flowing H_2 gas. Nakamura *et al.* also measured the oxygen chemical potential on Gd-doped samples using the ceramic method, the initial powder were mechanically blended in an agate mortar and heated several times between 1523 K and 1673 K for 12 and 24h, in an atmosphere of flowing He, with intermediate grinding and repelletizing.

A summary table with the route used by each author and the concentration range is presented below, see table 1.9.

Author	Route	Concentration range (%Gd)
Lindemer and Sutton	Wet route	10-80
Une and Oguma	Dry route	04-27
Nakamura	Dry route	05-30
Krishnan *et al.*	Dry route	10-80

Table 1.9: Manufacturing processes and concentration ranges of different authors that described the U-Gd-O phase diagram [47–49, 148].

Description of the U-Gd-O phase diagram

The burnable nature of the Gd atoms dissolved in UO_2 solid solutions has been made the focus of study of many authors. Different thermodynamic properties have been studied over the years like heat capacity [77, 83, 148, 149], or oxygen chemical potentials [47–49, 150], but no direct assessment of the phase diagram have been made up to date. Instead, Lindemer and Sutton evaluated the solubility of Gd in UO_2 by measuring the oxygen chemical potential at 1773 K, and described schematically the phase diagram at this temperature, see Figure 1.35. The studied concentrations were 10, 17, 20, 30, 40, 50, 60, 70 and 80%Gd at different O/M ratios. The heavy lines within the shaded area represent these concentrations [49].

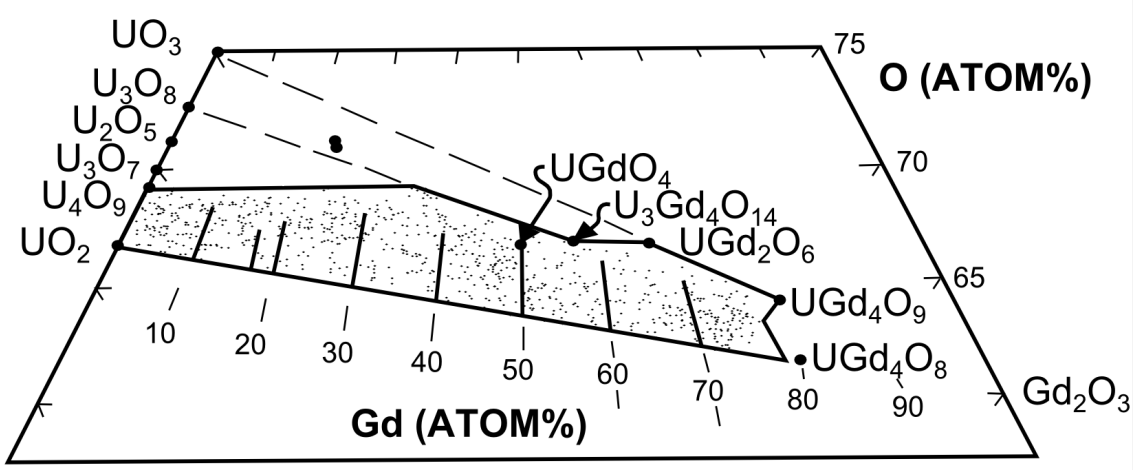

Figure 1.35: Phase diagram of the U-Gd-O system at 1773 K reported by Lindemer and Sutton in [49].

Also at 1273 K, 1573 K and 1773 K Une and Oguma measured the oxygen chemical potential on sampled doped with 14 and 27%Gd [47] indicating that the solubility of Gd in UO_2 was complete for an O/M ratio of 1.98 to 2.05. Nakamura measured also the oxygen chemical potential on samples doped with 5, 10, 20 and 30%Gd at 1273 K, where a monophasic system was seen in all cases [48].

Concerning the ternary phase diagram at room temperature, all authors detected the presence of the FCC phase for a concentration of Gd up to 80% and none of them detected the presence of a rhombohedral phase at any temperature. Krishnan *et al.* evaluated samples doped between 10 and 80%, where they reported an extra set of peaks which were indexed as Hexagonal Gadolinia Lines (HGL) [148]. this means that both U-La-O and U-Gd-O systems present a large solubility on the FCC phase up to around 80%. Beyond this concentration, there is no information to our knowledge of the phase diagram. For this reason different authors have used the description of the U-Nd-O and U-La-O systems to describe the U-Gd-O phase diagrams at high temperatures and concentrations [46, 49].

1.3 Conclusions

This chapter has reviewed relevant published data about the U-Nd-O system and the related binaries. This information consists of the crystallographic structures, thermodynamic properties and phase diagram for each system separately. In addition, other related U-Ac,Ln-O ternary diagrams, with Ac=Pu and Ln=Ce, La and Gd, were also reviewed.

U-Nd-O phase diagram is not unique. Some authors reported the presence of a miscibility gap in the hypo-stoichiometric region [91, 114, 118], other authors de-

tected only a monophasic system throughout a wide domain of concentration [50, 52, 115–117, 151]. Some authors predict a miscibility gap not in the hypo-stoichiometric region, but in the hyper-stoichiometric region of the phase diagram [51]. No experimental data that supports such statement. At present, to assess the U-Nd-O system it is still necessary to establish the presence of the miscibility gap.

Different Ac,Ln-based ternary systems have a miscibility gap, like Pu or Ce. They can exist with both valences +3 or +4. There are several biphasic regions in the U-La-O system related to phases RI, RII and RIII. There is no experimental evidence of a rhombohedral phase for Gd-related systems.

During the assessment of ternary phase diagrams, the authors suggest the manufacturing process does not affect the description of the phase diagram. Nevertheless, Venkata *et al.* stated that the solubility of La on the FCC phase was lower in samples made by dry route than in samples made by wet route [39]. The presence of the miscibility gap in U-Nd-O was reported in different occasions only on samples made by dry route processes [91, 114, 118], whereas a monophasic system is consistently reported in samples manufactured by wet route processes [52, 117, 151]. This observation requires critical review of the influence of the manufacturing process on the thermodynamic data used for the model. This analysis is the object of the following chapter of this dissertation where dry and wet route samples are analyzed in pristine and annealed conditions.

Chapter 2

Experimental characterization of the system U-Nd-O

"A failure is not always a mistake, it may simply be the best one can do under the circumstances. The real mistake is to stop trying."

-B. F. Skinner

This chapter is dedicated to characterize experimentally the hypo-stoichiometric region of the U-Nd-O phase diagram. To do so, it is mandatory to have a high-quality homogeneous set of samples.

In Chapter 1 it was seen that different authors described the phase diagram differently. Some of them detected a miscibility gap at low concentrations of Nd and some of them did not [50–52, 114]. A detailed assessment of these results revealed that the only significant difference between the authors that could justify the description of the phase diagram is the manufacturing process. The miscibility gap was described using samples manufactured by a process called dry route, whereas the single solid solution was seen by using samples manufactured by a different process named wet route. Thus, this chapter is meant to compare them both. The techniques used in both cases are assessed X-ray Diffraction (XRD), Scanning Electron Microscopy (SEM) and Transmission Electron Microscopy (TEM). In addition, samples manufactured through wet route are also assessed after a thermal annealing under reducing conditions and described by X-ray Absorption Spectroscopy (XAS).

2.1 Sample manufacturing through dry route

Dry route manufacturing methods are widely used around the globe to produce nuclear fuel pellets at an industrial scale. Indeed, all MOX fuel in France is produced through the MIMAS process (MIcronised MASter blend) that rely upon basically on the mixture of the fine powders of UO_2(s) and PuO_2(s) [152].

In this work, the mixture consists of powders of UO_2(s) and Nd_2O_3(s), to form the samples $U_{1-y}Nd_yO_{2\pm x}$, with y=0.04, 0.17, 0.27 and 0.33. These concentrations and manufacturing procedure were chosen similar to the works that allowed detecting the miscibility gap in first place [114, 118, 153]. The process involves the co-grinding of the UO_2 and Nd_2O_3 oxides, a sintering under a reducing atmosphere of Ar +5%H_2 at 1973 K for 72h and cooling down for 4h to insure that all elements reached the equilibrium. This process can be described schematically in figure 2.1 as follows:

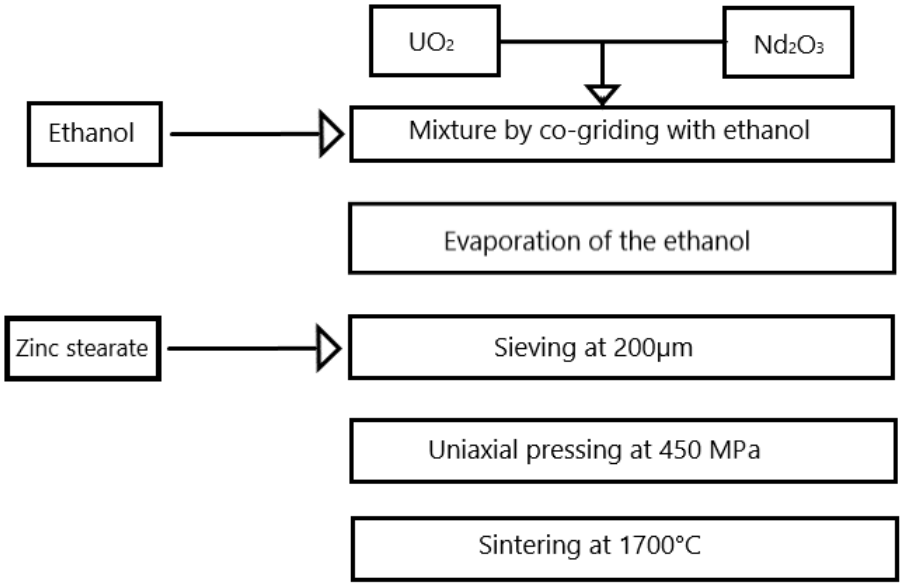

Figure 2.1: Manufacturing process through dry route of the mixed oxides (U,Nd)O_2, obtained from [118, 153].

2.1.1 Microstructural characterization

Scanning electron microscopy (SEM) analysis was performed on the samples to identify the shape and size of the grains, as well as the distribution of Nd across the fuel pellet. The SEM image and X-ray mapping, obtained by Energy Dispersive X-ray Spectroscopy (EDS), for three different samples are shown in Figure 2.2(4, 27 and 33%Nd, respectively). For the sample doped with 4%, SEM imaging reveals a microstructure formed by grains with a size of several microns and high porosity, where the zone rich in Nd (green) seem to be more porous than the U rich zone (blue), see Figure 2.2a. The same observations concerning the fluctuations of the Nd concentration and pore formation can be seen on the samples doped with larger amounts of Nd (Figures 2.2c to 2.2f). In these cases the samples display a more important formation of large pores, since they are associated to the concentration fluctuation, which is more evident on samples doped with higher amounts of Nd. The formation of the larger pores might related to the local Nd accumulations, since the low Nd diffusion coefficient limits densification, which unable the pores to develop uniformly

across the pellet.

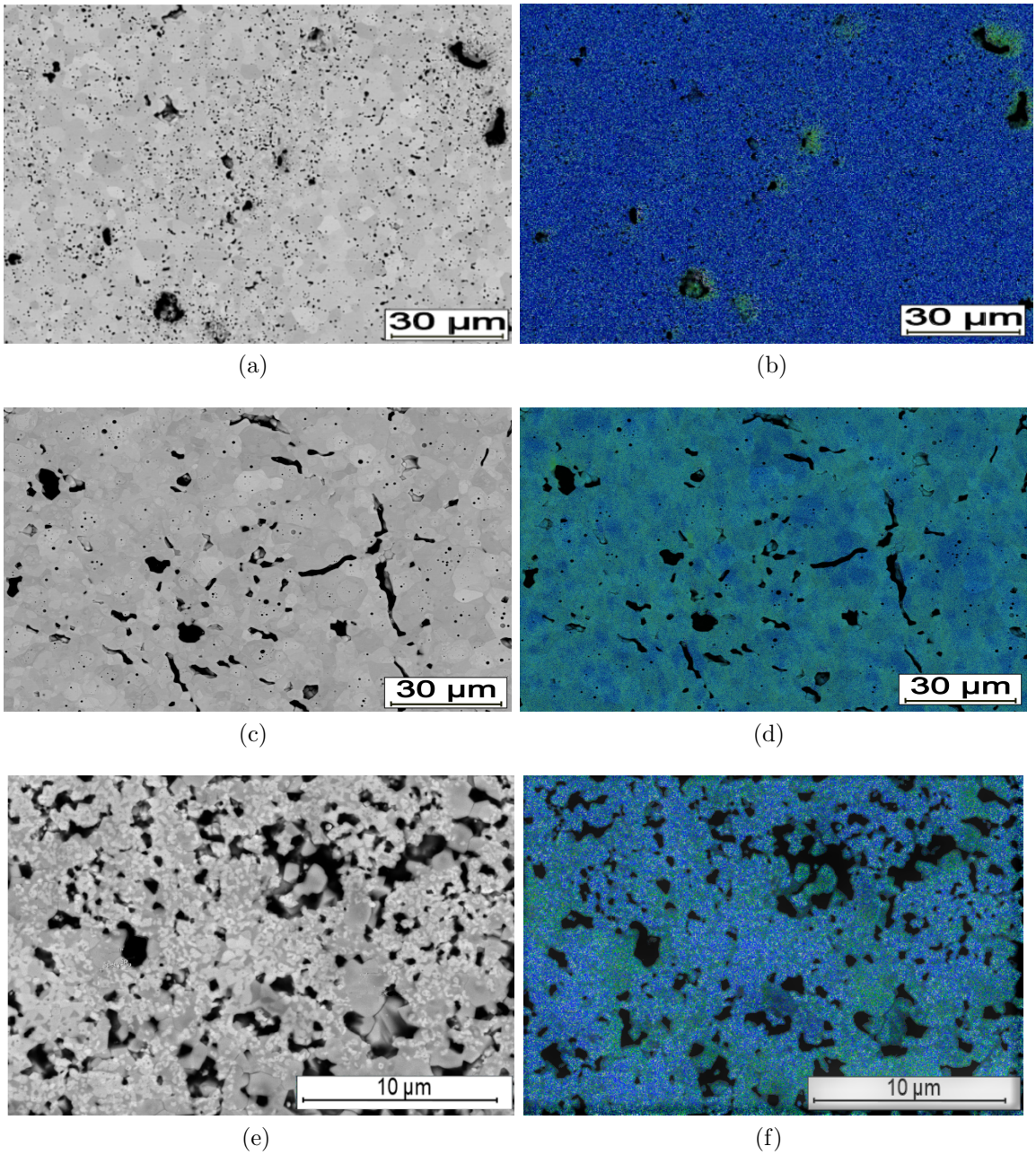

(a) (b) (c) (d) (e) (f)

Figure 2.2: SEM imaging and X-ray mapping for the samples doped with 4%Nd ((a) and (b)), 27%Nd ((c) and (d)) and 33%Nd ((e) and (f)).

Further characterizations by Electron Backscattered Diffraction (EBSD) were carried out to assess the grain size distribution. This technique is particularly appropriate to assess these samples, to avoid a chemical or thermal etching that might damage the sample. Only one sample characterized by EBSD (33%Nd) is presented in this

work (Figure 2.3). Figures 2.3a reveal the orientation of each grain, by representing it with different colors and shows a larger distribution of the grain size. After the EDS analyses we can confirm that the larger grains around the pores are rich in Nd. The grain distribution schematized in Figure 2.3b shows that the great majority of the assessed grains are smaller than 0.5 μm. In addition, this assessment allows also to relate the size of the grains with the Nd concentration, indicating a coarsening mechanisms followed by a densification mechanism in presence of Nd. Figure 2.3a indicates that the surroundings of the larger pores are mainly constituted by grains of micrometric size, which where seen to be rich in Nd by X-ray mapping in Figures 2.2b, 2.2d and 2.2f.

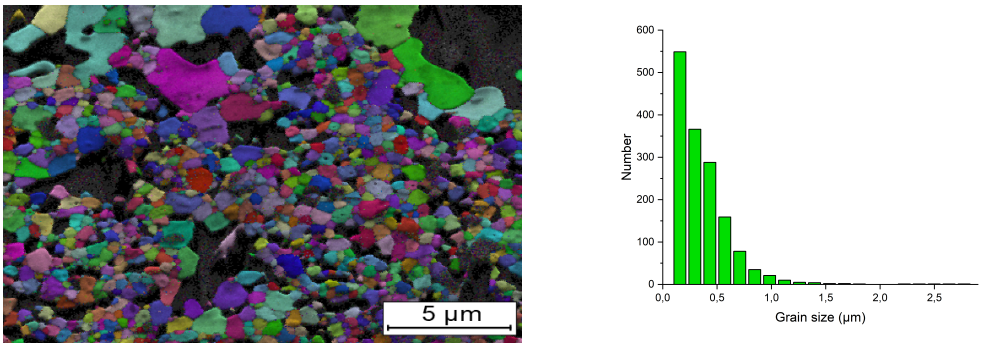

(a) (b)

Figure 2.3: EBSD imaging of the sample doped with 33%Nd in (a) and grain size distribution in (b).

A characterization at nanoscopic scale was made by Transmission Electron Microscopy on sample the doped with 33%Nd. Heterogeneous distributions of Nd were also observed at this scale. Different grains present two domains with different Nd concentration, see Figure 2.4. In Figure 2.4b is possible to see one domain richer in Nd (26%, green circle) and the other with no Nd (orange circle). This difference on the Nd content is not caused by the presence of a miscibility gap, since the tie lines defined by Dottavio *et al.* indicate in all cases some presence of Nd on each phase after phase separation [118]. Respecting the cooling time of the experience (6h) [118], low Nd mobility on the UO_2 lattice does not allow the migration of 26%Nd from one phase to the other in a matter of minutes at a temperature beneath 745 K, since its diffusion coefficient is extremely small [120]. This supports the fact that the presence of these two phases with different concentration of Nd are attributed to the manufacturing process and not to a thermodynamic instability. In addition, Figures 2.4a and 2.4c present the Selected Area Electron Diffraction (SAED) pattern indicating in a first approach that both these phases have the same crystallographic structure, which is the FCC structure projected in the [0 1 3] zone axis.

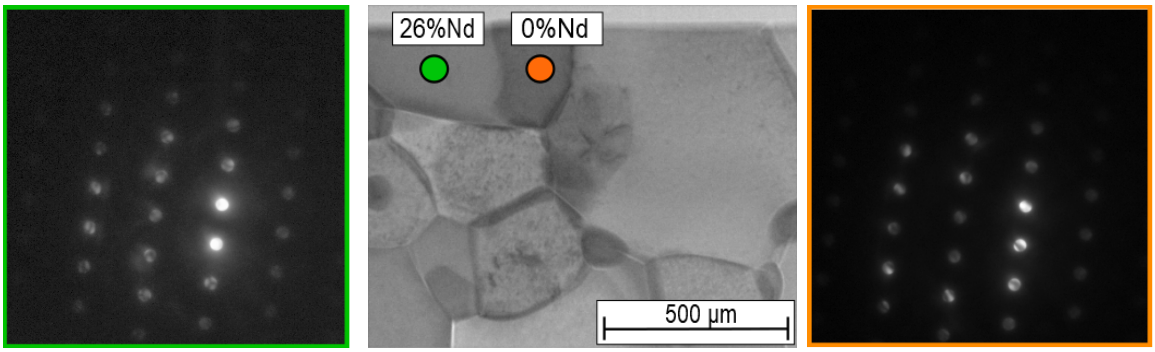

(a) (b) (c)

Figure 2.4: Figures (a) and (c) show the SAED corresponding to the green and orange circles and (b) TEM imaging of the sample doped with 33%.

2.1.2 Solubility studies

All four compositions haven been analyzed by XRD. The patterns were defined at room temperature on powder for the range of 2θ of 20-100° and 5-145°, using a step of 0.01° and a counting time of 0.5 s.step^{-1}. Different samples with the same composition have been studied to assess the heterogeneity observed by SEM.

Figure 2.5 shows the XRD patterns of two different samples doped with 4% Nd. Both acquisitions show the characteristic pattern of the single monophasic FCC structure, where only the peaks corresponding to the Kα_1 and Kα_2 wavelengths are seen. There are no supplementary peaks that might indicate the presence of a secondary phase. This first observation supports the observations made by Dottavio *et al.* in [118] where it claimed that 1973 K was a temperature sufficiently high to achieve homogeneity, and that at 4% the system is still monophasic (since the miscibility gap begins only appears with concentrations of Nd greater than 9%). The lattice parameter of the two samples remains sensibly the same. Table 2.1 shows the estimated values of the lattice parameters for both samples, which were estimated using the Le Bail method [154].

Sample	Lattice parameter (Å)
Sample 1 - 4%Nd	5.4710(9)
Sample 2 - 4%Nd	5.4700(6)

Table 2.1: Lattice parameter of the samples 1 and 2 doped with 4%Nd.

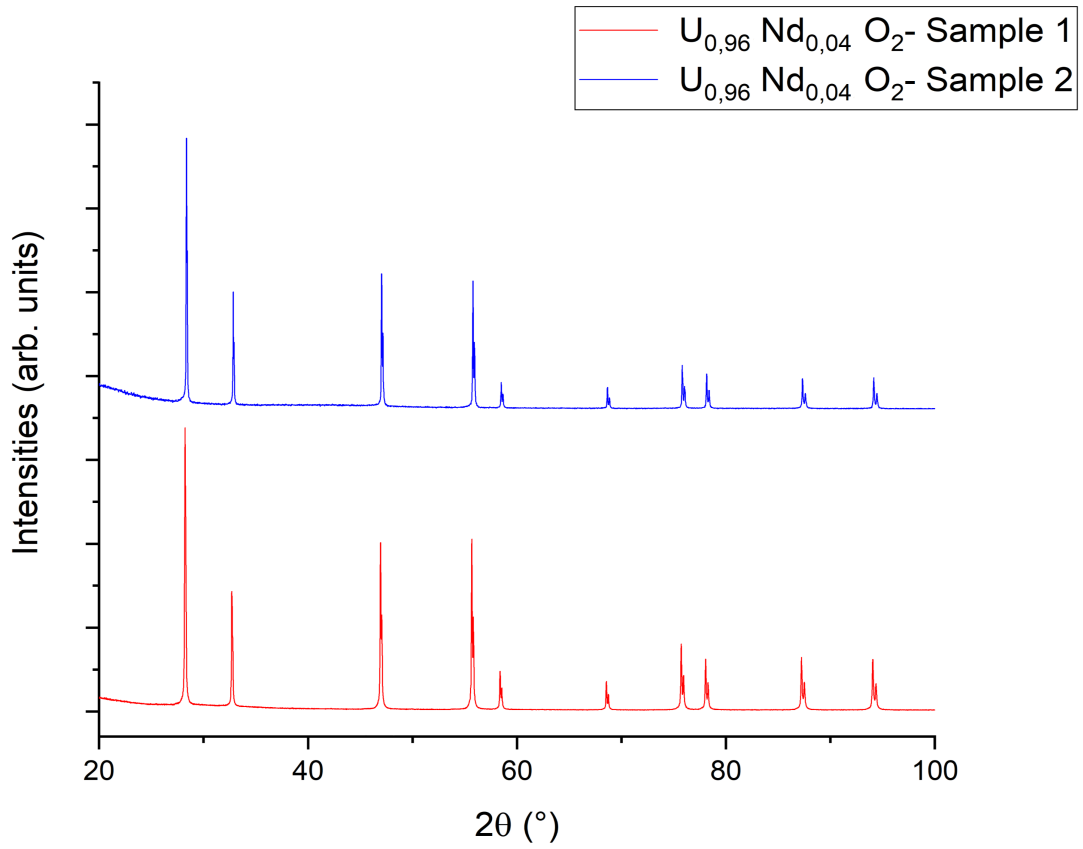

Figure 2.5: XRD patterns for the samples 1 and 2 doped with 4%Nd produced by dry route showing in both cases the presence of the FCC structure and a monophasic system.

Two other samples substituted with 17%Nd were also measured by XRD, see figure 2.6. A more detailed examination of the sample 3 (red) allows to see that the peaks related to the original FCC structure have a shoulder on each peak at lower angles, indicating the presence of a second crystalline phase, FCC-2 (Figure 2.6b). On the other hand, the sample 4 (blue) displays other peaks that are characteristic of hexagonal Nd_2O_3 (space group P6/mmm, number 191), signaled on the image with black stars, besides the main FCC phase, referenced with yellow triangles [155]. All these extra peaks seem to indicate that the samples 3 and 4 are not monophasic and that the synthesis process is not reproducible.

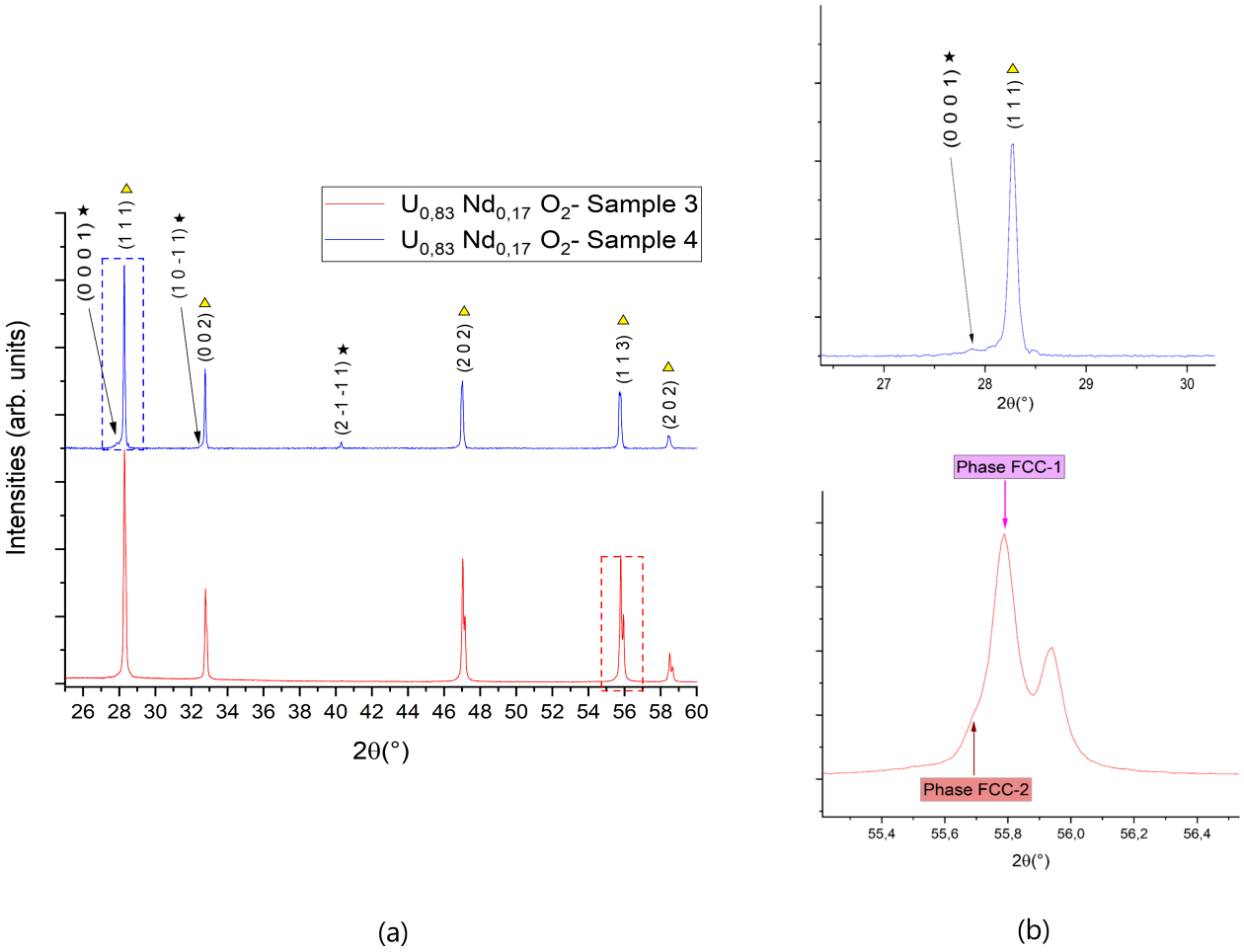

Figure 2.6: (a) illustrates the XRD patterns of two samples doped with 17%Nd through dry route and (b) presents a magnification of the framed region in red or blue to highlight the presence of the second crystallographic phase, FCC in sample 3 and hexagonal Nd_2O_3 in sample 4 (black stars).

One sample doped with 27%Nd was also analyzed by XRD (Figure 2.7). In a preliminary analysis it is possible to distinguish the FCC structure as the predominant phase. However, a Rietveld's refinement allowed to see that there is also a minoritary phase that can be indexed as the cubic bixbyite (C-Nd_2O_3), see Figure 2.7a [156]. Figure 2.7b details in a portion of the full pattern to highlight the main peaks that confirms the presence of this phase. In addition, there are also present the diffraction of the K_β wavelength corresponding to the peaks with higher intensities, specially at lower 2θ.

The refinement indicated that the phase fraction of the second minoritary phase was around 5(1)%. Further, the lattice parameter of the FCC phase of this sample was 5.4591(8) Å, which according to Wadier measurements, this value corresponds to the concentration of a sample doped with 20%Nd [52]. This implies that the global

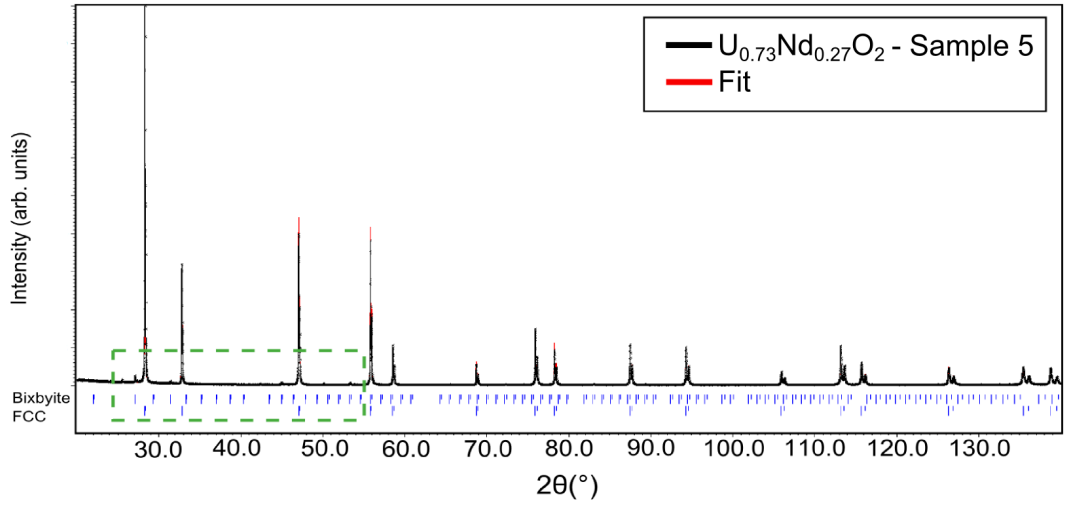

(a)

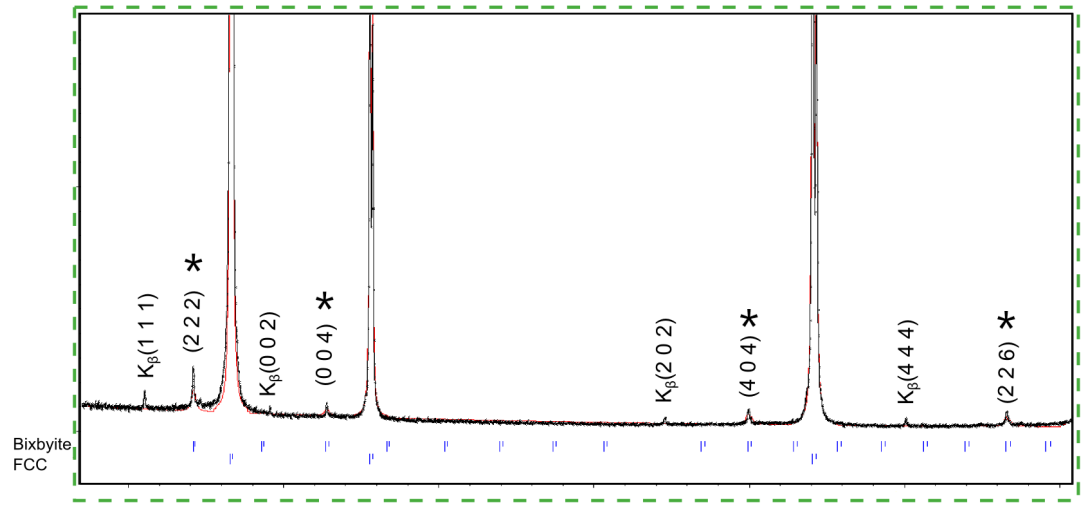

(b)

Figure 2.7: (a) presents the full XRD pattern of the sample doped with 27% Nd and (b) magnification of the pattern to highlight the presence of the cubic bixbyite C-Nd_2O_3(*).

concentration of Nd, which is 27% is distributed in both phases, the FCC phase and the cubic bixbyite. The refinement also revealed the lattice parameter of the second phase, the bixbyite, this value is 11.397(3) Å. According to a number of published articles, the value that this phase can adopt is around 11.08 Å [157, 158], which is lower than the obtained value. This observation leads to think that this phase is not the final state that can be found at the thermodynamic equilibrium, instead it is a phase formed as a consequence of the interplay of a random distribution of atoms at high temperature with specific conditions of oxygen partial pressure, and do not have enough energy at lower temperatures to settle on the stable form, which indicates that this phase is not stable, but it is metastable. This reasoning implies that a random fluctuation of the Nd concentration reacts differently to different oxygen partial pressures and is capable of forming different phases, which explains why it is possible to see the different phases on the assessed samples.

Finally, two other samples doped with 33%Nd were studied by XRD (Figure 2.8). They are sample 6 (light blue) and sample 7 (blue). Sample 6 is biphasic, since there is a clear peak splitting, one for each phase, designated in the inset image as Phase FCC 1 and Phase FCC 2, respectively. This is the opposite to what is observed in the sample 7 (dark blue), where the system is monophasic. In this sample the single solid phase is well crystallized. It is important to highlight the fact that the peak splitting is caused by the diffraction of the Kα_2 wavelength .

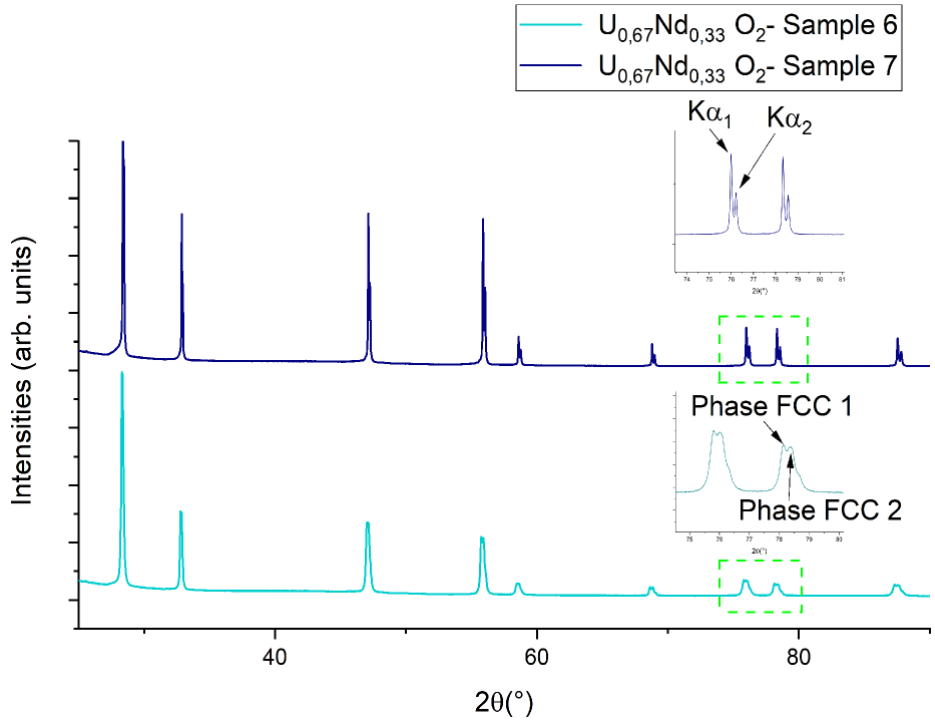

Figure 2.8: XRD patterns for the samples 6 (biphasic) and 7 (monophasic). Both patterns reveal the FCC structure.

These diffraction patterns outline certain conclusions about the behavior of these samples. First, the XRD patterns for the samples 1 and 2, doped with 4%Nd show a monophasic system with a lattice parameter of approximately 5.47 Å, close to the lattice parameter of pure UO_2 of 5.47127(8) Å [57]. On the other hand, samples 3, 4, 5 or 6 doped with higher amount of Nd show an heterogeneous system, where the concentration of Nd is not influential concerning the number of phases nor the type of crystalline structures present on the system.

2.1.3 Conclusions

Throughout this section it was presented the manufacturing process and characterization by multiple techniques (XRD, SEM and TEM) on samples produced by a dry route process. This process involves the mixture of two solids through intimate contact (pressing) and heating at elevated temperatures (sintering) (Figure 2.1). It was seen that regardless the attempts to produce homogeneous samples to probe the miscibility gap first detected by Desgranges *et al.* in [114] the samples remained in all cases not well adapted to evaluate the ternary phase diagram. It was seen also that local fluctuations of the Nd concentration are capable of inducing the formation of metastable phases that are not present on the phase diagram (Figure 2.7a).

Thus, to describe the ternary phase diagram it is necessary to study another set of samples. It is then proposed to work with samples made through a wet route process which is another synthesis process known to achieve an initial homogeneity of the powder by co-precipitation of U and Nd in solution at room temperature.

2.2 Sample manufacturing through wet route

2.2.1 Synthesis

Wet route manufacturing processes are commonly used to produce initially homogeneous oxides. These type of processes consists first of the co-precipitation of cations by using an anionic complex to precipitate such as carbonate, hydroxide or oxalate. In this study, the co-precipitation was made using oxalic acid to produce a mixed (U,Nd) oxalate, according to the reaction:

$$(1-y)U^{+4} + yNd^{+3} + 2C_2O_4^{-2} \rightarrow U_{(1-y)}Nd_y(C_2O_4)_2.nH_2O \downarrow$$

A detailed description of the precipitation process is reported in Appendix A. The compositions were selected to assess the formation of the miscibility gap reported in [114, 118]. XRD and SEM evaluations were made directly after the drying stage. The morphological appearance of the samples obtained by co-precipitation stage is presented in Figure 2.9. The characteristic square-shaped platelets of the monoclinic oxalates is observed in agreement with other mixed oxalate precipitates such as

U(IV)-Th(IV) [159]. The oxalate doped with 4% Nd displays a well-formed square-shaped platelet of approximately 2-3 μm. The other two oxalates also precipitated as squared platelets but in these cases the higher concentration of Nd seems to affect its formation.

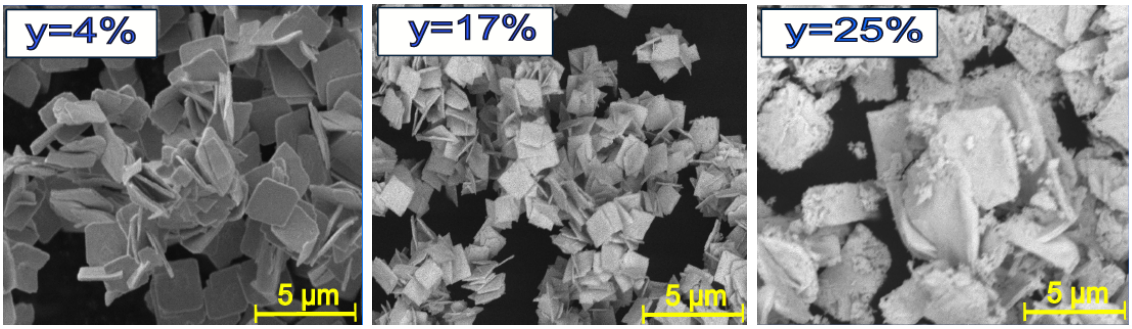

(a) (b) (c)

Figure 2.9: SEM imaging of the three samples after the stage of the oxalic precipitation.

After the co-precipitation of the mixed oxalates, the formation of the mixed oxides (U,Nd)O_2 is obtained by a calcination stage to induce dehydration and decomposition of the oxalate complex. This thermal treatment basically consists on heating the samples up to a temperature of 1273 K for 60h under a reducing atmosphere to avoid oxidation (10 K.min^{-1} and Ar + 5% H_2). A number of studies analyzed this decomposition through TGA on different oxalates precursors to detect the decomposition temperatures of the sample [160, 161]. These studies prove that above 873 K the weight loss of the sample is less than 1%, despite some carbon traces that may remain at the grain boundaries. The chemical decomposition can be schematized as follows,

$$U_{(1-y)}Nd_y(C_2O4)_2.nH_2O \rightarrow U_{(1-y)}Nd_yO_2 + nH_2O \uparrow + 2CO \uparrow + 2CO_2 \uparrow$$

The formation of the mixed oxides was equally verified by the acquisition of XRD patterns at room temperature after the calcination. Figure 2.10 shows the XRD patterns of the three samples, where it confirms the decomposition to form FCC structures. It is possible to see 1273 K is a temperature high enough to form the oxides phases, however, the samples are not well crystallized since all the peaks are fairly broad.

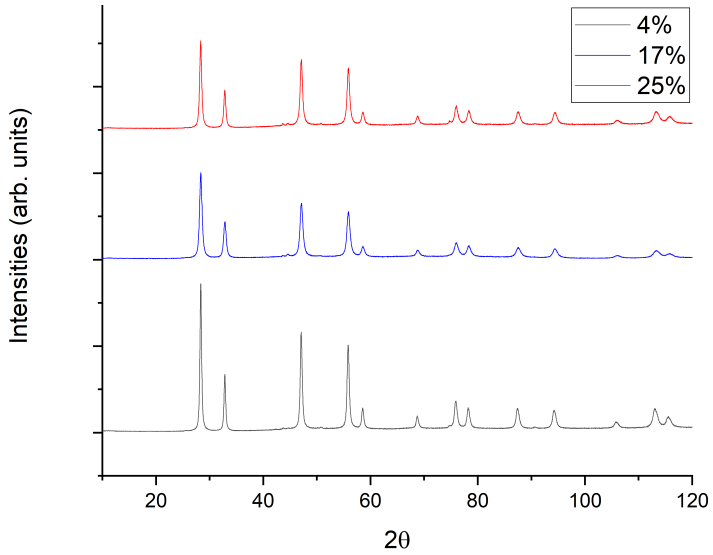

Figure 2.10: XRD patterns measured after the calcination at 1273 K. All three samples show the FCC structure.

This observation is also confirmed by TEM microscopy. Figure 2.11 (a) shows the sample doped with 25 % Nd where the crystallites at the edge of each platelet can be observed. Crystallite size in this region can reach values between 20 and 40 nm in good agreement with what is observed by XRD in Figure 2.10.

In addition, in Figure 2.11 (b) it is possible to observe the powder electron diffraction pattern of this sample. The presence of concentric rings confirm that many crystallites are affected on this image. The interplanar spacing of these rings is in agreement with the formation of the FCC structure.

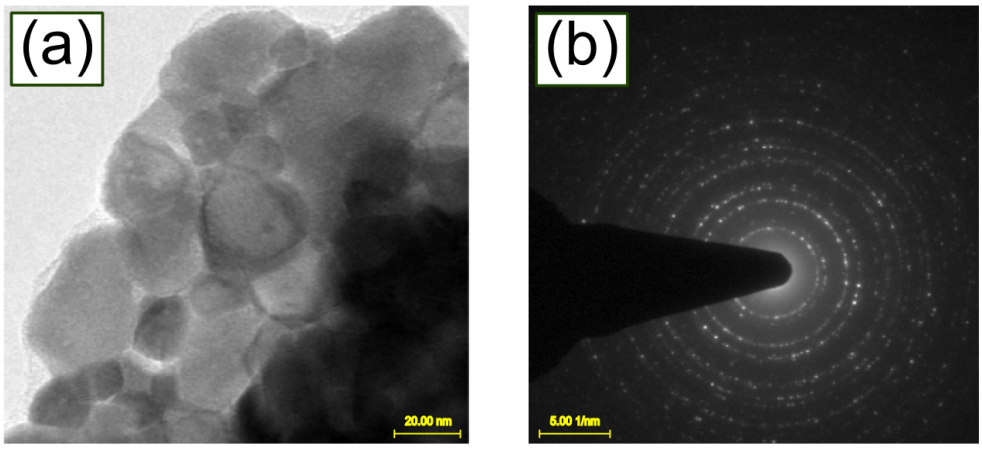

Figure 2.11: TEM imaging (a) and powder electron diffraction (b) for the oxide with 25 % Nd.

2.2.2 Sintering

The sintering process is a thermal treatment carried on green pellets at a temperature typically about 2/3 the melting point. This process consists on heating the sample at 1823 K under a reducing atmosphere of Ar+5% H_2 during 4h. The final result after the sintering stage is, thus, the formation of dense cylindrical pellets that have a 4mm radius and 3 mm height, and a mean density of 95% the theoretical density.

SEM imaging and X-ray mapping were performed on the three samples after the sintering process (Figure 2.12). Figure 2.12a displays that the sample doped with 4%Nd presents a region where the porosity is more pronounced than others. Figure 2.12b indicates the distribution of all three elements: Nd in red, U in blue and O in light blue. It is no possible to relate the distribution of Nd with the formation of pores, since in this case Nd is uniformly locate along the sample. Figure 2.12c and 2.12e present a more uniform grain formation along the sample. Small agglomerations of Nd of micrometric size can be seen where the Nd concentration is slightly higher than the rest of the pellet. These agglomerates could be caused during the co-precipitation stage. In both cases, the agglomerates do not represent an important degree of heterogeneity, important enough to influence the global formation of oxides.

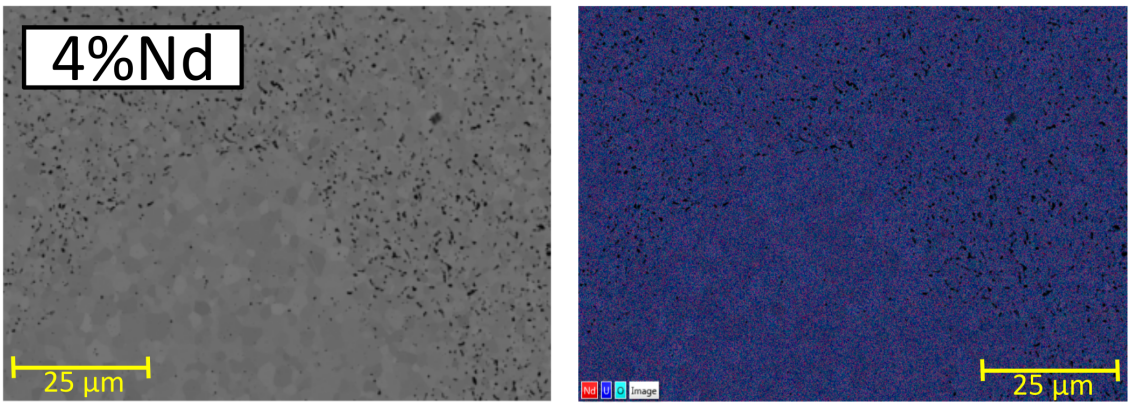

(a) (b)

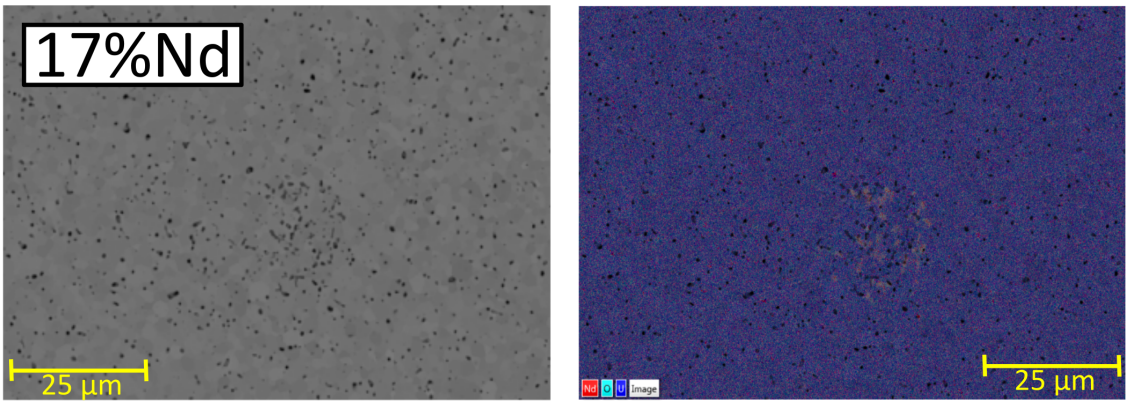

(c) (d)

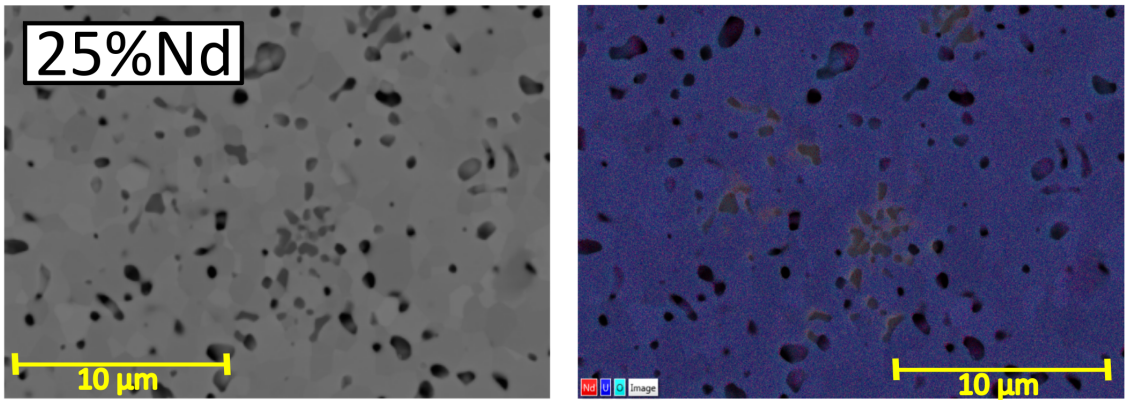

(e) (f)

Figure 2.12: SEM and X-ray mapping of the samples produced by wet route doped with 4, 17 and 25% after the densification process.

XRD measurements at room temperature on these samples were performed and compared to the ones obtained after calcination (Figure 2.13). Similar to the case of the samples produced by dry route, these acquisitions were also made on powder. The range of 2θ was defined from 5-120°, using a step of 0.01° and a counting time of 0.5 s.step^{-1}. The patterns display a good crystallization which allows to make a refinement according to the Rietveld method [156]. The FCC structure is still the crystallographic structure present on these systems. The results obtained by Rietveld refinement are presented in Table 2.2.

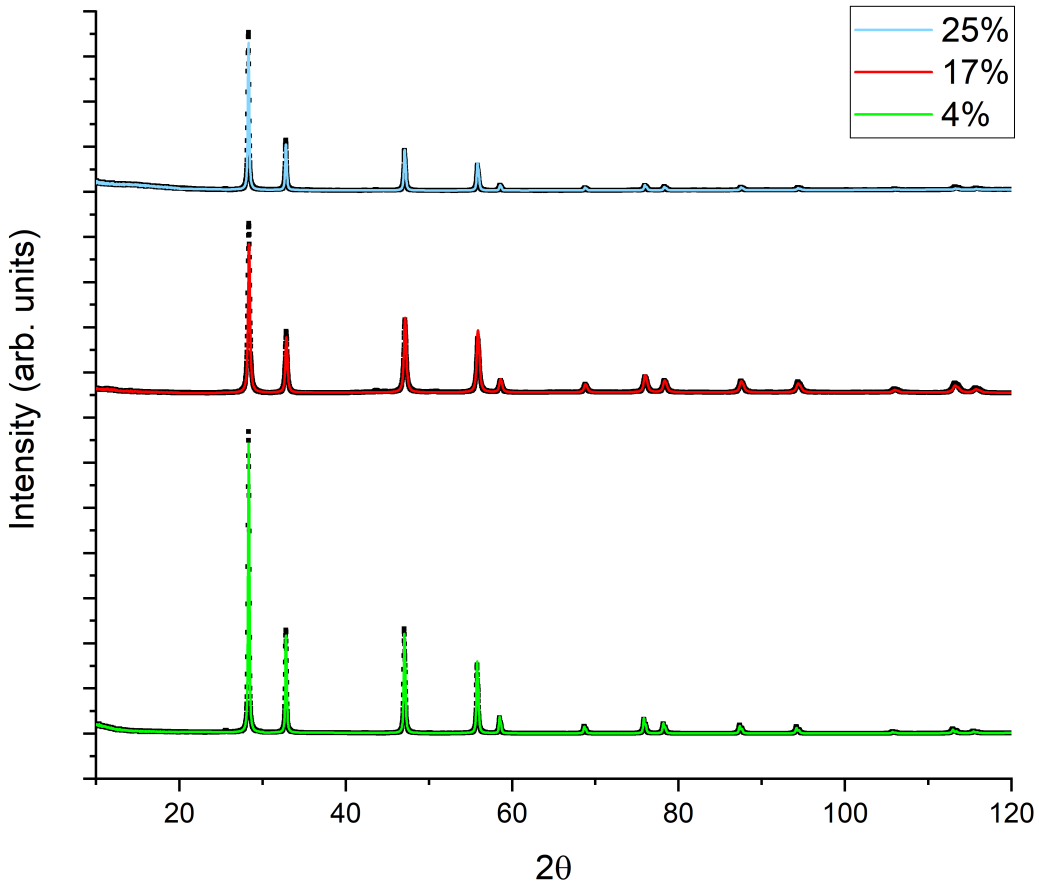

Figure 2.13: XRD data (black points) and Rietveld refinements (coloured lines) for the three sintered oxides.

Figure 2.14 presents the evolution of the lattice parameter as a function of the Nd concentration for stoichiometric samples in comparison with data published in open literature [51, 52, 57, 123, 162]. The tendency for the lattice parameter to follow a straight line in lanthanide-based ternaries was first described by Ohmichi *et al.* [162]. However, Lee *et al.* added the empirical term (1-y/200) to this equation in order to fit as close as possible all experimental data [151], visible in Figure 2.14 as green line. The expression of the lattice parameter as a function of the Nd concentration was described as,

Sample	Structure	Lattice parameter (Å)	Rp
4%	FCC	5.4671(8)	7.12
17%	FCC	5.4594(5)	8.17
25%	FCC	5.4568(3)	6.21

Table 2.2: Results obtained by the Rietveld refinements for the three sintered samples.

$$a = \frac{4}{\sqrt{3}} \left\{ (1-2y+2x) r_{U^{+4}} + (y-2x) r_{U^{+5}} + y r_{Nd^{+3}} + \frac{(2-x)}{2} r_{O^{-2}} + \frac{x}{2} r_{O_v} \right\} \cdot (1 - \frac{y}{200}) \quad (2.1)$$

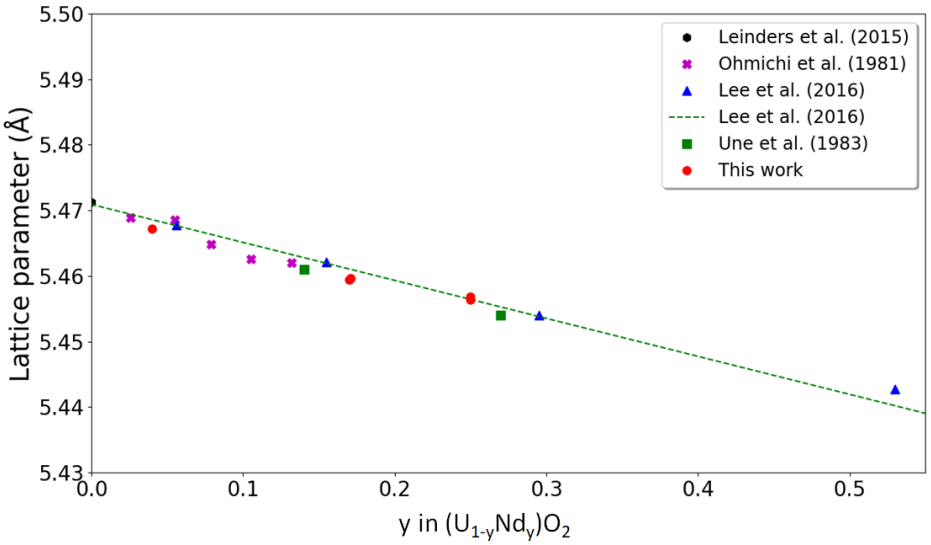

Figure 2.14: Lattice parameters calculated by the different authors and estimated straight line defined by Lee *et al.* as a function of the Nd concentration [57, 123, 151, 162].

The lattice parameters of the samples assessed in this work follow a linear evolution as a function of the Nd concentration, the comparison with other works lead to think that the O/M ratio of the sample is close to 2. Thus, in order to study the hypo-stoichiometric domain of the phase diagram is necessary to reduce the samples.

The next section is then dedicated to perform a thermal treatment to achieve hypo-stoichiometry and characterize the reduced samples in comparison to stoichiometric samples to assess the existence of a miscibility gap on the system U-Nd-O.

2.2.3 Reducing thermal treatment

The controversial miscibility gap on the system U-Nd-O was experimentally identified in the hypo-stoichiometric region of the phase diagram. Therefore, the first stage requires assessing the limits of the miscibility gap. Thermodynamic modeling was performed to evaluate the full extension of the miscibility gap at room temperature using the software Thermo-Calc and the thermodynamic database (TAF-ID), which includes the experimental results published by Dottavio *et al.* in [91]. This means that all calculations are based on those results since they present the only experimental data that characterize in temperature the miscibility gap. Next, the thermal treatment and the associated characterizations are presented. In first place, the solubility studies are probed by XRD at room temperature, and in second place, an analysis by X-ray Absorption Spectroscopy (XAS) is made to assess the charge compensation mechanisms as well as the local structure.

Definition of the operating conditions

The miscibility gap in the system U-Nd-O starts at room temperature at a relatively low concentration of Nd (9% at.) and it covers an important portion of the phase diagram. Figure 4.6 shows its full extension at room temperature. The tie lines define the phases 1 and 2 at the thermodynamic equilibrium. It is important to note that Phase 1 overlaps the horizontal line where O/M=2. This means that, according to this model, Phase 1 is always stoichiometric, (U,Nd)O_2, whereas the oxygen-poor phase (Phase 2) is always hypo-stoichiometric, (U,Nd)O_{2-x}.

The miscibility gap changes as temperature increases. The solubility of Nd in UO_2 is higher with higher temperatures, and therefore the extension of the biphasic region decreases with increasing temperature. A complete monophasic system is predicted above 1200 K, see Figure 2.16.

To enter the miscibility gap it is then necessary to define the right equilibrium temperature and O/M ratio, otherwise the system would remain monophasic. Figure 2.17 schematizes the transition curves for the samples with 17 and 25 % Nd. The miscibility gap is predicted below 725 K for the sample at 25% and 530 K for the one at 17% respectively (O/M=1.95 and O/M=1.97). This implies that the temperatures of the thermal treatment need to be about 670 K for the sample doped with 25%Nd and 470 K for the sample with 17%Nd to promote the cation ordering.

The control of the atmosphere of the thermal treatment is of major importance to achieve this right stoichiometry. Therefore, one must know the influence of the oxygen chemical potential (μ_{O_2}) on the O/M ratio at a certain temperature.

In practice, it is convenient to work in terms of ln(PO_2), as:

$$\Delta\mu_{O_2} = R \cdot T \cdot ln(\frac{P_{O_2}}{P_{O_2}^{ref}})$$

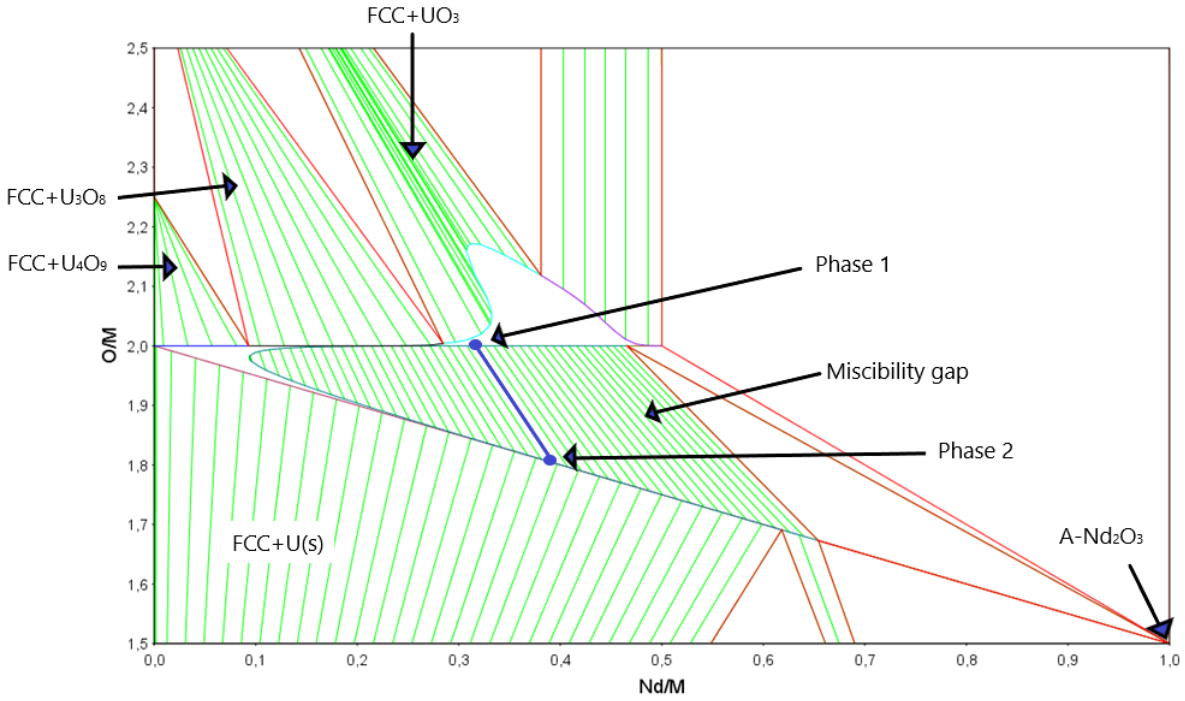

Figure 2.15: Detail of the phase diagram of the U-Nd-O system showing the extension of the miscibility gap at room temperature. The blue line is the prediction for the sample with 33%Nd.

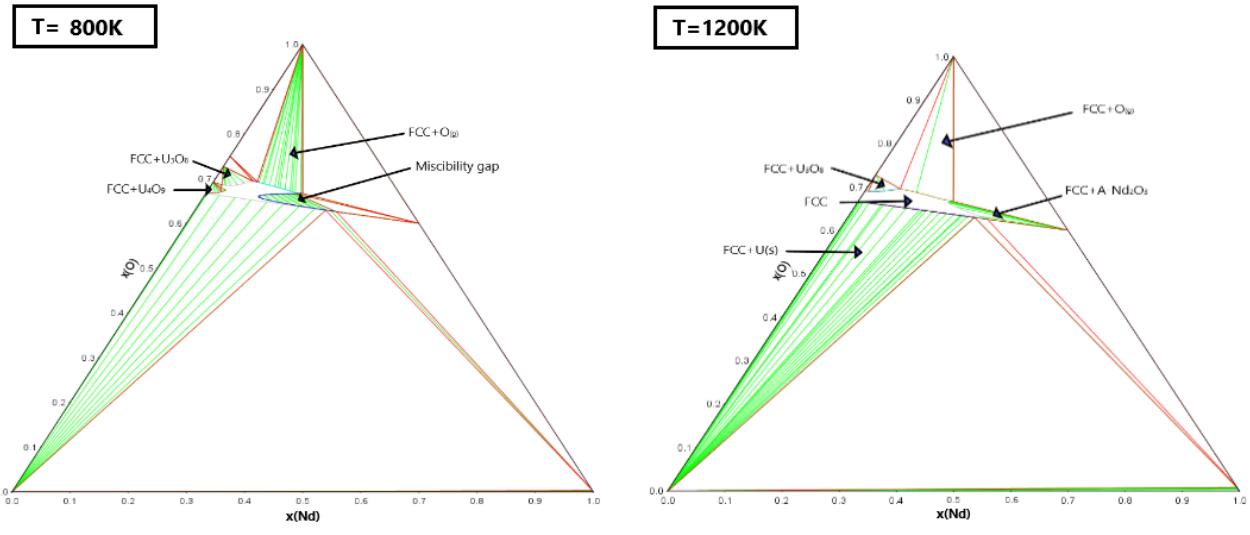

Figure 2.16: Isothermal sections of the U-Nd-O system at 800 K (left) showing the presence of miscibility gap and 1200 K (right) where the hypo-stoichiometric region is monophasic.

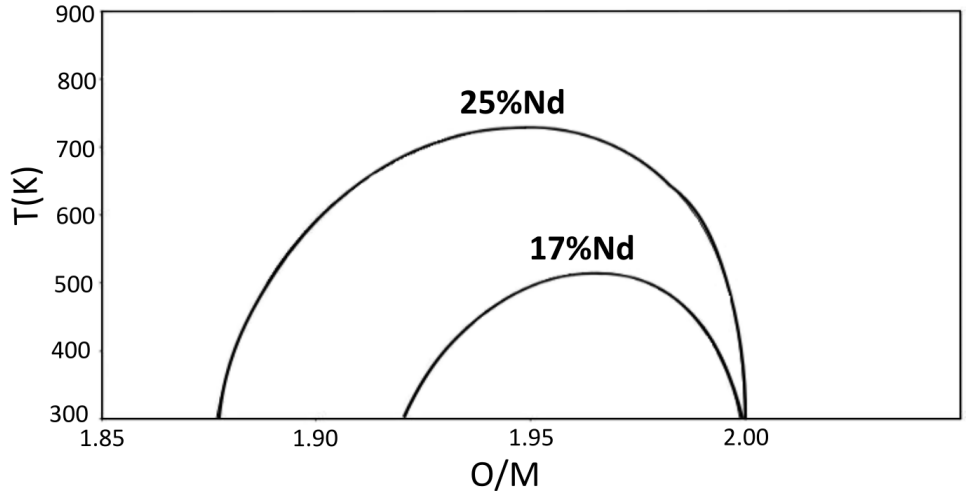

Figure 2.17: Transition curves for the samples doped with 17 an d 25 % Nd.

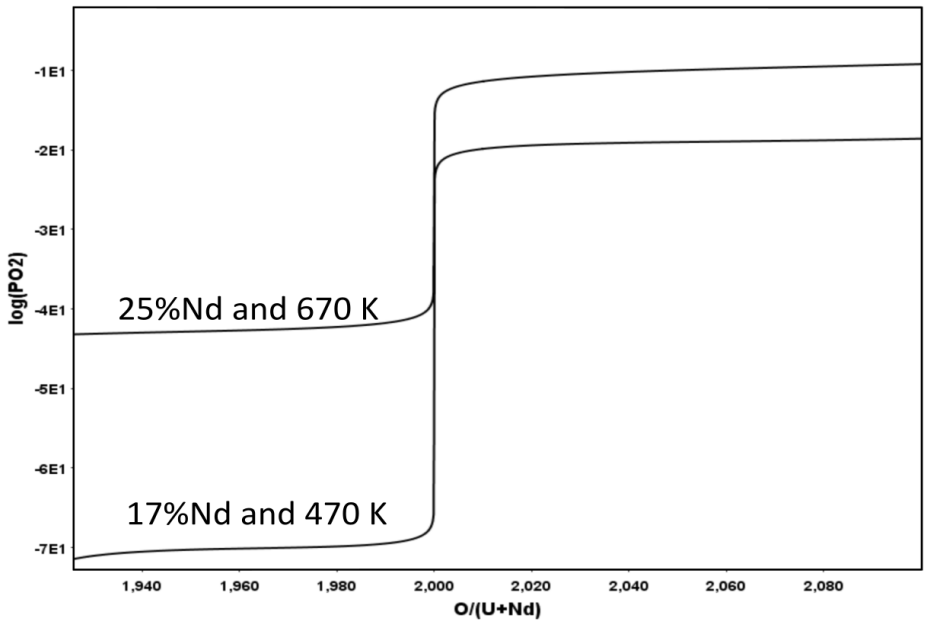

Figure 2.18: Oxygen chemical potentials for the samples doped with 17 and 25% Nd at 470 K and 670 K, respectively.

Observing the Figure 2.18 one can define the P_{O_2} to reach the right stoichiometry (1.95 and 1.97 for 25% and 17%Nd, respectively): 10^{-40} atm for 25% and 10^{-70} atm for 17%. In the practice, these values are impossible to reach with usual gas mixtures thus another methodology is proposed.

If we consider that the oxygen chemical potential increases with temperature (the curves move upwards with higher temperature), it becomes easier to reach lower O/M when the temperature rises. We propose then to reach the right stoichiometry

at higher temperature (1473 K) and quench (0.5 K.s^{-1} the samples below the miscibility limits temperatures, precisely at 670 K for 25% Nd and 470 K for 17 and 4% Nd.

A gas current of Ar+4%H_2 and an oxygen controlling device are used to control the atmosphere in the furnace. This device generates or consumes oxygen through a redox couple (Zr/ZrO) using an electrical current at a T=923 K until a PO_2=10^{-28} atm. A more detailed analysis of the oxygen controlling device can be found in Appendix B.

Figure 2.19 presents the calculation of the evolution of the P_{O_2} of the gas current Ar+4%H_2 as a function of the temperature when it has a fixed oxygen P_{O_2} of 10^{-27} atm at 923 K. The calculation is an approximation to reality since the concentrations of minor gas impurities like CO, CO_2 or CH_4 are only estimated. In this graphic the P_{O_2} rises with the temperature, reaching a value of 10^{-16} atm at 1473 K. According the curves of log(P_{O_2}) vs O/M at 1473 K for these two compositions, the O/M for the sample doped with 17% Nd is 1.98 and for the sample with 25% Nd is 1.92, these values are highlighted by the green circles in Figures 2.20a and 2.20b.

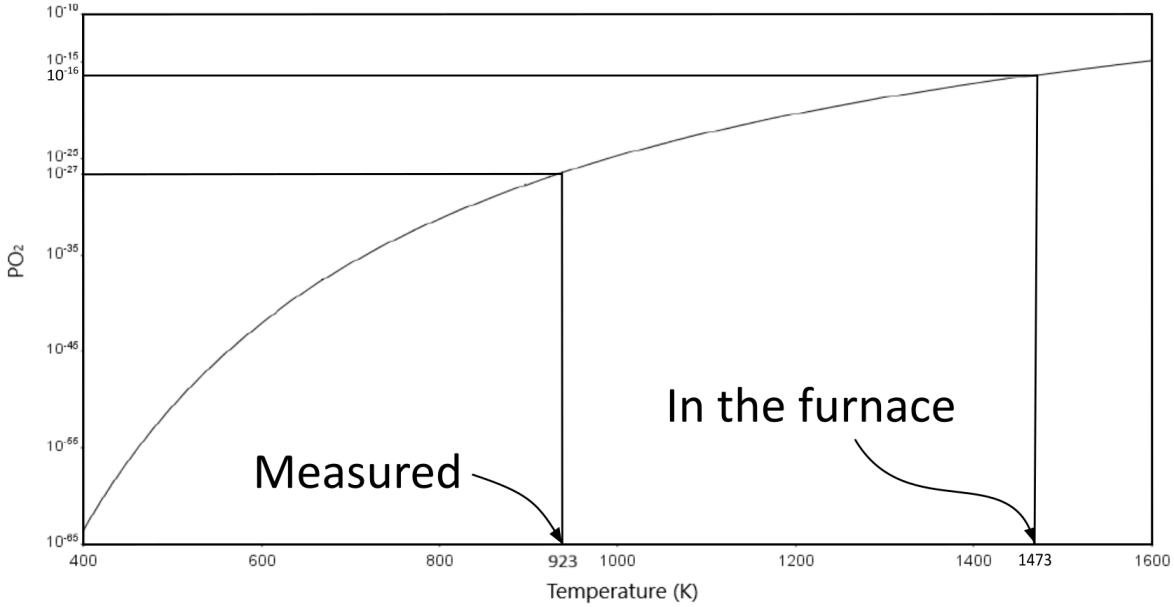

Figure 2.19: Evolution of the P_{O_2} in the furnace when the entering conditions of the gas vector are fixed at 10^{-27} atm and 923 K.

The thermal cycle performed on the two samples consisted on heating the sample with a ramp of 1 K.s^{-1}, with a dwell for 2h at 1473 K, to insure that oxygen is well distributed and the intended stoichiometry is achieved.

Afterwards, the temperature decreases until 670 K and 470 K for the samples doped with 25% and 17%Nd, respectively. At this point the P_{O_2} was set at its maximum reducing capacity, which is 10^{-28} atm. The dwell at 670 and 470 K was

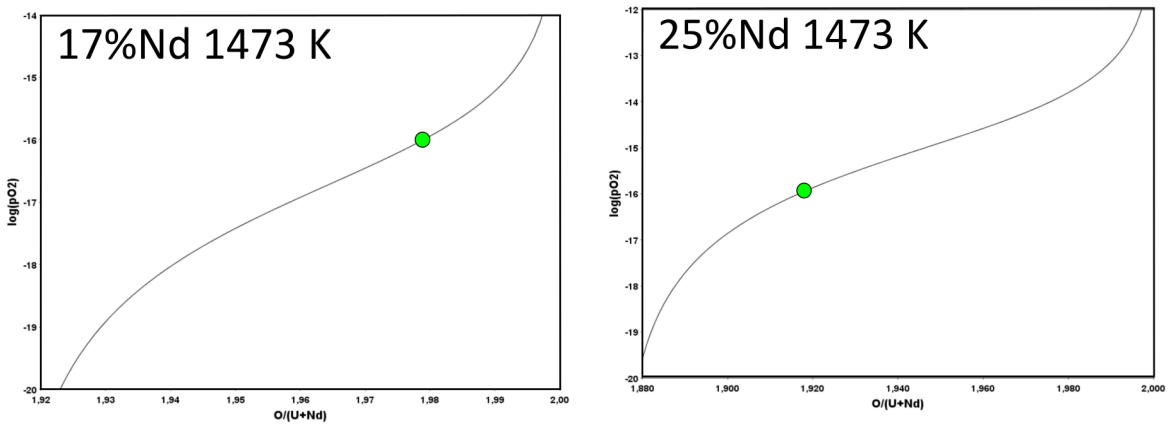

(a) (b)

Figure 2.20: Log(P_{O_2}) vs O/M for the samples with 17% Nd (a) and 25%Nd (b) at 1473 K. The green circles outline the intended stoichiometries.

performed for 5h in both cases. Finally, the sample was cooled down to room temperature with a ramp of 0.2 K.s^{-1}.

2.2.4 Nd solubility studies by XRD

After the thermal treatment, all samples were studied by XRD (Figure 2.21). Hereinafter, this document will refer as T0 for the samples non-treated thermally and TT for the samples treated thermally, where it is possible to see a clear narrowing of the FWHM of the peaks. Table 2.3 shows the lattice parameters obtained after the Rietveld refinement [156]. The behavior of the lattice parameter of the samples treated thermally is similar to the one of the pristine samples, since it decreases with the concentration of Nd.

Sample	Structure	Lattice parameter (Å)	Rp (%)
4% TT	FCC	5.468(1)	15.04
17% TT	FCC	5.4607(4)	10.81
25% TT	FCC	5.4582(3)	10.14

Table 2.3: Results obtained through the Rietveld refinement for the three samples after the thermal treatment.

Throughout all the patterns, the system shows only a single solid phase, these results agree with what is proposed by a number of authors under hypo stoichiometric

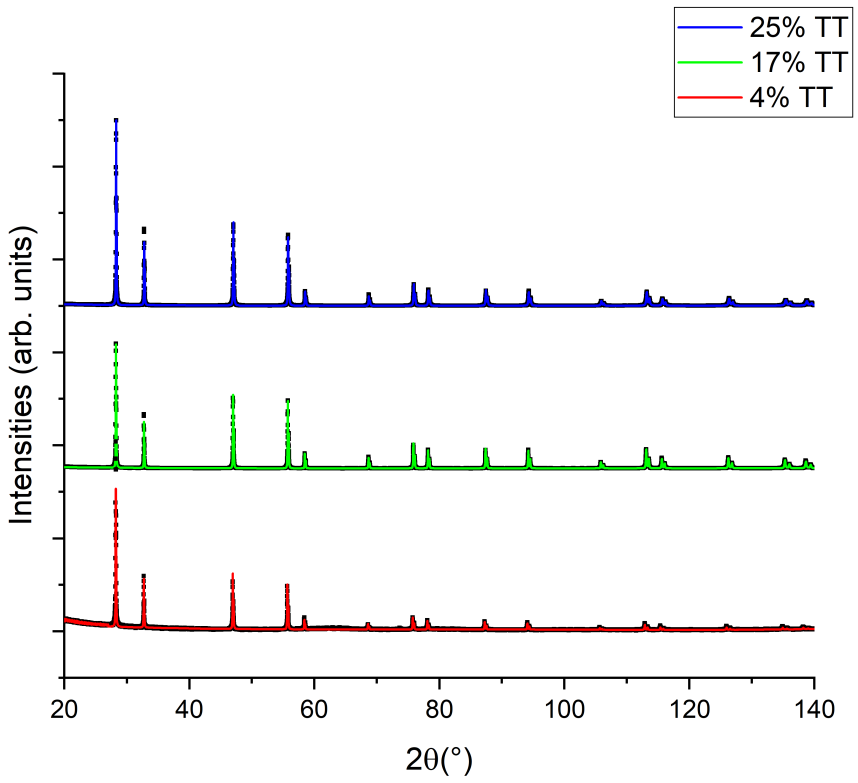

Figure 2.21: XRD patterns for the 3 compositions after the thermal annealing under reducing atmosphere.

conditions [50–52, 57, 123, 162] but differ from others, since no miscibility gap is seen [91, 114, 118].

A more detailed analysis of the results obtained after the thermal treatment (TT) in comparison with the results obtained directly after the sintering (T0). Table 2.4 presents a summary of the refined results of the XRD measurements before and after thermal treatment. There is also presented the O/M ratio calculated after equation 2.1 [151].

In order to see more clearly the effect of the thermal treatment, Figure 2.22a compares the lattice parameter of all samples before and after the thermal treatment. Table 2.4 reports a clear influence over the crystallite size before and after the thermal treatment for each sample and a reduction of the overall microstrain on each sample. This results is explained by the influence of the temperature during the thermal treatment, since at 1473 K it is possible to induce an increasing of the grain size and reduce the microstrain. In addition, Figure 2.22b compares the misalignment of the (1 1 1) peak corresponding to the samples at 25% of Nd before and after thermal treatment. This figure highlights the better crystallization of the sample treated thermally, since both peaks caused by Kα_1 and Kα_2 wavelengths are clearly visible; whereas the pris-

tine sample shows a single peak which is fairly broad, incapable of displaying the Kα_2 wavelength. The behaviour responsible for the misalignment is explained by the natural response of the U-Nd-O system to expand the crystal lattice when there is an oxygen deficiency respecting the stoichiometric FCC structure. Similar results have been repeatedly observed in other ternary U-Ln-O systems (being Ln=Gd, Ce, Eu or Y), where it is also seen the lattice expansion when oxygen vacancies are induced [40, 43, 117, 151, 162].

Samples →	4%		17%		25%	
Refined parameters ↓	T0	TT	T0	TT	T0	TT
Lattice parameter (Å)	5.4671(8)	5.468(1)	5.4594(5)	5.4607(4)	5.4568(3)	5.4582(3)
O/M	2.006(3)	1.998(3)	2.002(7)	1.999(7)	2.001(7)	1.993(7)
Crystallite size (nm)	65(1)	113(3)	41(1)	149(1)	61(1)	155(2)
Microstrain (%.10^{-4})	5.2(1)	1.7(2)	13.9(3)	2.6(1)	7.1(2)	5.9(1)

Table 2.4: Calculated parameters obtained through the Rietveld refinement for all samples before and after the thermal treatment.

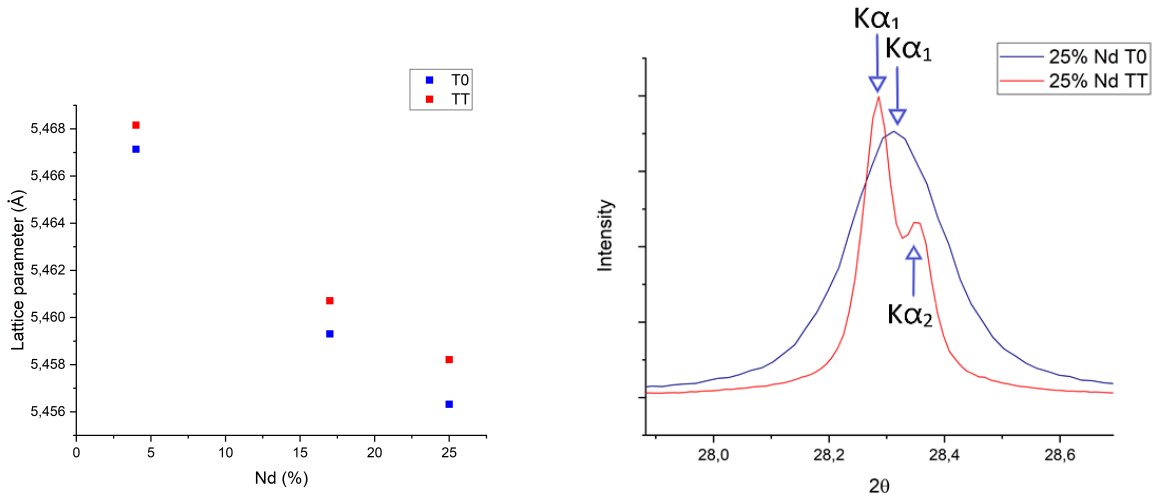

(a) (b)

Figure 2.22: (a) shows the evolution of the lattice parameter for all samples before and after thermal treatment, and (b) schematizes the shifting of the (1 1 1) peak for the sample doped with 25% to lower angles after the thermal treatment.

2.2.5 X-ray Absorption Spectroscopy

In order to understand better the behavior of Nd-doped samples at an atomic scale, all six samples (treated and non-treated thermally) were also studied by X-ray Absorption spectroscopy (XAS). This characterization allows to describe the charge compensations mechanisms and evolution of the local environments induced by the substitution of U^{+4} by Nd^{+3}. Knowing that Nd can only exist as a purely trivalent cation Nd^{+3} in solid solution, the doping effect is traduced directly on the oxidation of U^{+4} or the formation of oxygen vacancies needed to maintain the electro-neutrality of the system.

The XAS experiments were performed on the MARS beamline at the Soleil synchrotron (France) at the U M_4-edge, U L_3-edge and Nd_3-edge. The experimental conditions related to this study are reported in Appendix B. Multiple analyses on trivalent-doped UO_2 through X-ray Absorption Near Edge Spectroscopy (XANES) showed that initial U oxidation to pentavalent state demands lesser energy than the formation of vacancies or further oxidation to the hexavalent state [163]. In this work, U M_4-edge spectra was extracted by using high energy resolution fluorescence detected-XAS (HERFD-XAS). The use of this technique virtually reduces the core-hole broadening effect and evaluates directly metallic mixtures with different valence states [60, 164]. In addition, Extended X-ray Absorption Fine Structure (EXAFS) at the U L_3-edge and Nd_3-edge allows to probe of the FCC local environment of the samples. These results describe the evolution of the crystal lattice at an atomic scale and are complementary to the results provided by XRD analysis.

Charge compensation mechanisms

The U M4-edge spectra of all the samples (black lines) and all the references (blue lines) are shown in Figure 2.23. The references of UO_2, $NaUO_3$ and UO_3 correspond to pure U^{+4}, U^{+5} and U^{+6} valence state, respectively.

In the first place, it is clearly visible that all the samples present a sharp peak at 3725.8 eV, which belongs to the absorption energy of the U M_4-edge of U^{+4}. Further, they also present a shoulder at a higher energies respecting the U^{+4} white line that increases progressively with higher concentrations of Nd, independently if the samples were treated thermally or not. This behavior is explained by the formation of U^{+5} on the system to compensate the charge deficit when Nd^{+3} is introduced on the cationic sub lattice. Indeed, to maintain the electro neutrality in the system, each Nd^{+3} introduced increases the uranium valence state (to U^{+5} or U^{+6}.), or create an oxygen vacancy. On these measures, no sign of the uranyl bonding was observed which discards the presence of U^{+6}. The precise positions of the white line, as well as the inflection point (E_0) are detailed in Table 2.5.

From a strictly electrical-balance standpoint, three models can be defined to describe the charge compensation mechanisms, first described by Bès *et al.* in [163].

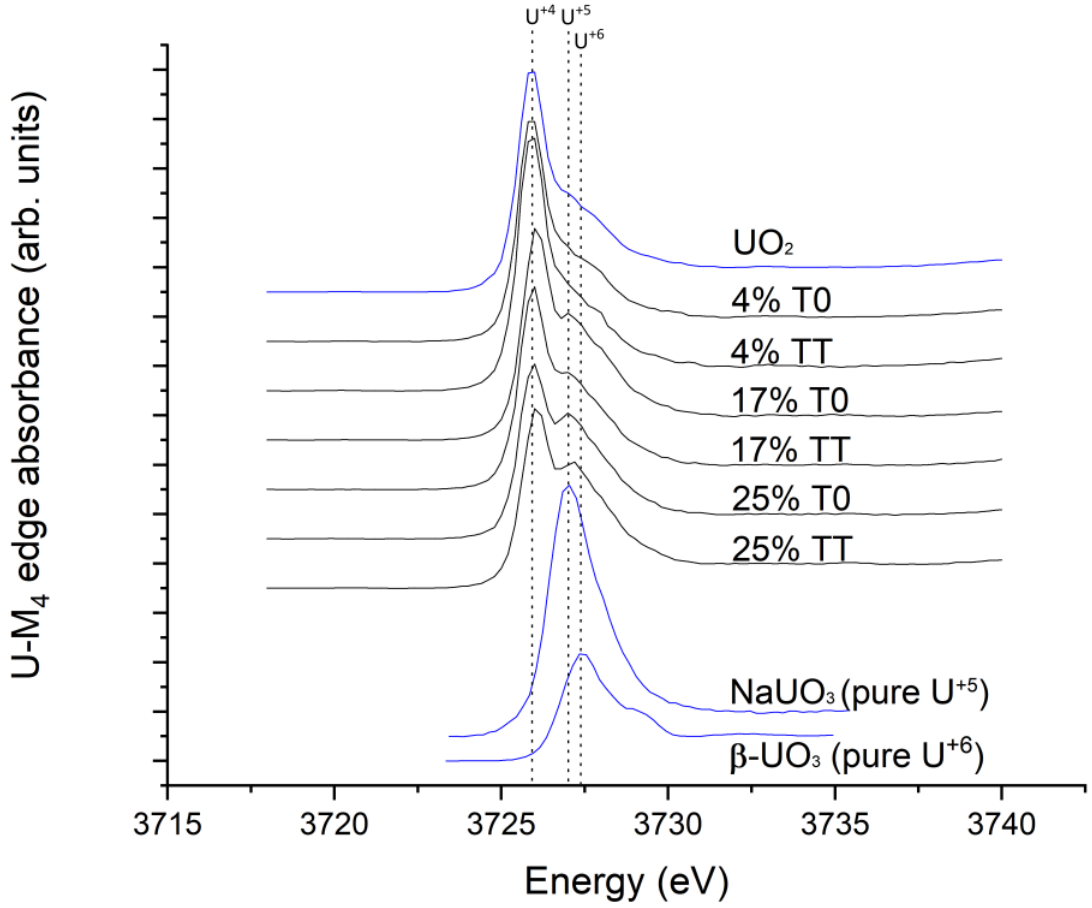

Figure 2.23: Experimental HERFD-XAS spectra of all measured samples and references. Spectra were vertically shifted to better visualization.

Using the Kröger-Vink notation, the models can be expressed as follows,

$$Model\,1 : (1-2y)U_U^{x} + yU_U^{\bullet} + yNd_U{}' \tag{2.2}$$

$$Model\,2 : (1-\frac{3}{2}y)U_U^{x} + \frac{1}{2}yU_U^{\bullet\bullet} + yNd_U{}' \tag{2.3}$$

$$Model\,3 : (1-y)U_U^{x} + \frac{1}{2}yV_O^{\bullet\bullet} + yNd_U{}' \tag{2.4}$$

These models explain the general behavior of the sample facing the introduction of a trivalent atom. Model 1 indicates the formation of one U^{+5} for each Nd^{+3} introduced. Similarly, Model 2 suggests the formation of one U^{+6} when two atoms of Nd^{+3} are introduced, whereas the Model 3 compensates the missing charge with 0.5 vacancy for each atom of Nd^{+3} introduced on the cationic sub lattice. This latter model is directly related to the global O/M ratio, since it does not affect the valence state of any species of the system. On the contrary, the Model 1 and Model 3 are used to explain the calculated chemical composition of all six samples, presented in

Sample	**E_0 (eV)**	**White Line (eV)**
UO_2	3725.3(2)	3725.8(2)
$NaUO_3$	3726.6(2)	3727.2(2)
β-UO_3	3727.1(2)	3727.6(2)
4% T0	3725.4(2)	3725.8(2)
4% TT	3725.4(2)	3725.9(2)
17% T0	3725.6(2)	3726.0(2)
17% TT	3725.6(2)	3725.9(2)
25% T0	3725.4(2)	3725.9(2)
25% TT	3725.6(2)	3726.1(2)

Table 2.5: Position of the E_0 and the white line for each sample at the U M_4-edge HERFD-XAS spectra.

Table 2.6. The U M_4-edge spectra was fitted by linear combination of the references. All six samples were adjusted to find the chemical composition of U^{+4}, U^{+5} or U^{+6}, and from these values it was also obtained the calculated O/M ratio. As expected, no U^{+6} was found in any sample. Figure 2.24a shows for illustrative purposes the results of the linear combination fitting of the sample with 25% Nd treated thermally.

Despite the small difference of U^{+4} between the as-produced (T0) and the thermally treated (TT), it is possible to confirm a decrease of U^{+5} after the thermal annealing. Figure 2.25 presents the comparison between the spectra of both samples at 25% Nd treated and non-treated thermally. The samples treated thermally present a lower intensity of the peak located at 3726 eV, which is proportional to the global concentration of U^{+5}, meaning that the formation of vacancies on the annealed samples treated are more important that on the samples non-treated thermally, which is in good agreement with the XRD analysis.

Sample	U^{+4}	U^{+5}	U^{+6}	O/M
4% T0	96(2)	4(2)	0(1)	2.00
4% TT	99(2)	1(2)	0(2)	1.98
17% T0	86(4)	14(4)	0(2)	1.97
17% TT	89(3)	11(3)	0(3)	1.96
25% T0	75(4)	25(4)	0(1)	1.96
25% TT	77(4)	23(4)	0(2)	1.96

Table 2.6: Calculated concentration of U^{+4}, U^{+5} and U^{+6} for each sample after the linear combination fitting of the HERFD-XAS data.

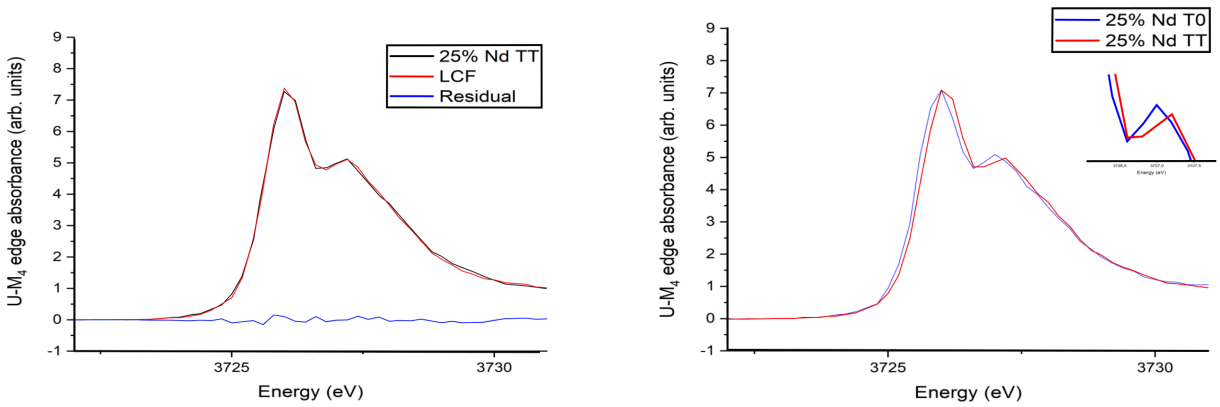

(a) (b)

Figure 2.24: (a) shows the results of the linear combination fitting (LCF) of the sample at 25% Nd treated thermally, (b) the comparison between the spectra of the samples at 25%Nd treated and non-treated thermally .

To be able to visualize more clearly the dominant charge compensation mechanisms, Bès et al. [163] schematized the composition of U^{+5} and U^{+6} and compared them with the theoretical Models 1, 2 or 3. Figure 2.25 presents the percentage of uranium for each valence state in comparison to Model 1, the curve that expresses Model 2 was not introduced in the graphic as no U^{+6} is seen in our samples. Notice that the fraction of uranium in $U_{(1-y)}Nd_yO_2$ is related to the amount of Nd, which means that the total amount of U for 100% of the sample at 4% Nd is not the same as 100% of uranium for the sample at 25% Nd. Thus, from Model 1 it is possible to express $[U^{+4}]$ = (1-2y) / (1-y) and $[U^{+5}]$ = y / (1-y).

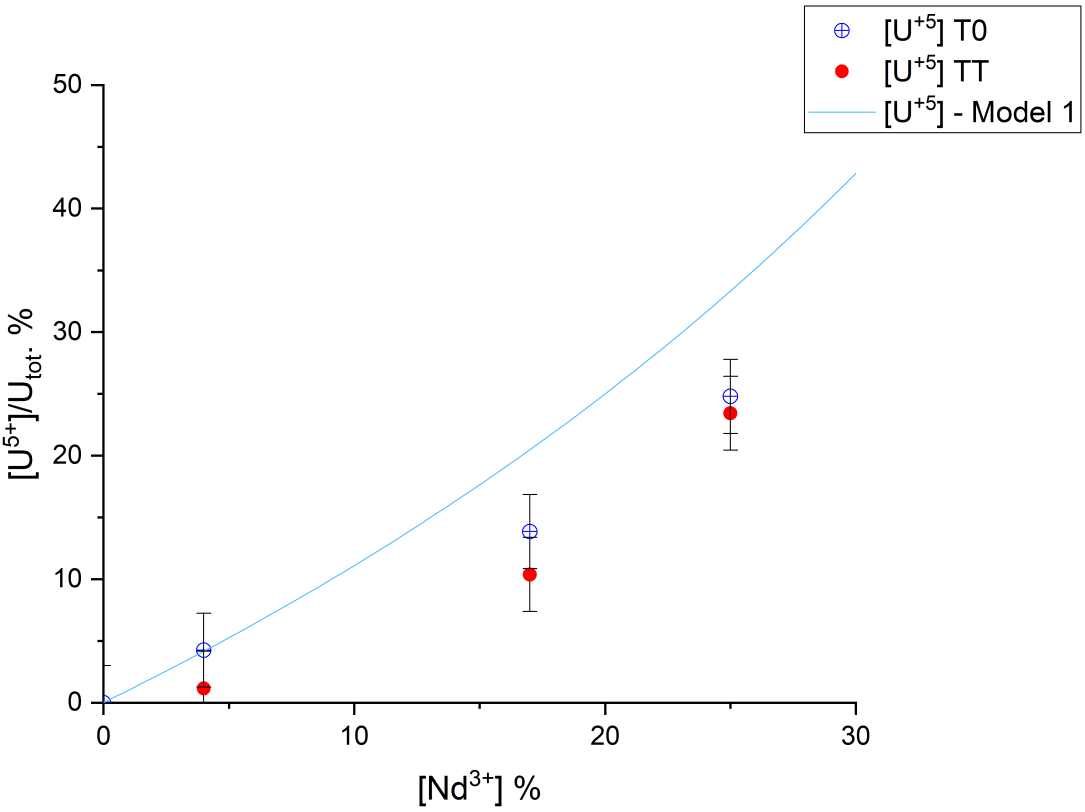

Figure 2.25: Concentration of U^{+5} for each sample before and after the thermal treatment and for Model 1 as a function of the Nd amount.

The evolution of all the samples shows a coherent behavior. In first place, the concentration of U^{+5} increases with the concentration of Nd^{+3}, and on the second place, no U^{+6} is seen for any sample. However, the charge compensation mechanisms for all six samples are not the same.

For the sample with 4% Nd, the experimental data fit perfectly the theoretical values calculated after Model 1 (Table 2.6). This value is in good agreement with the results reported in [163] where the experimental values match the theoretical curve for concentrations of Nd lower than 9%. For the samples with 17 % and 25% Nd the evolution is developed without reaching the full charge compensation through the Model 1. Instead, a mixed charge compensation between Model 1 and Model 3 are seen, where Model 1 is predominant as the experimental points are closer to the theoretical value. These results indicate that the substitution of U^{+4} by Nd^{+3} lead to oxidation of U^{+4} over the creation of vacancies, as a predominant charge compensation mechanisms. In any case was seen the formation of U^{+6}, which lead to conclude that of the three possible models, Model 3 is the less favorable energetically.

Local environment analysis

The EXAFS spectra have been measured at the Nd L_3-edge and U L_3-edge for the thermally treated (TT) samples, and the U L_3-edge for the non-thermally treated (T0) samples. An immediate inspection of the Fourier transform of the k space for the samples assessed at the U L_3-edge (Figures 2.26b and 2.26a) show a gradual decrease of the intensities when the concentration of Nd increases. This behaviour was evidenced in other UO_2-doped systems and it is explained by the destructive interference due to opposites phases and similar intensities for the U-U and U-Nd paths [40, 165, 166]. In contrast, no relevant differences can be observed between the intensities of the samples T0 and TT with equal concentration of Nd.

The k space with its respective Fourier transform and the structural fit for each sample are shown in Figure 2.27. The Nd L_3-edge for the sample at 4% Nd was also acquired but the concentration of Nd was so little that the measure was too noisy and a clean fit was not possible despite the statistics and good quality of measure, which is why it was not included in this document.

The small evolution of the k space on each set of samples indicates little differences on the local distances but no major changes on the local surroundings of the U or Nd atoms as the FCC structure remains in all cases as such. Figures 2.27b, 2.27d and 2.27f represent the Fourier transform of the k space for each set of samples. The two larger peaks reveal qualitative information about the U-O, U-Nd and U-U distances. The first peak around 1.8 Å is mainly contributed by the single scattering path of the nearest oxygen atom and the second peak around 3.8 Å results as the complex interaction between the single and multiple scattering paths of the first and second shells (M-O and M-M shells).

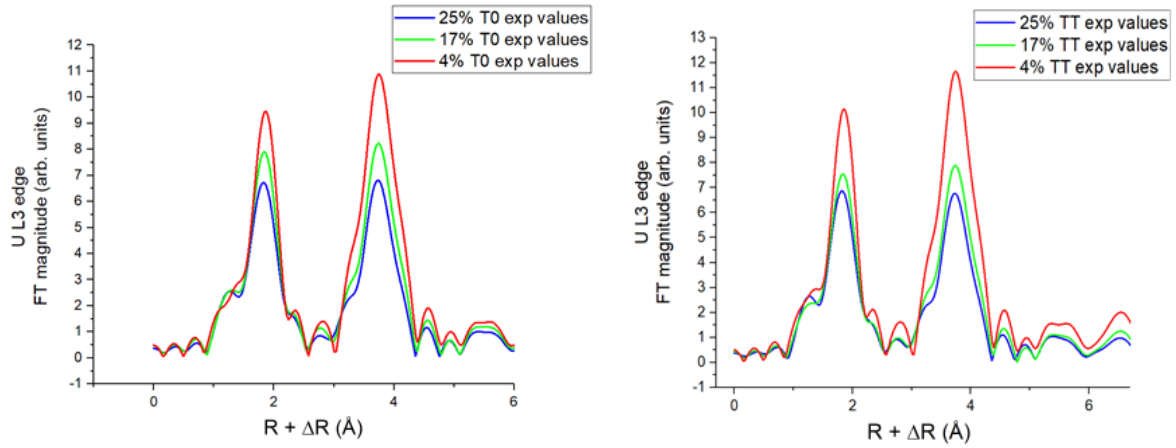

(a) (b)

Figure 2.26: Figure (a) and figure (b) schematize the Fourier transform of the as-produced samples (T0) and the samples treated thermally (TT).

It is possible to see that in all cases an overall good agreement between the experimental data and the structural fit was achieved allowing to extract general trends concerning the atomic distances and local disordering, the results of the refinements for all samples are shown in Table 2.7. In first place, all samples display a coherent decreasing of the atomic distances with increasing concentration of Nd regardless if it is the 1^{st}, 2^{nd} or 3^{rd} shell, that is $R_{04} > R_{17} > R_{25}$. As for the samples treated thermally, the distances remain systematically greater than those of the samples non-treated thermally, that is $R_{T0} < R_{TT}$, which is consistent with what is observed through XRD.

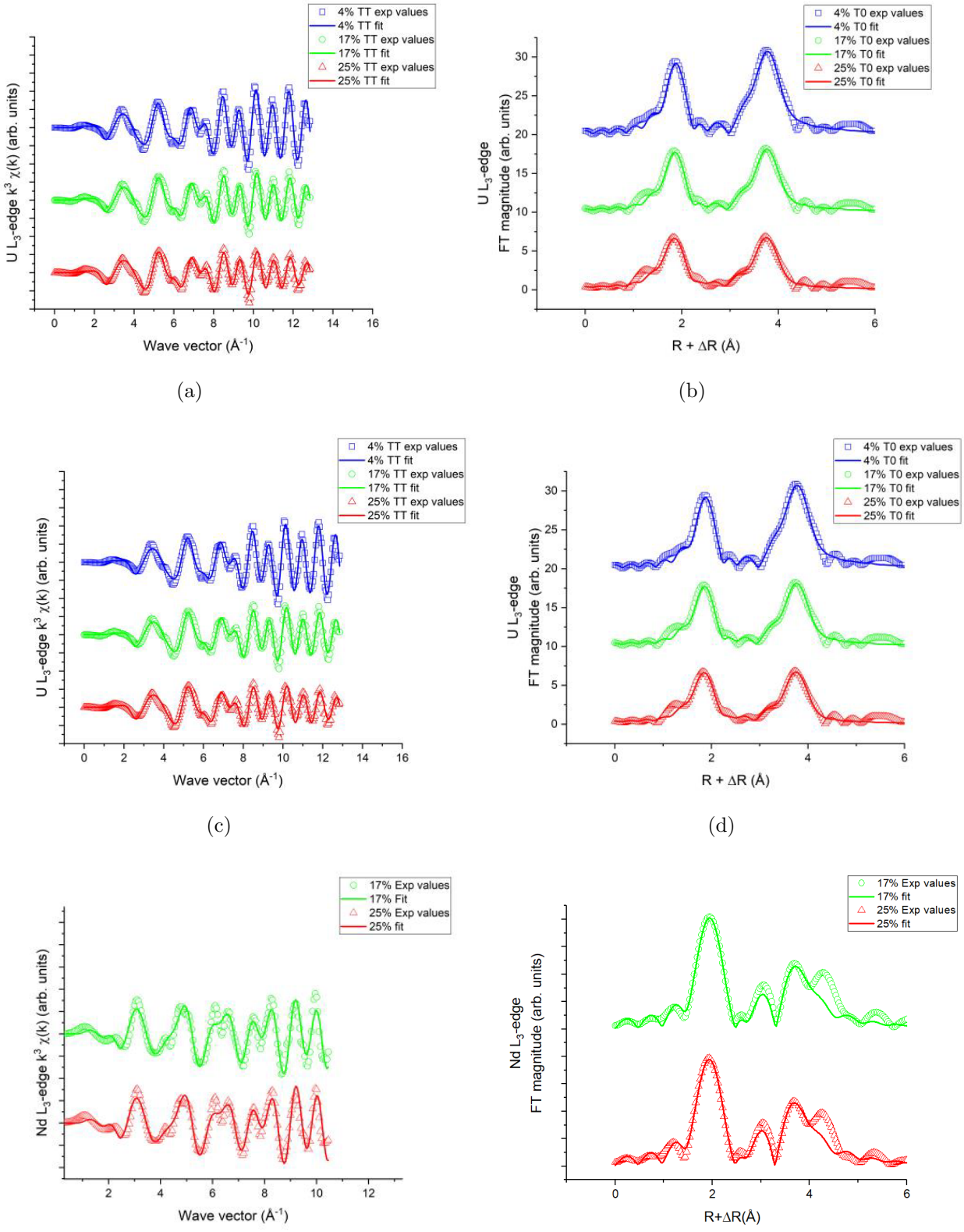

Figure 2.27: k space and Fourier transform of all samples.

Sample	Shell	R(Å)	σ^2 (10^{-3})	R-factor
	U-O_1	2.351(3)	5.8(4)	
4% T0	U-U	3.875(2)	2.9(2)	0.0128
	U-O_2	4.491(11)	10.0(1.5)	
	U-O_1	2.337(4)	7.4(6)	
17% T0	U-U	3.869(3)	3.6(3)	0.0139
	U-O_2	4.484(16)	10.5(2.2)	
	U-O_1	2.332(3)	9.0(4)	
25% T0	U-U	3.870(2)	4.2(2)	0.01315
	U-O_2	4.480(12)	12.5(1.7)	
	U-O_1	2.353(4)	5.5(5)	
4% TT	U-U	3.876(2)	2.5(2)	0.0182
	U-O_2	4.488(17)	11.0(2)	
	U-O_1	2.339(4)	7.79(5)	
17% TT	U-U	3.872(2)	3.72(2)	0.0124
	U-O_2	4.480(16)	11.48(1.9)	
	U-O_1	2.334(3)	8.7(5)	
25% TT	U-U	3.875(2)	4.0(2)	0.0143
	U-O_2	4.481(13)	12.7(1.8)	

Table 2.7: Results of the U L_3-edge EXAFS refinements of all samples.

Sample	Shell	R(Å)	σ^2 (10^{-3})	R-factor
	Nd-O_1	2.441(4)	6.5(6)	
17% TT	Nd-U	3.866(4)	4.1(5)	0.0170
	Nd-O_2	4.436(11)	11.7(2.2)	
	Nd-O_1	2.440(4)	6.9(6)	
25% TT	Nd-U	3.864(4)	3.2(5)	0.0150
	Nd-O_2	4.430(11)	12.7(1.7)	

Table 2.8: Results of the Nd L_3-edge EXAFS refinements of samples with 17 and 25 %Nd.

Another remark can be made concerning the Nd-O distances calculated from the Nd L_3-edge EXAFS spectra. In contrast with the U-O distances calculated from the U L_3-edge EXAFS analysis, the Nd-O distances are much larger and equal in value for the two analyzed samples (Table 2.8). This means that the local distances of the first shell will vary depending if it is U or Nd, which is consistent with the observation of the variation of the k space mentioned earlier in the document (see Figure 2.28). This observation is in good agreement with Barabash *et al.* [50], who stated that the atoms of Nd inserted randomly on the cationic sub lattice are able to push the surrounding atoms of oxygen out of their regular position, creating a lattice distortion along with the distortion created by the size mismatch between the Nd^{+3}, U^{+4} and U^{+5} cations. This behavior can also be justified by looking at the Debye-Waller factor (σ^2). It is possible to see that structural disorder on the surroundings

of the uranium atoms increases with the concentration of Nd, in contrast with what happen on the surroundings of the Nd atoms, since they are randomly introduced and fairly distanced to each other. The Debye-Waller factor calculated on the case of the Nd L_3-edge EXAFS spectra remains the same for every shell, independently the concentration of Nd.

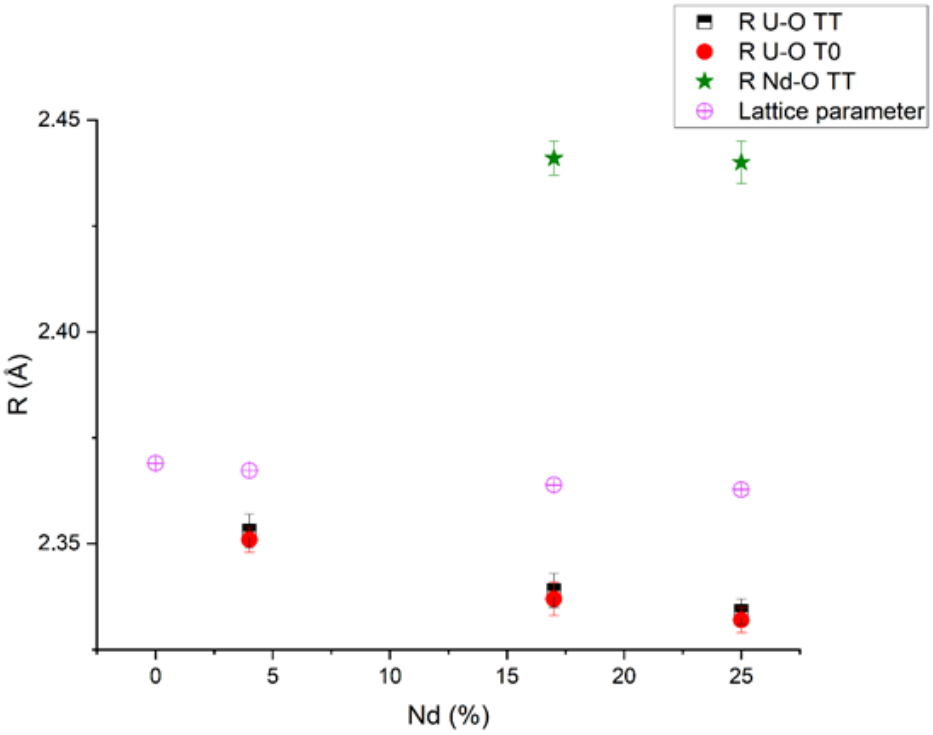

Figure 2.28: Distances of the first shell for all samples in comparison with the lattice parameter as a function of the concentration of Nd.

Summary: comparison with other ternary systems

Popa et al. studied the U-Bi-O system also by HERFD-XAS at the U M_4-edge [167]. The samples used in this study were doped with a concentration of Bi from 15% until 79%. They showed that despite the ability of Bi to change from trivalent to pentavalent it remained trivalent for all cases, which makes the reported values suitable for direct analysis. Their results show a complete absence of U^{+6} up to a concentration of Bi lower than 60%, which is in perfect agreement with our results.

Prieur et al. [40] compared both measures of U L_3-edge and U M_4-edge for the system U-La-O. They reported the valence state on stoichiometric samples with relatively low concentrations of La. Regardless the concentration of La, they found consistently some small fraction of U^{+6} on the U M_4-edge spectra. On homogeneous samples, this kind of behavior is highly unlikely if the number of trivalent dopants

remains inferior to 30%. To explain these findings, they stated the superficial oxidation of the samples, which justifies why the same amount of U^{+6} is seen on all samples.

Bès *et al.* [165] focused their study on the system U-Gd-O with samples at low concentration of Gd. As expected, they saw only the formation of U^{+5} predominantly as the main factor for charge compensation. Finally, Bès *et al.* calculated the concentration of U^{+5} and U^{+6} on the system U-Nd-O [163]. These measurements showed the presence of U^{+6} on the samples starting from 29% of Nd. However, the author named repeatedly that the samples were not completely homogeneous due to the nature of the manufacturing process. Therefore, these results have only a qualitative meaning.

All the reported values named previously are presented in Table 2.9. Throughout all systems, there are tendencies that repeat and that can be pointed out. First, it is evident that the concentration of U^{+5} increases with the number of trivalent dopants. Further, for very low concentrations of dopants ($y<0.1$), the only model for charge compensation that seems to predominate is the Model 1, as the experimental values are comparable to the theoretical values within the margin of error. For concentrations of Nd higher than 10%, the experimental values are slightly lower than the theoretical values, indicating a compromise between Model 1 and Model 3, justified by the presence of vacancies.

For concentration of dopants lower than 30%, no formation of U^{+6} is detected. Generally, its formation becomes predominant for concentration of trivalent dopants higher than 50%. This statement can be explained by the atomic disposition on the cationic sub-lattice. If a trivalent atom is surrounding only by uranium atoms and another trivalent atom is fairly distanced, the natural tendency is to increase the valence of uranium from U^{+4} to U^{+5}, which is the case on very low doped samples. With increasing concentration of dopants, the probability for two trivalent atoms to meet is higher. Hence, the charge compensation through oxidation of uranium will compete with the formation of one vacancy. When the concentration of dopants is over 30% there is a higher possibility for group dopants to meet locally, which leads to the formation of U^{+6} as it is the only alternative for charge compensation. Finally, if the sample has over 50% of trivalent dopants, all the uranium has been oxidized from U^{+4} to U^{+5} and the system will have no option but to oxidize the U^{+5} to U^{+6}.

Similar conclusions respecting the atomic distances were also achieved by assessing the U-Gd-O system by probing the Gd L_3-edge by EXAFS in [165], where also the fluorite structure is maintained for samples doped with low amounts of Gd. Indeed, the atomic distances U-O decrease with the amount of dopant and the Gd-O distances are constant for any Gd content. These results establish similarities between the chemical behavior the Gd-doped samples and the behavior of the Nd-doped samples.

Dopant	Concentration	Abs. Edge	Theoretical M. 1 (%) U^{+4}	Theoretical M. 1 (%) U^{+5}	Experimental (%) U^{+4}	Experimental (%) U^{+5}	Experimental (%) U^{+6}	Author
Bi	$(U_{0.85}, Bi_{0.15})O_2$	M_4	82.35	17.6	82.5(5)	18(5)	0	Popa et al.
	$(U_{0.68}, Bi_{0.32})O_2$	M_4	52.9	47.0	44(5)	56(5)	0	
	$(U_{0.50}, Bi_{0.50})O_2$	M_4	0	100	0	100(5)	0	
	$(U_{0.40}, Bi_{0.60})O_{1.95}$	M_4	0	0	0	74(5)	26(5)	
	$(U_{0.33}, Bi_{0.67})O_2$	M_4	0	0	0	0	100(5)	
	$(U_{0.21}, Bi_{0.79})O_{1.81}$	M_4	0	0	0	10(5)	90(5)	
La	$(U_{0.94}, La_{0.06})O_{2\pm x}$	L_3	93.6	6.3	94(5)	6(5)	0	Prieur et al.
	$(U_{0.89}, La_{0.11})O_{2\pm x}$	L_3	87.6	12.3	89(5)	11(5)	0	
	$(U_{0.78}, La_{0.22})O_{2\pm x}$	L_3	71.79	28.2	72(5)	28(5)	0	
	$(U_{0.94}, La_{0.06})O_{2\pm x}$	M_4	93.6	6.3	90(2)	8(2)	3(2)	
	$(U_{0.89}, La_{0.11})O_{2\pm x}$	M_4	87.6	12.3	86(2)	11(2)	3(2)	
	$(U_{0.78}, La_{0.22})O_{2\pm x}$	M_4	71.79	28.2	76(2)	21(2)	3(2)	
Gd	$(U_{0.96}, Gd_{0.04})O_2$	M_4	95.8	4.1	100(5)	0(5)	0	Bès et al.
	$(U_{0.93}, Gd_{0.07})O_2$	M_4	92.4	7.5	92(4)	8(4)	0	
	$(U_{0.89}, Gd_{0.11})O_2$	M_4	87.6	12.3	88(3)	12(3)	0	
	$(U_{0.86}, Gd_{0.14})O_2$	M_4	83.7	16.2	83(2)	17(2)	0	
Nd	$(U_{0.91}, Nd_{0.09})O_2$	M_4	90.1	9.8	93(3)	7(3)	0	Bès et al.
	$(U_{0.85}, Nd_{0.15})O_2$	M_4	82.35	17.6	83(3)	17(3)	0	
	$(U_{0.71}, Nd_{0.29})O_2$	M_4	59.1	40.8	73(3)	22(3)	5(3)	
	$(U_{0.38}, Nd_{0.62})O_2$	M_4	0	5.8	2(3)	0	98(3)	
Nd	$(U_{0.96}, Nd_{0.04})O_2$	M_4	95.8	4.1	96(3)	4(3)	0	This Work
	$(U_{0.96}, Nd_{0.04})O_{1.98}$	M_4	95.8	4.1	99(3)	1(3)	0	
	$(U_{0.83}, Nd_{0.17})O_{1.97}$	M_4	79.5	20.4	86(3)	14(3)	0	
	$(U_{0.83}, Nd_{0.17})O_{1.96}$	M_4	79.5	20.4	89(3)	11(3)	0	
	$(U_{0.75}, Nd_{0.25})O_{1.96}$	M_4	66.6	33.3	75(3)	25(3)	0	
	$(U_{0.75}, Nd_{0.25})O_{1.96}$	M_4	66.6	33.3	72(3)	28(3)	0	

Table 2.9: Theoretical and experimental concentration of U^{+4}, U^{+5} and U^{+6} when O/M=2, for the different ternary systems.

2.3 Conclusions

This chapter presents a detailed analysis of two different types of samples: samples produced by dry route and other ones produced by wet route. The characterizations by XRD, SEM and TEM performed on the samples produced by dry route indicate that they are capable of displaying different multiphasic systems where the random fluctuation of the Nd concentration is capable of leading to the formation of metastable phases. On the other hand, the set of samples produced by wet route were proved to be homogeneous and more appropriate for a solubility analysis. Indeed, after performing a thermal treatment under controlled conditions, the samples were assessed through XRD where only a monophasic system was found. However, since the reached hypo-stoichiometry is too small to allow the formation of a possible secondary phase.

Further characterizations made on these samples by XAS are in good agreement with the XRD observations. The effect of the thermal treatment on the formation of hypo-stoichiometric samples was assessed by HERFD-XAS where it is only seen on the global concentration of pentavalent U. No influence on the Nd solubility is detected other than the formation of U^{+5} and vacancies, since in all cases the system remained single phase. The evolution of the crystal lattice was also probed by EXAFS, the results on the interatomic distances of the second shell U-U obtained after the fitting are still in good agreement with the evolution of the lattice parameter evaluated through XRD. However, the distances U-O and Nd-O corresponding to the first shell were different, which proves that the local environment is affected differently depending on the evaluated atom.

Despite the fact that the results showed only a monophasic system, it is not possible to make a conclusive proposition of the phase diagram, since these samples were evaluated after a thermal treatment that might not be sufficient to reduce the samples up to a point where the miscibility gap is reached. For this purpose, a second thermal treatment is proposed at higher temperature to further reduce more sensibly the samples as well as *in-situ* studies by HT-XRD to minimize the oxidation effect when they are in contact with air.

Chapter 3

Behavior of Nd and Ce-doped samples under hypo-stoichiometric conditions

"Science never solves a problem without creating ten more."

-George Bernard Shaw

At the end of the previous chapter we were left with two questions:

1. The inability to observe the miscibility gap in homogeneously doped samples produced by wet route after performing a reducing annealing. Can this be a consequence of insufficient reduction or fast oxidation?

2. Is the duration of the annealing at the ordering temperature (higher limit of the miscibility gap) long enough to achieve thermodynamic equilibrium?

This chapter tries to answer these two questions. The first problem is addressed by performing an *in-situ* HT-XRD analysis followed by an even more reducing conditions and immediate characterization by XRD at room temperature. The second question is addressed by comparing this system to another ternary system U-Ce-O, where a miscibility gap was also predicted in a similar range of composition and temperature.

3.1 Study of the hypo-stoichiometric region of the U-Nd-O system

3.1.1 *In-situ* assessment of the evolution of the system U-Nd-O with temperature.

One possible reason for not seeing the miscibility gap on the U-Nd-O system was that it suffers from a fast oxidation. To assess this possibility we carried out an *in-situ* analysis of the sample doped with 25%Nd by using HT-XRD. The patterns

were measured within the 2θ range of 10-130° between the temperature 1373 K and room temperature, then to 1373 K, with a ramp of 0.5 K.s^{-1} and 100 K steps. The atmosphere employed to carry on the acquisitions was the same used for the thermal annealing (Ar+4%H_2).

Figure 3.1 shows the evolution of the peak (3 1 1) as a function of temperature. Beyond the expected thermal expansion, no sign of peak splitting was seen, indicating that the samples remain monophasic.

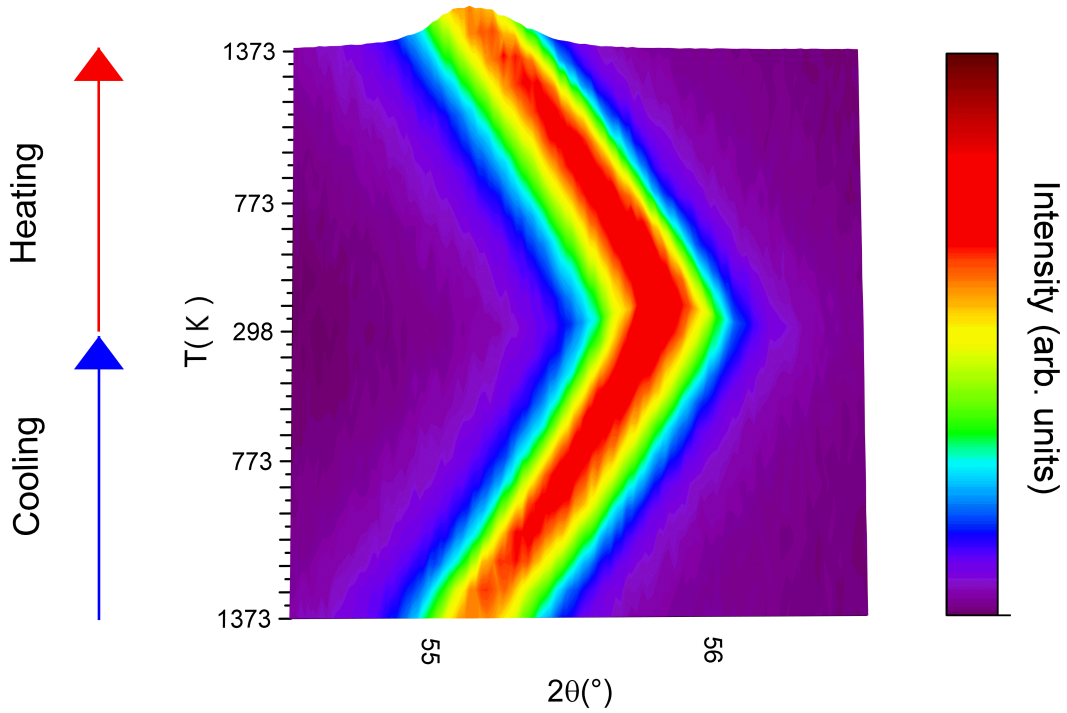

Figure 3.1: Evolution of the (3 1 1) peak in temperature for the sample doped with 25%.

A deeper analysis of these acquisitions, probing the lattice parameters leds us to realize that O/M ratio was actually changing with temperature, and that more reducing conditions were indeed achieved. The evolution of the lattice parameter as a function of the temperature was calculated and displayed in figure 3.2. In addition, it is presented for comparison the values reported by Grønvold corresponding to pure UO_2 and by Venkata *et al.* corresponding to different U-Nd-O solid solutions [27, 117]. The measurements made by Grønvold are in good agreement with those presented by Murray *et al.*, Martin, and Hutchings *et al.* for temperatures below 1200 K [86, 168, 169]. Therefore, the assessment will consider only the range of temperatures from 298 K until 1200 K, since there is an overall agreement between the authors concerning the thermal expansion of pure UO_2.

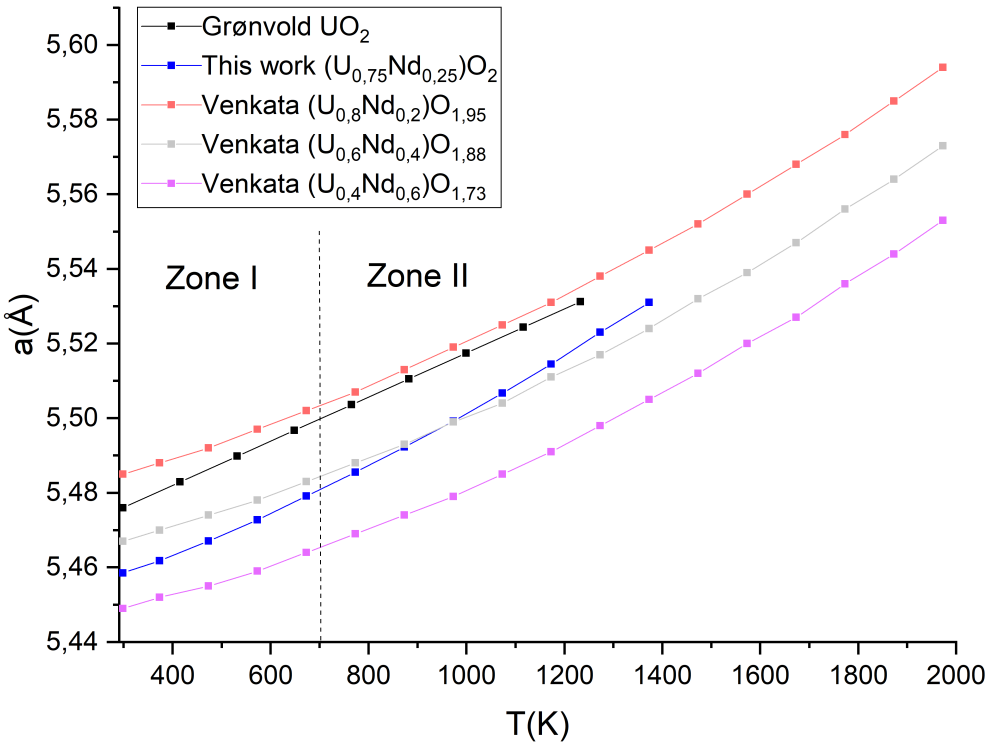

Figure 3.2: Evolution of the lattice parameter with temperature for the sample doped with 25%Nd in comparison with the values published by Grønvold and Venkata *et al.* [27, 117].

Considering that the measurements in a reducing atmosphere of the lattice parameter can change the O/M ratio within the assessed range of temperature, we differentiate two zones: Zone I below 700 K and Zone II above 700 K. Within Zone I, the evolution of the lattice parameter of the sample doped with 25%Nd can be considered parallel to the curve of UO_2, this is reasonable because of the O/M in this range does not change significantly, and therefore the thermal expansion of these two samples causes nearly the same evolution of the lattice parameter with temperature. On the other hand, above 700 K, the evolution of the sample doped with 25%Nd is faster than the one of the UO_2 and their evolution are no longer parallel. This behaviour is caused by the variation of the O/M ratio of the sample at 25%Nd. As it was showed in Equation 2.1, the lattice parameter can be a coupled function of the Nd and O concentrations. Therefore, the fact that the assessed lattice parameter increases faster than the one corresponding to stoichiometric UO_2 (where there is no variation of the O/M ratio), indicates that the sample is effectively reduced, as it was intended in the first place. A similar analysis can be made on the measurements made by Venkata *et al.*, in this case the difference is smaller but it is possible to see a variation in Zone I, where the lattice parameter increases slower than the one of

UO_2, and in Zone II, where it has faster change.

All these curves were fitted by polynomial expressions. Table 3.1 presents the curves that describe the evolution of the lattice parameter as a function of temperature. In the case of pure UO_2, the curve reported by Grønvold is linear, instead of being parabolic, like the rest of the authors, with a thermal expansion coefficient equal to $10.8{\cdot}10^{-6}K^{-1}$.

Author	Sample	Fit (Å)
Grønvold	UO_2	$5.4704[1+10.8{\cdot}10^{-6}(T-293)]$
	$U_{0.8}Nd_{0.2}O_{1.95}$	$5.485+3.9517{\cdot}10^{-5}(T-298)+1.5171{\cdot}10^{-8}(T-298)^2$
Venkata *et al.*	$U_{0.6}Nd_{0.4}O_{1.88}$	$5.467+3.5693{\cdot}10^{-5}(T-298)+1.6462{\cdot}10^{-8}(T-298)^2$
	$U_{0.4}Nd_{0.6}O_{1.73}$	$5.449+3.3292{\cdot}10^{-5}(T-298)+1.725{\cdot}10^{-8}(T-298)^2$
This work	$U_{0.75}Nd_{0.25}O_2$	$5.4569+4.7905{\cdot}10^{-5}(T-273)+1.7808{\cdot}10^{-8}(T-273)^2$

Table 3.1: Fitted polynomials of the evolution of the calculated lattice parameters as a function of temperature for each sample.

The analyses of the evolution of the lattice parameter as a function of the temperature proved that the *in-situ* HT-XRD acquisitions were capable of reducing the stoichiometry of the sample within the domain of the miscibility gap. As a reminder, Figure 1.22 indicates that a sample doped with 27%Nd, under the same atmosphere is capable of entering the miscibility gap at 745 K [91, 118]. On the other hand, regardless of the degree of hypo-stoichiometry achieved during the HT-XRD analyses, the system remains single-phase throughout the whole range of temperature. The only reason capable of explaining why biphasic samples are not observed is they were never reduced enough.

Consequently, one final annealing *ex-situ* is proposed, consisting of reducing the sample at high temperature, and cooling down the system (0.8 $K.s^{-1}$) when it is still hypo-stoichiometric to room temperature, since these conditions would bring the sample in the miscibility gap.

3.1.2 Implementation of a high-temperature thermal treatment on the U-Nd-O system

In the previous section it was seen an analysis by *in-situ* HT-XRD which allowed to follow the thermal evolution of the sample. However, the temperature at which the

reduction was effective was above 700 K with the gas mixture available in the furnace setup.

Figure 3.3 displays the oxygen chemical potential in temperature of the sample doped with 25% calculated using the software Thermo-Calc. Thus, we performed a thermal treatment with a temperature of 1973 K with a heating ramp of 1 $K.s^{-1}$ and a dwell for 2 hours, capable of reaching the thermodynamic equilibrium with a chemical potential more reducing than -200 $kJ.mol^{-1}$.

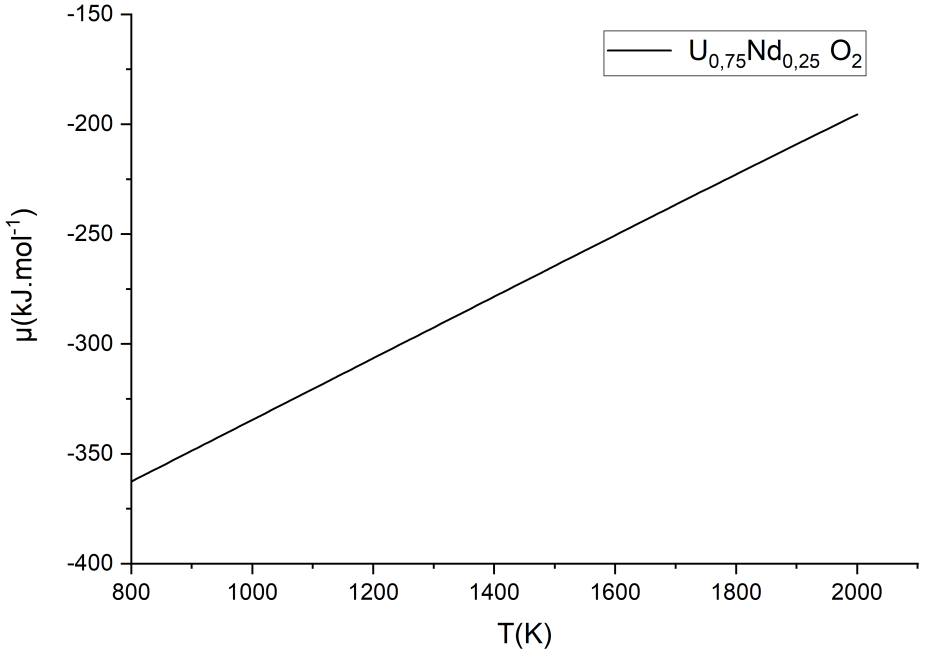

Figure 3.3: Calculation of the chemical potential as a function of the temperature for the sample doped with 25%Nd.

The cooled sample (cooling ramp of 0.65 $K.s^{-1}$) was immediately assessed by XRD acquiring patterns every hour during the first 10 hours, then every two hours during the following 8 hours. It was important that these measurements were examined as soon as possible once the samples were removed from the furnace, since there is a serious risk of quick oxidation once they are in contact with air.

Figure 3.4 presents the results obtained after the XRD acquisitions of the sample treated at high temperature. An immediate inspection of the patterns confirm that the sample remains monophasic. In addition, the pattern obtained 1 h after the thermal treatment reveals broader and weaker peaks, that narrow and gain intensity progressively on the following patterns. Further, it is also visible that their position shifted towards higher angles, which means that the sample starts to oxidize since it is contact with air.

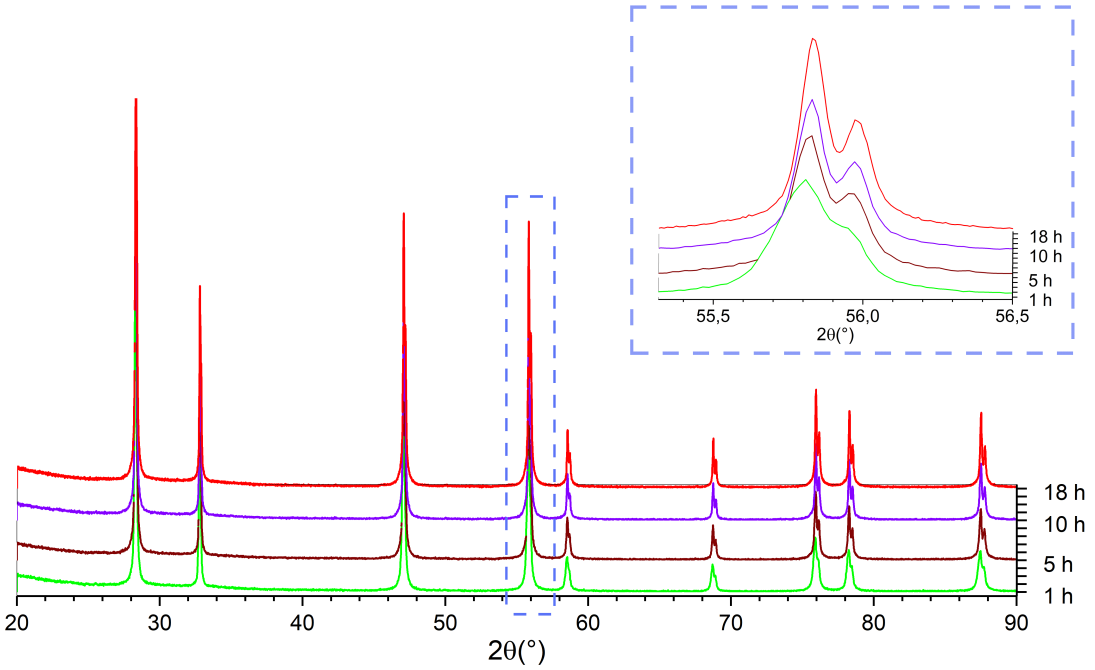

Figure 3.4: Selected XRD patterns of the sample doped with 25% at different times after the thermal treatment at high temperature.

An analysis of these patterns through Rietveld refinement allowed the calculation of the lattice parameter, the microstrain and the crystallite size, presented in figures 3.5a and 3.5b, respectively [156]. The evolution of the lattice parameter is in agreement with what it is stated after the patterns in figure 3.4: there is a progressive decreasing of the lattice parameter confirming that the displacement of the peaks is due to increasing oxidation. Figure 3.5 displays both the strain and crystallite size obtained as refined parameters after the Rietveld refinement. The microstrain seems to decrease also with time, same as the lattice parameter. This observation leads to think that the insertion of the oxygen atoms into the grain, i.e. the oxidation of the sample, reduces local strains that are related to the degree of oxidation. Once the oxygen atoms are introduced on the anionic sublattice, the amount of strain in the sample diminishes, the peak narrows, and it also shifts towards higher angles.

After the thermal treatment, the results were verified by studying the samples through SEM and EDS, see figures 3.6a and 3.6b. On the X-ray mapping obtained after EDS analysis, it can be seen that the distribution of Nd (presented in green) is uniform across the sample, confirming the results obtained through XRD.

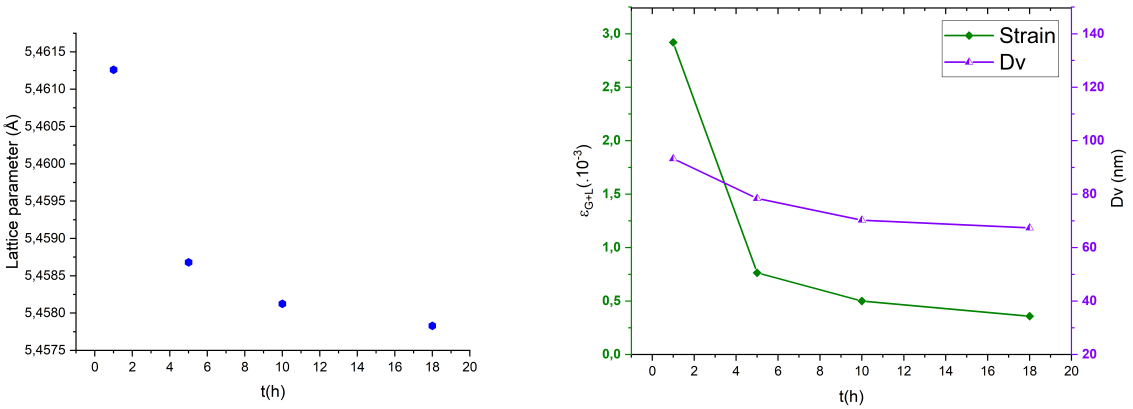

(a) (b)

Figure 3.5: (a) decreasing of the lattice parameter after the oxidation of the sample, (b) evolution of the strain and weighted crystalline volume of the samples obtained after the Rietveld refinement.

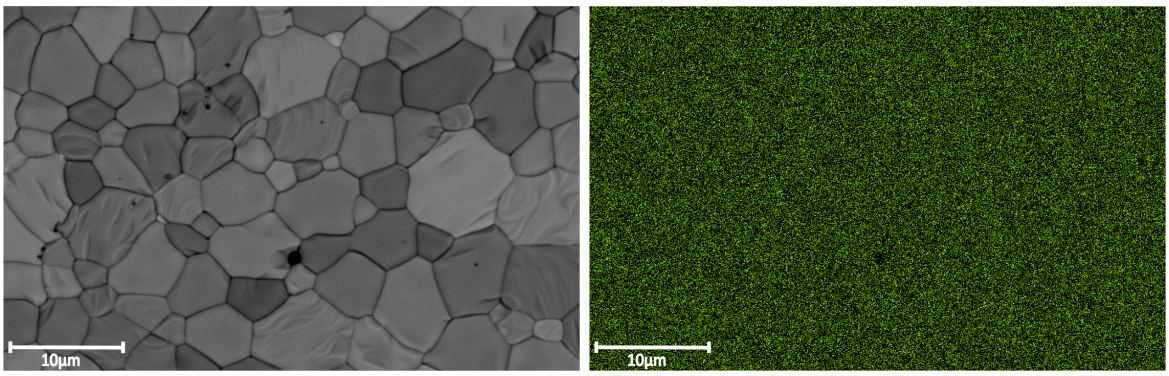

(a) (b)

Figure 3.6: SEM imaging and Nd X-ray mapping of the sample after the high temperature thermal annealing. The sample remains single-phase and presents a uniform distribution of Nd.

3.1.3 Reoxidation of hypo-stoichiometric samples

Description of the oxidation profile along the grain

The XRD analysis of the sample doped with 25%Nd directly after the thermal annealing shows a very fast oxidation rate of the outer surfaces. Using the equation proposed by Lee *et al.* in (Equation 1.25 [151]), we can estimate the average O/M ratio of the sample as a function of the average lattice parameter. The lattice parameter corresponding to the XRD pattern acquired one hour after the thermal annealing indicated the O/M ratio of the sample was 1.98 and the one corresponding to the last measurement was 1.994, indicating that the sample re-oxidized almost completely

over 18 h.

The position of the peak as a function of time relates lower angles to lower O/M ratios. The oxidation profile of the sample can be modeled using Fick's second law of diffusion,

$$\frac{dC}{dt} = D \cdot \bigtriangledown^2 C \tag{3.1}$$

This equation relates the concentration variation rate with the laplacian of the oxygen concentration through the diffusion coefficient, D. The resolution of this differential equation describes the oxygen concentration as a function of time and position in the sample.

To start this analysis it is necessary first to establish some basic hypothesis that will allow us to solve the equation 3.1.

- The grains are considered to be spherical.

- The oxygen diffusion coefficient used is the self-diffusion coefficient, which is not a function of the oxygen concentration.

- The surface exchange constant, K, is neglected.

- C_0 and C_f are the initial and boundary oxygen concentration and are both constants.

In spherical coordinates, the resolution of the equation is, if we define the substitution, u=C·r:

$$\frac{du}{dt} = D \cdot \frac{d^2u}{dr^2} \tag{3.2}$$

With a concentration at the surface as a constant, equal to C_f, we define the initial condition and boundary conditions,

Boundary conditions:

- u=0 for r=0, t>0

- u=R·C_f for r=R t>0

Initial condition:

- u=r ·f(r) for 0<r<R, t=0

Defining f(r) as the initial concentration profile and supposing f(r)=C_0 constant, then C(r,t) is,

$$C(r,t) = C_f + 2(C_0 - C_f)\sum_{n=1}^{\infty}(-1)^{n+1}.e^{[\frac{-Dn^2\pi^2t}{R^2}]}.\frac{sin(n\pi r/R)}{n\pi r/R} \tag{3.3}$$

The mathematical description to obtain equation 3.3 can be found in Appendix C. We are now in condition to determine an oxygen diffusion coefficient, D, that explains the oxidation of the sample if we suppose the lattice parameter obtained by the refinement as the average value over the depth probed by the X-rays.

Estimation of the oxygen diffusion coefficient

In our particular case, we make the assumption that grains are spherical with radius of 2.5 μm, the oxygen concentration (expressed as O/M) of the sample at t=0, C_0 (inside the furnace), is uniform and equal to 1.98 and the concentration at the surface of the grain for all t$\geq$0, C_f is equal to 2.

XRD patterns contain information on the sample over the range of the attenuation length. This value (L) was estimated [170] as a function of 2θ using the following conditions:

- Nd concentration equal to 25 %;
- Density equal to 10.06 $g.cm^{-3}$;
- Energy of the beam 8048 eV;

Figure 3.7 displays the attenuation length of X-rays in Bragg-Brentano geometry for copper radiation in the sample (Beer-Lambert law). If we carry on the analysis on the reflection (113) at 2θ=55.7°, the corresponding attenuation length is 1.63 μm. 95% of the signal of this reflection comes from a beam whose path is 3L in the sample. Since both entered and diffracted beams are both absorbed, the maximum depth reduced by the entered beam is 3/2L, that is 2.5μm.

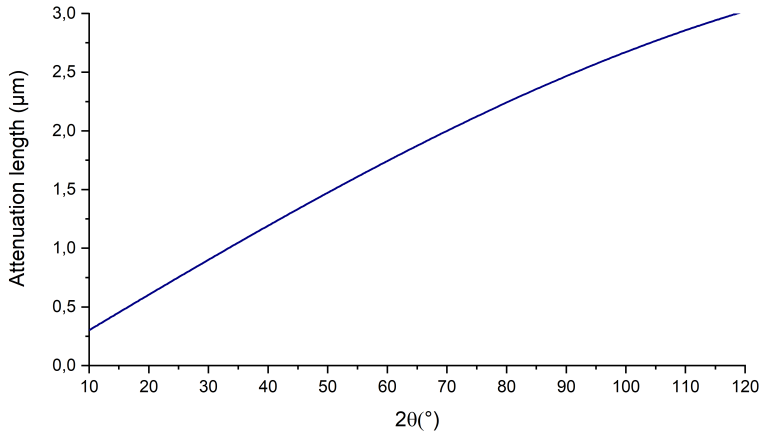

Figure 3.7: X-ray attenuation length on a sample doped with 25% Nd.

The estimated value of the diffusion coefficient is $\mathbf{D = 1.94.10^{-13}} cm^2.s^{-1}$. Figure 3.8 presents the evolution of the oxygen concentration along the radius r for the XRD patterns obtained after 1 h, 5 h, 10 h and 18 h. The initial value at t=0 h represents the initial condition when the sample is still in the furnace.

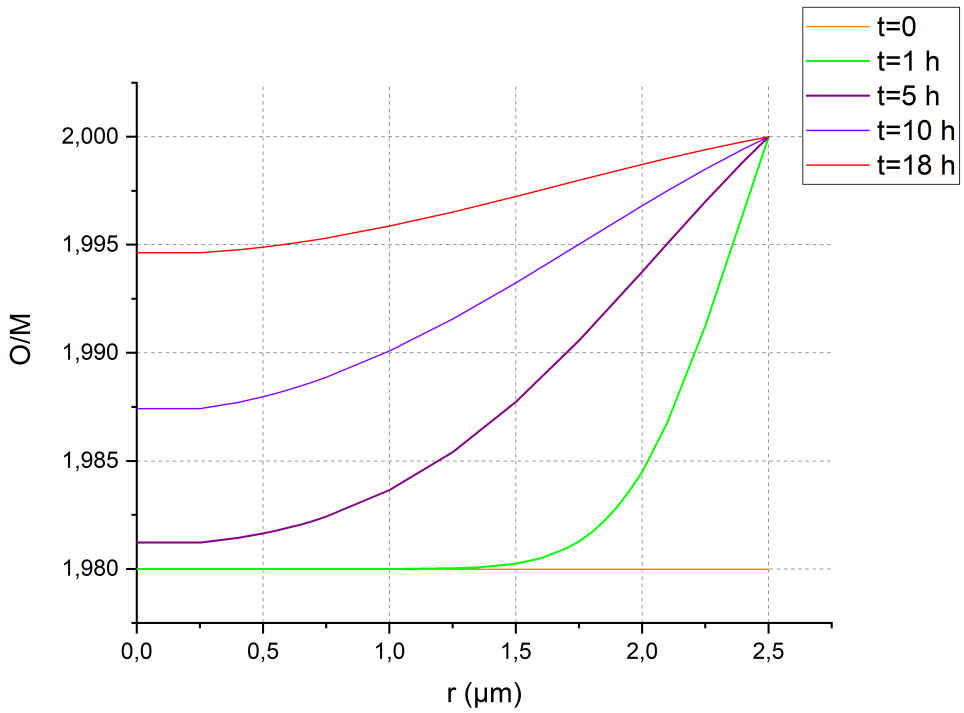

Figure 3.8: Oxygen concentration profile on a spherical grain with a radius R = 2.5 μm.

The validation of the value of D was made by comparing the lattice parameter

obtained after the Rietveld refinement with the lattice parameter calculated from the weighted average of the diffused profiles with D =$1.94.10^{-13} cm^2.s^{-1}$. The expression that relates the lattice parameter and oxygen concentration is the one from Lee *et al.* [151],

$$a = \frac{4}{\sqrt{3}}\{(1-2y+2x)r_{U^{+4}}+(y-2x)r_{U^{+5}}+yr_{Nd^{+3}}+\frac{(2-x)}{2}r_{O^{-2}}+\frac{x}{2}r_{OV}\}(1-\frac{y}{200})$$

where y is the Nd atomic fraction, x is the oxygen atomic fraction and r is the radius of the ion.

Table 3.2 summarizes the values of the lattice parameter for the O profiles calculated at different times and the values obtained from the refinement. On one hand, the value a_{Ref} indicates the value obtained directly after the refinement (Figure 3.5a), and on the other hand, the value a_{mean} calculated after the mean value of the O/M ratio of each profile, showed in Figure 3.8, by using the Equation 2.1.

Time (h)	a_{Ref} (Å)	a_{mean} (Å)
1	5.4612	5.4603
5	5.4586	5.4593
10	5.4581	5.4582
18	5.4578	5.4573

Table 3.2: Comparison between the lattice parameter obtained from the Figure 3.4 and those of the weighted average of the curves of Figure 3.8.

Comparison with oxygen diffusion coefficients found in literature

Oxygen self-diffusion, D_{sd}, is a subject that was widely studied over the years. Its values are normally evaluated by tracing the stable oxygen isotopes ^{18}O or ^{17}O by different techniques, such as mass spectrometry. Different mechanisms are defined to explain how oxygen can diffuse. In different stoichiometry ranges oxygen self-diffusion experiments differentiate three compositional ranges: hypo-stoichiometry, stoichiometry and hyper-stoichiometry.

In general terms, the oxygen self-diffusion coefficient in an isotropic crystal can be defined as [171],

$$D_{sd-j} = A_j S^2 \nu . e^{(-\Delta H_D/RT)} \tag{3.4}$$

where D_{sd-j} is the self-diffusion coefficient of the specie j, A is a geometrical factor determined by the crystal structure and mechanism, S is the jump distance, ν is the

lattice vibrational frequency and ΔH_D is overall activation energy. In practice, the preexponential terms can be grouped and referred as D_0 and the activation energy as Q. Table 3.3 lists these two coefficients for pure UO_2 for different temperature ranges obtained by different authors.

Temperature range (°C)	$D_0(cm^2.s^{-1})$	Q (KJ/mol)	Author
550-780	1200	273	Auskern and Belle [172]
600-1500	1.15	237	Belle [173]
780-1250	0.26	248	Marin and Contamin [174]

Table 3.3: Oxygen self-diffusion parameters for stoichiometric UO_2.

When it comes to a variation of the stoichiometry, oxygen self-diffusion can vary sensitively. This variation can appear in both hypo or hyper-stoichiometric systems. Ando and Oishi reported in figure 3.9 a comparison of the values of the D_{sd} estimated by different authors [171]. Particularly for hypo-stoichiometric samples, Kim and Olander stated that the activation energy is not a function of the non-stoichiometry, with a constant value of 49 $kJ.mol^{-1}$. In addition, they concluded that the dominant defect was the oxygen vacancy, and defined a value of D_{sd} as a function of temperature and a dependence with the non-stoichiometry x as,

$$D_{sd} = 4.4.10^{-4}\frac{x}{2}(1-\frac{x}{2})e^{(-49(KJ/mol)/RT)} \quad [cm^2.s^{-1}] \tag{3.5}$$

For comparison purposes, the activation energy for PuO_{2-x} calculated by Bayoglu and Lorenzelli was close to the one of UO_2 46 $KJ.mol^{-1}$ [175]. Further, the activation energy for $CeO_{1.92}$ is also within the same order of magnitude, with a value of 50 $KJ.mol^{-1}$ [176].

In UO_2 oxygen ions diffuse by the vacancy and interstitial mechanisms simultaneously. From the fractional contribution of the energy of formation of Frenkel pairs, Kim and Olander deduced that above 1673 K this mechanism becomes dominant, whereas at lower temperatures the vacancy mechanism has a higher contribution to the global self-diffusion coefficient [177].

By definition, oxygen self-diffusion coefficient does not depend on the concentration gradient. Oxygen chemical diffusion relates D_{sd} and the chemical gradient according to the Darken's relationship [Ref Darken 1948], which can be described within the range of temperature of analysis as,

$$D^C = \frac{2 \pm x}{2x} D_{sd}\big(\pm \frac{dlnP_{O_2}}{dlnx_{O_2}}\big) \tag{3.6}$$

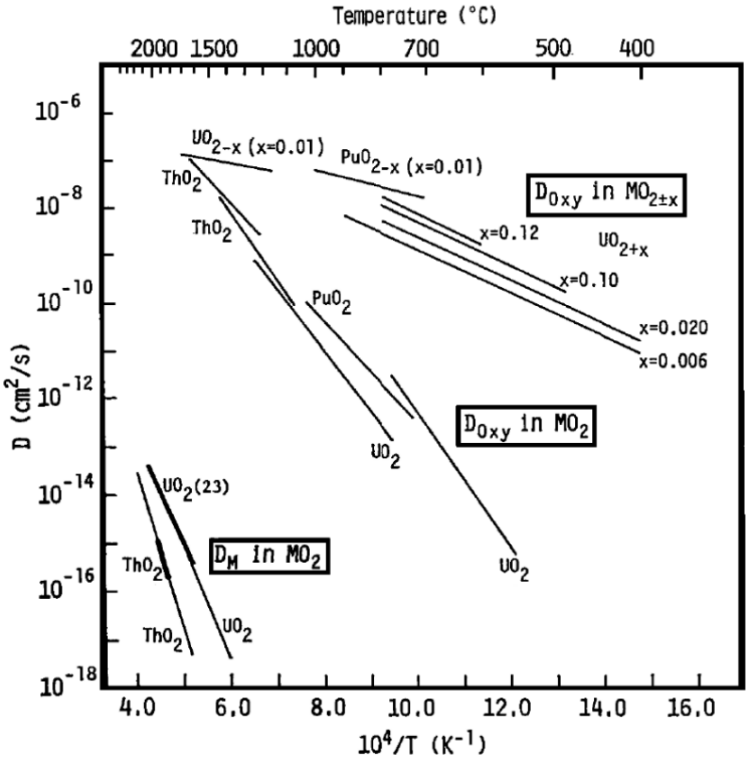

Figure 3.9: Comparison of the different D_{sd} for stoichiometric UO_2 [171].

where D^C is the oxygen chemical diffusion, P_{O_2} is oxygen partial pressure, and the positive and negative signs apply for the hypo and hyper-stoichiometric ranges, respectively.

Figure 3.10 compares the different D^C with D_{sd} for stoichiometric and hypo-stoichiometric UO_2 and PuO_2. For both oxides the behaviour is the same, the D^C is around 2 orders of magnitude higher. For the system PuO_2, Bayoglu and Lorenzelli calculated experimentally D^C using the TGA technique in contrast with the dilatometry method [175]. The measurements show an important difference within the range of $0 < x < 0.1$. Above this value, D^C depends only on the temperature.

In all cases, it was proved that both D^C and D_{sd} are sensitive to small variations of temperature and stoichiometry with values that range from $10^{-14} cm^2.s^{-1}$ for UO_2 at lower temperatures to $10^{-7} cm^2.s^{-1}$ for hypo-stoichiometric UO_{2-x} at 1473 K. In the case of hypo-stoichiometric samples, the value can only be significant above 1473 K, since below this value the formation of U^{+3} is not possible , and U can only exist as a metallic form (visible on the U-O phase diagram and the U-O chemical potential, see Figures 1.1 and 1.8). Concerning the calculated value presented here after the mathematical development of the second Fick's law, this process describes the evolution of the samples in terms of oxidation profile and oxidation kinetics. This analysis allows to explain the changes in the XRD patterns of the sample after it was removed from the furnace. They clearly highlight the importance on performing

in-situ analyses to detect the presence of a miscibility gap because the oxidation of the system overshadows the oxidation of the system would outcome phase separation.

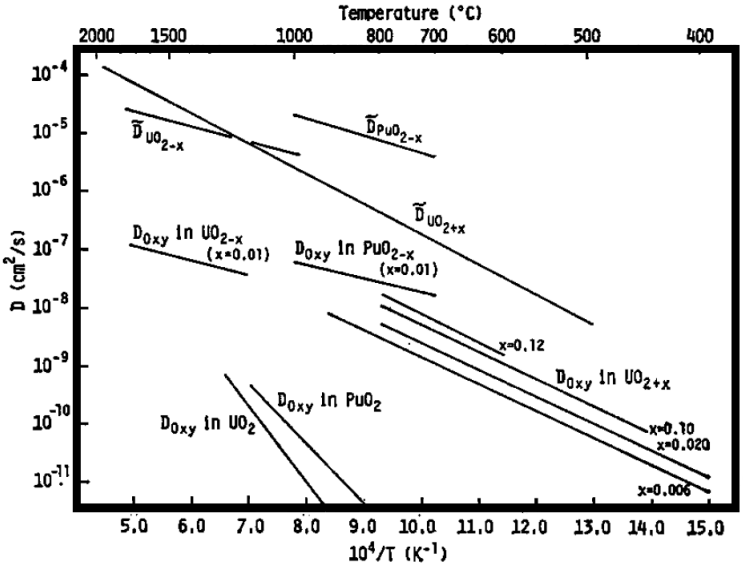

Figure 3.10: Comparison of the different D_{sd} for UO_2 [171].

3.1.4 Conclusions on the HT-XRD study and high temperature thermal annealing

The results presented on this chapter suggest that there is an initial hypo-stoichiometric phase that oxidizes progressively from the rim of the grain boundary. In this scenario, the center of the grain is more reduced than the outer boundary region of the grain.

A more detailed analysis of the progressive oxidation of the grains was presented to describe a mode to estimate the average oxygen diffusion coefficient by a comparison with the diffraction experiment.

3.2 Study of the U-Ce-O system

This section is dedicated to the study of the U-Ce-O system. One way of validating the conclusions about the system U-Nd-O is to compare its behaviour with another system displaying a miscibility gap. Different authors have detected the presence of a biphasic domain on the U-Ce-O system for a concentration of Ce greater than 30% and hypo-stoichiometric conditions [42, 134, 135, 140]. For that purpose, we propose to analyze three different samples with concentrations of 10, 20 and 45%. In the first place, the analysis will be presented on the as-produced samples by XRD and SEM. Then, *in-situ* HT-XRD acquisitions are also presented under reducing conditions, and

finally a thermal treatment at elevated temperatures, similar to the one performed on the previous sections for the sample doped with 25%Nd is analyzed.

3.2.1 Characterization of as-produced Ce-doped samples

The Ce-doped samples used on this work were produced by the same procedure as the Nd-doped samples, presented previously on Chapter 2. The three compositions obtained by wet route from (U,Ce)-based oxalates were sintered at 1773 K under Ar+4%H_2.

The initial characterizations by XRD of the samples doped with 10, 20%Ce were presented in Figure 3.11. As expected, a monophasic domain is seen in both patterns. The implementation of the Rietveld refinement allowed to extract the values of the lattice parameter [156], all samples indicated to have a linear contraction of the crystal lattice as a function of the Ce concentration, following the Vegard's law. Multiple authors assessed this evolution of the lattice parameter at room temperature for samples with an O/M ratio equal to 2 , see Figure 3.12 [42, 134, 166]. In the works published by Markin *et al.* and Lorenzelli [42, 134], the stoichiometry was achieved by using a 1/1 has mixture of CO/CO_2, which has an oxygen chemical potential μ_{O_2}=-88 kcal at 1123 K. This means the O/M ratio =2 was achieved at 1123 K and that once the system lowers its temperature the samples reoxidize. This observation implies that the measurements of the lattice parameter were made on systems out-of-thermodynamic equilibrium, and the reason why this O/M ratio is still 2 is because oxidation was not complete at the moment the XRD acquisitions were taken.

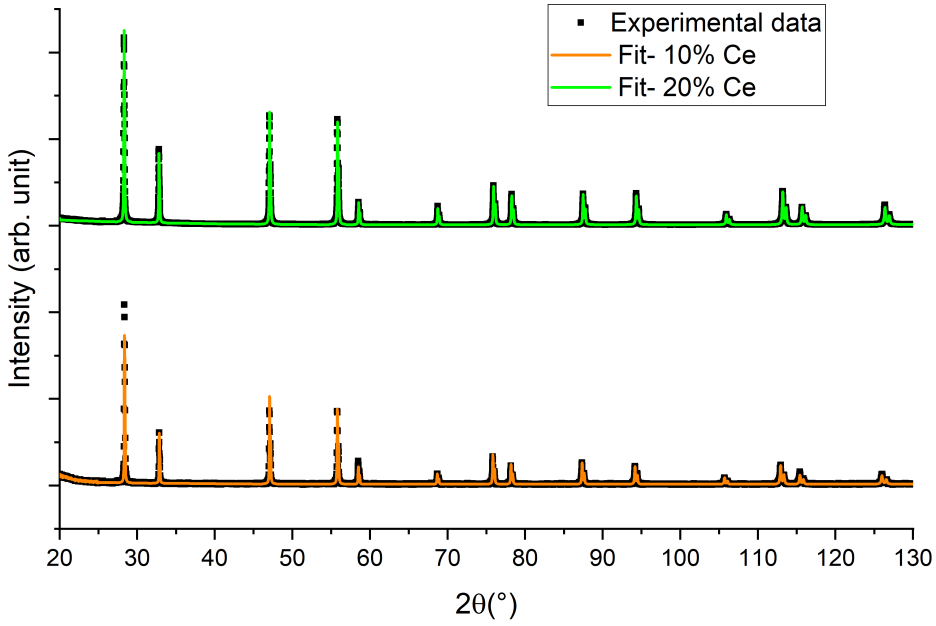

Figure 3.11: XRD patterns of the two assessed samples doped with Ce at 10, 20% along with the fit obtained after the Rietveld refinement.

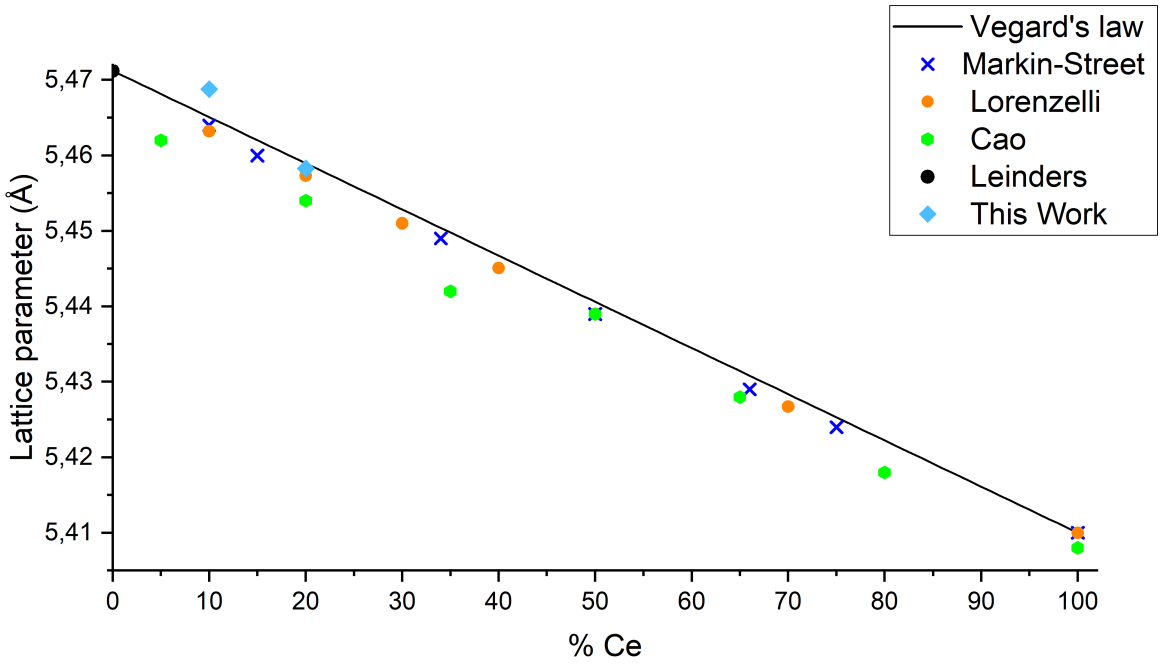

Figure 3.12: Evolution of the lattice parameter as a function of the Ce concentration. The system follows Vegard's law [42, 57, 134, 166].

Unlike the samples doped with 10 and 20%, the sample doped with 45%Ce presents a set of small low-intensity peaks at low angles that define a structure that is slightly different from the perfect fluorite, see Figure 3.13. This new structure has a trigonal structure (space group $R\bar{3}$, number 148) and lattice parameters a=13.883 Å and c=9.422 Å. The formation of this phase involves the selective creation and ordering of oxygen vacancies which are capable of relaxing the crystal lattice and allows local metallic displacement.

One way of explaining the formation of these oxygen vacancies could be related to a particular evolution of the oxygen chemical potential during the cooling ramp. At high temperatures, the cationic sublattice is mainly composed by U^{+4} and Ce^{+3}. However, when the system lowers its temperature, the oxygen chemical potential of the sample decreases and the sample oxidizes. In this scenario, the oxygen atoms localize selectively on the surroundings of the U atoms by partially oxidizing U^{+4} to U^{+5}.

The validation of the existence of this phase, as well as its extension on the phase diagram are still needed. Indeed, the structural arrangement of this new phase could be defined by further characterizations such as TEM or EXAFS analysis.

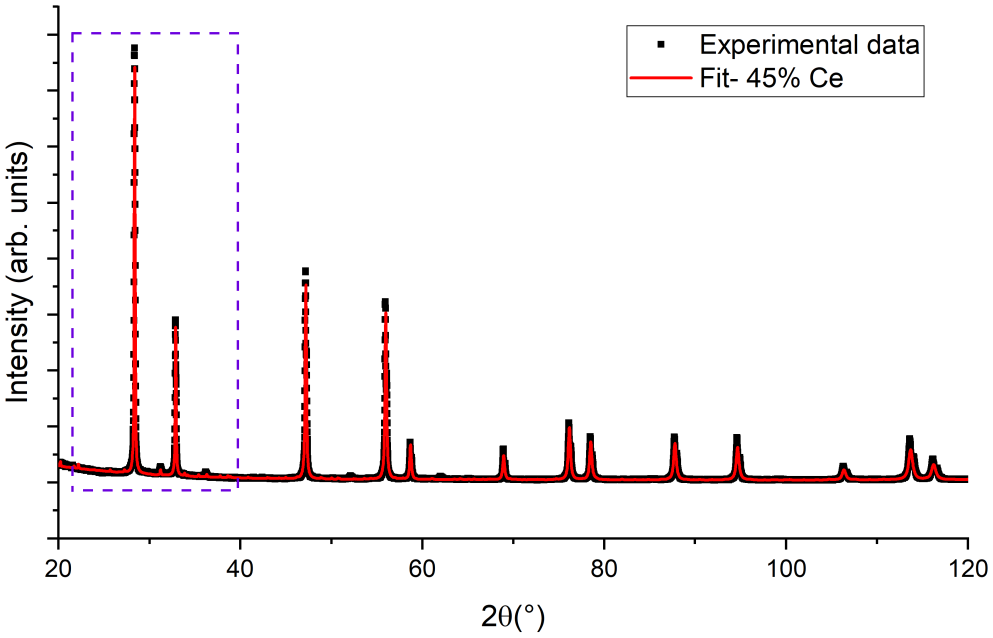

(a)

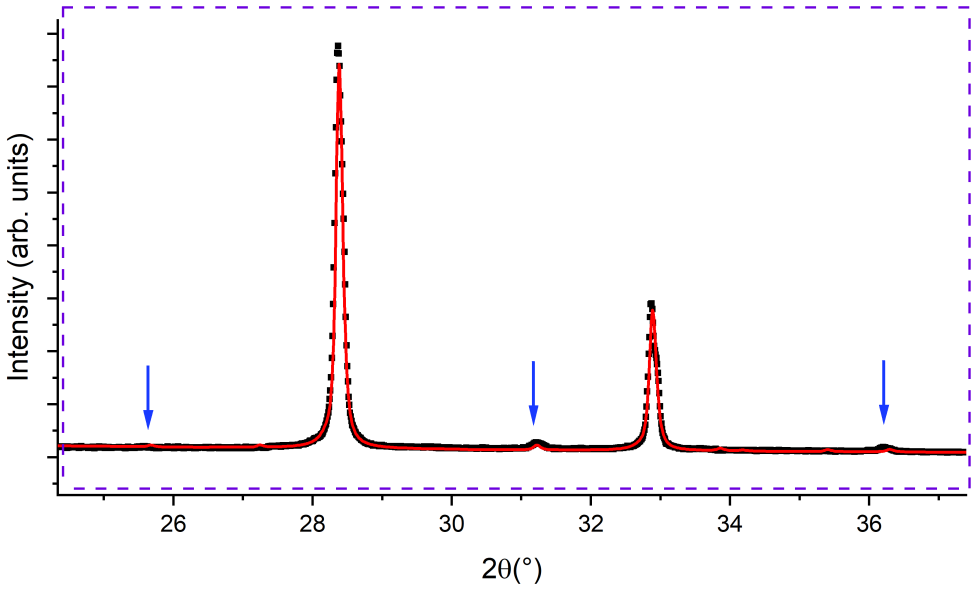

(b)

Figure 3.13: (a) XRD pattern of the sample doped with Ce at 45% along with the fit obtained after the Rietveld refinement, (b) detail to see the small peaks.

3.2.2 *In-situ* HT-XRD study of Ce-doped samples

This section is dedicated to analyze the samples doped at 20 and 45%Ce by *in-situ* HT-XRD. According to reported literature [42, 134], the first sample does not present a phase separation, as it is outside the biphasic domain for any degree of hypo-stoichiometry. On the contrary, the sample doped with 45% is reported to present a miscibility gap on the hypo-stoichiometric region on the phase diagram. This assessment allows to make a direct comparison with the sample doped with 25%Nd, which presented only a monophasic system.

Figure 3.14 displays the HT-XRD pattern of the peak (3 1 1) as a function of temperature for the sample doped with 20%Ce. The result is similar to the one already presented in Figure 3.1 for Nd, since both systems remain monophasic at all the temperatures of the experiment.

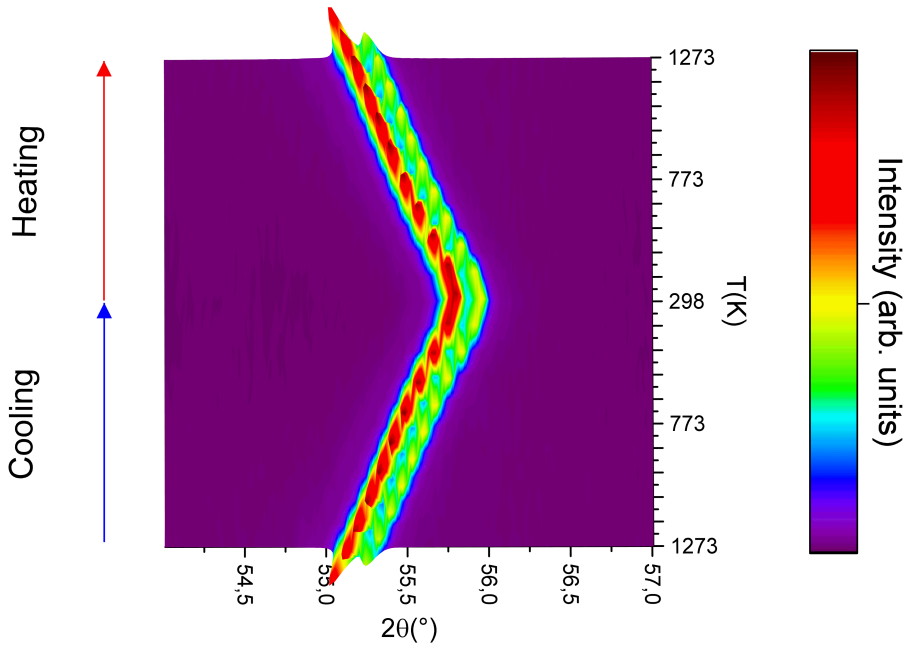

Figure 3.14: HT-XRD patterns of the peak (3 1 1) for the sample doped with 20%Ce. The system remains monophasic as there is no evidence of a second crystallographic phase.

A systematic analysis of the thermal evolution of the lattice parameter was obtained by the Lebail method. Similar to what was observed on the system U-Nd-O, the sample has also the tendency to reduce the O/M ratio when the temperature rises. This conclusion is made by comparing the evolution of the lattice parameter with the one of pure UO_2 and with the measurements reported by Venkata *et al.* for a sample made with the same amount of Ce and O/M=2 for the assessed range of temperature [27, 45], see Figure 3.15. Knowing that the lattice parameter of UO_2 cannot change

its stoichiometry and assuming that the thermal expansion is the same in both cases, the tendency of the lattice parameter of the sample doped with 20%Ce to outgrow the one of the UO_2 can only be given by the lattice expansion due to the decrease of the O/M ratio. The temperature at which the lattice parameter of the sample with 20% starts to increase is lower than the one for the sample doped with 25%Nd (400 K and 700 K, respectively). Norris and Kay, and Wadier described the evolution of the chemical potential of a sample doped with 20%Ce and 20%Nd at 1123 K in [52, 178], their measurements show that the oxygen chemical potential for the system U-Ce-O at these conditions is higher than the one of U-Nd-O. This observation justifies why a Ce-doped system is more easily reduced than the Nd-doped system.

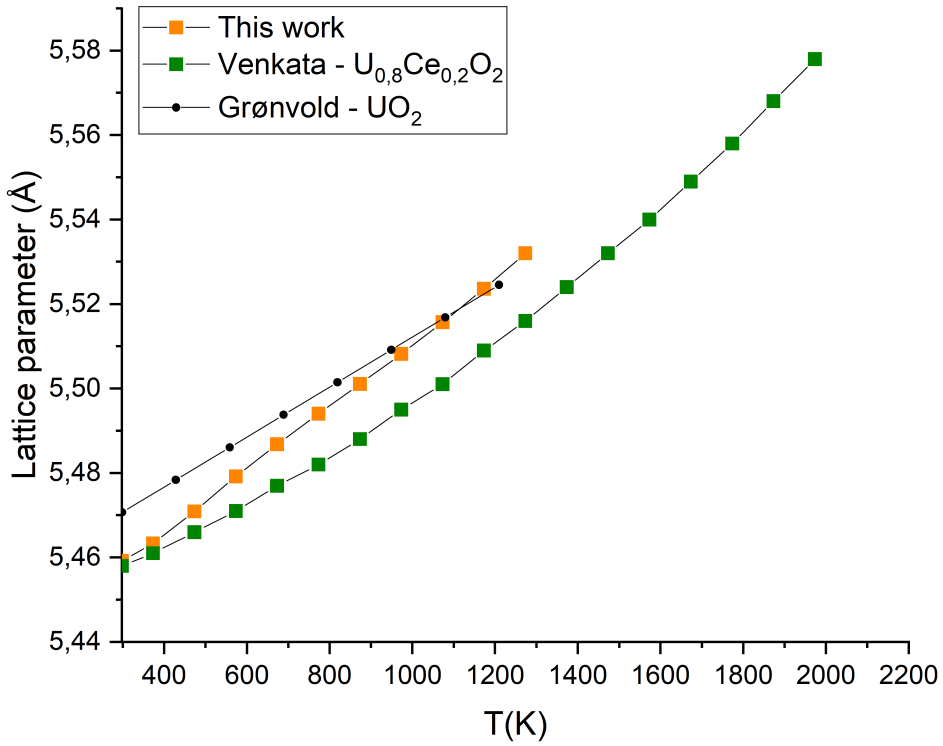

Figure 3.15: Evolution of the lattice parameter in temperature for the sample doped with 20%Ce in comparison with another sample doped with 20% and pure UO_2 [27, 45].

The next analysis through HT-XRD is made on a sample doped with 45%. The preliminary characterization of the sample doped with 45% displayed the formation of a superstructure which was defined using a trigonal structure. However, HT-XRD patterns acquired also for a sample doped with 45% present another set of peaks, different from those presented in Figure 3.13, see Figure 3.16. At the temperatures of 1373 K and room temperature, these peaks do not match the structure proposed for the sample assessed by XRD at room temperature. The results obtained by

characterizing the sample doped with 45%Ce by XRD at room temperature and HT-XRD are inexpected and might be related to an undefined phase on the U-Ce-O phase diagram. Further characterizations at different compositions must be made to explain the nature of these peaks. On the following assessment, we focus on studying the formation of the miscibility gap. For that purpose, we assume that structure is fluorite, following the reasoning of the authors that define the actual U-Ce-O phase diagram [42, 134]. A more thorough analysis would define a model for this new set of peaks and include the biphasic domain in it. Unfortunately in this work the time restrictions could not allow to perform such assessment.

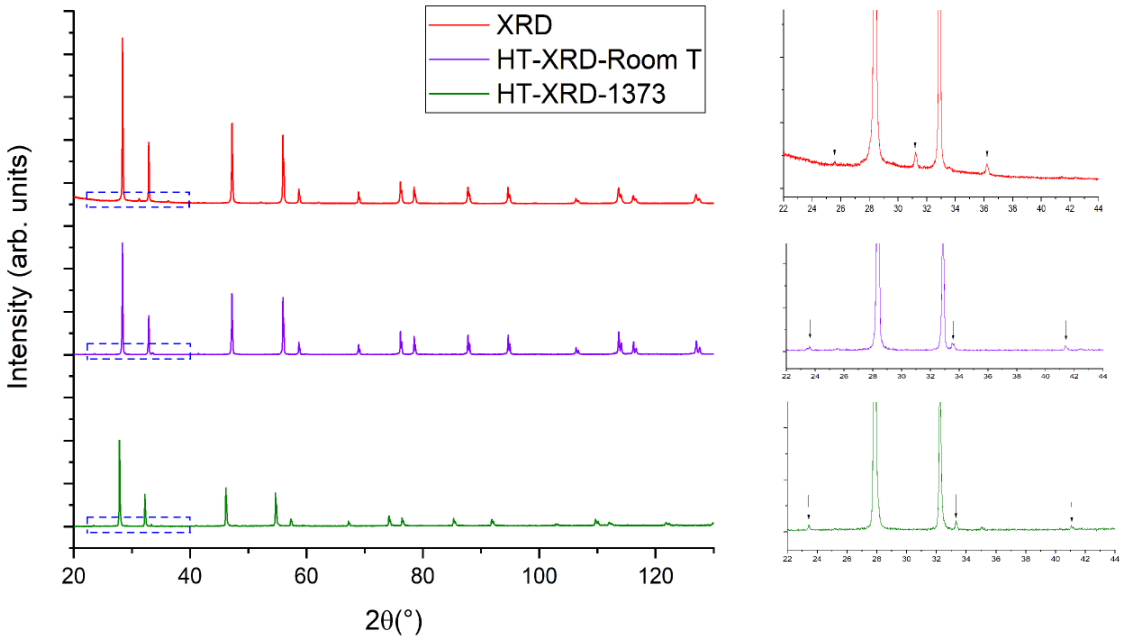

Figure 3.16: Comparison of different XRD patterns obtained on the sample doped with 45%Ce.

Figure 3.17 shows the evolution of the peak (2 0 2) from 1273 K cooling down to room temperature and then heating up again up to 1273 K. On this image it is possible to see an increasing of the intensity of a peak at lower angles of the peak (2 0 2) at the temperature of 473 K. This observation is seen because the system enters a biphasic domain. As previously seen in Chapter 2, once the O/M ratio is lower than 2, the system is capable of forming a second phase which would appear in the XRD pattern with a peak at lower angles than the peak with an O/M=2, since this phase is poorer in oxygen.

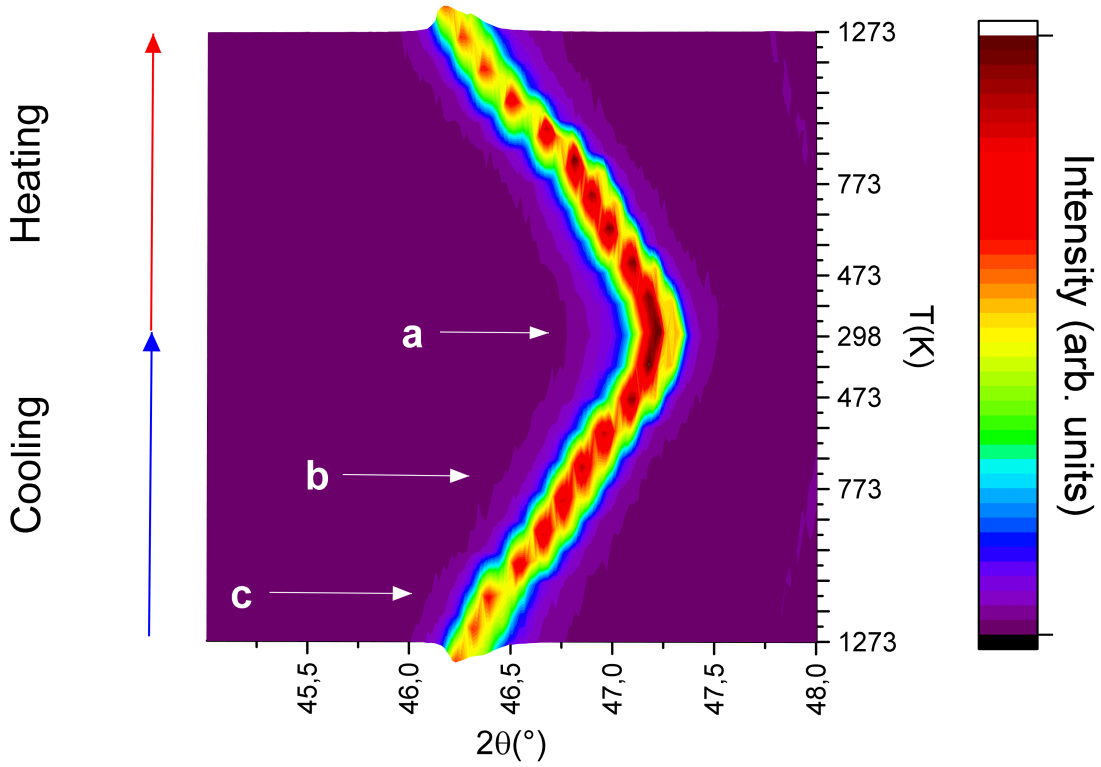

Figure 3.17: HT-XRD patterns of the peak (2 0 2) for the sample doped with 45%Ce. Below T=473 K the system presents a second phase.

To be able to see clearer the apparition of the second phase, three XRD patterns at different temperatures (298 K, 773 K and 1173 K) pointed with white arrows are presented in Figure 3.17 as a, b and c, respectively. Precisely, these three patterns are presented individually in Figures 3.18a, 3.18b and 3.18c. In Figure 3.18a the pattern obtained at room temperature displays the formation of a peak that represents the growth of the second phase at 2θ=47°. This peak is no longer seen at 773 K and 1273 K (Figures 3.18b and 3.18c), where the system becomes single-phase. It is also possible to observe that the sample presents broader peaks at the temperatures 773 K and 1173 K, this behavior can be explained because of the strains induced by the changes in the oxygen concentration, similar to what is observed in Figure 3.4.

The evolution of the lattice parameter during the cooling ramp was also made on the HT-XRD measurements, see Figure 3.19. As said previously, the lattice parameter of the second phase is higher since this phase contains less oxygen than the other one, which can be described as $U_{(1-y)}Ce_yO_{2-x}$. The development of the lattice parameter as a function of the temperature for similar concentrations was also reported in [42, 134, 140]. These values indicate that the lattice parameter for the secondary phase is higher than the value presented in this work. In principle, both Markin and Street and Lorenzelli indicated that phase separation was not immediate [42, 134]

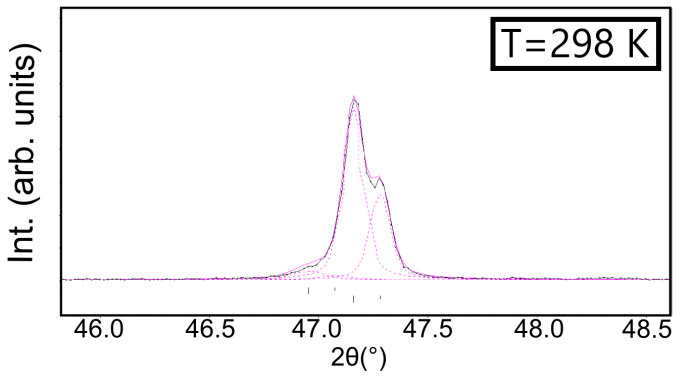

(a)

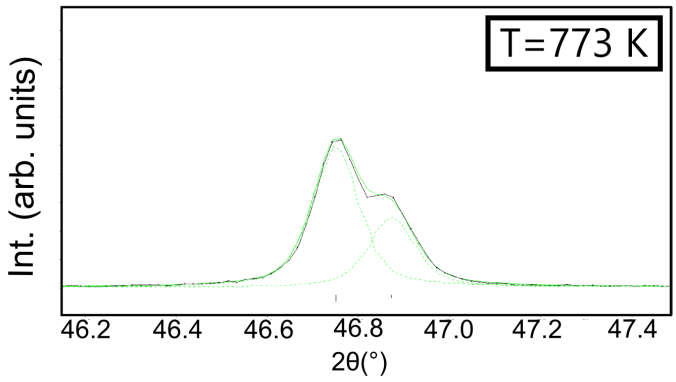

(b)

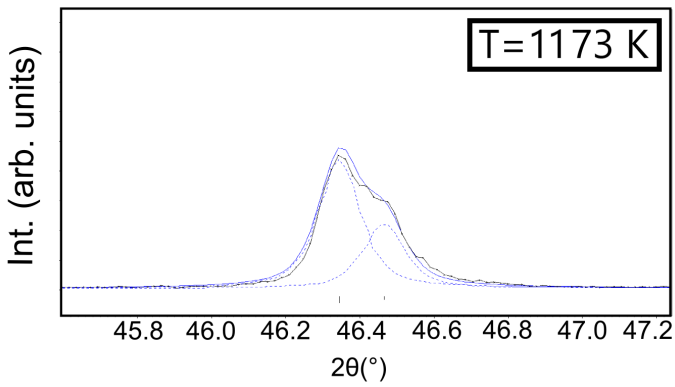

(c)

Figure 3.18: Extraction of the XRD pattern of the peak (2 0 2) along with the Rietveld refinement, showing a biphasic system at room temperature (a), and a monophasic system at 773 K (b) and at 1173 K (c).

and that it was necessary to either have a dwell at low temperature for days (333 K to 353 K) or proceed with a slow cooling. On the other hand, Simeone *et al.* did not report a dwell at low temperatures, but instead a quenching was done from 1173 K down to 573 K, and made XRD acquisitions every 50 K until room temperature.

These observations might indicate that in our experiment the formation of the second phase is not complete.

In addition, the phase fractions were also obtained after the Rietveld's refinement. Figure 3.19b shows that the fraction of the second phase is higher after entering the biphasic domain (22%) and lower at room temperature (10%), which is explained by the oxidation of the sample when the temperature decreases.

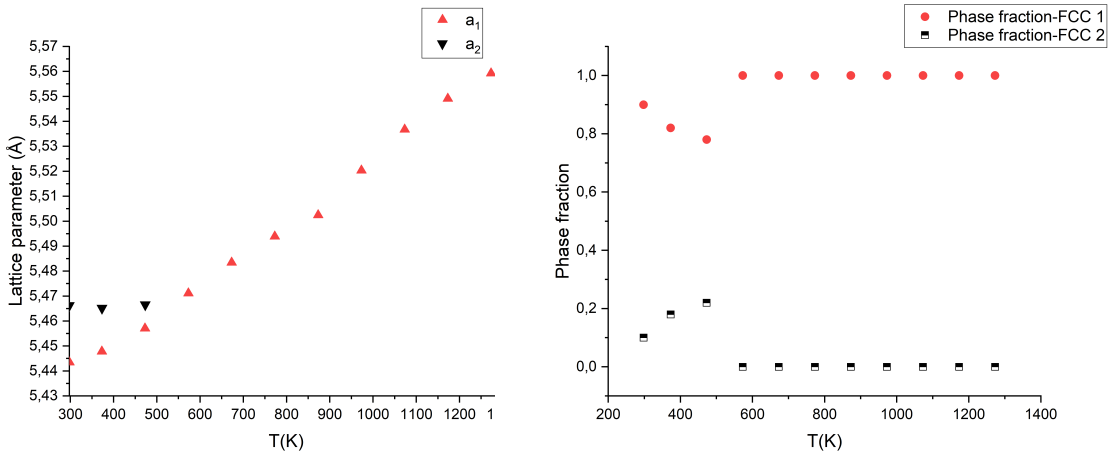

(a) (b)

Figure 3.19: (a) evolution of the lattice parameter for each temperature on the sample doped with 45%Ce. (b), phase fraction of FCC 1 (red) and FCC 2 (black). The FCC 2 fraction decreases with decreasing temperatures, which means that the sample also oxidizes at low temperature.

We can estimate the O/M ratio achieved at 1273 K on the sample with 45%Ce, by using the results reported by Markin *et al.*, since they evaluated the O/M ratio along with the lattice parameter as a function of the temperature. The comparison with the samples doped with 34 and 50%Ce indicate that the O/M ratio of our sample is close to 1.94 at 1273 K. According to their results, this value is close to the lowest O/M ratio of the miscibility gap for 50%Ce at room temperature, which is also in agreement with the values reported by Simeone *et al.* in [140].

Finally, the results obtained by *in-situ* HT-XRD measurements allow us to conclude that both $U_{0.75}Nd_{0.25}O_{2-x}$ and $U_{0.8}Ce_{0.2}O_{2-x}$ systems are monophasic for all assessed temperatures, whereas the system $U_{0.55}Ce_{0.45}O_{2-x}$ is not for temperatures below 473 K.

3.2.3 Implementation of a high-temperature thermal treatment on the system U-Ce-O

This section is dedicated to analyze the system U-Ce-O after a thermal annealing at high temperature. Similarly to what was presented for the U-Nd-O system, the sample doped with 45% is heated at a higher temperature and then analyzed through means of XRD at room temperature. In this case, the temperature was not as high as 1973 K, since the oxygen chemical potential of the U-Ce-O system at 45%Ce is lower than the one of the U-Nd-O system at 25%. Therefore, the temperature chosen to carry on this thermal annealing is 1773 K. The experimental procedure to implement this thermal annealing consisted on heating at high temperature for 2 h, then cooling down to room temperature (0.65 $K.s^{-1}$), and finally analyzing the sample through XRD with the first 10 patterns for one hour each, and the next 4 patterns for two hours each, to evaluate the degree of oxidation.

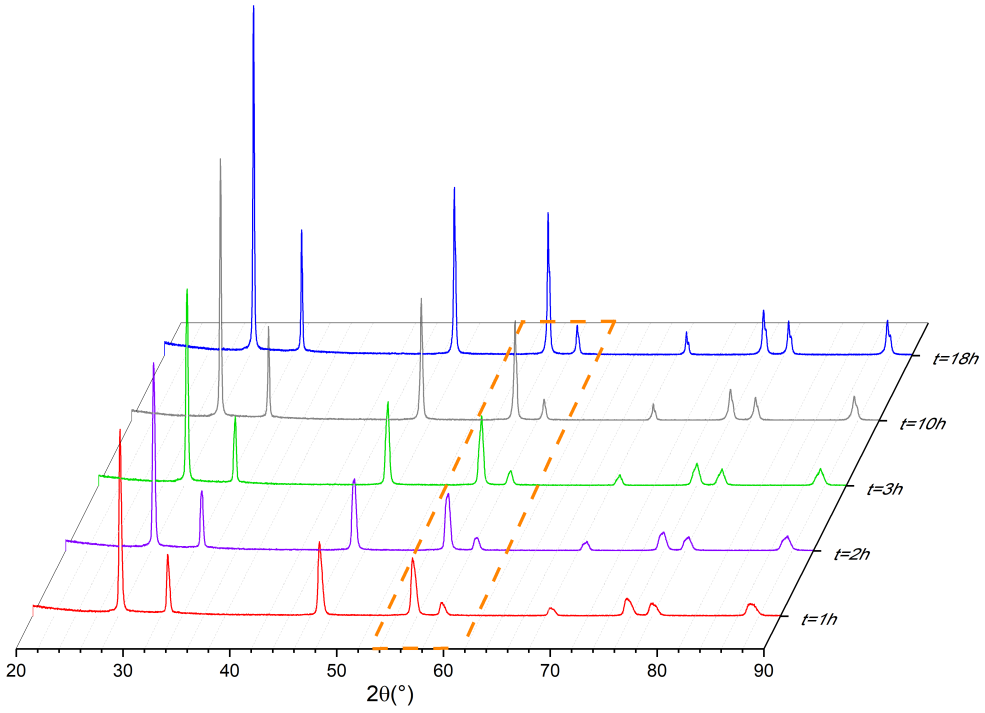

Figure 3.20: Complete XRD patterns of the sample doped with 45%Ce. The orange section highlights the peaks (3 1 1) and (2 2 2), which will be discussed later in figure 3.21

Figure 3.20 displays the XRD patterns of the sample during the first 3h, followed by one at 10h and finally at 18h. A quick inspection of the patterns can highlight the changes on the peaks over time from the first one to the last. However, in this case, the oxidation does not occur as presented in Figure 3.4 for the U-Nd-O system. Further, unlike the previous XRD patterns probed for the preliminary analysis or the

in-situ HT-XRD, there is no formation of another structure other than the fluorite, meaning that the conditions during the sintering process that took place to form the other two structures (Figure 3.16) were no longer achieved. A more detailed analysis is made on the orange section that highlights the peaks (3 1 1) and (2 2 2), which are presented along with the fitting through the Rietveld refinement in Figure 3.21.

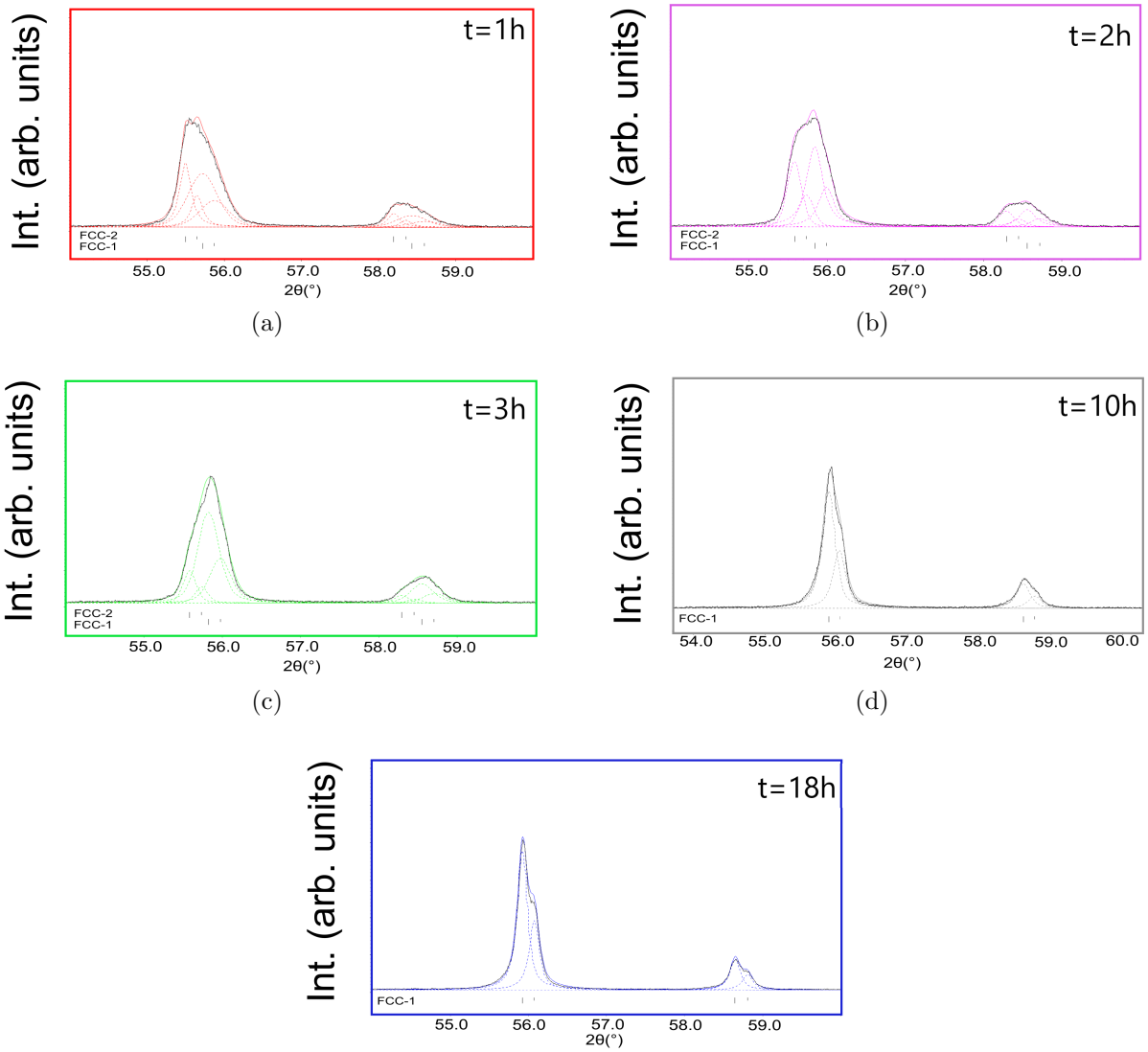

Figure 3.21: Extraction of the XRD patterns after 1, 2, 3, 10 and 18 h of the peaks (3 1 1) and (2 2 2) after the thermal annealing of the sample at 45%Ce.

The first image (Figure 3.21a) shows the presence of a biphasic system, in which the stoichiometric phase is not completely formed, since the sample reached a higher degree of hypo-stoichiometry, because of the higher temperature of the thermal treatment. On the second image (Figure 3.21b) the fraction of the second phase is more than the first one. This behaviour is also repeated after 3h (Figure 3.21c), where the hypo-stoichiometric phase has almost disappeared. By the time of the XRD pattern at 10h is measured, the sample no longer is biphasic but only monophasic, and from then on the sample only tends to stabilize the stoichiometric phase, which occurs eventually at 18h, see Figure 3.21e. In any case the sample achieved the thermodynamic equilibrium, since the formation of the second phase competes with the oxidation of the sample, since it is in permanent contact with air.

The measurements of the lattice parameter for each pattern are presented in Figure 3.22. In the first three hours, both phases decrease their lattice parameter when the sample oxidizes (black dots and inverse green triangles). This behaviour indicates that the phase one is in formation at the same time that the sample oxidizes, which is no longer the case at 10 and 18h, where the system is single-phase.

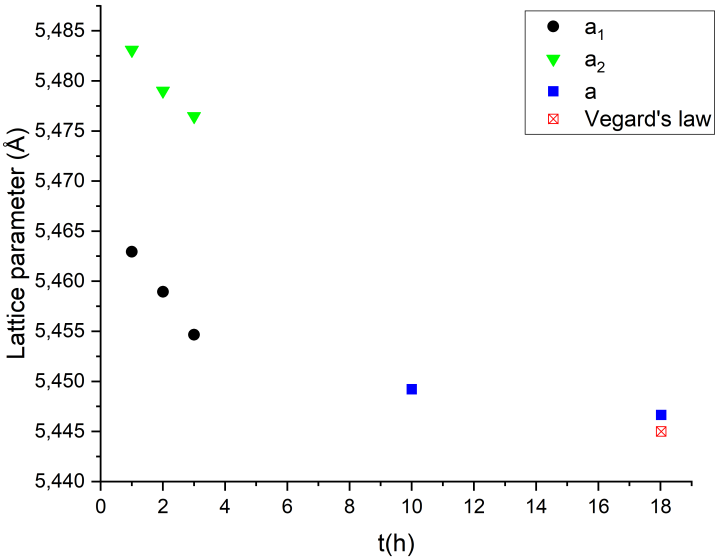

Figure 3.22: Evolution of the lattice parameter as a function of time of the sample doped with 45%Ce after the thermal annealing at 1773 K.

Both experiments, the HT-XRD and the thermal annealing along with the XRD at room temperature, are capable for describing a biphasic domain on the U-Ce-O system. Further, the temperature at which the stoichiometric phase is observed through HT-XRD (magenta triangles) of Figure 3.19 is T_C=473 K in agreement with [42, 134], it is possible to reproduce the stoichiometric side of the miscibility gap. Respecting the hypo-stoichiometric side, one has to consider the first XRD pattern

at room temperature after the thermal annealing, which is the one less affected by the oxidation. It is seen in that pattern that the lattice parameter corresponding to the hypo-stoichiometric phase ($a_{2,1h}$=5.483 Å), is in agreement with the one stated by Markin and Street, and Simeone *et al.* in [134, 140], which corresponds to an O/M ratio of 1.932. However, the latter finally indicated through studies of XRD and neutron diffraction that the structure was better fitted as an ordered oxygen deficient C-type bixbyite, instead of a fluorite. On the other hand, these O/M ratio and lattice parameter are not the ones reported by Lorenzelli *et al.*, which are greater than 5.485 Å for the lattice parameter and lower than 1.89 for the O/M ratio (in this work the values were reported for a sample doped with 40%, and not 45% like in our case).

These conclusions allow us to reproduce a schematic representation of the miscibility gap for a sample doped with 45%Ce, see Figure 3.23. It can be seen that one phase starts at O/M=2, and the other reaches an O/M=1.932 at room temperature, with a biphasic domain that is capable of reaching a critical T_C=473 K. In green line it is marked the evolution made on the HT-XRD during the cooling down of the sample (the heating evolution would be the same, since the HT-XRD pattern is symmetrical respecting the temperature). At this point it reaches an O/M=1.94 at 1273 K, then slowly cooling at the same time XRD measurements are acquired, until 473 K when it founds a biphasic domain and displays the presence of a second peak that decreases progressively its phase fraction, and therefore, approaching the O/M ratio to 2. In addition, the blue line represents the evolution of the sample submitted to a thermal annealing. This sample was heated up to 1773 K, where it reaches an O/M lower than the one achieved on *in-situ* HT-XRD, then this sample is rapidly cooled to room temperature, at this point the system is already biphasic. Next, the sample is examined by XRD, where it shows a biphasic system, see Figure 3.18a, that will eventually disappear due to the oxidation with air, until the system is finally monophasic with an O/M=2 at t=18h.

3.3 Conclusions

Careful preparations of U-Nd-O and U-Ce-O samples with homogeneous distributions of the substituted lanthanide were studied *in-situ* and *ex-situ* XRD while performing systematic annealing in reducing conditions.

Both systems do not behave similarly. The U-Nd-O system displayed a single-phase system in all assessed temperatures. A detailed analysis of the evolution of the lattice parameter as a function of the temperature during the HT-XRD measurements indicated that the reduction of the sample was effective for temperatures above 700 K. In addition, a high temperature thermal annealing proved that the reduced sample remained monophasic at room temperature, despite reaching an O/M ratio around 1.98. Identical results were obtained for the sample doped with 20%Ce, since this sample remained monophasic after both *in-situ* and *ex-situ* XRD measurements. On the other hand, the sample doped with 45%Ce displayed a different behavior.

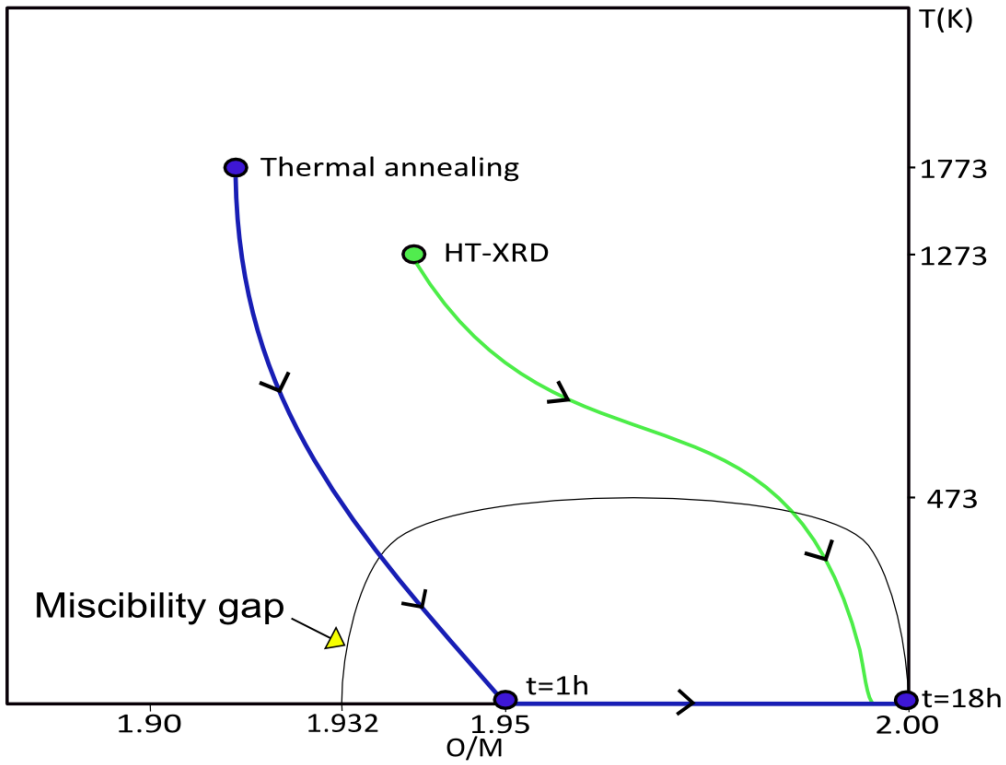

Figure 3.23: Representation of the miscibility gap in temperature on the system U-Ce-O for a sample doped with 45%. The green line stands for the evolution of the sample during the HT-XRD and the blue line for the thermal annealing at 1773 K.

The initial characterization of the as-produced sample displayed a sharp second set of peaks of fluorite symmetry. These peaks are probably not related to the miscibility gap predicted in the U-Ce-O system. Indeed, under no particular annealing conditions and cooling ramp, we were able to observe a different phase of symmetry $R\bar{3}$ where vacancies order and superlattice peaks are observed in addition to those of the fluorite. This phase might not be an equilibrium phase and further studies are needed to assess if different cooling protocols do not produce patterns with the same superlattice reflections. After the sample was probed by *in-situ* HT-XRD, the system presented another set of sharp peaks, different from those of the phase defined before. The assessment of the evolution of the miscibility gap was made by assuming the system is a fluorite, which allows to detect the incomplete formation of a second phase for temperatures below 473 K. This secondary phase was again detected by performing XRD measurements at room temperature directly after a high temperature annealing.

These results suggest that the U-Nd-O system is monophasic for O/M ratio <2, whereas the U-Ce-O system is not. However, the presence of sharp set of peaks might indicate that the actual definition of the biphasic domain predicted in literature might be incomplete, since it was reported that the system is capable of presenting a fluorite or a bixbyite structures.

Chapter 4

Optimization of the thermodynamic modeling of the system U-Nd-O

"Classical thermodynamics..is the only physical theory of universal content which I am convinced..will never be overthrown."

-Albert Einstein

In the early 1970s, a small group of scientists directed by Larry Kaufman and Himo Ansara started to work on the calculation of phase diagrams and the description of thermodynamic properties based on experimental and phase boundary data. For this purpose, this group developed a semi-empirical method named the CALPHAD (CALculation of PHAse Diagrams) method. Since then, and with the continuously-increasing computer performance, the CALPHAD approach has expanded both in the number of scientists engaged in the work and in the type of materials where this method can be applied [179]. Today, there are mainly two sophisticated commercial thermodynamic software packages that use the CALPHAD method, Thermo-Calc and Factsage. This chapter has for primary objective to present the fundamental concepts under which the CALPHAD method is defined, and for secondary objective to apply these concepts to optimize the existent model that defines the U-Nd-O system by using the software Thermo-Calc.

4.1 Description of the CALPHAD methodology: the sublattice model

The CALPHAD method allows to create models capable of predicting thermodynamic properties and stable equilibria for phase diagram construction based on the thermodynamic functions (expressions of the Gibbs free energy) of a system.

The most basic concept of the CALPHAD method is that the equilibrium state is the one with the lowest Gibbs free energy. The expressions of the Gibbs free energy are defined for each phase present in the system using a sublattice approach based on the Compound Energy Formalism (CEF) model, G^{CEF} [180]. The expression of the G^{CEF} can be defined in terms of three functions as follows:

$$G^{CEF} = G^{sr} + S^{CEF} + G^{xs} \tag{4.1}$$

The first term, G^{sr}, is the surface of reference Gibbs energy and it is defined as the summation of all terms over every possible combination of sublattice where there is only one element at once. Each term of this summation corresponds to a given end-member. Not all end-members have physical nature, instead some of them can only be defined in solution and not as a pure substance. Mathematically, G^{sr} can be expressed as,

$$G^{sr} = \sum_{J} G_J^{\circ} \prod_{s} y_J^s \tag{4.2}$$

with a temperature dependence given by,

$$G^{sr} = a + bT + cTln(T) + d_i T^n \tag{4.3}$$

where G_J° is the Gibbs energy for the end-member J, y_J^s molar fraction of the sublattice s, and a-d_i are adjustable coefficients.

The second term, S^{CEF}, is the configurational entropy of mixing. This term describes the contribution to the Gibbs energy from ideal random mixing of the components upon the crystal sites (sublattices), and it is expressed as:

$$S^{CEF} = -R.T(\sum_{s}\sum_{J} n^s y^s ln y_J^s) \tag{4.4}$$

where y^s is the site fraction for the end-member J on the sublattice s, and n^s is stoichiometric coefficient of the sublattice s. Finally, the G^{xs} term is the excess Gibbs free energy, and it represents the interactions between two (or more) elements in a same sublattice. This term is mathematically defined by the Redlich-Kistler polynomial expression [181] as,

$$G^{xs} = \prod_{s} y_J^s [y_K^i \sum_{n=0}^{N} (y_J^i - y_K^i)^n . L_{J-K}^n] \tag{4.5}$$

were y_J^i and y_K^i are the interacting constituents on the sublattice i, and L_{J-K}^n is the interaction parameter between the compounds L and K, defined as a function of temperature according to the expression

$$L_{J-K}^n = a + bT + cTln(T) + dT^2 + eT^3 ... \tag{4.6}$$

The adjustable parameters of this method are the interaction parameters, L^n. These parameters only exist when there is a non-negligible interaction between two

or more compounds within a same sublattice. The adjustment is made to have the best possible fit of the experimental results using a least-square minimization method. Once the thermodynamic representation of the system is satisfactory and the assessment of the model is complete, a database is created. This database will allow the modeling of an entire system based on a model that is built by few experimental results.

4.2 Analysis of the existent thermodynamic models

As mentioned in Chapter 1, a thermodynamic model of the U-Nd-O ternary system was developed by two authors using the CALPHAD method with different approaches. The system was modeled by Dottavio *et al* using the software Thermo-Calc, and by Lee *et al.* using the software Factage [51, 91]. Looking at the phase diagrams it is possible to observe some important differences basically due to the expressions of the end-members and interaction parameters that will determine the presence and extension of the domain of existence of a miscibility gap in the hypo-stoichiometric region. The model used by Lee *et al.* also defines a rhombohedral phase, not present in the model by Dottavio *et al.* Thus, this section has for objective to discuss the terms that define these two (fluorite and rhombohedral) phases.

4.2.1 The FCC phase

Three sublattices are used to model the FCC phase: the cationic sublattice, the anionic sublattice and the interstitial sublattice. They can be expressed as follows,

$$(U^{+3}, U^{+4}, U^{+5}, Nd^{+3})(O^{-2}, Va)(O^{-2}, Va) \tag{4.7}$$

According to Equation 2.1, the expression of the Gibbs free energy using the CEF for the fluorite phase of the U-Nd-O ternary system is be,

$$G_{fluorite}^{(U,Nd)O_{2\pm x}} = \sum_J G_J^{\circ} \prod_S y_J^S + RT \left(\sum_S \sum_J n^S y_J^s ln y_J^S \right) + G_{fluorite}^{xs} \tag{4.8}$$

In Table 4.1 there are summarized the end-members and the interaction parameters used in the both models for the fluorite phase.

Model	End-member	Interaction parameter
Dottavio *et al.*	$G^{fluorite}_{(Nd^{+3})(Va)2(O^{-2})}$	${}^{0}L^{fluorite}_{(U^{+5},Nd^{+3})(O^{-2})(Va)}$
$(U^{+3},U^{+4},U^{+5},Nd^{+3})$	$G^{fluorite}_{(Nd^{+3})(O^{-2})2(Va)}$	${}^{0}L^{fluorite}_{(U^{+4},Nd^{+3})(O^{-2})(Va)}$
$(O^{-2},Va)(Va)$	$G^{fluorite}_{(Nd^{+3})(Va)2(Va)}$	${}^{0}L^{fluorite}_{(U^{+4},Nd^{+3})(O^{-2},Va)(Va)}$
	$G^{fluorite}_{(Nd^{+3})(O^{-2})2(O^{-2})}$	${}^{0}L^{fluorite}_{(U^{+5},Nd^{+3})(O^{-2})(O^{-2},Va)}$
		${}^{0}L^{fluorite}_{(U^{+5},Nd^{+3})(O^{-2})(O^{-2})}$
		${}^{0}L^{fluorite}_{(U^{+4},Nd^{+3})(O^{-2})(O^{-2},Va)}$
	$G^{fluorite}_{(U^{+6})(O^{-2})(O^{-2})}$	${}^{0}L^{fluorite}_{(U^{+3},Nd^{+3})(O^{-2})(Va)}$
	$G^{fluorite}_{(U^{+6})(O^{-2})(O^{Va})}$	${}^{1}L^{fluorite}_{(U^{+3},Nd^{+3})(O^{-2})(Va)}$
	$G^{fluorite}_{(U^{+6})(Va)(O^{-2})}$	${}^{0}L^{fluorite}_{(U^{+4},Nd^{+3})(O^{-2})(O^{-2})}$
Lee *et al.*	$G^{fluorite}_{(U^{+6})(Va)(Va)}$	${}^{0}L^{fluorite}_{(U^{+4},Nd^{+3})(O^{-2})(Va)}$
$(U^{+3},U^{+4},U^{+5},U^{+6},$	$G^{fluorite}_{(Nd^{+3})(O^{-2})(O^{-2})}$	${}^{0}L^{fluorite}_{(U^{+4},Nd^{+3})(Va)(Va)}$
$Nd^{+3})(O^{-2},Va)$	$G^{fluorite}_{(Nd^{+3})(O^{-2})(Va)}$	${}^{0}L^{fluorite}_{(U^{+5},Nd^{+3})(O^{-2})(O^{-2})}$
	$G^{fluorite}_{(Nd^{+3})(Va)(O^{-2})}$	${}^{0}L^{fluorite}_{(U^{+5},Nd^{+3})(O^{-2})(Va)}$
	$G^{fluorite}_{(Nd^{+3})(Va)(Va)}$	${}^{0}L^{fluorite}_{(U^{+5},Nd^{+3})(Va)(Va)}$
		${}^{0}L^{fluorite}_{(U^{+6},Nd^{+3})(O^{-2})(Va)}$

Table 4.1: Thermodynamic parameters used for the two models to describe the FCC phase [51, 91].

It is also possible to see that both end-members and interaction parameter defined by Lee *et al.* take into account U^{+6} on the fluorite phase. The existence of this particular cation on the fluorite phase is today a subject of great debate on the scientific community and no experimental evidence support this statement. Although it is true that the fluorite phase was found in solutions with more than 60% of a trivalent dopant [52, 116] where the presence of U^{+6} should dominate these studies do not assess the local environments and keep the characterization at a macroscopical level.

4.2.2 The rhombohedral phase

The other important difference between these two models is the presence of a rhombohedral phase. Indeed, several authors reported this phase in similar systems such as U-La-O or U-Gd-O [41, 142, 144, 182]. The absence of this phase can be considered as a substantial limitation of the model defined by Dottavio *et al.* [91]. This phase was also defined using three sublattices:

$$(U^{+4}, U^{+5}, U^{+6})(Nd^{+3})_6(O^{-2}, Va)_{12} \tag{4.9}$$

The equation that describes this phase, according to the CEF is,

$$G^{UNd_6O_{12}}_{rhombohedral} = \sum_J G^{\circ}_J \prod_S y^S_J + RT\left(\sum_S \sum_J n^S y^s_J ln y^S_J\right) \tag{4.10}$$

This equation does not take into account the interaction between the elements in each sublattice, thus, no interaction parameters are used. Finally, Table 4.2 presents all end-members used to describe the rhombohedral phase according to the model defined by Lee *et al.* [51].

Model	End-member
	$G^{rhombohedral}_{(U^{+4})(Nd^{+3})(O^{-2})}$
Lee *et al.*	$G^{rhombohedral}_{(U^{+4})(Nd^{+3})(Va)}$
$(U^{+3}, U^{+4}, U^{+5}, U^{+6})$	$G^{rhombohedral}_{(U^{+5})(Nd^{+3})(O^{-2})}$
$(Nd^{+3})_6(O^{-2}, Va)_{12}$	$G^{rhombohedral}_{(U^{+5})(Nd^{+3})(Va)}$
	$G^{rhombohedral}_{(Nd^{+3})(O^{-2})(O^{-2})}$
	$G^{rhombohedral}_{(U^{+6})(Nd^{+3})(Va)}$

Table 4.2: Thermodynamic parameters used to define the rhombohedral phase [51].

4.3 Selection of the experimental data used to perform the optimization

The selected thermodynamic data used to perform the assessment through the CALPHAD method were obtained from [51, 52, 115–117, 123, 151, 162], as follows:

1. Concerning analysis of the phase diagram, the experimental characterizations made by Keller and Boroujerdi, Lambertson, and Wadier were taken into account to define the solubility limits of the FCC and the rhombohedral phase, particularly at higher temperatures [52, 115, 116]. Further, the measurements of the lattice parameter along with the O/M ratio at room temperature in [117, 151, 162] were used to define the ternary phase diagram at 300 K. Finally, the results presented in Chapter 2 and 3 contributed to the definitive assessment indicating the complete solubility of Nd within the cation sublattice.

2. The oxygen chemical potential data was extracted mainly from three references. Wadier measured the oxygen chemical potential for concentrations of Nd of 20%, 30% and 40% at 1123 K in [52]. Une and Oguma reported data for concentration of Nd of 14% and 27% in [123]. The last published data by Lee *et al.* concerns concentrations of Nd of 5.5%, 15.5%, 29.5% and 53% [51]. The highest concentration data was not used because it requires a model for oxygen vacancies for the compensation of U^{+6}. Also, it is necessary to know the distribution of Nd in the rhombohedral phase and the boundary of this phase. In addition, it is not clear what would happen with this boundary if the stable polymorphic state of the sesquioxide, Nd_2O_3 would be the cubic bixbyite, C-Nd_2O_3, instead of the A-Nd_2O_3.

3. Some reliable thermodynamic data were not used in this model, particularly the heat capacity, the enthalpy increment and the entropy increment published in [117]. However, an assessment of these data would require further analysis that would involve not only the adoption of the end-members and interaction parameters of both the FCC and rhombohedral phases, but also a model development including the definition of the binary Nd_2O_3 parameters. This kind of assessment was not possible within the duration of this PhD.

4. Finally, the anion site fractions measured in our experiment as a function of the O/M ratio and the $\log(P_{O_2})$, and the cation fractions obtained after the LCF of the XANES spectra were not used since these values cannot be considered at the thermodynamic equilibrium.

4.4 Modeling and assessment for the U-Nd-O system

4.4.1 Interaction parameters

In our model, as in Dottavio *et al.* one [91], the cation sublattice is occupied by U^{+3}, U^{+4}, U^{+5} and Nd^{+3}, the anion sublattice by O^{-2} and vacancies and the interstitial sublattice by O^{-2} and vacancies. The first sublattice has all possible cations found on the FCC phase at all domains of temperature. The second sublattice is defined by O^{-2} but also by vacancies, to allow to model $(U_{1-y},Nd_y)O_{2-x}$. The third sublat-

tice allows to model $(U_{1-y},Nd_y)O_{2+x}$, where the oxygen occupies interstitial positions.

The end-members were not modified in our model. On the other hand, all interaction parameters were altered. As concluded in Chapter 3 the FCC phase of the U-Nd-O system does not present a miscibility gap, and Nd is miscible up to 60% substitution. Hence, this model intends to redefine the FCC phase where there a full miscibility of Nd in both the hyper-stoichiometric and hypo-stoichiometric side of the phase diagram.

The ensemble of the interaction parameters belonging to these FCC phase were obtained by using the Parrot optimization module of the software Thermo-Calc, listed in table 4.3. The numerical values adopted for each interaction parameter can be found in Appendix D.

Model	Interaction parameters
	${}^0L^{fluorite}_{(U^{+4},Nd^{+3})(O^{-2})(*)}$
This work	${}^0L^{fluorite}_{(U^{+5},Nd^{+3})(O^{-2})(Va)}$
$(U^{+3},U^{+4},U^{+5},Nd^{+3})$	${}^1L^{fluorite}_{(U^{+5},Nd^{+3})(O^{-2})(Va)}$
$(O^{-2},Va)(O^{-2},Va)$	${}^0L^{fluorite}_{(U^{+5},Nd^{+3})(O^{-2})(O^{-2})}$
	${}^0L^{fluorite}_{(U^{+4},U^{+5},Nd^{+3})(*)(*)}$

Table 4.3: Optimized interaction parameters of the FCC phase. The symbol "*" means all species, in this case it would include O^{-2} and oxygen vacancies.

Each parameter has a particular impact on a specific region of the phase diagram. One way of visualizing the influence of each parameter on the system can be made in Figure 4.1. This figure displays a section of the ternary phase diagram where each interaction parameter has the greatest impact.

All interaction parameters are used to stabilize or destabilize a phase, they increase the domain of existence of a phase, or even describe the existence of a miscibility gap. These parameters adopt the expression of A+B.T, where A is the enthalpic term and B corresponds to the entropic term. The first term, A, is responsible for the extension of the solubility of the phase (or the miscibility gap, if it would be the case), and the second, B, models its evolution as a function of temperature, that is the extension of a phase from one isotherm to the next. As listed in table 4.3, five interaction parameters were used to model the system. The wide extension of the FCC phase up to concentration of Nd of over 60% requires that the parameter ${}^0L^{fluorite}_{(U^{+5},Nd^{+3})(O^{-2})(O^{-2})}$ adopts a very negative value, also in company with an entropic term. The same reasoning

is applied to the terms ${}^0L^{fluorite}_{(U^{+5},Nd^{+3})(O^{-2})(Va)}$ and ${}^1L^{fluorite}_{(U^{+5},Nd^{+3})(O^{-2})(Va)}$. This latter was useful to model the chemical potentials, however, by definition this parameter is multiplied by the term $(y_{U^{+5}} - y_{Nd^{+3}})$, that depending on its value it stabilizes one side at the expenses of the other. Similarly, the ${}^0L^{fluorite}_{(U^{+4},Nd^{+3})(O^{-2})(*)}$ was needed to model the wide extension of solubility of the FCC phases. This concerns the line that joins UO_2 and Nd_2O_3, where U is assumed as U^{+4}. Finally, the parameter ${}^0L^{fluorite}_{(U^{+4},U^{+5},Nd^{+3})(*)(*)}$ has a predominant role on stabilizing the region $(U^{+4},U^{+5})O_{4.5}$ with Nd_2O_3.

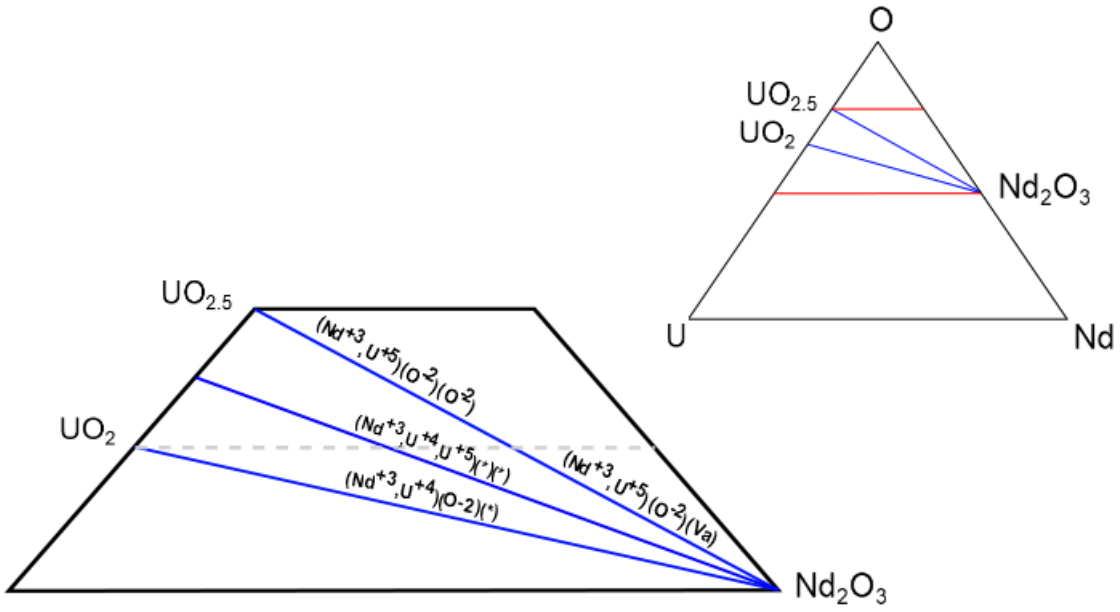

Figure 4.1: Schematization of the regions where the interaction parameters are most relevant for the ternary phase diagram.

On the other hand, the rhombohedral phase, also defined by three sublattices (see equation 4.9), does not use interaction parameters, but a set of six end-members. Table 4.4 summarizes all parameters of this phase. A more detailed description with numerical values can be found in Appendix D.

Model	Interaction parameters
This work	$G^{rhombohedral}_{(U^{+4})(Nd^{+3})(O^{-2})}$
	$G^{rhombohedral}_{(U^{+5})(Nd^{+3})(O^{-2})}$
	$G^{rhombohedral}_{(U^{+6})(Nd^{+3})(O^{-2})}$
[183]	$G^{rhombohedral}_{(U^{+4})(Nd^{+3})(Va)}$
	$G^{rhombohedral}_{(U^{+5})(Nd^{+3})(Va)}$
	$G^{rhombohedral}_{(U^{+6})(Nd^{+3})(Va)}$

Table 4.4: Parameters obtained after the assessment of the rhombohedral phase.

4.4.2 Oxygen chemical potentials

Figures 4.2, 4.3, 4.4 and 4.5 show the modeled chemical potentials at different temperatures and O/(U+Nd) ratios and the experimental data found in literature. A general good agreement is found, however, some differences are still present at high temperature.

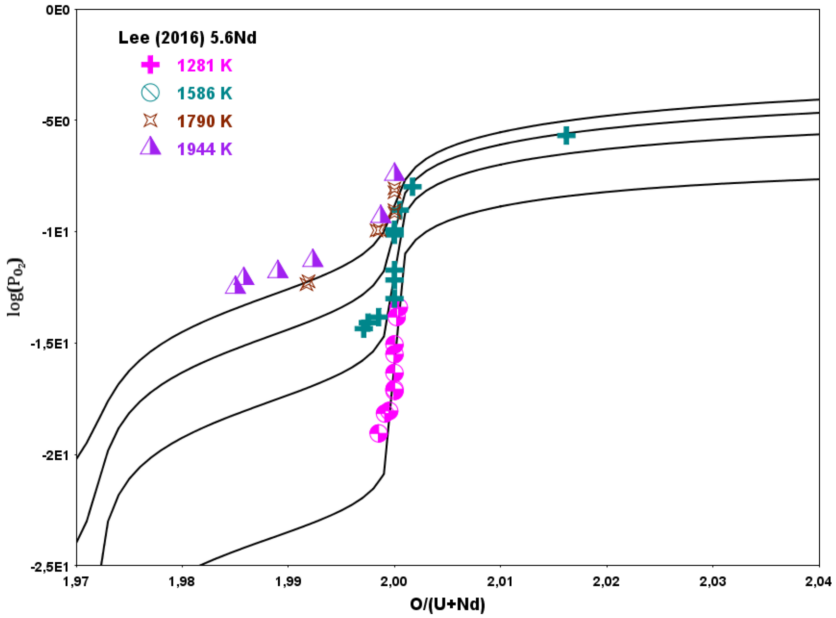

Figure 4.2: Calculated oxygen chemical potentials for different temperatures and comparison with experimental data from [51] for a concentration of Nd of 5.5%Nd.

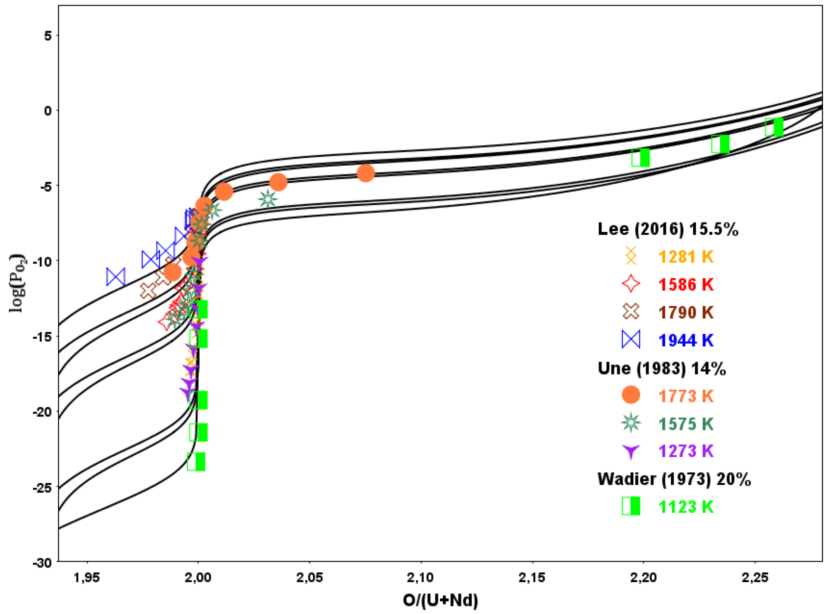

Figure 4.3: Calculated oxygen chemical potentials at temperatures from 1123 K up to 1944 K for concentrations of Nd of 14, 15.5 and 20 %, and comparison with experimental data extracted from [51, 52, 123].

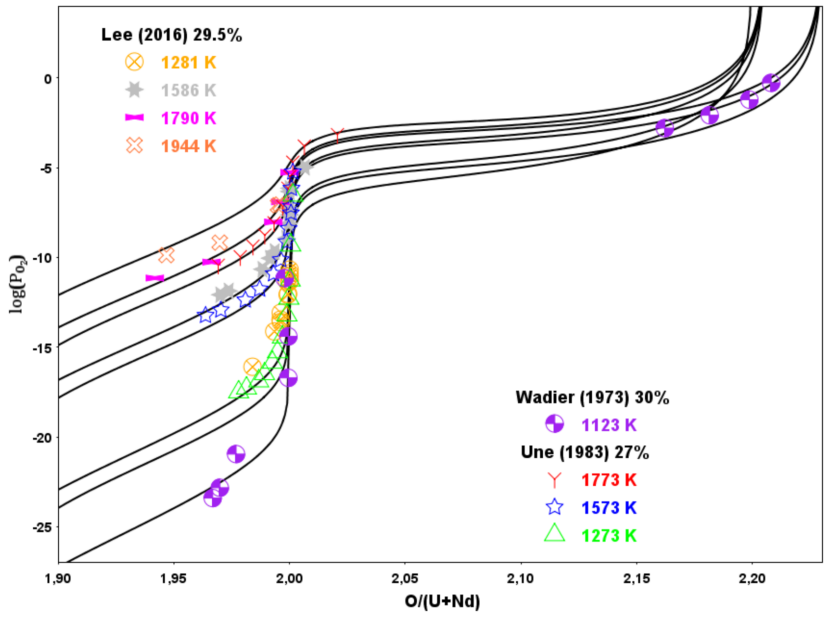

Figure 4.4: Calculated oxygen chemical potentials at different temperatures for concentrations of Nd of 27, 29.5 and 30%, and comparison with experimental data from [51, 52, 123].

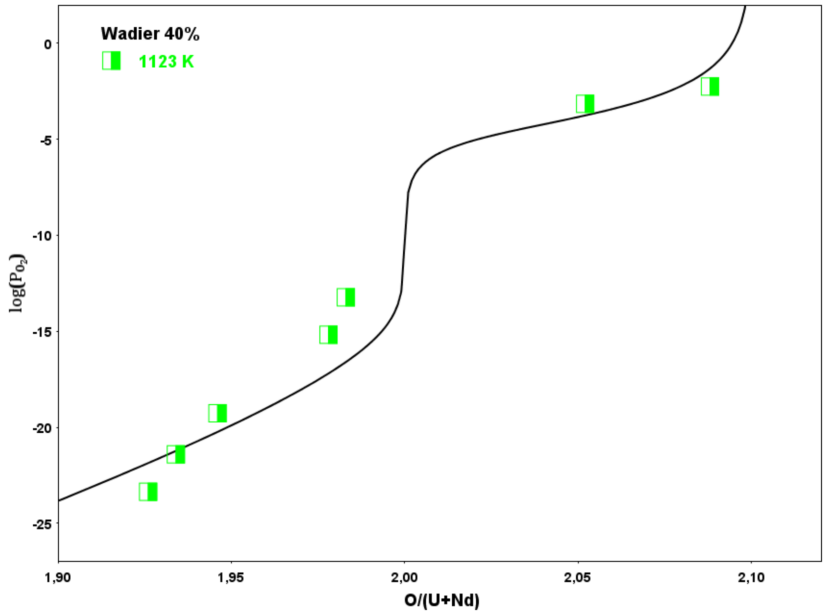

Figure 4.5: Calculated oxygen chemical potentials at 1123 K at 40%Nd and comparison with experimental data from Wadier in [52].

4.4.3 Phase diagram

The isothermal sections were also computed at different temperatures. Figures 4.6, 4.7 and 4.8 show the calculated ternary diagrams and contrast the experimental data from [51, 52, 116, 117, 123]. The tie-lines of the biphasic domains are displayed in green and the three-phase regions are defined by a red perimeter.

In first place, Figure 4.6 schematizes the ternary phase diagram at room temperature. Unlike both previous models, in this diagram there is no miscibility gap, whether it is on the hypo-stoichiometric region or the hyper-stoichiometric region. In addition, one can visualize the results at this temperature from different authors probing that, effectively, there is only a monophasic system for a wide range of concentrations. Starting from a concentration of around 54% Nd the FCC phase ends and the rhombohedral phase appears. The lower limit of existence of this phase at room temperature is unknown. The extension of the rhombohedral phase presented in this model is not complete. According with [52, 116], the boundary with the A-Nd_2O_3 phase should indicate a biphasic region with the rhombohedral and A-Nd_2O_3 phases. Instead, this model predicts a triphasic region between the FCC, rhombohedral, and the A-Nd_2O_3 phases. This limitation will be present also for higher temperatures.

Figure 4.7a reflects the isotherm at 1123 K and Figure 4.7b details the upper section of the diagram. Following the evolution of Figure 4.6, the FCC phase covers a large extension of the phase diagram. Wadier analyzed this region with four different concentrations: 20, 30 and 40%Nd, and a single point with 80%Nd [52], which this

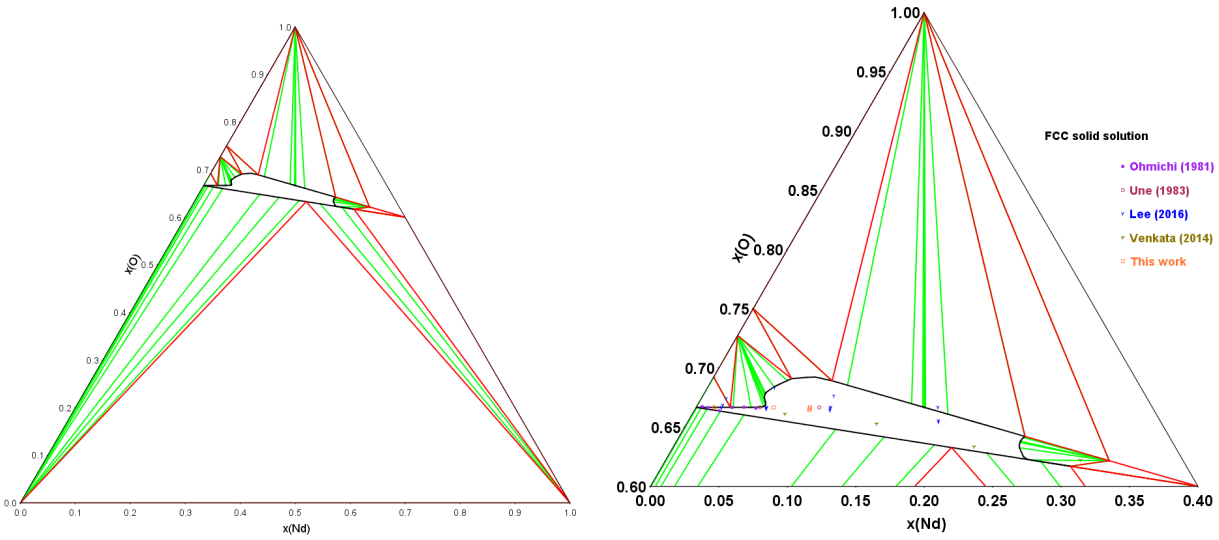

(a) (b)

Figure 4.6: (a) calculated isotherm at 300 K. (b) section of the isotherm at 300 K and comparison with experimental data from [117, 123, 151, 162] .

model is not able to reproduce. These concentrations were also used by Wadier to analyse the oxygen chemical potential, also at 1123 K, see figures 4.3, 4.4, 4.5.

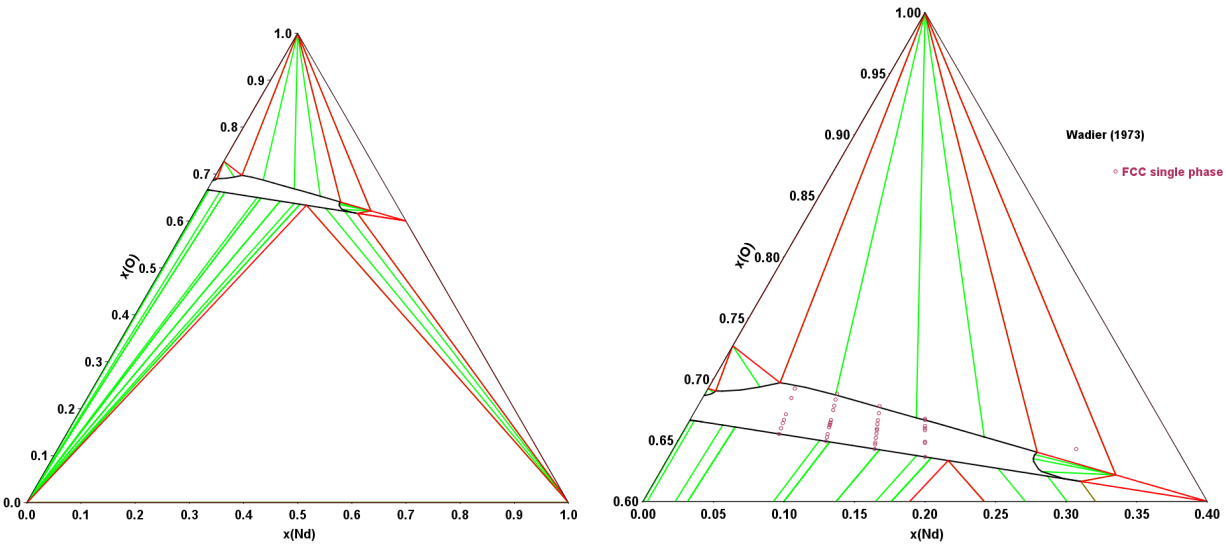

(a) (b)

Figure 4.7: (a) calculated isotherm at 1123 K. (b) section of the isotherm at 1123 K and comparison with experimental data from [52].

Another isotherm was calculated at 1523 K. Figure 4.8 displays the ternary phase

diagram along with the experimental data from [116]. They are four phases at the thermodynamic equilibrium, each one represented by a different color. The first of them, U_3O_8 is in equilibrium with the FCC phase. According to the experimental data, this domain of coexistence can appear up to a concentration of 35%Nd. Our model does not predict this large domain of existence but a smaller region up to 15%Nd. This difference does not question the oxygen solubility in the FCC phase, only the relative extension of the FCC and the U_3O_8 phases. Concerning the FCC phase, the solubility of Nd has an overall good agreement with the presented model. However, some experimental points indicate a higher oxygen solubility all along the domain of existence of the FCC phase. These experimental data seem somehow difficult to model, since the upper limit of the domain that defines this phase contains the maximum tolerable amount of U^{+5} the FCC phase can have. Instead, Keller and Boroujerdi's experimental data suggest the FCC phase can host U^{+6} if sufficient oxygen atoms are inserted in the interstitial sublattice. Further, even in a model involving the presence of U^{+6} of the FCC phase, like the one of Lee *et al.* in [51], there are some difficulties modeling all the experimental data.

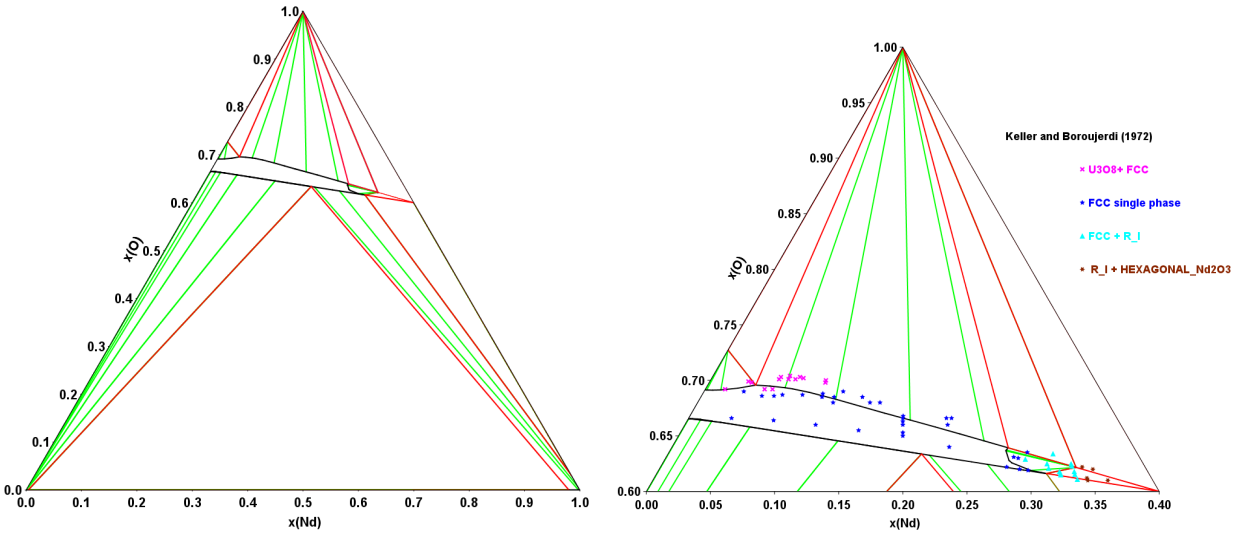

(a) (b)

Figure 4.8: (a) calculated isotherm at 1523 K. (b) section of the isotherm at 1523 K and comparison with experimental data from [116].

The rhombohedral phase characterized by Keller and Boroujerdi has a small domain of existence starting from 78% up to 85%Nd. The domain of coexistence of this phase is with the FCC phase in one side and with A-Nd_2O_3 on the other, and it does not seem to be particularly sensitive to temperature. At lower temperature the region where this rhombohedral phase is present increases slightly, this result in agreement with the phase diagram reported by Wadier, see Figure 1.19. Indeed, it was mentioned that this phase has a lower Nd limit of 80%Nd at 1123 K, not far from the 75%Nd at 1523 K stated by Keller and Boroujerdi, in Figure 1.18. The final

observed region involves the rhombohedral phase in coexistence with the FCC and A-Nd_2O_3 phases. The upper limit of the domain of coexistence between the FCC and rhombohedral phases is near 85%Nd. All authors, Keller and Boroujerdi, Wadier and Lamberston are consistent with these values, which is in fairly good agreement with the predictions of our model.

4.4.4 Site fractions

Site fractions were also calculated at the temperature of 1473 K with the proposed model. Figures 4.9, 4.10 and 4.11 display the site occupancies for the analyzed samples. The experimental data obtained by XRD and XAS in Chapter 2 are not reported, since these values are not at the thermodynamic equilibrium. It is possible to see that the formation of U^{+5} is more important for higher concentrations of Nd, which affects directly the oxygen chemical potential needed to achieve an O/M<2.

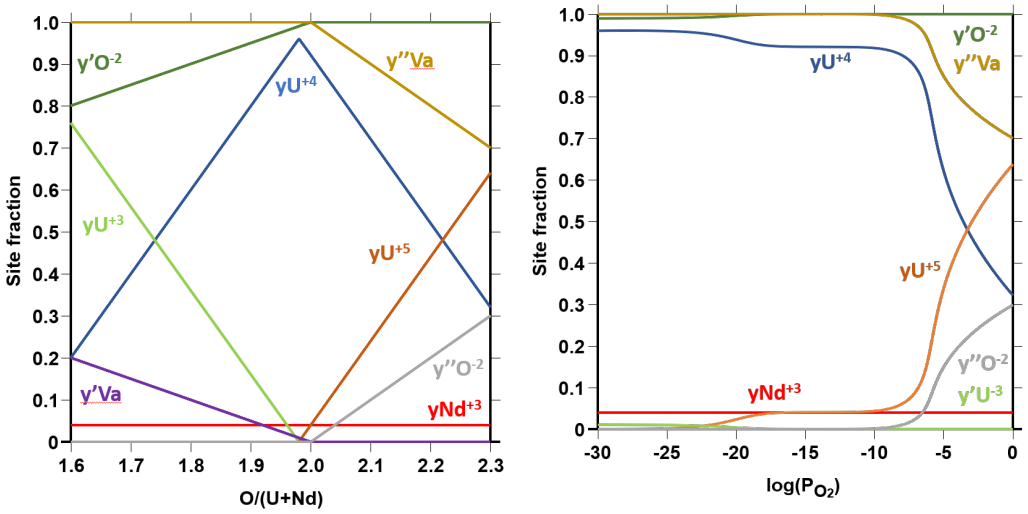

(a) (b)

Figure 4.9: Site fractions of the sample doped with 4%Nd.

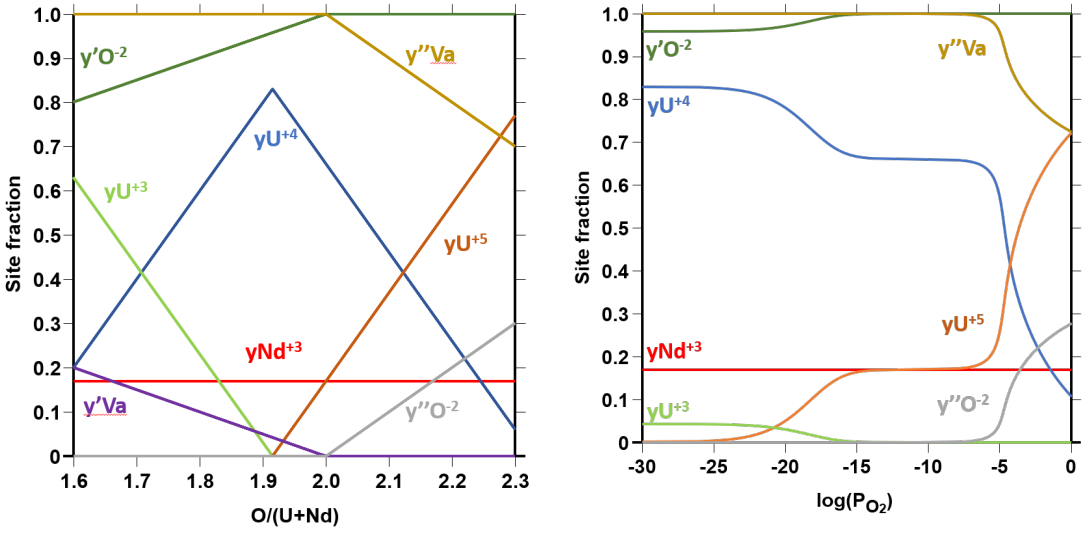

(a) (b)

Figure 4.10: Site fractions of the sample doped with 17%Nd.

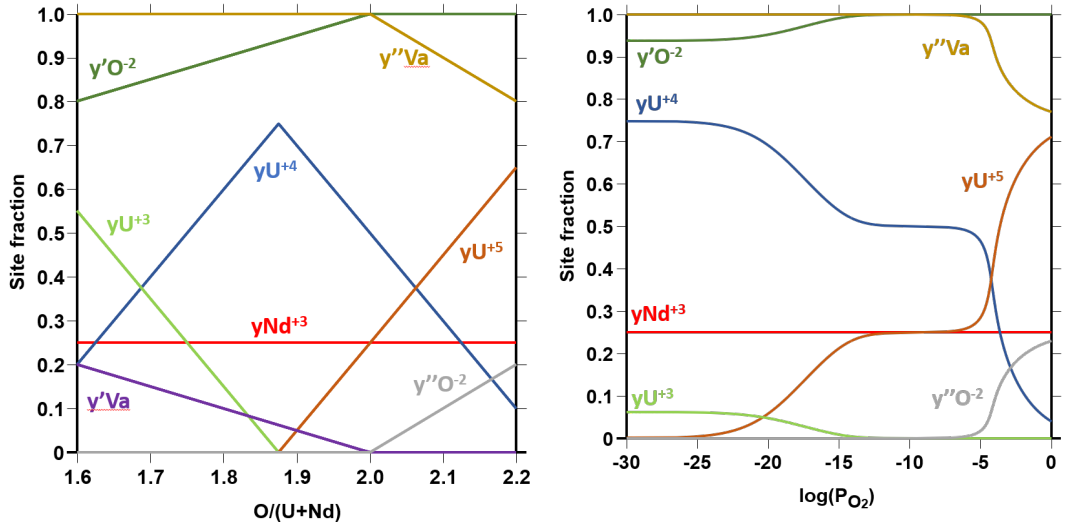

(a) (b)

Figure 4.11: Site fractions of the sample doped with 25%Nd.

4.5 Conclusions

This chapter was dedicated to describe the CALPHAD method. It was seen that through the definition of the Gibbs free energies according the CEF it is possible to define the phases that will confirm a thermodynamic model. Two models were used to describe the U-Nd-O system. The first model, made by Dottavio *et al.* [91], presents a miscibility gap at room temperature that exists until over 745 K. This model also excludes the formation of a rhombohedral phase, reported on [52, 116]. On the other

hand, the second model made by Lee *et al.*, has a good agreement with the published experimental data concerning the different thermodynamic properties and also presents the rhombohedral phase in agreement with the experimental data reported by Keller and Boroujerdi [116, 117]. However, this model predicts a miscibility gap on the hyper-stoichiometric region of the phase diagram that is not supported by any experimental data.

In addition, the results presented in Chapter 2 and 3 indicate that no miscibility gap is present on this system even if the samples oxidize rapidly at room temperature, in agreement with different authors [52, 117, 123, 151, 162]. Despite the fact that the samples are out-of-thermodynamic equilibrium, it was concluded that the system was monophasic for over 50%Nd. Consequently, a thermodynamic assessment using the software Thermo-Calc was made from the current model where a miscibility gap is predicted on the hypo-stoichiometric region [91].

The proposed model calculates only a monophasic system on the FCC phase for all temperatures in both the hypo-stoichiometric and hyper-stoichiometric regions. Experimental data respecting the oxygen chemical potentials were used to make the optimization of the model. No major differences are seen respecting the former model, except the data reported by Wadier [52], where some discrepancies were found. The values of chemical potentials published by Lee *et al.* in [51] were used complementary to the ones of Une and Oguma [123].

Nevertheless, the model introduced in this chapter is only preliminary. Indeed, there are some aspects that remain undefined, like the calculation of the heat capacity, or the extension of the biphasic domain where the FCC phase is in equilibrium with the phase U_3O_8, or the limit of coexistence of the A-Nd_2O_3, among others. Further, more experimental data are needed respecting the formation, limit of existence, and thermodynamic properties of the rhombohedral phase, since there is few information about this phase, particularly at lower temperatures.

Conclusions and perspectives

"Where there is no vision the people perish..."

- Proverbs 29:18

The understanding of the evolution of the microstructure and properties of nuclear fuel under irradiation has been the focus of intense research works due its complexity and commercial importance of nuclear reactors. Many properties that play a key role in fuel performance, transient conditions or accident scenarios are capable of changing after the primary irradiation effects, such as swelling or thermal conductivity. A starting point for the prediction of the evolution of these properties demands a knowledge of all involved phases. This work presented the study of the structure and microstructure and two systems with utmost importance for nuclear fuel: the U-Nd-O and U-Ce-O systems.

The first stage of this manuscript starts by making a critical assessment of the open literature related to the U-Nd-O system as well as its three composing binaries in terms of the phase diagrams, crystallographic structures and thermodynamic properties. This review showed that the U-Nd-O phase diagram was defined differently according various authors. Some of them detected the presence of a miscibility gap and some others only reported a monophasic system for any concentration of Nd on the FCC phase. A detailed observation of the conditions under which the miscibility gap was predicted revealed that the differences between the authors could be explained by the manufacturing processes used to assess the system. Hence, other Ac,Ln-based ternary diagrams as well as the manufacturing processes used to define them were carefully examined, being Ac= Pu and Ln= Ce, La, Gd. In most cases, the manufacturing process did not affect the phase diagram, however, in some cases it was stated that the mechanical mixing of the samples was capable of affecting the limit of solubility of the dopant. This observation led to think that the presence of a biphasic domain was somehow related to the manufacturing process.

For this purpose, a first set of samples doped with Nd, to form $U_{1-y}Nd_yO_{2\pm x}$ (y=0.04, 0.17, 0.27, 0.33) produced by dry route means were probed by multiple techniques. SEM imaging highlighted the existence of regions rich in Nd with elevated porosity and uneven grain size distribution, confirmed also by EBSD means. The formation of large pores was seen to be important around the zones rich in Nd,

this was explained by the low mobility of Nd that unables the pore to spread uniformly. Observations by TEM indicated local fluctuations of the Nd concentrations, where this variation might be present on intergranular domains without having a concentration gradient. Further characterizations through XRD displayed that some samples were capable of being monophasic and other multiphasic. However, these phases were the result of random distribution of U and Nd out-of-equilibrium, which were affected differently by the oxygen partial pressure throughout the sintering process. This distribution gave place to the formation of metastable phases that are not present on the phase diagram where the thermodynamic equilibrium is effectively achieved, such as the bixbyite C-Nd_2O_3.

A second set of samples were also studied to assess the ternary phase diagram; these new samples were produced by wet route means and close concentrations to the previous ones (y=0.04, 0.17, 0.25). They displayed a more uniform cationic distribution, which was verified by SEM and EDS imaging. An analysis by XRD on the crystallographic structure indicated that in all cases the samples were monophasic after the sintering with a stoichiometry near to O/M=2. These results were compatible with the phase diagram proposed by the authors who reported the miscibility gap, since it is only for O/M<2 that it was reported. Therefore, a thermal treatment under reducing conditions was proposed. Thermodynamic calculations of the oxygen chemical potential indicated that 1473 K is a sufficiently high temperature to achieve an O/M ratio reducing enough to detect the presence of a miscibility gap. The following characterizations by XRD stated that the O/M ratio of the samples close to 2 by the time these measurements were taken. A complementary analysis by XAS before and after the thermal treatment allowed to further characterize the U-Nd-O at an atomistic scale. The results obtained by HERFD-XAS showed that the charge compensation mechanism is governed mainly by the oxidation of U^{+4} to U^{+5} and secondly by the formation of vacancies when the Nd concentration increases. No formation of U^{+6} was seen in any sample. On the other hand, the EXAFS results indicated that the fluorite structure was confirmed in both U L_3-edge and Nd L_3-edge, and that the contraction of the lattice was given by U^{+5}. These results were comparable with analogue systems based of UO_2 with trivalent dopants.

The fact that the sample was not reduced enough to study the hypo-stoichiometric domain stressed the need of performing *in-situ* studies and more reducing conditions. Therefore, the following experimental campaign was dedicated to study the evolution of Nd-doped samples in temperature by *in-situ* HT-XRD. The comparison with the evolution of the lattice parameter of UO_2 and similar Nd-doped samples indicated that the samples were reduced at temperatures over 700 K. Finally, a high temperature thermal treatment under reducing conditions allowed to understand the behavior of the sample with an O/M=1.98 at room temperature. XRD measurements were taken directly after the thermal treatment to minimize the effect of reoxidation, which nevertheless happened within the next few hours. The reoxidation of the sample was evidenced by observing the displacement of the XRD pattern along with the ordering of the crystal lattice.

The results obtained after analyzing the two different sets of samples allowed us to make the following conclusions. In first place, random fluctuations on the Nd concentration are capable of forming different multiphasic systems. These multiphasic systems can be conformed only of the FCC phase, or they can also include out-of-equilibrium metastable phases formed at higher temperatures and particular conditions of oxygen partial pressure, which are considered sensibly important as they remained stable at room temperature. These phases are not likely to form on homogeneous samples. On the contrary, the cation/vacancy ordering in homogeneous samples after the different thermal annealings displayed systematically the same result, a monophasic system. These results are meant to contribute to the definition of the U-Nd-O phase diagram where until to date there is a debate respecting the presence of a miscibility gap on the FCC phase.

The results obtained from the U-Nd-O system were compared with an analogue system, the U-Ce-O ternary system. Samples doped with 20%Ce displayed a similar behavior respecting the U-Nd-O system. They suggested a monophasic system, as no peak splitting was seen. On the contrary, the initial characterization of a sample doped with 45%Ce revealed the formation of a well-defined set of peaks that were related to a superstructure with $R\bar{3}$ symmetry. The formation of this phase is not defined on the phase diagram. Further assessments by HT-XRD showed the presence of a different set of peaks. A model explaining this new pattern was not proposed, therefore, the patterns of the *in-situ* HT-XRD experiment were treated assuming the behavior of a fluorite structure. Three patterns were analyzed through the Rietveld refinement at the temperatures of 298 K, 773 K and 1173 K. In good agreement with different authors, the system displayed two phases at room temperature and it was only monophasic for the other higher temperatures. Finally, a high temperature thermal annealing was performed, the following XRD patters acquired at room temperature also showed the presence of a second crystallographic phase, while the sample oxidized. In both studies the system did not achieve to form completely the second phase. It was only by using both studies that the miscibility gap presented on the open literature was reproduced.

The analysis of the samples doped with 45%Ce displayed two set of peaks associated to the formation of superstructures that are not defined to date in the phase diagram. The origin that causes these particular arrangements is unknown, and their presence can only be given to a particular ordering of vacancies or short-range cation displacement during the sintering process. Indeed, a metallic arrangement would need temperatures well beyond the critical temperature of the miscibility gap described to date on the phase diagram (473 K for a sample doped with 45%Ce). It is only for temperatures higher than 1300 K that cation displacement can be relevant. This means that these superstructures could be related to another biphasic domain (one or many) that were only possible to see after the sintering. Indeed, a longer thermal annealing would promote a higher grain coarsening and cation ordering would be limited to a fluorite which would not represent the real equilibrium state, making impossible to

reproduce these structures. The fact that the U-Ce-O system is capable of displaying the formation of different superstructures other than the fluorite is highly important to understand and predict any irradiation driven behavior. Even if these structures represent possible phases out-of-equilibrium they are likely to exist in irradiated fuel, which is a continuously evolving system and far from equilibrium, and their presence would affect the formation and recombination of defects, that would determine the lattice strain and would impact ultimately the swelling or transport properties of the fuel.

After the results obtained respecting the U-Nd-O system, it was possible to propose an optimization of the existing thermodynamic model using the CALPHAD method. This model included the definition of the FCC phase for a wide range of Nd concentration, but also the presence of a rhombohedral phase for higher Nd concentrations, which was reported in multiple occasions. The new proposed model was made with recently published experimental data respecting the oxygen chemical potential, at different concentrations and temperatures. However, this model is unfortunately incomplete. Different experimental data such as the enthalpic increment or the heat capacity were not included because some planning inconveniences came up by the end of this PhD. Nevertheless, good agreements with the phase diagrams and oxygen chemical potentials were globally achieved.

This work pointed out the fact that further analysis on the U-Nd-O, as well as the U-Ce-O system are still necessary. Concerning the U-Nd-O phase diagram, higher O/M ratios must be evaluated since there is almost no experimental data on hyper-stoichiometric conditions. It is also necessary to evaluate the U-Nd-O system for concentrations of Nd greater than 30% to establish a clear limit between the FCC and the rhombohedral phases, since this latter was only stated at high temperatures and never at room temperature. In addition, the definition of the U-Ce-O system is also incomplete. Indeed, this work pointed out the formation of superstructures that have no clear relation with the phase diagram established to date. New experimental campaigns with different compositions, and characterization techniques at atomic scale are still necessary to understand the formation of this phase. In addition, there is no global consensus concerning the limit of the hypo-stoichiometric phase of the miscibility gap or its real structure. These factors are of major importance to improve the understanding of the behavior of Nd and Ce in UO_2 as they play a key role on the properties that govern the nuclear fuel behavior.

This work also proved that for O/M<2, three of the most relevant ternaries in irradiated fuel have similar behaviors, they are the U-Nd-O, the U-La-O and U-Gd-O systems. All three dopants (Nd, La and Gd) displayed comparable solubility in UO_2. They also present similar charge compensations mechanisms where U^{+5} is always more favored than the formation of vacancies and U^{+6}. It was seen that for over 80%, these three systems are most likely to form at least one rhombohedral phase. These conclusions are very meaningful, as they lead to think that the results obtained for one system, can be extrapolated to the other when there is no experimental data.

On the other hand, the U-Ce-O and U-Pu-O systems were proved to form a biphasic domain for O/M<2. One way if increasing the level of complexity would be by studying the possible formation of a biphasic domain on systems doped with U-Pu-Ce-O. Multiple authors reported the presence of a miscibility gap on the system U-Pu-O for concentrations of Pu higher than 17%, whereas for the case of the U-Ce-O system, this limit is around 30%Ce. These concentrations are reasonably achieved already in highly irradiated MOX fuels for Generation II and III reactors and will be even more easily reached in Generation IV reactors, since the Pu concentration directly after the manufacturing can be over 30%. The study of the quaternary U-Pu-Ce-O would be then necessary to assess the possible presence of a biphasic domain in irradiated fuel.

Bibliography

[1] "Key World Energy Statistics 2014". In: (2014), p. 82.

[2] EIA projects world energy consumption will increase 56% by 2040 - Today in Energy - U.S. Energy Information Administration (EIA). July 2013.

[3] D. Weisser. "A guide to life-cycle greenhouse gas (GHG) emissions from electric supply technologies". In: *Energy* 32.9 (Sept. 2007), pp. 1543–1559.

[4] D. R. Olander. Fundamental aspects of nuclear reactor fuel elements. Tech. rep. TID-26711-P1. California Univ., Berkeley (USA). Dept. of Nuclear Engineering, Jan. 1976.

[5] J. Noirot, L. Desgranges, and J. Lamontagne. "Detailed characterisations of high burn-up structures in oxide fuels". In: *Journal of Nuclear Materials* 372.2-3 (Jan. 2008), pp. 318–339.

[6] V. V. Rondinella and T. Wiss. "The high burn-up structure in nuclear fuel". In: *Materials Today* 13.12 (Dec. 2010), pp. 24–32.

[7] T. Wiss et al. "Properties of the high burnup structure in nuclear light water reactor fuel". In: *Radiochimica Acta* 105.11 (Jan. 2017).

[8] H. Kleykamp. "The chemical state of the fission products in oxide fuels". In: *Journal of Nuclear Materials* 131.2 (Apr. 1985), pp. 221–246.

[9] J. Bruno and R. C. Ewing. "Spent Nuclear Fuel". In: *Elements* 2.6 (Dec. 2006), pp. 343–349.

[10] F. Lemoine, D Baron, and P Blanpain. "Key parameters for the High Burnup Structure formation thresholds in oxide fuels". In: (2010), p. 14.

[11] J-L. Nigon and G. Le Bastard. *Fabrication des combustibles au plutonium pour les REP et REB*. Text. Archive Location: 2003 Library Catalog: www.techniques-ingenieur.fr Publisher: Editions T.I. — Techniques de l'Ingénieur. Jan. 2003.

[12] C. Guéneau et al. "Thermodynamic modelling of advanced oxide and carbide nuclear fuels: Description of the U–Pu–O–C systems". In: *Journal of Nuclear Materials* 419.1-3 (Dec. 2011), pp. 145–167.

[13] L. R. Morss et al., eds. *The Chemistry of the Actinide and Transactinide Elements (3^{rd} ed., Volumes 1-5)*. Springer Netherlands, 2006.

[14] R. K. Edwards and A. E. Margin. "Phase Relations in the Uranium-Uranium Dioxide System at High Temperatures". In: *Thermodynamics. Vol. II. Proceedings of the Symposium on Thermodynamics with Emphasis on Nuclear Materials and Atomic Transport in Solids* (1966).

[15] J. K. Fink. "Thermophysical properties of uranium dioxide". In: *Journal of Nuclear Materials* 279.1 (Mar. 2000), pp. 1–18.

[16] R. E. Latta and R. E. Fryxell. "Determination of solidus-liquidus temperatures in the UO_{2+x} system (-0.50<x<0.20)". In: *Journal of Nuclear Materials* 35.2 (May 1970), pp. 195–210.

[17] C. Guéneau et al. "Liquid immiscibility in a (O,U,Zr) model corium". In: *Journal of Nuclear Materials* 254.2-3 (Apr. 1998), pp. 158–174.

[18] S. D. Conradson et al. "Local Structure and Charge Distribution in the (UO_2-U_4O_9) System". In: *Inorganic Chemistry* 43.22 (), pp. 6922–6935.

[19] D. A. Andersson et al. "Density Functional Theory Calculations of UO_2 Oxidation: Evolution of UO_{2+x}, U_4O_{9-y}, U_3O_7, and U_3O_8". In: *Inorganic Chemistry* 52.5 (Mar. 2013), pp. 2769–2778.

[20] B. Belbeoch, J. C. Boivineau, and P. Perio. "Changements de structure de l oxyde U_4O_9". In: *Journal of Physics and Chemistry of Solids* 28.7 (July 1967), pp. 1267–1275.

[21] D. J. M. Bevan, I. E. Grey, and B. T. M. Willis. "The crystal structure of β-U_4O_{9-y}". In: *Journal of Solid State Chemistry* 61.1 (Jan. 1986), pp. 1–7.

[22] R. I. Cooper and B. T. M. Willis. "Refinement of the structure of β-U_4O_9". In: *Acta Crystallographica Section A: Foundations of Crystallography* 60.4 (July 2004), pp. 322–325.

[23] L. Desgranges et al. "Structural Changes in the Local Environment of Uranium Atoms in the Three Phases of U_4O_9". In: *Inorganic Chemistry* 55.15 (Aug. 2016), pp. 7485–7491.

[24] A. Soulié et al. "Clusters of Oxygen Interstitials in UO_{2+x} and α-U_4O_9: Structure and Arrangements". In: *Inorganic Chemistry* 58.19 (Oct. 2019), pp. 12678–12688.

[25] L. Desgranges et al. "Refinement of the α-U_4O_9 Crystalline Structure: New Insight into the U_4O_9 - U_3O_8 Transformation". In: *Inorganic Chemistry* 50.13 (July 2011), pp. 6146–6151.

[26] M. Baichi et al. "Thermodynamics of the O–U system: III – Critical assessment of phase diagram data in the U–UO_{2+x} composition range". In: *Journal of Nuclear Materials* 349.1 (Feb. 2006), pp. 57–82.

[27] F. Grønvold. "High temperature X-ray study of uranium oxides in the UO_2-U_3O_8 region". In: *Journal of Inorganic and Nuclear Chemistry* 1.6 (Dec. 1955), pp. 357–370.

[28] P. E. Blackburn. "Oxygen Dissociation Pressures over Uranium Oxides". In: *The Journal of Physical Chemistry* 62.8 (Aug. 1958), pp. 897–902.

[29] G. C. Allen and N. R. Holmes. "A mechanism for the UO_2 to α-U_3O_8 phase transformation". In: *Journal of Nuclear Materials* 223.3 (June 1995), pp. 231–237.

[30] H. R. Hoekstra and S. Siegel. "The uranium-oxygen system: U_3O_8 UO_3". In: *Journal of Inorganic and Nuclear Chemistry* 18 (Mar. 1961), pp. 154–165.

[31] L. Nowicki et al. "Polytypic arrangements of cuboctahedral oxygen clusters in U_3O_7". In: *Journal of Physics and Chemistry of Solids* 61.11 (Nov. 2000), pp. 1789–1804.

[32] L. Desgranges et al. "Neutron Diffraction Study of the in Situ Oxidation of UO_2". In: *Inorganic Chemistry* 48.16 (Aug. 2009), pp. 7585–7592.

[33] N. Brincat et al. "Density functional theory calculations of defective UO_2 at U_3O_7 stoichiometry". In: *Journal of Nuclear Materials* 467.Part 2 (Dec. 2015), pp. 724–729.

[34] G. Leinders et al. "Assessment of the U_3O_7 Crystal Structure by X-ray and Electron Diffraction". In: *Inorganic Chemistry* 55.19 (Oct. 2016), pp. 9923–9936.

[35] N. A. Brincat et al. "Ab Initio Investigation of the UO_3 Polymorphs: Structural Properties and Thermodynamic Stability". In: *Inorganic Chemistry* 53.23 (Dec. 2014), pp. 12253–12264.

[36] L. Casillas-Trujillo et al. "Comparison of bonding and charge density in δ-UO_3, γ-UO_3 and La_6UO_{12}". In: *Physical Review Materials* 1.6 (Nov. 2017), p. 065404.

[37] I. Grenthe et al. *Chemical thermodynamics of uranium*. Vol. 61. June 2004.

[38] H. R. Hoekstra, A Santoro, and S Siegel. "The low temperature oxidation of UO_2 and U_4O_9". In: (Mar. 1961), p. 13.

[39] R. Venkata Krishnan et al. "Solubility studies and thermal expansion coefficient of uranium–lanthanum mixed oxide system". In: *Journal of Nuclear Materials* 403.1 (2010), pp. 25–31.

[40] D. Prieur et al. "Aliovalent Cation Substitution in UO_2: Electronic and Local Structures of $U_{1-y}La_yO_{2\pm x}$ Solid Solutions". In: *Inorganic Chemistry* 57.3 (Feb. 2018), pp. 1535–1544.

[41] R. M. Rojas et al. "Structural study of the rhombohedral fluorite-related RIII phase $U_{1-y}La_yO_{2\pm x}$, $0.56 \leqslant y \leqslant 0.67$". In: *Journal of Solid State Chemistry* 112.2 (Oct. 1994), pp. 322–328.

[42] R. Lorenzelli and B. Touzelin. "Sur le système UO_2-CeO_2; étude cristallographique à haute température". In: *Journal of Nuclear Materials* 95.3 (Dec. 1980), pp. 290–302.

[43] T. L. Markin, R. S. Street, and E. C. Crouch. "The uranium-cerium-oxygen ternary phase diagram". In: *Journal of Inorganic and Nuclear Chemistry* 32.1 (Jan. 1970), pp. 59–75.

[44] A. D. Murray and B. T. M. Willis. "A neutron diffraction study of anion clusters in nonstoichiometric uranium dioxide". In: *Journal of Solid State Chemistry* 84.1 (Jan. 1990), pp. 52–57.

[45] R. Venkata Krishnan et al. "Synthesis, characterization and thermal expansion measurements on uranium-cerium mixed oxides". In: *Journal of Nuclear Materials* 414.3 (July 31, 2011), pp. 393–398.

[46] J. W. McMurray et al. "Thermodynamic reassessment of U–Gd–O system". In: *Journal of Nuclear Materials* 452.1 (Sept. 2014), pp. 397–406.

[47] K. Une and M. Oguma. "Oxygen potentials of (U, Gd)$O_{2\pm x}$ solid solutions in the temperature range 1000–1500°C". In: *Journal of Nuclear Materials* 115.1 (Mar. 1983), pp. 84–90.

[48] A. Nakamura. "Thermodynamic Study of $U_{1-y}Gd_yO_{2+x}$ by Solid State EMF Measurements". In: *Zeitschrift für Physikalische Chemie* 207.1 (1998), pp. 223–243.

[49] T. B. Lindemer and A. L. Sutton Jr. "Study of Nonstoichiometry of ($U_{1-z}Gd_zO_{2\pm x}$)". In: *Journal of the American Ceramic Society* 71.7 (1988), pp. 553–561.

[50] R. I. Barabash et al. "Cation and vacancy disorder in $U_{(1-y)}Nd_yO_2$ alloys". In: *Journal of Materials Research* 30.20 (Oct. 2015), pp. 3026–3040.

[51] S. M. Lee et al. "Measurement of the oxygen partial pressure and thermodynamic modeling of the U–Nd–O system". In: *Journal of Nuclear Materials* 473 (May 2016), pp. 272–282.

[52] J-F Wadier. *Phase diagrams and thermodynamic properties of the uranium-neodymium-oxygen system*. Tech. rep. Rapport CEA-R-4507, Commisariat à l'énergie atomique, 1973.

[53] F. Lebreton. "Synthèse et caractérisation d'oxydes mixtes d'uranium et d'américium". PhD thesis. Oct. 2014.

[54] T. L. Markin and R. S. Street. "The uranium-plutonium-oxygen ternary phase diagram". In: *Journal of Inorganic and Nuclear Chemistry* 29.9 (), pp. 2265–2280.

[55] A. Komeno et al. "Phase separation behaviour of ($U_{0.7}Pu_{0.3}$) O_{2-x}(1.92<x<2.00) based fuels containing actinides and/or lanthanides". In: *IOP Conference Series: Materials Science and Engineering* 9 (Mar. 2010), p. 012016.

[56] T. Truphémus et al. "Structural studies of the phase separation in the UO_2–PuO_2–Pu_2O_3 ternary system". In: *Journal of Nuclear Materials* 432.1 (Jan. 2013), pp. 378–387.

[57] G. Leinders et al. “Accurate lattice parameter measurements of stoichiometric uranium dioxide”. In: *Journal of Nuclear Materials* 459 (Apr. 2015), pp. 135–142.

[58] G. Baldinozzi, L. Desgranges, and C. Petot. “A statistical approach of the thermodynamic properties of UO_2 at high temperature”. In: *Nuclear Instruments and Methods in Physics Research Section B: Beam Interactions with Materials and Atoms* 327 (May 2014), pp. 68–73.

[59] S. D. Conradson et al. “Charge distribution and local structure and speciation in the $(UO)_{2+x}$ and $(PuO)_{2+x}$ binary oxides for x<0.25”. In: *Journal of Solid State Chemistry*. f-element Spectroscopy and Coordination Chemistry 178.2 (Feb. 2005), pp. 521–535.

[60] K. O. Kvashnina et al. “Chemical State of Complex Uranium Oxides”. In: *Physical Review Letters* 111.25 (Dec. 2013), p. 253002.

[61] B. T. M. Willis. “Structures of UO_2, UO_{2+x} andU_4O_9 by neutron diffraction”. In: *Journal de Physique* 25.5 (1964), pp. 431–439.

[62] B. T. M. Willis. “Positions of the Oxygen Atoms in $UO_{2.13}$”. In: *Nature* 197.4869 (Feb. 1963), pp. 755–756.

[63] B. T. M. Willis. “Crystallographic studies of anion-excess uranium oxides”. In: *Journal of the Chemical Society, Faraday Transactions 2* 83.7 (1987), p. 1073.

[64] K. Naito, Toshihide Tsuji, and Tsuneo Matsui. “An electrical conductivity and X-ray study of a high-temperature transition in U_4O_9”. In: *Journal of Nuclear Materials - J NUCL MATER* 48 (Aug. 1973), pp. 58–66.

[65] L. Desgranges et al. “Influence of the U_3O_7 domain structure on cracking during the oxidation of UO_2”. In: *Journal of Nuclear Materials* 402.2-3 (July 2010), pp. 167–172.

[66] B. O. Loopstra. “The structure of β-U_3O_8”. In: *Acta Crystallographica Section B* 26.5 (1970), pp. 656–657.

[67] B. O. Loopstra. “The phase transition in α-U_3O_8 at 210°C”. In: *Journal of Applied Crystallography* 3.2 (1970-03-01), pp. 94–96.

[68] R. J. M. Konings et al. *The Thermodynamic Properties of the f-Elements and their Compounds. Part 2. The Lanthanide and Actinide Oxides*. Jan. 2014.

[69] G. E. Moore and K. K. Kelley. “High-temperature heat contents of uranium, uranium dioxide and uranium trioxide”. In: *Journal of the American Chemical Society* 69.9 (1947-09), pp. 2105–2107.

[70] J. B. Conway and R. A. Hein. “Enthalpy of uranium dioxide to 2350°C”. In: *Journal of Nuclear Materials (Netherlands)* Vol: 15 (Jan. 1, 1965).

[71] A. E. Ogard and J. A. Leary. *High temperature heat content and heat capacity of uranium dioxide and uranium dioxide-plutonium dioxide solid solutions*. LA-DC-8620; CONF-670915-5. Los Alamos Scientific Lab., N. Mex., Oct. 31, 1967.

[72] R. A. Hein, P. N. Flagella, and J. B. Conway. "High-Temperature Enthalpy and Heat of Fusion of UO_2". In: *Journal of the American Ceramic Society* 51.5 (1968), pp. 291–292.

[73] R. A. Hein, L. H. Sjodahl, and R. Szwarc. "Heat content of uranium dioxide from 1200 to 3100 K". In: *Journal of Nuclear Materials* 25.1 (Jan. 1, 1968), pp. 99–102.

[74] L. Leibowitz, L. W. Mishler, and M. G. Chasanov. "Enthalpy of solid uranium dioxide from 2500 K to its melting point". In: *Journal of Nuclear Materials* 29.3 (Mar. 1, 1969), pp. 356–358.

[75] D. R. Fredrickson and M. G. Chasanov. "Enthalpy of uranium dioxide and sapphire to 1500 K by drop calorimetry". In: *The Journal of Chemical Thermodynamics* 2.5 (Sept. 1, 1970), pp. 623–629.

[76] K. C. Mills et al. "Heat capacity and enthalpy of UO_2 and gadolinia-doped UO_2". In: *Thermochimica Acta* 139 (Mar. 1, 1989), pp. 107–120.

[77] Y. Takahashi and Masami A. "High-temperature heat-capacity measurements on (U, Gd)O_2 by drop calorimetry and DSC". In: *Journal of Nuclear Materials* 201 (May 2, 1993), pp. 108–114.

[78] F. Grønvold et al. "Thermodynamics of the UO_{2+x} phase I. Heat capacities of $UO_{2.017}$ and $UO_{2.254}$ from 300 to 1000 K and electronic contributions". In: *The Journal of Chemical Thermodynamics* 2.5 (Sept. 1, 1970), pp. 665–679.

[79] C. Ronchi et al. "Thermal conductivity of uranium dioxide up to 2900 K from simultaneous measurement of the heat capacity and thermal diffusivity". In: *Journal of Applied Physics* 85.2 (Dec. 29, 1998), pp. 776–789.

[80] J. P. Hiernaut, G. J. Hyland, and C. Ronchi. "Premelting transition in uranium dioxide". In: *International Journal of Thermophysics* 14.2 (Mar. 1, 1993), pp. 259–283.

[81] D. I. Marchidan and M. Ciopec. "Enthalpy of uranium to 1500 K by drop calorimetry". In: *The Journal of Chemical Thermodynamics* 8.7 (July 1, 1976), pp. 691–701.

[82] C. Ronchi et al. "A Universal Laser-Pulse Apparatus for Thermophysical Measurements in Refractory Materials at Very High Temperatures". In: *International Journal of Thermophysics* 20.3 (May 1, 1999), pp. 987–996.

[83] M. Amaya, K. Une, and K. Minato. "Heat capacity measurements on unirradiated and irradiated fuel pellets". In: *Journal of Nuclear Materials*. 10th Int. Symp. on Thermodynamics of Nuclear Materials 294.1 (Apr. 1, 2001), pp. 1–7.

[84] C. Ronchi et al. "Laboratory Measurement of the Heat Capacity of Urania up to 8000 K: I. Experiment". In: *Nuclear Science and Engineering* 113.1 (Jan. 1993), pp. 1–19.

[85] C. Ronchi and G. J. Hyland. "Analysis of recent measurements of the heat capacity of uranium dioxide". In: *Journal of Alloys and Compounds*. International Conference on Actinides 213-214 (Oct. 1, 1994), pp. 159–168.

[86] M. T. Hutchings. “High-temperature studies of UO_2 and ThO_2 using neutron scattering techniques”. In: *Journal of the Chemical Society, Faraday Transactions 2: Molecular and Chemical Physics* 83.7 (Jan. 1987), pp. 1083–1103.

[87] M. T. Hutchings et al. “Investigation of thermally induced anion disorder in fluorites using neutron scattering techniques”. In: *Journal of Physics C: Solid State Physics* 17.22 (Aug. 1984), pp. 3903–3940.

[88] K. Clausen et al. “Investigation of oxygen disorder, thermal parameters, lattice vibrations and elastic constants of UO_2 and ThO_2 at temperatures up to 2930 K”. In: *Revue de Physique Appliquee* 19.9 (1984), pp. 719–722.

[89] D. Labroche, O Dugne, and C Chatillon. “Thermodynamics of the O–U system. I – Oxygen chemical potential critical assessment in the UO2–U3O8 composition range”. In: *Journal of Nuclear Materials* 312.1 (Jan. 2003), pp. 21–49.

[90] H. Sano et al. “Solubility of Oxygen in Neodymium.” In: *Shigen-to-Sozai* 115.1 (1999), pp. 49–53.

[91] G. Dottavio et al. “Characterising the U–Nd–O miscibility gap by an experimental and a theoretical approach”. In: *Journal of Nuclear Materials* 458 (Mar. 2015), pp. 394–405.

[92] I. Warshaw and Rustum Roy. “Polymorphism of rare earth sesquioxides”. In: *The Journal of Physical Chemistry* 65.11 (Nov. 1961), pp. 2048–2051.

[93] R. D. Shannon and C. T. Prewitt. “Effective ionic radii in oxides and fluorides”. In: *Acta Crystallographica Section B: Structural Crystallography and Crystal Chemistry* 25.5 (May 1969), pp. 925–946.

[94] J. Coutures et al. “Etude a haute température des systèmes formes par le sesquioxyde de lanthane et les sesquioxydes de lanthanides. I. Diagrammes de phases (1400°C < T < T Liquide)”. In: *Journal of Solid State Chemistry* 17.1 (Feb. 1, 1976), pp. 171–182.

[95] P. Aldebert and J. P. Traverse. “Etude par diffraction neutronique des structures de haute temperature de La_2O_3 et Nd_2O_3”. In: *Materials Research Bulletin* 14.3 (Mar. 1, 1979), pp. 303–323.

[96] M. Zinkevich. “Thermodynamics of rare earth sesquioxides”. In: *Progress in Materials Science* 52.4 (May 1, 2007), pp. 597–647.

[97] O. A. Mordovin, N. I. Timofeeva, and L. N. Drozdova. “Determining the melting temperatures of rare-earth oxides.” In: *Izv. Akad. Nauk SSSR, Neorg. Mater., 3: 187-9(Jan. 1967).* ().

[98] W. A. Lambertson and F. H. Jr Gunzel. *Refractory oxides melting points.* AECD-3465. Argonne National Lab.

[99] T. Noguchi and M. Mizuno. “Freezing points of lanthanides oxides measured with a solar furnace”. In: *Solar Energy* 11.2 (Apr. 1, 1967), pp. 90–94.

[100] J. Coutures, R. Verges, and M. Foex. "Etude a haute temperature des systemes formes par le sesquioxyde de neodyme avec les sesquioxydes d'yttrium et d'ytterbium". In: *Materials Research Bulletin* 9.12 (Dec. 1, 1974), pp. 1603–1611.

[101] M. Mizuno et al. "Solidification Point Measurements for Oxides in Several Kinds of Atmospheres with a Solar Furnace". In: *Yogyo Kyokaishi* 89.1033 (1981), pp. 488–494.

[102] J. P. Coutures. "The Al_2O_3-Nd_2O_3 Phase Diagram". In: *Journal of the American Ceramic Society* 68.3 (1985), pp. 105–107.

[103] B. Granier and S. Heurtault. "Density of Liquid Rare-Earth Sesquioxides". In: *Journal of the American Ceramic Society* 71.11 (1988), pp. C466–C468.

[104] E. H. P Cordfunke and R. J. M Konings. "The enthalpies of formation of lanthanide compounds: II. Ln^{3+}(aq)". In: *Thermochimica Acta* 375.1 (July 2001), pp. 51–64.

[105] L. Merli, F. Rorif, and J. Fuger. "The Enthalpies of Solution of Lanthanide Metals in Hydrochloric Acid at Various Concentrations. Relevance to Nuclear Waste Long Term Storage". In: *Radiochimica Acta* 82.s1 (Jan. 1998).

[106] E. Huber and C. Holley. "The Heat of Combustion of Neodymium". In: *Journal of the American Chemical Society* 74.21 (Nov. 1952), pp. 5530–5531.

[107] G. C. Fitzgibbon, D. Pavone, and C. E. Holley. "Enthalpy of formation of Nd_2O_3-hexagonal". In: *Journal of Chemical & Engineering Data* 13.4 (Oct. 1968), pp. 547–548.

[108] A. T. Dinsdale. "SGTE data for pure elements". In: *Calphad* 15.4 (Oct. 1, 1991), pp. 317–425.

[109] J. O. Blomeke and W. T. Ziegler. "The Heat Content, Specific Heat and Entropy of La_2O_3, Pr_6O_{11} and Nd_2O_3 Between 30 and 900° C". In: *Journal of the American Chemical Society* 73.11 (Nov. 1, 1951), pp. 5099–5102.

[110] L. B. Pankratz, E. G. King, and K. K. Kelley. *High-temperature heat contents and entropies of sesquioxides of europium, gadolinium, neodymium, samarium and yttrium.* BM-RI-6033. Bureau of Mines, Berkeley, CA (USA), Dec. 1, 1961.

[111] H. W. Goldstein, E. F. Neilson, and Patrick N. Walsh. "David White: The Heat Capacities Yttrium Oxide(Y_2O_3) Lanthanum Oxide (La_2O_3), and Neodymium Oxide (Nd_2O_3) from 16 to 300K". In: *The Journal of Physical Chemistry* 63.9 (Sept. 1, 1959), pp. 1445–1449.

[112] B. H. Justice and E. F. Westrum. "Thermophysical properties of the lanthanide oxides. Heat capacities, thermodynamic properties, and some energy levels of lanthanum (III) and neodymium (III) oxides from 5 to 350 K." In: *The Journal of Physical Chemistry* 67.2 (Feb. 1, 1963), pp. 339–345.

[113] J. F. Haefling and A. H. Daane. "The immiscibility limits of uranium with the rare-earth metals". In: *Trans. Met. Soc. AIME* Vol: 215 (Apr. 1, 1959).

[114] L. Desgranges et al. "Miscibility Gap in the U–Nd–O Phase Diagram: a New Approach of Nuclear Oxides in the Environment?" In: *Inorganic Chemistry* 51.17 (Sept. 2012), pp. 9147–9149.

[115] W. A. Lambertson and M. H. Mueller. *Uranium oxide phase equilibrium systems: V, UO_2-Nd_2O_3; VI, U_3O_8-MgO; VII, U_3O_8-TiO_2*. Sept. 14, 1954.

[116] C. Keller and A. Boroujerdi. "Phasengleichgewichte in den systemen UO_2-UO_3-$NdO_{1,5}$ und $NpO_{2+x}NdO_{1,5}$". In: *Journal of Inorganic and Nuclear Chemistry* 34.4 (), pp. 1187–1193.

[117] R. Venkata Krishnan et al. "Solubility studies and thermophysical properties of uranium–neodymium mixed oxides system". In: *Ceramics International* 40.3 (Apr. 2014), pp. 4395–4405.

[118] G. Dottavio et al. "Existence of a miscibility gap in uranium neodymium oxide materials used as nuclear fuels simulants". In: *Progress in Nuclear Energy* 72 (Apr. 2014), pp. 22–26.

[119] R. J. Hawkins and C. B. Alcock. "A study of cation diffusion in UO_{2+x} and ThO_2 using alpha-ray spectrometry". In: *Journal of Nuclear Materials* 26.1 (Apr. 1, 1968), pp. 112–122.

[120] X. Han and B. J. Heuser. "Radiation enhanced diffusion of Nd in UO_2". In: *Journal of Nuclear Materials* 466 (Nov. 1, 2015), pp. 588–596.

[121] X. Han. "Radiation enhanced diffusion of neodymium in single crystal thin film UO_2". In: (), p. 69.

[122] M. Tetenbaum. *Some aspects of the high temperature vaporization behavior and valence effects in actinide-oxide rare-earth-oxide systems. [Nd_2O_3; U–Nd–O; U–Pu–O; U–Pu–Ce–O]*. CONF-770662-2. Argonne National Lab., Ill. (USA), Jan. 1, 1977.

[123] K. Une and M. Oguma. "Oxygen potentials of $(U,Nd)O_{2\pm x}$ solid solutions in the temperature range 1000–1500°C". In: *Journal of Nuclear Materials* 118.2 (Sept. 1, 1983), pp. 189–194.

[124] V. Ghetta et al., eds. *Materials issues for generation IV systems: status, open questions and challenges*. NATO science for peace and security series Series B: Physics and biophysics. OCLC: 254052563. Dordrecht: Springer, 2008.

[125] C. Guéneau, A. Chartier, and L. Van Brutzel. "Thermodynamic and Thermophysical Properties of the Actinide Oxides". In: *Comprehensive Nuclear Materials*. Elsevier, 2012, pp. 21–59. ISBN: 978-0-08-056033-5.

[126] C. Sari, U. Benedict, and H. Blank. "A study of the ternary system UO_2-PuO_2-Pu_2O_3". In: *Journal of Nuclear Materials* 35.3 (June 1970), pp. 267–277.

[127] T. L. Markin and R. S. Street. "The uranium-plutonium-oxygen ternary phase diagram". In: *Journal of Inorganic and Nuclear Chemistry* 29.9 (Sept. 1967), pp. 2265–2280.

[128] M. Kato et al. "Solidus and liquidus temperatures in the UO_2–PuO_2 system". In: *Journal of Nuclear Materials* 373.1 (Feb. 2008), pp. 237–245.

[129] T. Truphémus et al. "Phase Equilibria in the Uranium-Plutonium-Oxygen Ternary Phase Diagram at $(U_{0.55},Pu_{0.45})O_{2-x}$ and $(U_{0.45},Pu_{0.55})O_{2-x}$". In: *Procedia Chemistry*. ATALANTE 2012 International Conference on Nuclear Chemistry for Sustainable Fuel Cycles 7 (Jan. 2012), pp. 521–527.

[130] R. Vauchy et al. "High temperature X-ray diffraction study of the kinetics of phase separation in hypostoichiometric uranium–plutonium mixed oxides". In: *Journal of the European Ceramic Society* 34.10 (Sept. 2014), pp. 2543–2551.

[131] R. Vauchy et al. "Effect of cooling rate on achieving thermodynamic equilibrium in uranium–plutonium mixed oxides". In: *Journal of Nuclear Materials* 469 (Feb. 2016), pp. 125–132.

[132] Y. Sagayama. *GLOBAL 2005: Proceedings of the international conference on nuclear energy systems for future generation and global sustainability*. Japan, 2005.

[133] P. A. Bingham et al. "The Use of Surrogates in Waste Immobilization Studies: A Case Study of Plutonium". In: *MRS Online Proceedings Library Archive* 1107 (2008).

[134] T. L. Markin, R. S. Street, and E. C. Crouch. "The uranium-cerium-oxygen ternary phase diagram". In: *Journal of Inorganic and Nuclear Chemistry* 32.1 (Jan. 1970), pp. 59–75.

[135] A. D. Murray, C. R. A. Catlow, and B. E. F. Fender. "A neutron powder diffraction study of $U_{1-y}Ce_yO_{2-x}$". In: *Journal of the Chemical Society, Faraday Transactions 2: Molecular and Chemical Physics* 83.7 (Jan. 1, 1987), pp. 1113–1120.

[136] R. Venkata Krishnan and K. Nagarajan. "Heat capacity measurements on uranium–cerium mixed oxides by differential scanning calorimetry". In: *Thermochimica Acta* 440.2 (Jan. 2006), pp. 141–145.

[137] A. T. Nelson et al. "An Evaluation of the Thermophysical Properties of Stoichiometric CeO_2 in Comparison to UO_2 and PuO_2". In: *Journal of the American Ceramic Society* 97.11 (2014), pp. 3652–3659.

[138] K. Suzuki et al. "Thermal and mechanical properties of CeO_2". In: *Journal of the American Ceramic Society* 102.4 (2019), pp. 1994–2008.

[139] H. S. Kim et al. "Applicability of CeO_2 as a surrogate for PuO_2 in a MOX fuel development". In: *Journal of Nuclear Materials* 378.1 (Aug. 2008), pp. 98–104.

[140] D. Simeone et al. "Phase Separation in Fluorite-Related $U_{1-y}Ce_yO_{2-x}$: A Re-Examination by X-ray and Neutron Diffraction". In: *Inorganic Chemistry* 58.17 (Sept. 2019), pp. 11599–11605.

[141] M. Hoch and F. J. Furman. *Thermodynamics. Vol. II. Proceedings of the Symposium on Thermodynamics with Emphasis on Nuclear Materials and Atomic Transport in Solids*. 1966.

[142] P. Herrero, P. Garcia-Chain, and R. M. Rojas. "Microstructural characterization of the fluorite phase in the U-La-O system. I. Rhombohedral microdomain formation in $(U_{1-y}La_y)O_{2+x}$, $0.56 \leqslant y \leqslant 0.67$". In: *Journal of Solid State Chemistry* 87.2 (Aug. 1, 1990), pp. 331–343.

[143] P. Garcia-Chain et al. "Microstructural Characterization of the Fluorite Phase in the U-La-O System: II. Hexagonal Microdomain Formation in $(U_{1-y}La_y)O_{2-x}$, $0.70 \leqslant y \leqslant 0.80$". In: *Journal of Solid State Chemistry* 108.2 (Feb. 1994), pp. 236–242.

[144] H. G. Diehl and C. Keller. "Das system UO_2-UO_3-$LaO_{1.5}$". In: *Journal of Solid State Chemistry* 3.4 (Nov. 1971), pp. 621–636.

[145] T. Cardinaels et al. "Dopant solubility and lattice contraction in gadolinia and gadolinia–chromia doped UO_2 fuels". In: *Journal of Nuclear Materials* 424.1-3 (May 2012), pp. 289–300.

[146] M. Durazzo et al. "Phase studies in the UO_2–Gd_2O_3 system". In: *Journal of Nuclear Materials* 400.3 (May 2010), pp. 183–188.

[147] IAEA. "Characteristics and use of urania-gadolinia fuels". In: (Nov. 1995), p. 190.

[148] R. Venkata Krishnan et al. "Heat Capacity and Thermal Expansion of Uranium-Gadolinium Mixed Oxides". In: *Journal of Nuclear and Radiochemical Sciences* 10.1 (2009), 1_19–1_26.

[149] H. Inaba, K. Naito, and M. Oguma. "Heat capacity measurement of $U_{1-y}Gd_yO_2$ $(0.00 \leqslant y \leqslant 0.142)$ from 310 to 1500 K". In: *Journal of Nuclear Materials* 149.3 (Aug. 1987), pp. 341–348.

[150] K Teske et al. "Investigation of nuclear mixed oxide fuel-gas interaction by a solid electrolyte based coulometric technique". In: (1992), p. 6.

[151] S. M. Lee et al. "Lattice Parameter Behavior with Different Nd and O Concentrations in $(U_{1-y}Nd_y)O_{2\pm x}$ Solid Solution". In: *Nuclear Technology* 193.2 (Feb. 2016), pp. 287–296.

[152] "Advanced Fuel Pellet Materials and Designs for Water Cooled Reactors". In: (2003), p. 329.

[153] M. Marcet. "Etude de la fracturation mécanique de la structure à haut taux de combustion des combustibles irradiés (RIM) en traitement thermique". thesis. Aix-Marseille 2, Dec. 2010.

[154] A. Le Bail, H. Duroy, and J. L. Fourquet. "Ab-initio structure determination of $LiSbWO_6$ by X-ray powder diffraction". In: *Materials Research Bulletin* 23.3 (Mar. 1988), pp. 447–452.

[155] K. Persson. *Materials Data on Nd_2O_3 (SG:191) by Materials Project*. type: dataset. 2014.

[156] H. M. Rietveld. "A profile refinement method for nuclear and magnetic structures". In: *Journal of Applied Crystallography* 2.2 (June 1969), pp. 65–71.

[157] S. Huang et al. "Investigation of chemical composition and crystal structure in sintered $Ce_{15}Nd_{15}Fe_{bal}B_1$ magnet". In: *AIP Advances* 4.10 (Oct. 2014), p. 107127.

[158] G. Adachi and N. Imanaka. "The Binary Rare Earth Oxides". In: *Chemical Reviews* 98.4 (June 1998), pp. 1479–1514.

[159] N. Hingant et al. "Preparation, sintering and leaching of optimized uranium thorium dioxides". In: *Journal of Nuclear Materials*. Nuclear Materials III 385.2 (Mar. 2009), pp. 400–406.

[160] M. S. Subramanian, R. N. Singh, and H. D. Sharma. "Reaction kinetics of some actinide oxalates by differential thermal analysis". In: *Journal of Inorganic and Nuclear Chemistry* 31.12 (Dec. 1969), pp. 3789–3795.

[161] D. Horlait et al. "Synthesis and characterization of $Th_{1-x}Ln_xO_{2-x/2}$ mixed-oxides". In: *Materials Research Bulletin* 47.12 (Dec. 2012), pp. 4017–4025.

[162] T. Ohmichi et al. "On the relation between lattice parameter and O/M ratio for uranium dioxide-trivalent rare earth oxide solid solution". In: *Journal of Nuclear Materials* 102.1 (Nov. 1981), pp. 40–46.

[163] R. Bès et al. "New insight in the uranium valence state determination in $U_yNd_{1-y}O_{2\pm x}$". In: *Journal of Nuclear Materials* 507 (Aug. 2018), pp. 145–150.

[164] O. Proux et al. "High-Energy Resolution Fluorescence Detected X-Ray Absorption Spectroscopy: A Powerful New Structural Tool in Environmental Biogeochemistry Sciences". In: *Journal of Environmental Quality*. Synchrotron radiation-based methods for environmental biogeochemistry 46.6 (2017), pp. 1146–1157.

[165] R. Bès et al. "Charge compensation mechanisms in $U_{1-x}Gd_xO_2$ and $Th_{1-x}Gd_xO_{2-x/2}$ studied by X-ray Absorption Spectroscopy". In: *Journal of Nuclear Materials* 489 (June 2017), pp. 9–21.

[166] H. Cao et al. "Differential interplay between Ce and U on local structures of $U_{1-x}Ce_xO_2$ solid solutions probed by X-ray absorption spectroscopy". In: *Journal of Nuclear Materials* 515 (Mar. 2019), pp. 238–244.

[167] K. Popa et al. "Further insights into the chemistry of the Bi–U–O system". In: *Dalton Transactions* 45.18 (May 2016), pp. 7847–7855.

[168] D. G. Martin. "The thermal expansion of solid UO_2 and (U, Pu) mixed oxides — a review and recommendations". In: *Journal of Nuclear Materials* 152.2-3 (May 1988), pp. 94–101.

[169] P. Murray and R. W. Thackray. *Differential thermal analysis of the uranium oxides*. Tech. rep. AERE-M/R-632. Gt. Brit. Atomic Energy Research Establishment, Harwell, Berks, England, Jan. 1951.

[170] *CXRO X-Ray Interactions With Matter*. URL: `http://henke.lbl.gov/optical_constants/`.

[171] K. Ando and Y. Oishi. “Diffusion Characteristics of Actinide Oxides”. In: *Journal of Nuclear Science and Technology* 20.12 (Dec. 1983), pp. 973–982.

[172] A. B. Auskern and J. Belle. “Self-Diffusion of Oxygen in Uranium Dioxide”. In: *The Journal of Chemical Physics* 28.1 (Jan. 1958), pp. 171–172.

[173] J. Belle. “Oxygen and uranium diffusion in uranium dioxide (a review)”. In: *Journal of Nuclear Materials* 30.1 (Apr. 1969), pp. 3–15.

[174] J. F. Marin and P. Contamin. “Uranium and oxygen self-diffusion in UO_2”. In: *Journal of Nuclear Materials* 30.1-2 (Apr. 1969), pp. 16–25.

[175] A. S. Bayoglu and R. Lorenzelli. “Etude de la diffusion chimique de l’oxygène dans PuO_{2-x} par dilatométrie et thermogravimétrie”. In: *Journal of Nuclear Materials* 82.2 (July 1979), pp. 403–410.

[176] J. M. Floyd. “Interpretation of transport phenomena in non-stoichiometric ceria.” In: *Indian J Technol* 11.11 (1973), pp. 589–594.

[177] K. C. Kim and D. R. Olander. “Oxygen diffusion in UO_{2-x}”. In: *Journal of Nuclear Materials* 102.1 (Nov. 1981), pp. 192–199.

[178] D. I. R. Norris and P. Kay. “Oxygen potential and lattice parameter measurements in (U, Ce)O2 - zx”. In: *Journal of Nuclear Materials* 116.2 (June 1983), pp. 184–194.

[179] P. J. Spencer. “A brief history of CALPHAD”. In: *Calphad* 32.1 (Mar. 2008), pp. 1–8.

[180] A. Kroupa. “Modelling of phase diagrams and thermodynamic properties using Calphad method – Development of thermodynamic databases”. In: *Computational Materials Science*. Multiscale simulation of heterogeneous materials and coupling of thermodynamic models 66 (Jan. 2013), pp. 3–13.

[181] M. Hillert. “Partial Gibbs energies from Redlich-Kister polynomials”. In: *Thermochimica Acta* 129.1 (June 1988), pp. 71–75.

[182] E. A. Aitken, S. F. Bartram, and E. F. Juenke. “Crystal chemistry of the rhombohedral $MO_3.3R_2O_3$ Compounds”. In: *Inorganic Chemistry* 3.7 (July 1, 1964), pp. 949–954.

[183] *NEA Nuclear Science Committee - Thermodynamics of Advanced Fuels – International Database (TAF-ID).*

[184] S. Grandjean et al. *Method for co-precipitation of actinides in different oxidation states and method for preparation of mixed actinide compounds.* Nov. 2017.

[185] S. M. Manna, S. B. Roy, and J. B. Joshi. *Study of crystallization and morphology of ammonium diuranate and uranium oxide — Elsevier Enhanced Reader.* Dec. 2013.

[186] B. Narasimha Murty et al. “Influence of temperature of precipitation on agglomeration and other powder characteristics of ammonium diuranate”. In: *Powder Technology* 115.2 (Apr. 2001), pp. 167–183.

[187] S. Manna et al. "Study of calcinations of ammonium diuranate at different temperatures". In: *Journal of Nuclear Materials* 426.1 (July 2012), pp. 229–232.

[188] G. Heisbourg et al. "The kinetics of dissolution of $Th_{1-x}U_xO_2$ solid solutions in nitric media". In: *Journal of Nuclear Materials* 321.2 (Sept. 2003), pp. 141–151.

[189] *Pompe jauge à oxygène GEN'AIR SETNAG*. URL: `https://www.setnag.com/fr/produits/gen-air-23.html`.

[190] M. Dusek, V. Petricek, and L. Palatinus. "Introduction to JANA2006". In: *Acta Crystallographica Section A Foundations of Crystallography* 62.a1 (Aug. 2006), s46–s46.

[191] B. Ravel and M. Newville. "ATHENA, ARTEMIS, HEPHAESTUS: data analysis for X-ray absorption spectroscopy using IFEFFIT". In: *Journal of Synchrotron Radiation* 12.Pt 4 (July 2005), pp. 537–541.

List of Figures

List of Tables

Appendix A

Synthesis of (U,Nd) mixed oxalate

Wet route manufacturing processes are commonly used to produce homogeneous samples. These type of processes consists on the co-precipitation of actinides and lanthanides by using an anionic complex to precipitate as a salt, then they consist on performing a calcination stage to decompose the precursors and form the mixed oxides. Finally, a sintering process is done to press the powder and form the pellet.

For the precipitation of a multi-element solution to happen, there are some important conditions that need to be considered [184], such as:

- The solubility of all mixed elements must be similar an relatively high before the precipitation,
- The solubility of all mixed elements must be similar and relatively low during the precipitation ,
- The precipitation kinetics of all elements must be sensibly the same,

During the mixture there are a number of parameters that need to be taken into account to carry out the precipitation properly like the pH, the concentration of the initial solutions, the solution mixing methods, drying techniques, temperature of the system, time and stirring conditions. Indeed, several manufacturing methods were developed to produce homogeneous samples through ionic co-precipitation such as the Sol-Gel route, oxalic-precipitation or the Ammonium DiUranate (ADU) route, among others [185–187]. Of all these different methods, the oxalic co-precipitation was selected to produce the samples used in this work, manufactured at the ICSM/LIME.

The manufacturing process through the co-precipitation is particularly convenient since the anionic complex under reducing conditions has the flexibility of hosting both a tetravalent and a trivalent cation where, depending on the proposed synthesis method, is capable of presenting different spatial arrangements with different crystallographic structures.

This work is based on the study of the U-Nd-O system, where the co-precipitation of these two cations (U^{+4} and Nd^{+3}) is meant to imply the formation of an oxalate

precursor using only H_3O^+ as a single charge compensator. Three different concentrations were chosen to be prepared as a result of mixing the initial solutions to form the precipitate $(H_3O)_yU_{(1-y)}Nd_y(C_2O_4).nH_2O$, with y=0.04, 0.17, 0.25. The U^{+4} containing solution was obtained from metallic uranium and hydrochloric acid (HCl) to form UCl_4 with a final concentration of $4.07.10^{-4}$ mol/g. The Nd^{+3} containing solution was prepared from the dissolution of $NdCl_(3)$ and dilution to reach a final concentration of $4.721.10^{-4}$ mol/g.

The mixture of the metallic containing solutions (U^{+4} and Nd^{+3}) was made by pouring dropwise these two solutions into a large excess of oxalic acid (0.5 M) to insure the precipitation of all cations at room temperature under stirring conditions. After few minutes, the precipitation was complete and the solution centrifuged, washed with water and ethanol, and finally dried at 363 K. The co-precipitation reaction is developed almost instantaneously [188] and it can be expressed as,

$$(1-y)U^{+4} + yNd^{+3} + yH_3O^+ + 2C_2O_4^{-2} \rightarrow (H_3O)_yU_{(1-y)}Nd_y(C_2O4)_2.nH_2O \downarrow$$

Appendix B

Experimental techniques

B.1 Generation and control of atmospheres containing oxygen

The oxygen controlling device allows generating and measuring the oxygen atmospheres based on the zirconia ionic conductions principle. At high temperature, zirconia allows migration of oxygen ions. An electrochemical voltage appears between the two metal plated faces of a zirconia wall when they are in contact with two gaseous atmospheres which are at different partial pressures. This voltage obeys the Nernst law,

$$E = \frac{RT}{4F} \cdot ln\frac{(P^{meas})}{(P^{ref})}$$

where E is the voltage (in V), T the temperature (in K), R and F the gas and Faraday constants. Knowing one of the oxygen partial pressures (reference pressure), and measuring the voltage (E) and the temperature (T), it is possible to obtain the P^{meas} [189].

B.2 X-ray Diffraction

All XRD characterizations at room temperature before and after the thermal treatments were carried on with two identical equipments, one located at the CEA in Cadarache and the other at the Institut de chimie séparative de Marcoule (ICSM). Both consisted of a Bruker D8 Advanced X-Ray diffractometer (Cu K$\alpha_{1,2}$ radiation, λ=1.5418 Å) equipped with a linear Lynx-Eye detector. The step used on the collection of the diffraction pattern was 0.01° and a counting time of 0.5 s/step within the 2θ range of 5-145° for the patterns before the thermal treatment and 20-90° for the patterns after the thermal treatment.

In situ high temperature XRD acquisitions were obtained at the ICSM facility. The powders were heated with a ramp of 10 K.min^{-1} using a gas mixture of Ar+4%H_2.

XRD patterns were measured within the 2θ range of 10-130° with steps of 0.02° and couting time of 0.5 s.step^{-1}. The maximal assessed temperature was 1373 K and then cooled down to room temperature and again heated up until 1373 K, with intermediate measures every 100 K. The cooling and heating ramp were estimated to be 0.5 K.s^{-1}.

All XRD patterns were evaluated using the Jana2006 software [190]. The samples were probed by the Le Bail method to assess the lattice parameter [154]. The characterization and identification of the different crystallographic phases along this work were assessed by performing the Rietveld refinement [156]. This method consists on defining the best possible values that represent the crystallographic state of the samples (lattice parameter, strain, cristallite size, phase fraction, Debye-Waller factor). Additional illumination corrections were needed to the patterns of the Nd-based pristine samples up to a 2θ=24.62° to perform the Rietveld refinements.

B.3 X-ray Absorption Spectroscopy

B.3.1 Principles

The principle of the X-ray Absorption Spectroscopy is the photoelectric effect that occurs when an atom is irradiated with X-rays with an energy lower than 500 keV. This effect takes place when the incident X-ray matches the electron binding energy, which produces the promotion of the electron to an empty higher energy level or to the continuum. This promotion is seen on the diagram as sharp peak that starts at the absorption edge. During this work, the assessed levels were the U and Nd L_3-edge (17.166 keV and 6.208 keV, respectively) and the U M_4-edge (3.7 keV). Following the promotion of the excited electron, there is a disexcitation of this electron by emitting X-rays of well-defined energy. The intensity of the X-ray emission I_f is related to the absorption coefficient μ(E) according to the Lambert-Beer's law, which can be measured in transmission geometry. The representation of the absorption coefficient as a function of the incident energy is called X-ray absorption spectrum. Figure B.1 schematizes the spectra collected on the sample doped with 4, 17 and 25%Nd at the U L_3-edge.

The full XAS spectrum is divided into two regions: X-ray Absorption Near Edge Structure (XANES) and the Extended X-ray Absorption Fine-structure Spectroscopy (EXAFS). The XANES assessment is normally dedicated to probe the oxidation states and coordination chemistry, while EXAFS region is defined by the local environments in terms of the interatomic distances, coordination number and species of the neighbors of the absorbing atom.

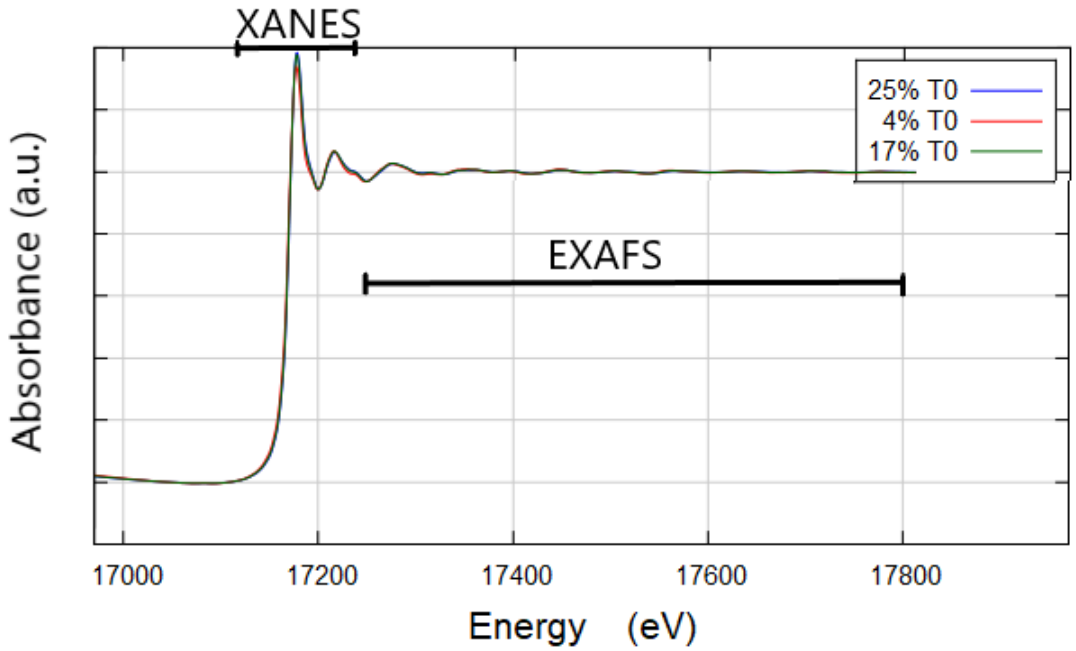

Figure B.1: XAS spectra collected on this work at the U L_3-edge.

B.3.2 Experimental setup of the acquisitions at the Mars beamline

The U M_4-edge (3.7 keV) HERFD-XANES measurements of all samples were performed at the MARS beamline of the Soleil Synchrotron located in Saclay. All spectra were acquired using the available emission spectrometer equipped with a Si(220) spherically bent diced crystal with curvature radius of 1 m, a KETEK single element silicon solid state (SDD) detector, along a Rowland type geometry. Samples were oriented at 45° from the incident beam, and the emission spectrometer was positioned at 90° from the incident beam to minimize self-absorption effects. A He-chamber was used to reduce the X-rays path through air. The incident beam size was 300x200 μm^2. In addition, U L_3-edge (17.166 keV) and Nd L_3-edge (6.208 keV) EXAFS spectra were also collected in fluorescence mode using a 13-element HPGe detector from ORTEC. The beamline double-crystal monochromator (DCM) consists in a pair of Si(220) crystals for the U L_3-edge and a pair of Si(111) crystals for the Nd L_3-edge. Energy calibration was performed by measuring Y K-edge (17.038 keV) of a Y metallic foil for U L_3-edge and Fe K-edge (7.112keV) of a Fe metallic foil for Nd L_3-edge.

B.3.3 Data analysis

The treatment of the XAS data was performed with the software package Demeter [191]. ATHENA software was used to remove the pre-edge data, as well as to normalize the post-edge using linear functions at the U M_4-edge. Finally, the energy threshold (E0) was defined as the maximum of the first derivative of the white-line

relative to the incident energy. For EXAFS, the ATHENA software was used for extracting the EXAFS oscillations. The ARTEMIS software was used for the curve fitting in the k space and Fourier transform.

Appendix C

Solution of the differential equation in spherical coordinates by separation of variables

One way to solve this problem is express the equation 3.2 as the product of two functions, $u(r,t) = P(r)T(t)$, which satisfy also the initial and boundary conditions, or

$$\frac{du}{dt}(r,t) = D.[\frac{d^2u}{dr^2}(r,t) + \frac{2}{r}.\frac{du}{dr}(r,t)],$$

for $0 \leq r \leq R$ and $t \geq 0$

Considering the initial and boundary conditions as,

$$u(r,0) = u_0 \text{ for } 0 \leq r \leq R,$$

$$u(R,t) = 0 \text{ for } t \geq 0$$

Separating variables, we find that t must satisfy,

$$T' = -\lambda DT, \tag{C.1}$$

while, P must satisfy,

$$-\left\{P'' + \frac{2}{r}P'\right\} = \lambda P \; and \; P(a) = 0, \tag{C.2}$$

where λ is a constant. The solution to C.1 is

$$T(t) = e^{-\lambda Dt} \tag{C.3}$$

To solve this equation, it is first necessary to express the equation C.2 like the Sturm-Liouville equation, which means that we have to find a function *p(r)* so that,

$$p[P'' + \frac{2}{r}P'] = [pP']' = pP'' + p'P'$$

This requires that *p' = 2p/r*, so $p(r) = r^2$ will suffice.

$$-[r^2P'' + 2rP'] = -[r^2P']' = \lambda r^2 P \tag{C.4}$$

Equation C.4 has the form of a Sturm-Liouville equation with the weight function r^2. To simplify the equation C.4, we can substitute $S = rP$. Then, $S' = rP' + P$ and $S'' = rP'' + 2P'$. Making this substitution into the differential equation, we have $-rS'' = \lambda rS$, or $-S'' = -\lambda S$.

From equation C.4 after the substitution of S, the boundary conditions satisfied by S are *S(0)=0.P(0)=0* and *S(R)=R.P(R)=0*. Hence, the function *S(r)=rP(r)* must satisfy,

$$-S'' = \lambda S, \text{ with } S(0)=S(R)=0$$

The solutions for the Sturm-Liouville problems are,

$$\lambda_n = \frac{n^2\pi^2}{R^2} \text{ and } S_n = sin\frac{n\pi r}{R}, \text{for } n = 1, 2, 3, ... \tag{C.5}$$

To better visualize P_n, notice that there is not an actual singularity at *r=0*, since

$$P = S/r,\ P(0) = \lim_{r\to 0} P_n(r) = \lim_{r\to 0} \frac{sin(n\pi r/R)}{r} = \frac{n\pi}{R}$$

From C.4 and the C.5, the solution of the product is,

$$V_n(r,t) = e^{-Dn^2\pi^2t/R}.\frac{sin(n\pi r/R)}{r}, \text{ for } n = 1, 2, 3, ... \tag{C.6}$$

By superposition a convergent infinite series of the form

$$u_n(r,t) = \sum_{n=1}^{\infty} A_n u_n(r,t)$$

$$u_n = \sum_{n=1}^{\infty} A_n e^{(-Dn^2\pi^2t/R^2} \frac{sin(n\pi r/R)}{r} \tag{C.7}$$

We have to choose the coefficient A_n so that *u(r,0)=u*$_0$. Multiplying r at both members and evaluating t=0, it becomes,

$$u_0 r = \sum_{n=1}^{\infty} A_n sin\frac{n\pi r}{R} \tag{C.8}$$

This is the Fourier sine series for the function $u_0 r$ =. The coefficients are $A_n = (-1)^{(n+1)}.2Ru_0/\pi n$, so

$$\frac{1}{2} = \sum_{n=1}^{\infty} (-1)^{(n+1)} \frac{sin(n\pi r/R)}{n\pi r/R} \text{ for } 0 < r < R \tag{C.9}$$

Inserting the coefficients A_n into equation C.7 gives the solution,

$$u_n(r,t) = 2u_0 \sum_{n=1}^{\infty} (-1)^{(n+1)} e^{(-Dn^2\pi^2 t/R^2)} \frac{sin(n\pi r/R)}{n\pi r/R} \tag{C.10}$$

Now we are in conditions of expressing the actual oxygen concentration, $C(r,t)$ in terms of the transient oxygen concentration $u(r,t)$, like

$$C(r,t) = C_f + V(r,t)$$

To give the final expression,

$$\mathbf{C(r,t)} = C_f + 2(C_0 - C_f) \sum_{n=1}^{\infty} (-1)^{(n+1)} e^{(-Dn^2\pi^2 t/R^2)} \frac{sin(n\pi r/R)}{n\pi r/R} \tag{C.11}$$

Appendix D

Parameters obtained after the optimization of the thermodynamic model

The previously existent thermodynamic model was optimized also through a CALPHAD assessment. As presented in Chapter 4 of this manuscript, all interaction parameters of the FCC phase were changed. In addition, the rhombohedral phase was added to improve the calculation of the ternary phase diagrams at different temperatures. Finally, a single parameter of the Liquid phase was also modified to stabilize this phase at higher temperatures.

A three-sublattice model was to describe the FCC phase, they can be numbered as,

$$(U^{+3}, U^{+4}, U^{+5}, Nd^{+3})\ (O^{-2}, Va)\ (O^{-2}, Va)$$

Therefore, with the optimized parameters, the Gibbs energy according the CEF, G^{CEF}, for the FCC phase would be,

$$\begin{aligned} G^{(U,Nd)O_2} = \sum_i \sum_j \sum_k G^{(U,Nd)O_2}_{i:j:jk} + RT \sum_i y_i.ln(y_i) + 2RT \sum_j y_j.ln(y_j) \\ +RT \sum_k y_k.ln(y_k) + \sum_{i_1} \sum_{i_2} \sum_j \sum_k y_{i_1} y_{i_2} y_j y_k [{}^0L^{(U,Nd)O_2}_{i_1 i_2 jk} + (y_{i_1} - y_{i_2}).{}^1L^{(U,Nd)O_2}_{i_1 i_2 jk}] \\ \sum_{i_1} \sum_{i_2} \sum_{i_3} \sum_j \sum_k y_{i_1} y_{i_2} y_{i_3} y_j y_k [{}^0L^{(U,Nd)O_2}_{i_1 i_2 i_3 jk}] \end{aligned} \tag{D.1}$$

where y_i represents the fraction of the species i in the first sublattice (j and k for the second and third sublattices, respectively), $G^{(U,Nd)O_2}_{i:j:jk}$ are the Gibbs energies for the different compounds considering the species i, j and k, for the first, second and third sublattices, respectively, and ${}^nL^{(U,Nd)O_2}$ are the interaction parameters between

the species, in this case, in the first sublattice.

The optimized interaction parameters for the FCC phase are listed in Table D.2.

Thermodynamic parameters of the $(U, Nd)O_2$ phase	Reference
$G_{(U^{+3})(O^{-2})(O^{-2})}$	
$G_{(U^{+4})(O^{-2})(O^{-2})}$	
$G_{(U^{+5})(O^{-2})(O^{-2})}$	
$G_{(U^{+3})(Va)(O^{-2})}$	
$G_{(U^{+4})(Va)(O^{-2})}$	
$G_{(U^{+5})(Va)(O^{-2})}$	
$G_{(U^{+3})(O^{-2})(Va}$	[12]
$G_{(U^{+4})(O^{-2})(Va}$	
$G_{(U^{+5})(O^{-2})(Va)}$	
$G_{(U^{+3})(Va)(Va)}$	
$G_{(U^{+4})(Va)(Va)}$	
$G_{(U^{+5})(Va)(Va)}$	
${}^0L_{(U^{+3},U^{+4})(O^{-2})(Va)}$	
${}^1L_{(U^{+3},U^{+4})(O^{-2})(Va)}$	
${}^0L_{(U^{+4},U^{+5})(O^{-2})(O-2)}$	
$G_{(Nd^{+3})(O^{-2})(O^{-2})}$	
$G_{(Nd^{+3})(Va)(O^{-2})}$	[91]
$G_{(Nd^{+3})(O^{-2})(Va)}$	
$G_{(Nd^{+3})(Va)(Va)}$	
${}^0L_{(Nd^{+3},U^{+4})(O^{-2})(*)}$ = -870000	
${}^0L_{(Nd^{+3},U^{+5})(O^{-2})(Va)}$ = -862309.9	
${}^1L_{(Nd^{+3},U^{+5})(O^{-2})(Va)}$ -290018	This work
${}^0L_{(Nd^{+3},U^{+5})(O^{-2})(O^{-2})}$ = -1076209-345*T	
${}^0L_{(Nd^{+3},U^{+4},U^{+5})(*)(*)}$ = +50000	

Table D.1: Optimized thermodynamic parameter used on the different models to define the FCC phase [51, 91].

A three-sublattice model was also used to define the rhombohedral phase, stable at higher concentrations of Nd (typically over 70%).

$$(U^{+4}, U^{+5}, U^{+6})(Nd^{+3})_6(O^{-2})_{12}$$

The expression of the Gibbs energy according to the energy formalism can be defined as,

$$G^{UNd_6O_{12}} = \sum_l \sum_m \sum_n G^{UNd_6O_{12}}_{l:m:n} + RT \sum_l y_l ln(y_l) + 2RT \sum_m y_m ln(y) + \sum_n y_n ln(y_n) \tag{D.2}$$

where y_l represents the fraction of the species l in the first sublattice (m and n for the second and third sublattices, respectively), $G^{U,Nd_6O_{12}}_{l:m:n}$ are the Gibbs energies for the different compounds considering the species l, m and n, for the first, second and third sublattices, respectively.

Thermodynamic parameters of the UNd_6O_{12} phase	Reference
$G_{(U^{+4})(Nd^{+3})(O^{-2})}$= -803484 + 40*T + G_{UO_2} + $3G_{Nd_2O_3}$ + $0.5G_{GO_2-GAS}$	This work
$G_{(U^{+5})(Nd^{+3})(O^{-2})}$= -908641 + 62*T + $0.5G_{UO_2}$ + $0.5G_{UO_3}$ + $3G_{Nd_2O_3}$ + $0.25G_{GO_2-GAS}$	This work
$G_{(U^{+6})(Nd^{+3})(O^{-2})}$=-400000+40*T + G_{UO_3} + $3G_{Nd_2O_3}$	This work
$G_{(U^{+4})(Nd^{+3})(Va)} = G^{SER}_U + 6G^{SER}_{Nd}$	[183]
$G_{(U^{+4})(Nd^{+3})(Va)} = G^{SER}_U + 6G^{SER}_{Nd}$	[183]
$G_{(U^{+4})(Nd^{+3})(Va)} = G^{SER}_U + 6G^{SER}_{Nd}$	[183]

Table D.2: Optimized thermodynamic parameter used on the different models to define the rhombohedral phase [183].

Résumé

Etude du diagramme de phase du système U-Nd-O sous conditions stœchiométriques et sous-stœchiométriques.

Le combustible nucléaire évolue lors de son passage en réacteur, à la fois au niveau de ses propriétés physiques mais aussi chimiques par la création continue de produits de fission. Dans le cas de l'UO_2, la concentration en produits de fission est particulièrement élevée à la périphérie de la pastille de combustible, ce qui conduit à la formation d'une microstructure particulière appelée High Burn-up Structure (HBS). Cette microstructure est constituée de grains plus petits (submicroniques) que les grains trouvés dans le centre de la pastille, et d'une porosité très importante (pouvant atteindre environ 20%). La présence de cette microstructure HBS a une influence sur les propriétés du combustible, comme la dureté, la conductivité thermique et la capacité de rétention des produits de fission. Ce dernier point est primordial dans l'évaluation du terme source (nature et quantité de produits de fission relâchés) en situation d'accidents graves. Plusieurs mécanismes sont proposés pour expliquer l'origine du HBS. L'un d'entre eux suggère une origine chimique liée à la formation d'une seconde phase cristallographique lorsque la concentration en lanthanides (Ln) augmente et associée à une lacune de miscibilité dans un certain domaine du diagramme de phase (environ 5%wt Ln). En effet, l'existence d'une lacune de miscibilité a déjà été mis en évidence dans différent systèmes ternaires, telles que (U,Pu,O), (U,Ce,O) ou (U,Nd,O).

C'est dans ce contexte que la thèse s'intéresse à la description du diagramme de phase des systèmes (U,Nd,O) et (U,Ce,O), plus particulièrement le domaine sous-stœchiométrique ($U_{1-y}Nd_yO_{2-x}$ et $U_{1-y}Ce_yO_{2-x}$), dans lesquelles la lacune de miscibilité dans la phase fluorine a été identifiée. Pour cela, une étude expérimentale a été menée sur deux types de composés $(U,Nd)O_{2-x}$: des échantillons synthétisés par co-broyage (voie sèche) et des échantillons obtenus par co-précipitation (voie humide). Différentes techniques de caractérisation ont été mises en œuvre: diffraction des rayons X, observation aux microscopes électroniques à balayage et à transmission couplée à de l'analyse chimique (EDX), ainsi que spectroscopie d'absorption de rayons X.

Les analyses faites sur les échantillons produits par voie sèche ont montré un élevé degré d'hétérogénéité de composition, conduisant à la formation de plusieurs phases

métastables de structure et de composition variables. En revanche la voie humide produit des composés parfaitement homogènes, permettant ainsi l'étude des oxydes (U,Nd)O_{2-x} en conditions réductrices. Les différents traitements thermiques associés à des analyses structurales fines ont permis de définir l'évolution du paramètre de maille et du rapport O/(U+Nd) en fonction de la température pour trois compositions en Nd (4%, 17% et 25%). Ils ont aussi montré une solubilité complète du Nd dans UO_2. Une démarche analogue a été effectuée sur le système (U,Ce,O), également pour trois compositions différentes (10%, 20% et 45%). Les résultats obtenus sur ce deuxième système ont mis en évidence la présence d'une phase trigonale, caractérisée par une mise en ordre particulière des lacunes, inexistante dans la description du diagramme de phase du système (U,Ce,O) à l'heure actuel.

L'ensemble des résultats ont permis de souligner le conflit ouvert existent dans la littérature entre l'équilibre thermodynamique et les phénomènes cinétiques. En effet, la formation de phases différentes pour des teneurs de dopant proches est expliquée par la faiblesse du transport cationique à longue portée dans le domaine des températures d'intérêt. De plus, ces résultats ont mené à faire une réévaluation critique du diagramme de phases du système (U,Nd,O).

Enfin, un nouveau modèle thermodynamique du système (U,Nd,O) est proposé en utilisant la méthode CALPHAD. Ceci exclu la présence d'une lacune de miscibilité pour des conditions sous-stœchiométriques, suggérant la solubilité totale du Nd en UO_2 jusqu'à teneurs de 60%, ainsi que la présence d'une phase rhomboédrique à forte teneurs de Nd (au-delà de 60%Nd), absente dans le modèle précédent.

En résumé, ces travaux contribuent à la redéfinition des diagrammes de phase ternaire (U,Nd,O) et (U,Ce,O), permettant une meilleure connaissance des limites d'utilisation des combustibles fortement irradiés par rapport aux conditions de sécurités optimales.

université PARIS-SACLAY

ÉCOLE DOCTORALE
INTERFACES
Approches Interdisciplinaires : Fondements, Applications et Innovation

Titre: Etude du diagramme de phase du système U-Nd-O sous conditions stœchiométriques et sous-stœchiométriques.

Mots clés: Uranium, Néodyme, Lacune de miscibilité, Diagramme de phases

Résumé: Cette thèse concerne l'étude expérimentale et la modélisation thermodynamique du comportement des combustibles utilisés dans les centrales nucléaires actuelles et de génération future. L'objet de la thèse est plus précisément l'étude du système ternaire (U,Nd,O) et pour comparaison, du système ternaire (U,Ce,O). Ce système est particulièrement représentatif des produits de fission accumulés dans le combustible pour des taux de combustion élevés mais aussi dans le cas du dopage initial du combustible avec des poisons neutroniques. L'étude de ce système présente des défis importants en raison de la compétition entre phénomènes thermodynamiques et cinétiques. Il s'agit, en effet, d'un système hors équilibre où la mise en ordre à longue portée des structures locales est défavorisée par la lenteur du transport cationique dans la plage de températures d'intérêt. Au cours de cette thèse, une analyse de la littérature existante a motivé la fabrication d'échantillons aux caractéristiques bien définies par des méthodes de métallurgie des poudres et par des méthodes de chimie douce assurant un contrôle de la répartition des dopants. Les résultats obtenus par de nombreuses techniques de caractérisation (DRX, MEB, MET, XAS) sur des échantillons traités thermiquement dans des conditions oxydantes ou réductrices ont permis une réévaluation critique des diagrammes de phases actuellement utilisés. Nous avons pu proposer des modifications conduisant à un nouveau diagramme de phases (U,Nd,O), permettant ainsi une meilleure connaissance des limites d'utilisation des combustibles en conditions nominales.

Title: Assessment of the ternary phase diagram on the stoichiometric and hypo stoichiometric U-Nd-O system.

Keywords: Uranium, Neodymium, Miscibility gap, Phase diagram.

Abstract: This thesis concerns the experimental study and thermodynamic modeling of the behavior of advanced fuels used in current and future generation nuclear power plants. The subject of the thesis is more precisely the study of the ternary system (U,Nd,O) and for comparison purposes of (U,Ce,O). Using Nd as dopant can be considered particularly representative of the fission products accumulated in the fuel for high combustion rates and also of the initial atomic substitutions in the fuel doped by neutron poisons. The study of this system presents significant challenges due to the open conflict between thermodynamic and kinetic phenomena. It is indeed an out-of-equilibrium system where the long-range ordering of local structures is not favored by the negligible atomic transport in the cation sublattice over the range of temperatures of interest. During this thesis, a review of the existing literature motivated the manufacture of samples with well-defined characteristics by powder metallurgy methods and by soft chemistry methods leading to a control of dopant distributions. The results obtained by numerous characterization techniques (XRD, SEM, TEM, XAS) on samples treated thermally under oxidizing or reducing conditions allowed a critical re-evaluation of the currently used phase diagrams. We have modeled a new phase diagram that includes new experimental results allowing a better knowledge of the limits of use of nuclear fuels respecting nominal conditions.

Université Paris-Saclay
Espace Technologique / Immeuble Discovery
Route de l'Orme aux Merisiers RD 128 / 91190 Saint-Aubin, France